SUSCEPTIBILITY OF LOW-TEMPERATURE PLASMA NITRIDED 17-4 PH (H1150D) TO SULPHIDE STRESS CRACKING (SSC) IN TYPICAL OILFIELD ENVIRONMENT

by

Mario Sergio Della Roverys Coseglio

A thesis submitted to the University of Birmingham for the degree of
DOCTOR OF PHILOSOPHY

School of Metallurgy and Materials
College of Engineering and Physical Sciences
University of Birmingham
April 2018

Abstract

To attend the growing global demand for energy, oil production—expected to grow in the foreseeable future—relies on the extraction from unconventional resources, such as deep deposits off the coast and ultra-deep water. These environments are contaminated with significant amounts of hydrogen sulphide, a by–product that promotes hydrogen absorption and subsequent failure by sulphide stress cracking (SSC). The 17-4 PH—a stainless steel widely used for oilfield components—is susceptible to SSC, in spite of its favourable combination of properties. In this study, plasma–based treatments, often used to improve wear resistance, were identified as potential methods to increase the resistance to SSC. To evaluate it, the 17-4 PH was surface–modified by conventional and low–temperature plasma nitriding (LTPN) and submitted to standard SSC experiments. LTPN resulted in superior resistance to SSC compared to both unmodified and HTPN conditions, attributed to the formation of a nitrogen–rich layer comprising mixed iron nitrides (ε–$Fe_{2\text{-}3}N$ and γ'–Fe_4N) and expanded martensite without precipitation of chromium nitrides. The protection provided by this structure was mainly due to the compressive residual stress induced by nitriding, combined with the superior resistance to localised corrosion and the reduced hydrogen uptake by the substrate.

Dedicated to my wife Mariane and my son Pedro.

Acknowledgements

I am grateful to all who somehow contributed to this work, specially those who engaged in valuable discussions which helped me clarify and view this research from different perspectives. That included formal and informal conversations with scientists, technicians, experienced professionals from industry and even with friends and family members with no background on the subject.

I am honoured to have been awarded a scholarship from the University of Bir-mingham and CAPES (Coordenação de Aperfeiçoamento de Pessoal de Nível Superior), a Brazilian federal agency that coordinates the quality improvement of higher education professionals in Brazil. This programme was created to enhance collaborative research between Brazil and the University of Birmingham and I felt pleased to be able to contribute with a topic of great industrial interest for both countries. This work would not have been possible without the financial support from these institutions.

I am thankful to the professors from the postgraduate programme in mechanical and materials engineering (PPGEM) at the Federal University of Technology (UTFPR) in Brazil that encouraged me to get started.

Thank you to my former supervisor, Dr. Brian Connolly, now at the University of Manchester, for the guidance in the first year of this project and for having set up the connections between this PhD, one of his industrial partners (Exova Corrosion Centre) and the Surface Engineering group at the University of Birmingham.

I would like to express my sincere gratitude to my supervisor Dr Xiaoying Li and co-supervisor Professor Hanshan Dong, from the Surface Engineering group in Metallurgy and Materials, who assumed the supervision of my PhD from the second year until the end of the programme and provided constant support and valuable advices. A special thanks to their efforts to maintain the scope of the project and the original deadlines

after the transition of supervision. My gratitude is extended to the following members of the Surface Engineering group for their support with the equipment in our department: Dr Zhenxue Zhang, Dr Kaijie Lin, Dr Shaojun Qi, Yana Liang, Xiaochao Ji and specially to Behnam Dashtbozorg and Valter Jantara Junior for the insightful discussions about metallurgy and surface engineering.

I would like to thank Dr Chris Fowler and Mr Phil Dent from Exova Corrosion Centre in UK for the professional advices and for having allowed me to use their facilities in Dudley for the experiments with hydrogen sulphide. My gratitude is extended to Phil Williamson (laboratory manager), to all the technicians (especially Philippa Smyth and Paul Dunn) and to Kim Chua, Aaron Plant, Dr Karsten Wiegers and Dr Richard Doyle (Corrosion Engineering).

Lastly, I would like to thank my supportive wife Mariane for her patience, encouragement and for being my inspiration to keep going. When our son Pedro was born, by the end of the third year, he brought additional joy to our lives and I became even more inspired and productive. Writing and parenting at the same time was challenging, of course, but I enjoyed every moment. That was only possible because of the unconditional support from my loving wife, the best mammy ever.

List of Publications

Mario Sergio Della Roverys Coseglio, "Sulphide stress cracking of 17-4 PH for applications in oilfield components", *Materials Science and Technology*, 33:16, 1863-1878, 2017. DOI: 10.1080/02670836.2017.1330230.

Mario S. D. R. Coseglio , Brian J. Connolly, Xiao-Ying Li, Hanshan Dong, Phil Dent, Chris Fowler, "Susceptibility of plasma nitrided 17-4 PH to sulfide stress cracking (SSC) in H_2S-containing environments", NACE-2017-9342, CORROSION 2017, 26-30 March, New Orleans, Louisiana, USA.

Contents

List of Figures

List of Tables

List of Abbreviations

AIDE	**A**dsorption-**I**nduced **D**islocation **E**mission
AISI	**A**merican **I**ron and **S**teel **I**nstitute
API	**A**merican **P**etroleum **I**nstitute
ASPN	**A**ctive-**S**creen **P**lasma **N**itriding
ASS	**A**ustenitic **S**tainless for **S**teel
ASTM	**A**merican **S**ociety for **T**esting and **M**aterials
CR	**C**orrosion **R**ate
CRA	**C**orrosion-**R**esistant **A**lloys
DCPN	**D**irect **C**urrent **P**lasma **N**itriding
DCB	**D**ouble **C**antilever **B**eam
DIN	**D**eutsches **I**nstitut für **N**ormung
EAC	**E**nvironmentally-**A**ssisted **C**racking
EBSD	**E**lectron **B**ack**S**catter **D**iffraction
EDM	**E**lectrical **D**ischarge **M**achining
EDS	**E**nergy-**D**ispersive X-ray **S**pectroscopy
EFC	**E**uropean **F**ederation of **C**orrosion
EIS	**E**lectrochemical **I**mpedance **S**pectroscopy
EPR	**E**lectrochemical **P**otentiodynamic **R**eactivation
HAC	**H**ydrogen-**A**ssisted **C**racking
HE	**H**ydrogen **E**mbrittlement

HEDE	**H**ydrogen-**E**nhanced **DE**cohesion
HEE	**H**ydrogen-**E**nvironment **E**mbrittlement
HELP	**H**ydrogen-**E**nhanced **L**ocalised **P**lasticity
HSLAS	**H**igh-**S**trength **L**ow-**A**lloy **S**teel
HTPN	**H**igh-**T**emperature **P**lasma **N**itriding
ICDD	**I**nternational **C**entre for **D**iffraction **D**ata
IHE	**I**nternal **H**ydrogen **E**mbrittlement
LME	**L**iquid-**M**etal **E**mbrittlement
LTPN	**L**ow-**T**emperature **P**lasma **N**itriding
NACE	**N**ational **A**ssociation of **C**orrosion **E**nginners (NACE International)
OCP	**O**pen **C**ircuit **P**otential
PH	**P**recipitation **H**ardening
RSRT	**R**ippled **S**train **R**ate **T**est
SA	**S**olution **A**nnealed
SCE	**S**tandard **C**alomel **E**lectrode
SEM	**S**canning **E**lectron **M**icroscopy
SSC	**S**ulphide **S**tress **C**racking
SCC	**S**tress **C**orrosion **C**racking
SSRT	**S**low **S**train **R**ate **T**est
TEM	**T**ransmission **E**lectron **M**icroscopy
UNS	**U**nified **N**umbering **S**ystem

Chapter 1

Introduction

This chapter describes and contextualises the problem being investigated and states the general and specific objectives of this work. It presents a brief description of the research methods, scope, contributions and overview of the thesis.

1.1 Problem statement

Global oil consumption has been continuously growing [1] (Figure 1.1) and it is expected to continue to grow in the next decades, as predicted by the Energy Information Association [2]. To attend this demand, oil is being extracted from unconventional reserves, which require advanced technology to become operational and economically viable [3]. Offshore deposits in ultra-deep water (i.e. water depth greater than 2000 m) and deep reservoirs ($>$ 3000 m), as those located off the coast of Brazil, for example, require sophisticated drilling technology to extract oil from under a thick pre-salt layer. Moreover, these environments contain significant amounts of hydrogen sulphide (H_2S), a toxic gas [4] generated naturally in oil and gas reservoirs [5] that promotes hydrogen absorption into metallic components and thereby increases the chances of hydrogen-assisted failures. For high-strength steels, widely used in unconventional offshore installations to overcome high pressures from these

environments [6, 7], failures associated with hydrogen embrittlement are a major concern. In the presence of H_2S, sudden brittle fracture of high-strength steels can occur when sufficiently high tensile stress is applied to the component. This phenomenon, known as sulphide stress cracking (SSC) [8], was first reported in 1951 [9] and became subject of intense research to avoid further catastrophic failures.

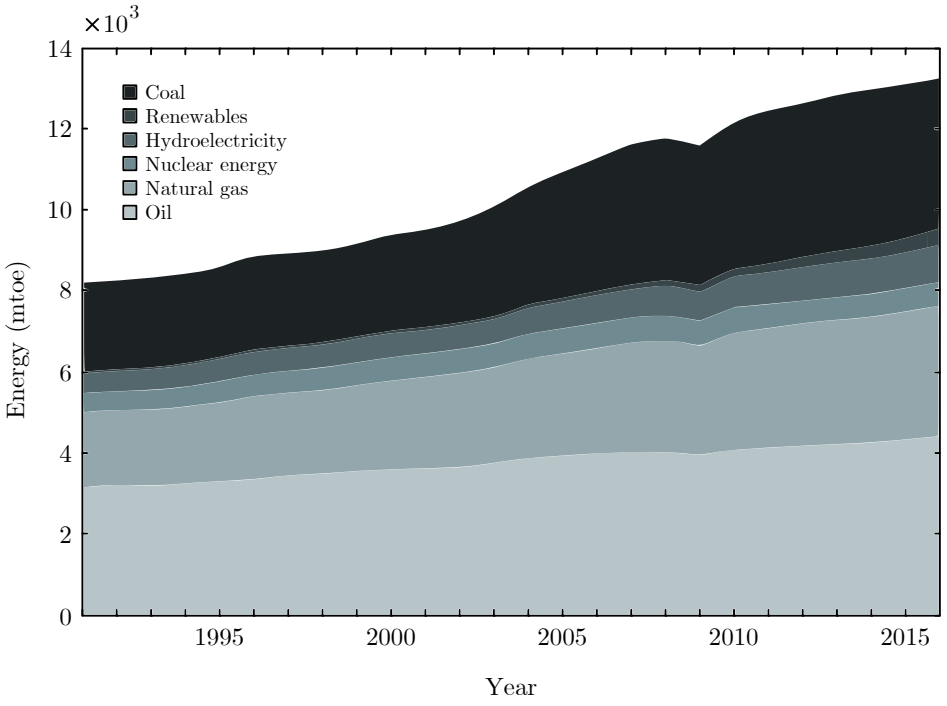

FIGURE 1.1: Global primary energy consumption in million tones of oil equivalent from 1991 to 2016. Data from [1]

A variety of high-strength steels are used in the oil and gas industry, including precipitation hardening (PH) stainless steels, of which the 17-4 PH (UNS S17400) is the most used for subsea components [10]. Despite being attractive due to its favourable combination of strength, toughness, corrosion resistance and cost [11, 12], the 17-4 PH is highly susceptible to SSC [13–15]. This low resistance has been acknowledged by NACE

MR0175/ISO 15156 [16]—an international standard providing recommendations and requirements for qualification of materials exposed to H_2S—which specifies environment conditions (e.g. minimum pH and maximum H_2S concentration), heat treatment parameters and maximum hardness to prevent SSC of valves, tubing hangers and other subsurface components. Recently, an additional limitation—maximum allowable stress —was added to the standard [17], recognising that failures can occur at stress levels as low as 20 % of the yield strength of the material, even when the other criteria are met. This restriction clearly poses limitations for the use of the 17-4 PH in the oil and gas industry.

An additional limitation of the 17-4 PH is its low wear resistance, which can be improved by thermochemical treatments, such as plasma nitriding [18]. These treatments result in the formation of thin hard layers supersaturated with nitrogen, which can also provide superior corrosion resistance if the treatment is performed at sufficiently low temperature to avoid chromium depletion from the grain boundaries [19]. A recent attempt to use similar treatment (i.e. plasma oxy-nitriding) to increase cracking resistance of the 17-4 PH [20] showed high susceptibility to SSC, comparable to that obtained for the unmodified material in different studies. Plasma nitriding, however, seems to be a promising technology to prevent SSC, provided that the treatment temperature is maintained below that used in conventional nitriding and a compound layer is formed near the surface. For these conditions, the nitrided layer can act as a barrier for hydrogen entry into the substrate, as suggested in permeation studies with iron and steels [21–29] , without detrimental effect on its corrosion resistance. Besides, the compressive residual stress induced by the treatment [30] can reduce or suppress the tensile stress and therefore minimise the chances of failure by SSC.

1.2 Objectives

The main aim of this work was to use low-temperature plasma nitriding (LTPN) to reduce the susceptibility of the 17-4 PH to SSC in typical oilfield environment containing H_2S and CO_2 as balance gas. In this context, low temperature is defined as any temperature—below that used in conventional nitriding (i.e. 450-500 °C)—that prevents the precipitation of chromium nitrides and result in the formation of a compound layer on the top of the modified section. The secondary objectives are as follows:

- Select appropriate method(s) to evaluate the SSC susceptibility;
- Determine the SSC susceptibility of the unmodified 17-4 PH in typical oilfield environment containing H_2S (CO_2 as balance gas);
- Select adequate plasma nitriding parameters (e.g. time, temperature and gas mixture) and method (direct current or active screen techniques) to obtain the required structure;
- Determine the corrosion resistance of the unmodified and plasma nitrided 17-4 PH in typical oilfield environment with mixed H_2S/CO_2, pure H_2S and pure CO_2;
- Determine the SSC susceptibility of plasma nitrided 17-4 PH in pure H_2S;
- Evaluate the residual stress induced by the nitriding treatment;
- Evaluate the hydrogen uptake by the substrate material after nitriding;
- Analyse the mechanisms of SSC in plasma nitrided 17-4 PH.

1.3 Rationale, significance and novelty

To date, there is no reference in the literature to the use of low-temperature plasma nitiding to increase the resistance to SSC of PH stainless steels and therefore this work is an original contribution to the current knowledge in this field. Moreover, this subject is of great technological interest to the oil and gas industry, since the limits of application of the unmodified 17-4 PH in oilfield components are being narrowed. If greater susceptibility is obtained after the surface modification, there is potential to reduce failures by SSC and the costs associated with it (e.g. replace and shut down, downtime) and the current limits can be reviewed. Moreover, there is no published work on the corrosion resistance of plasma nitrided 17-4 PH in H_2S-containing environments and thus the present work also contributes in this aspect.

1.4 Scope

The material selected to be evaluated in this work is the martensitic precipitation-hardening stainless steel 17-4 PH, heat treated to the H1150D condition, recommended by NACE MR0175/ISO 15156 [16] for applications in H_2S-containing environments. All the experiments were conducted at $(23 \pm 2)\,°C$ and ambient pressure and the material—unmodified and plasma nitrided—was exposed to the same environment (i.e. synthetic produced containing $165\,g\,L^{-1}$ of NaCl and pH 4.5 ± 0.2 saturated with $3.4\,kPa$ of H_2S (CO_2 as balance gas) and loaded to stress levels varying from 30 to 100 % of the yield strength of the material. Additional measurements were taken in pure H_2S (SSC and corrosion) and in pure CO_2 (corrosion), particularly for the low-temperature plasma nitrided condition. Two plasma nitriding conditions were evaluated: conventional (at $500\,°C$) and

low-temperature (at 420 °C). Details about the reasoning for the selection of each parameter are presented in each chapter.

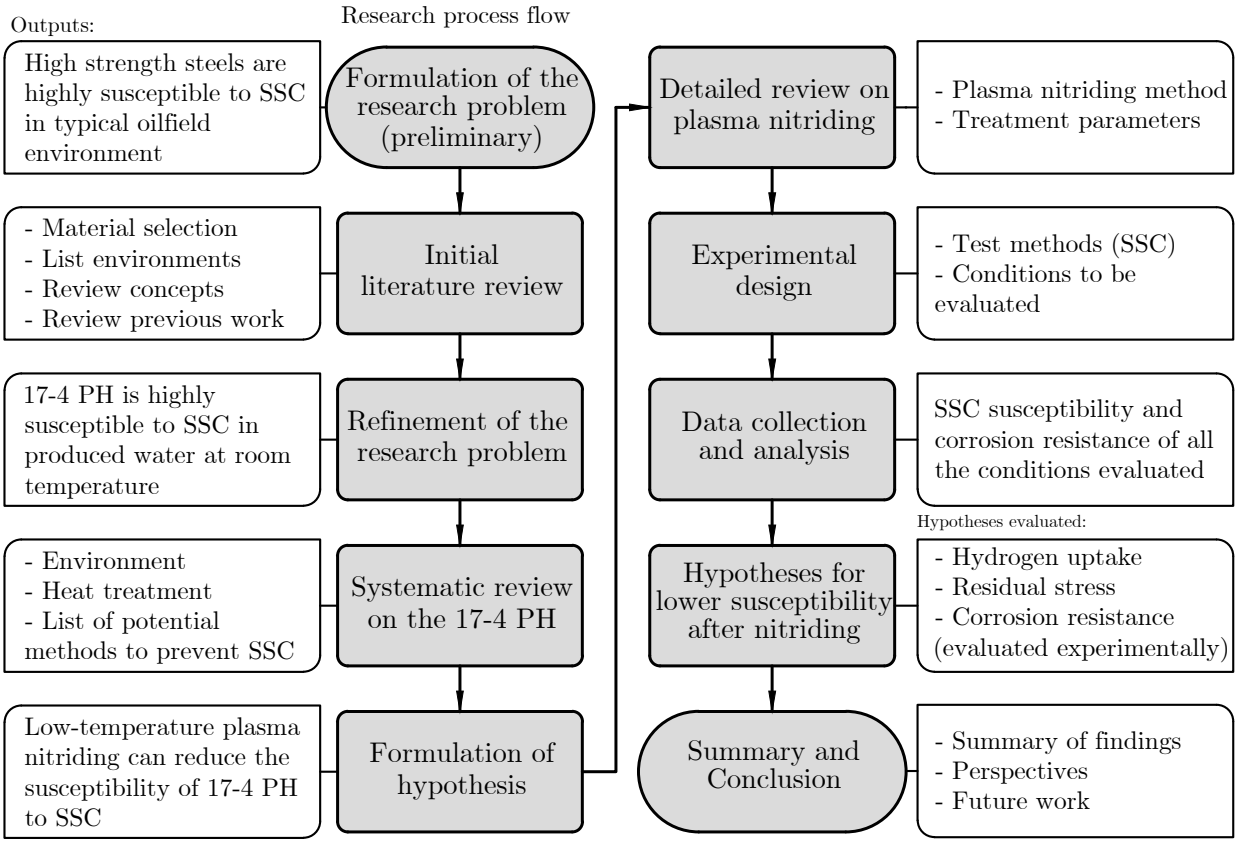

FIGURE 1.2: Flow diagram of the research process

1.5 Research method

The present work consists in a research motivated by a practical application in the oil and gas industry. The flow diagram presented in Figure 1.2 illustrates the research method and the major stages used to solve the research problem. This is a simplified representation to provide an overview of the process and therefore the feedback loops were omitted.

The research problem, for example, was frequently revisited—and adjusted when necessary—and the literature review was continuously performed until the end of the research to account for recent findings.

1.6 Thesis overview

The diagram in Figure 1.3 is presented at the beginning of the main chapters to highlight the topics covered in that specific section and to clarify the links between major experiments.

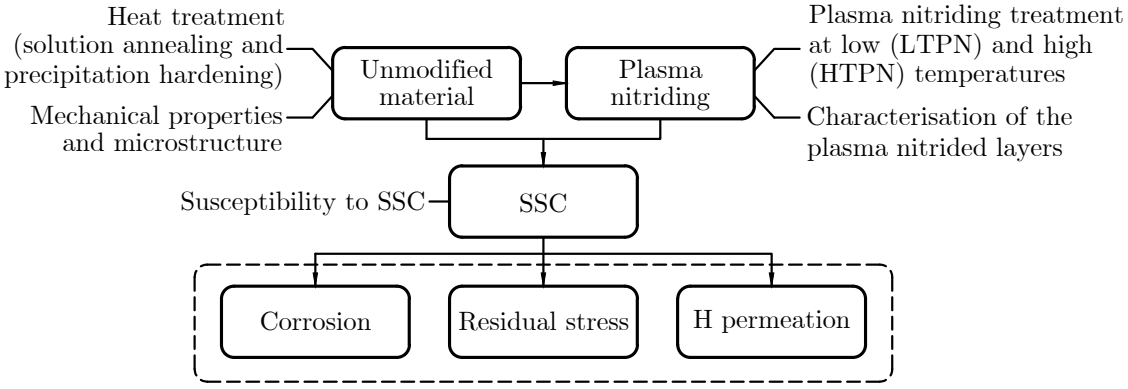

FIGURE 1.3: Schematic diagram situating the topics covered in each chapter in the complete experimental context of this work.

Chapter 2 introduces relevant aspects associated with the susceptibility of the 17-4 PH to SSC and summarises results from laboratory and field failure investigations related to the oil and gas industry. The chapter also outlines current knowledge about phenomenological aspects of SSC and restrictions of the use of this material in environments containing H_2S. It finishes with a brief outline about surface modification techniques, particularly plasma nitriding, which can be potentially applied to prevent SSC. The third chapter presents the characterisation of microstructure and the mechanical properties

of the 17-4 PH after the double precipitation hardening treatment and the structure of the modified layer obtained after plasma nitriding at two different temperatures, i.e low temperature and conventional temperature. The two following chapters (Chapter 4 and Chapter 5) present the results from the SSC and localised corrosion investigations with the unmodified and plasma nitrided conditions. Chapter 6 presents experimental and theoretical framework about the role of the plasma nitridied layer on the SSC susceptibility, with emphasis on the residual stress induced after plasma nitriding and on the hydrogen uptake by the substrate material (barrier effect of the nitrided case). Chapter 7 starts with a summary of the correlations between corrosion resistance, residual stress, hydrogen permeation and SSC susceptibility and ends with the conclusions. The last chapter (Chapter 8) list perspectives, technological implications and recommendations for future work.

Chapter 2

Literature review: SSC and plasma nitriding of the 17-4 PH

This chapter summarises results from field failure analysis and laboratory investigations conducted to determine the susceptibility of the 17-4 PH to sulphide stress cracking (SSC). These data provide an outline of the current knowledge and practical limitations of this material within the context of oil and gas production systems containing hydrogen sulphide (H_2S). The chapter also describes the current understanding of the mechanisms and phenomenology of SSC and synthesises relevant aspects of surface modification, particularly plasma nitriding, which can be potentially applied to prevent it.

A major part of this chapter is adapted from a review paper on the SSC resistance of the 17-4 PH [31], recently published by the author. Permitted use was granted according to the copyright agreement.

2.1 The 17-4 PH in the oil and gas industry

17-4 PH (UNS S17400 – ASTM A564 Type 630 ot DIN 1.4542) is a high-chromium, low–carbon precipitation–hardening (PH) stainless steel developed in the 1940s to meet

the demand of the military industry for high–strength steels with greater corrosion resistance at reasonable cost [11]. These characteristics have led to their extensive application in the oil and gas industry since the early 1960s [10]. Despite its successful use in subsea components exposed to environments containing H_2S [32]—also known as sour environments—there have been recent debates about its limits of application [10]. Aqueous H_2S dissolved in the production fluids can promote the absorption of atomic hydrogen into the metal and cause failure by SSC. This process consists of hydrogen absorption and subsequent fracture under either applied or residual tensile stress. Incidents involving SSC were first reported in the 1950s and further occurrences in different oil fields promoted the advance of research on the subject [9]. Detailed laboratory investigations [33] confirmed that most of the materials evaluated, including the 17-4 PH, failed by SSC. The data suggested that local embrittlement at the crack tip accelerated crack propagation, although the exact mechanisms of failure remained unclear. Further committees and task groups were formed and, in 1975, NACE (National Association of Corrosion Engineers)—now NACE International—issued the standard MR0175 specifying the requirements for the qualification of corrosion–resistant alloys (CRA) exposed to H_2S-containing environments. Later, it became an international standard in association with the ISO 15156 [16]. The European Federation of Corrosion (EFC) published related guidelines [34, 35] in the 1990s.

The recommendations from the MR0175/ISO 15156-3 [16] restrict the applications of wrought 17-4 PH to low partial pressures of H_2S and limited acidity. Moreover, the document recommends specific heat treatments and maximum loading conditions. These limits—established based on the industrial experience and supported by numerous laboratory investigations—might allow safer use of the 17-4 PH in the oil and gas industry, even though there are still cases of failure when the materials meet these criteria.

Figure 2.1 shows simplified cross section of typical offshore production unit exemplifying the application of the 17-4 PH in the oil and gas industry. This system, widely used in the coast of Brazil, comprises a floating platform (FPSO - floating production, storage and offloading) equipped with processing facilities extracting oil and gas with high concentrations of H_2S from ultra–deep water and deep reservoirs. At the seabed level, the 17-4 PH is mainly used for well head components, such as tubing hangers (as illustrated in Figure 2.1) and valve stems.

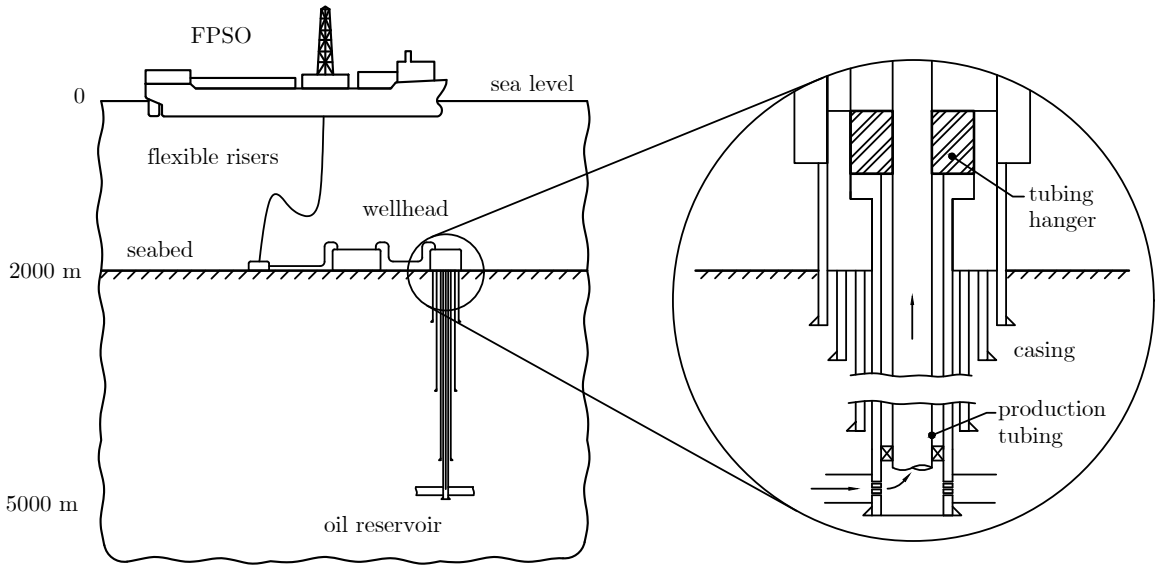

FIGURE 2.1: Simplified cross section of typical offshore production unit and an amplified view of the tubing hanger assembly on the seabed

2.1.1 Typical service conditions in oil and gas production systems

In offshore installations, the 17-4 PH is primarily used for wellhead components and valve assembly systems located at the seabed level, as illustrated in Figure 2.1, in which the operating temperature ranges from 25 to 60 °C [36]. Typical sour environment (i.e.

contaminated with H_2S) in oil production systems comprises the main following elements: H_2S, CO_2 and water.

H_2S is a toxic [4] by-product that occurs naturally in the reservoirs or can be generated by sulphate–reducing bacteria [5]. An environment is classifed as sour if the amount of H_2S is sufficiently high to cause cracking [37], which can be as low as the minimum detectable level for highly susceptible materials. The International Energy Agency [38, 39] estimates that more than 40% of the gas reserves are sour and another source [40] indicates that the same applies for nearly 80% of crude oil reserves. The main issue associated with the presence of H_2S is that it enhances hydrogen absorption and, as a result, susceptible steels can experience premature failures. Besides, iron sulphide is deposited on the surface as a result of the reaction of H_2S with iron and the susceptibility to SSC, as noted in some studies [41], can be associated with all the conditions that determine the stability of these deposits.

The water present in oil reservoirs is originated from geological formations (produced water) or can be artificially injected in the system to overcome pressure fall. H_2O with dissolved H_2S flow with the hydrocarbons (production fluids) and becomes in contact with the internal walls of tubing and other internal components, increasing the chances of failure by SSC. Produced waters from oil reservoirs typically contain up to $200\,\mathrm{g\,L^{-1}}$ of sodium chloride (NaCl) [36] and pH approximately 4.5 at ambient temperature [35]. In gas reservoirs, water is formed by condensation and it usually has higher acidity ($\mathrm{pH} \leq 3.5$) and only traces of produced water and thereby low NaCl content ($1\,\mathrm{g\,L^{-1}}$) [36].

CO_2 can be formed from carbonate minerals or injected into the oil field via oil–enhanced recovery processes [42] used to increase the extraction rate of oil. Environments containing CO_2 tend to form iron carbonate ($FeCO_3$) scales [43] with protective characteristics conditioned to adequate surface coverage and integrity during service.

2.1.2 Characteristics and properties of the 17-4 PH

2.1.2.1 Chemical composition

Table 2.1 shows current requirements [44] and reported elemental composition ranges of the 17-4 PH obtained from published work [10, 18–20, 45–76], along with a brief description of the major function of each alloying element added to this grade. The elements are balanced to allow the formation of a martensitic structure at room temperature, yet martensite alone is not sufficient to provide the required strength due to the low carbon content (maximum 0.07 wt.%) and therefore further hardening is obtained by the precipitation of copper during ageing (i.e. tempering), as detailed in the next section. Austenite promoters, such as nickel, copper and manganese, are essential elements added to increase toughness and ductility. The roles of particular elements on the corrosion characteristics and on the cracking process are described throughout the next sections.

2.1.2.2 Microstructure and phase composition

Typical microstructure of precipitation–hardened 17-4 PH, schematically illustrated in Figure 2.2, comprises a matrix of low–carbon martensite formed within prior–austenite grains, which are divided into packets and subdivided into blocks containing martensite laths. These are the main features of martensitic structures [77], which are obtained in the 17-4 PH after standard multiple–step treatments [44] comprising solution annealing at 1040 °C and one or two precipitation–hardening (or ageing) cycles conducted at 480-760 °C for up to 4 h. The martensitic structure is formed after annealing and a fraction of austenite is retained at room temperature. This phase forms preferentially along prior–austenite grains and lath contours. Further austenite is formed during the precipitation hardening stage, simultaneously with copper precipitation.

TABLE 2.1: Elemental composition requirements, actual composition ranges of the 17-4 PH and the major functions of alloying elements

Element	**ASTM A564 maximum or range (wt.%)**	**Typical composition range minimum - maximum (average, wt.%)**	**Major function**
C	0.07	0.01-0.06 (0.04)	Provides mechanical strength. Due to the low content, further strengthening is required (Cu precipitation)
Cr	15-17	15.00-17.00 (16.00)	Corrosion resistance [13]
Ni	3-5	3.20-5.15 (4.30)	Added to increase toughness and ductility by promoting the presence of austenitic structure
Cu	3-5	2.75-4.15 (3.40)	Provides most of the mechanical strength by forming fine precipitates within the martensitic structure [12]
Mn	1.00	0.20-0.85 (0.55)	Similar to Ni, it contributes to toughness and ductility by promoting austenite [78]
P	0.040	0.002-0.030 (0.020)	Added to improve machinability. It has adverse effect on SSC (promotes intergranular cracking) [52]
S	0.030	0.001-0.030 (0.012)	Similar to P, it is added to increase machinability. It has negative effect on intergranular corrosion [79]
Si	1.00	0.15-0.80 (0.45)	Used to prevent oxidation at high temperature during the manufacturing process
Others	0.15 + 0.45 (Nb + Ta)	0.03-3.10 (0.35) Mo 0.15-0.35 (0.25) Nb Traces of Al, Ti, Ta	Mo: strength at high temperature (ferrite promoter); Ti, Nb and Ta: prevent the precipitation of chromium carbides [12]

The transformation of austenite (γ) into martensite (α') upon cooling from the annealing temperature is diffusionless, so that solute atoms that are in solid solution in the face–centred cubic (f.c.c.) crystal of austenite remain in solid solution after the transformation of this phase into the distorted body–centred tetragonal (b.c.t.) structure of

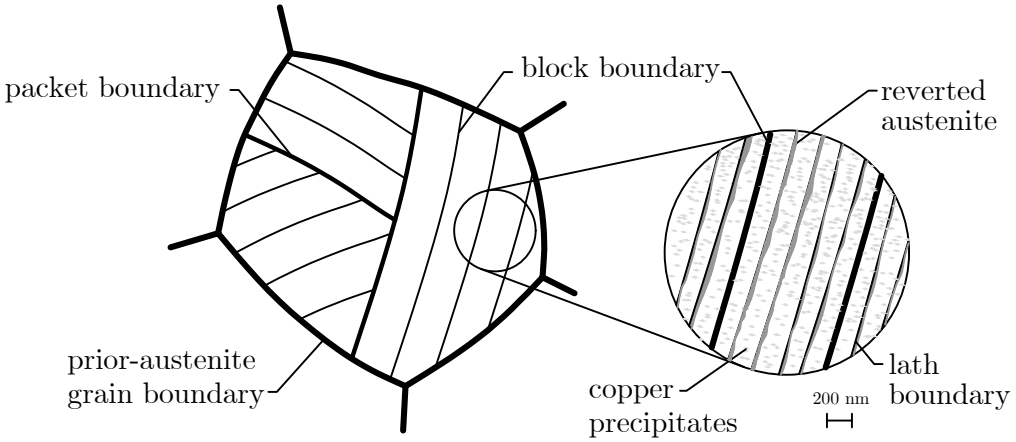

FIGURE 2.2: Typical microstructure of the 17-4 PH obtained after precipitation hardening.

martensite. This rearrangement of atoms involves lattice distortion and, according to the classical Bain strain theory, the b.c.t. structure is obtained by shearing of the f.c.c. lattice [80]. In this case, the plane $(010)_{\gamma}$ coincides with the plane $(\bar{1}10)_{\alpha'}$ and the lattice parameters of martensite at this stage, as illustrated in Figure 2.3a, are $a_{\alpha'} = a_{\gamma}/\sqrt{2}$ and $c_{\alpha'} = a_{\gamma}$. To complete the transformation, $a_{\alpha'}$ expands in the x' and y' directions so that the lattice parameter is equivalent to that of body–centred cubic (b.c.c.) crystals (a_{α}). To obtain a nearly cubic arrangement, $c_{\alpha'}$ must be compressed (about 15%) in the z direction (Figure 2.3b) and, as a result, the f.c.c. and b.c.t. phases are oriented according to the Kurdjumov–Sachs relationship, i.e. $\{111\}_{\gamma} \| \{110\}_{\alpha'}$ and $\langle 1\bar{1}0\rangle_{\gamma} \| \langle 1\bar{1}1\rangle_{\alpha'}$. The distortion of the b.c.t. unit cell with respect to the b.c.c. lattice depends on the carbon content (C), e.g. $c_{\alpha'}/a_{\alpha'} = 1 + 0.045$ C [81], but since the concentration of carbon is very low in the 17-4 PH (maximum 0.07 wt.%), the approximation $a_{\alpha'} \approx c_{\alpha'} \approx a_{\alpha}$ can be made when quantifying the lattice parameters of martensite. This is particularly convenient when analysing X-ray diffraction data.

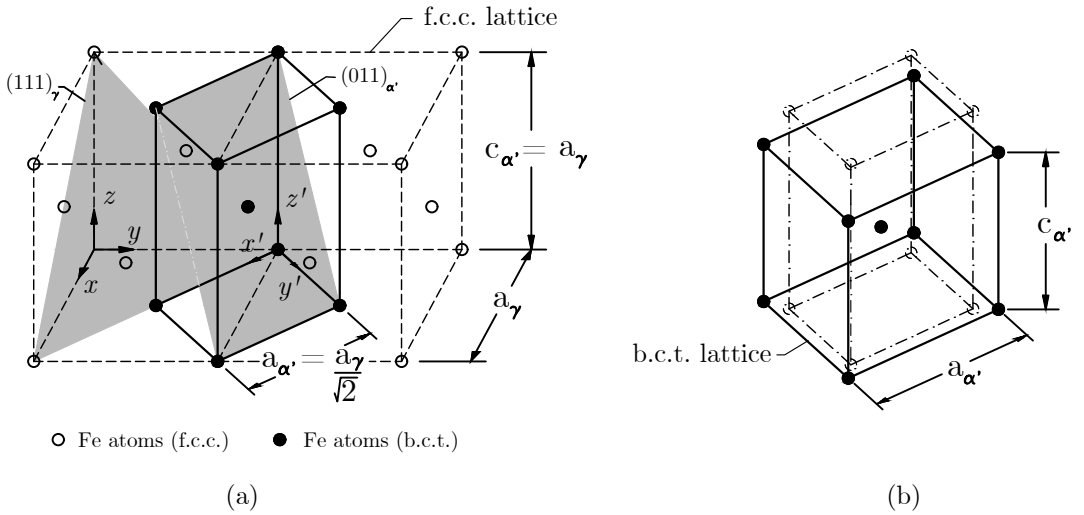

FIGURE 2.3: Schematic representation of the transformation of austenite into martensite according to the Bain strain theory: (a) transition state; (b) resultant b.c.t. lattice

The temperature at which martensite starts to form on cooling, M_s, and that at which the transformation is completed, M_f, are useful parameters to analyse the martensitic transformation and they are primarily associated with the elemental composition of the material. The following empirical formulae (Eq. 2.1 [81] and Eq. 2.2 [12]) are often used to evaluate the transformation, with the concentrations expressed in wt.%:

$$M_s\,(^\circ C) = 539 - 423\ \mathrm{C} - 30.4\ \mathrm{Mn} - 17.7\ \mathrm{Ni} - 12.1\ \mathrm{Cr} - 7.5\ \mathrm{Mo} \tag{2.1}$$

$$M_s\,(^\circ F) = 2160 - 66\ \mathrm{Cr} - 102\ \mathrm{Ni} - 2620\ (\mathrm{C} + \mathrm{N}) \tag{2.2}$$

For the 17-4 PH, M_s varies from 250-320 °C and M_f is estimated to be $\approx$ 32 °C [82]. When the material is cooled to 32 °C, the following empirical relationship [81] predicts that the volume fraction of austenite transformed into martensite (ϕ) during cooling from

the annealing temperature (often 1040 °C), will be larger then 95%:

$$1 - \phi = \exp\left[\beta\left(M_s - T\right)\right] \text{ where } \beta = -0.011 \tag{2.3}$$

At room temperature, it is therefore expected that the microstructure is essentially martensite after the solution annealing stage is completed. The parameters of the subsequent precipitation hardening stage (e.g. time and temperature) can be controlled to obtain different mechanical properties. The precipitation–hardening temperature (expressed in °F) preceded by the letter "H" is used to designate standard heat treatments, namely H900, H925, H1025, H1075, H1100, and H1150. Two double precipitation hardening conditions (H1150D and the modified version H1150M), developed to increase fracture toughness, are recommended by NACE MR0175 [16] for applications in the oil and gas industry due to their superior resistance to SSC. The description of microstructural features of the 17-4 PH after precipitation hardening are therefore concentrated on these two conditions. Their main mechanical requirements are reproduced in Table 2.2 [44].

TABLE 2.2: Minimum mechanical requirements and precipitation hardening parameters for the 17-4 PH (conditions H1150D and H1150M)

Parameter/treatment	**H1150D**	**H1150M**
Precipitation hardening	PH1[(a)]: 620 °C (4h)	PH1: 760 °C (2h)
	PH2[(b)]: 620 °C (4h)	PH2: 620 °C (4h)
Tensile strength (MPa)	860	795
Yield strength (MPa)	725	520
Elongation % in 50 mm	16	18
Reduction in area %	50	55
Hardness (Rockwell C)	24 (maximum 33)	24
Impact Charpy-V (J)	41	75

[(a)]First and [(b)]second precipitation hardening cycles

Typical microstructural evolution during the different stages of the heat treatment specified by ASTM A564 [44] for the H1150D and H1150M conditions is schematically illustrated in Figure 2.4. In both cases, solution annealing (SA) is performed at 1040 °C for 30 minutes, the microstructure being essentially austenite at this point. On cooling to below 32 °C, the majority of the austenite is transformed into low–carbon martensite (as previously discussed) and a fraction is retained (γ_{ret}) within the martensitic matrix—the material supplied at this condition is often referred to as "Condition A". For the H1150D, two consecutive precipitation–hardening cycles at (620 ± 14) °C for 4 hours are performed after SA. In the modified version (H1150M), the first precipitation–hardening cycle is conducted at (760 ± 14) °C.

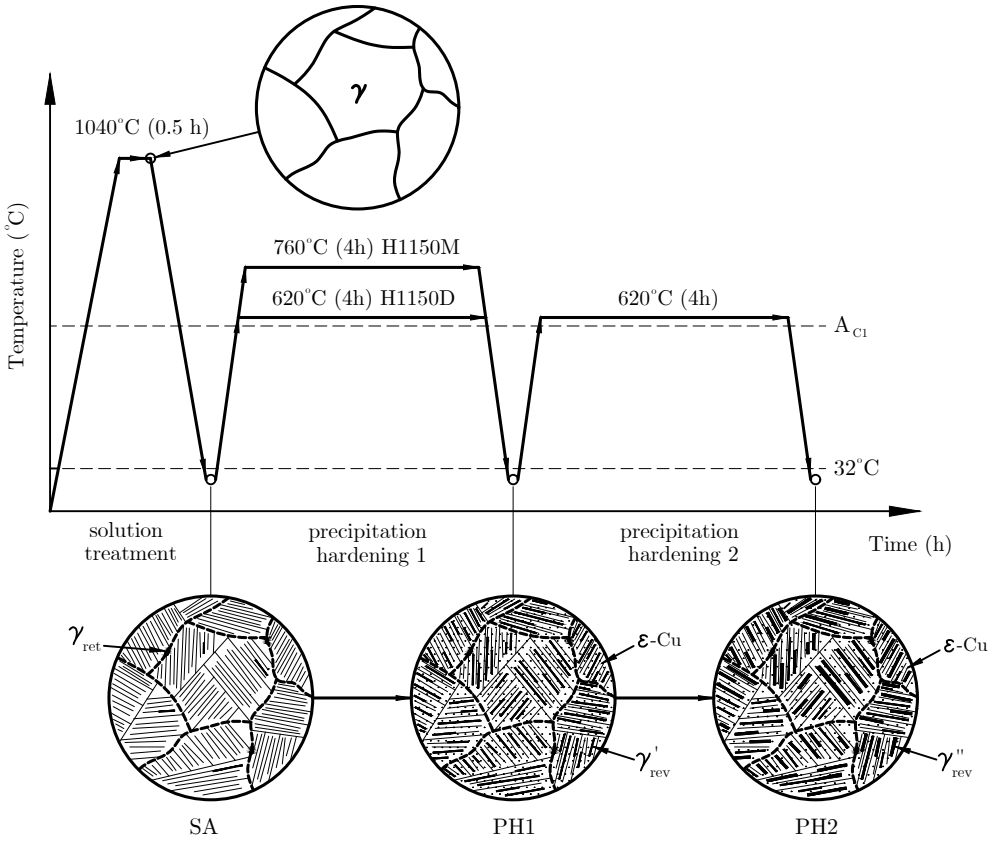

FIGURE 2.4: Schematic representation of typical microstructure evolution of the 17-4 PH (conditions H1150D and H1150M).

During the first (PH1) and the second (PH2) precipitation hardening stages, copper precipitates (ε–Cu) and reverted austenite grains (γ'_{rev} and γ''_{rev}) are formed in different proportions. Reverted austenite is formed as follows: when the material is heated from Condition A to above the temperature at which austenite starts to form (A_{c1}), estimated to be from 614 to 620 °C [60, 83], martensite will be converted into austenite during PH1 and PH2 and a fraction of this phase will be retained when the material is subsequently cooled to the room temperature after the end of each stage. Few quantitative data on the austenite content of the 17-4 PH is available in the literature. In a recent investigation [46], retained and reverted austenite were determined for each stage by using metallographic examination and X-ray diffraction techniques [84]. It was observed that, in both H1150D and H1150M, about 1% by volume of austenite was retained after SA and 3 and 15 vol.% of reverted austenite were present after PH1 for H1150D and H1150M, respectively. The higher γ'_{rev} content obtained for the latter was attributed to the higher temperature used in the PH1 cycle. At the end of PH2, the total amount of austenite ($\gamma_{ret} + \gamma'_{rev} + \gamma''_{rev}$) was 21 vol.% for the H1150D and 33 vol.% for the H1150M. These results demonstrate the role of the second hardening, performed to increase the austenite content and thereby increase the toughness of the material. By comparing these results with aditional data [73, 82], a wide range of total austenite content was noticed (6 to 21% for the H1150D and from 19 to 33% for the H1150M condition).

Although well–defined parameters are specified for the heat treatment of H1150D and H1150M, the final microstructure may vary due to the complexity associated with the hardening phenomena. A rigorous control of the final microstructure is therefore essential to minimise unexpected failures of components during service. Detailed investigations on the microstructural evolution of the 17-4 PH during precipitation hardening [55, 68, 85]

contributed to the better understanding of the hardening process. In spite of small variations in the treatment parameters used in each of these studies, similar microstructures and equivalent hardening mechanisms were reported. Transmission electron microscopy (TEM) was used to characterise the lath structure of martensite for a variety of precipitation hardening conditions and to analyse the morphology of the copper precipitates. It was observed that ε–Cu precipitates (from 15 to 30 nm wide) were arranged in a f.c.c. structure oriented with the martensitic structure according to the Kurdujumov–Sachs relationship. It was also noticed that, at 620 °C (i.e. temperature used in PH1 and PH2 for the H1150D condition), peak hardening was achieved after about 30 minutes due to the formation of coherent (i.e. perfect match of the crystals at ε–Cu/α' interfaces) and finely distributed copper precipitates [55]. By increasing the precipitation hardening time to above that corresponding to the maximum hardness (i.e. over ageing), coarsening of ε–Cu occurred and the harness decreased, as illustrated in Figure 2.5. These results demonstrate that ε–Cu precipitates are essential features controlling the mechanical properties of the 17-4 PH.

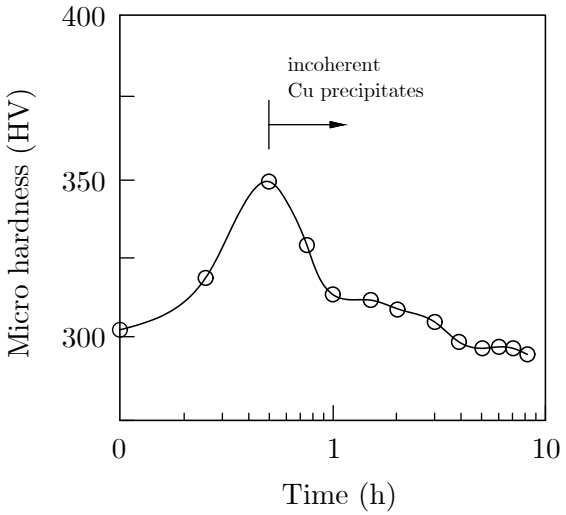

FIGURE 2.5: Microhardness evolution of the 17-4 PH by precipitation hardening at 620 °C. Data from [55]

TEM micrographs were also helpful in revealing the formation of reverted austenite along lath contours of the martensitic structure. Austenite was observed when the 17-4 PH was over aged at relatively low temperatures, i.e. 350 °C [85] or treated at elevated temperatures (600-620 °C) for shorter periods (from 4 to 8 h) [55, 68]. These observations are in agreement with data obtained by electron beam backscatter diffraction (EBSD) [48] to generate phase maps of the 17-4 PH for different ageing times. In the latter case, the authors detected the presence of retained and reverted austenite along the lath contours and prior–austenite grains boundaries.

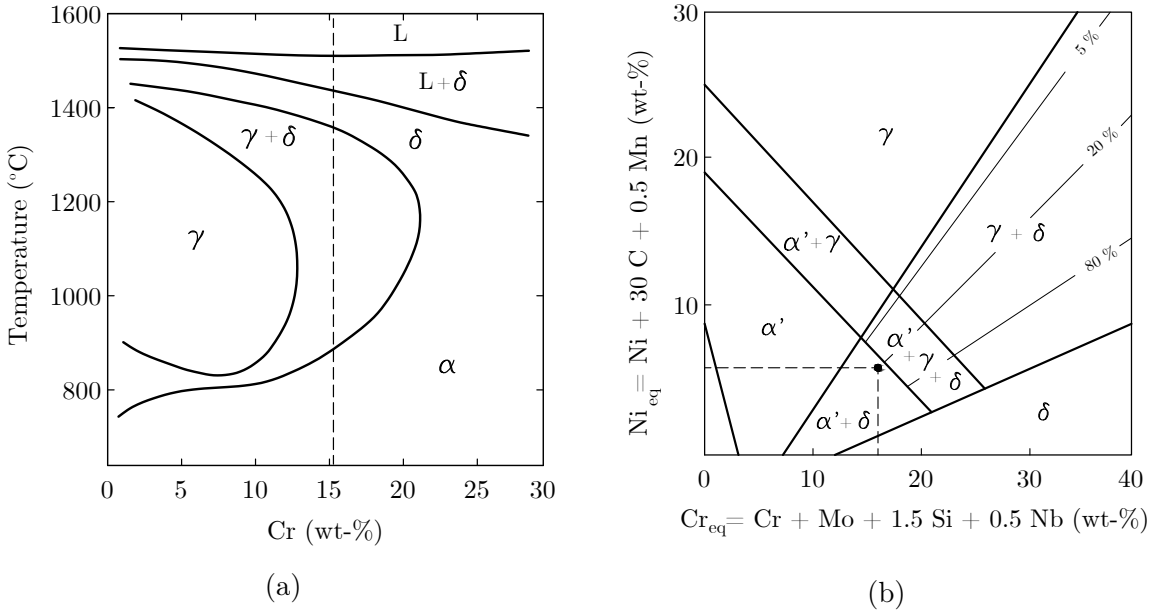

FIGURE 2.6: (a) Portion of the binary Fe-Cr phase diagram indicating the formation of δ–ferrite in high-chromium stainless steels (adapted from [86] (b) Schaeffler diagram representing the effect of the alloying elements (proportions of Cr_{eq} and Ni_{eq}) on the microstructure (adapted from [87])

The formation of δ–ferrite was also observed [68] in the 17-4 PH and this can be rationalised by analysing the Fe-Cr diagram shown in Figure 2.6a. Due to the high Cr content, δ–ferrite is expected to be formed when the material is solution annealed at

1040 °C and this phase will remain in the structure when the material is cooled to the room temperature. The Schaeffler diagram presented in Figure 2.6b supports the formation of δ–ferrite based on the proportions of ferrite and austenite promoters. By determining the chromium and nickel equivalent numbers from typical elemental composition of the 17-4 PH, the diagram predicts that δ–ferrite will be in the microstructure along with martensite.

2.2 Sulphide stress cracking

Standard terminology relating to corrosion [8] defines sulphide stress cracking (SSC) as a type of environmentally–assisted cracking (EAC) that occurs due to the simultaneous action of corrosion and tensile stress in aqueous environments containing H_2S. The role of H_2S in SSC is to enhance the absorption and thereby diffusion of hydrogen into the metal so that brittle cracks perpendicular to the applied or residual stress can be formed. Although the acronym SSC has been used since 1952 [88], there are still inconsistencies within the literature and the phenomena is often referred to as stress corrosion cracking (SCC), which designates cracking due to simultaneous anodic dissolution and tensile stress. SCC is a wider term that involves numerous aqueous corrosive environments, including H_2S (sulphide SCC) and in this case SSC can be considered a specific type of SCC. For clarity and consistency, however, this chapter adopts the term SSC to designate any failure in the presence of H_2S, unless otherwise specified.

This section presents a brief review of the phenomenological aspects and mechanisms of SSC as well as a description of the main variables affecting the SSC susceptibility. Unless otherwise specified, the discussions are mainly based on results obtained from research data or documented field work on the 17-4 PH heat–treated to either H1150D or

H1150M conditions. In particular cases, when data from the 17-4 PH are not available, materials with similar microstructure are used for reference.

2.2.1 Phenomenology and mechanisms

2.2.1.1 SSC mechanisms

In H_2S–H_2O systems, H_2S gas can be dissolved into aqueous H_2S_{aq} [89], a weak acid that can either remain in the aqueous state or dissociate in two steps to form sulphide ions (S^{-2}) and hydrosulphides (HS^-) [90]:

$$H_2S_{(aq)} \longrightarrow H^+ + HS^- \tag{2.4}$$

$$HS^- \longrightarrow H^+ + S^{2-} \tag{2.5}$$

Potential-pH diagrams of sulphur–water systems [91, 92] predict that $H_2S_{(aq)}$ will be stable in acid solutions at room temperature, while its dissociation products will be the main constituents at higher pH levels. At the metal surface, the corrosion in acid environments involves the anodic dissolution of iron (Equation 2.6) accompanied by the half-cell reaction at the cathode side, which consists of hydrogen adsorption (Equation 2.7) and subsequent hydrogen evolution (Equation 2.8) [93].

$$Fe \longrightarrow Fe^{2+} + 2\,e^- \tag{2.6}$$

$$2\,H^+ + 2\,e^- \longrightarrow 2\,H_{ads} \tag{2.7}$$

$$2\,H_{ads} \longrightarrow H_2 \tag{2.8}$$

Different theories for hydrogen charging by H_2S have been proposed based on distinct entry mechanisms. Investigations based on the classical model [93] suggest that the hydrogen adsorbed at the surface (H_{ads}) can either recombine to form H_2 or be absorbed into the metal in the atomic form (Figure 2.7a). This effect, referred as recombination poisoning, was also observed [94] when different gaseous hydrides and other impurities stimulated the entry of hydrogen in nickel. According to this model, hydrogen atoms segregate and diffuse preferentially along grain boundaries, promoting intergranular embrittlement. Crack propagation occurs when the applied tensile stress is sufficiently high (Figure 2.7b).

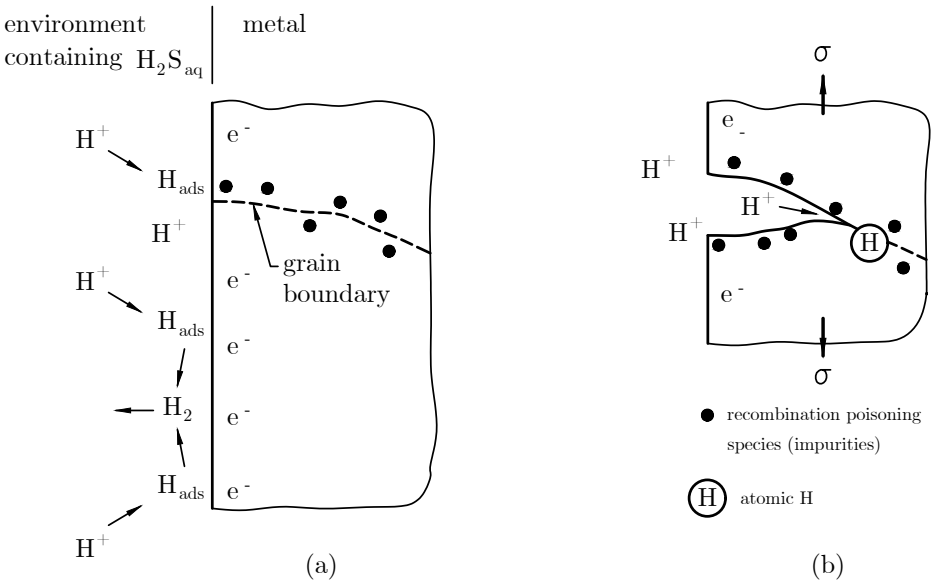

FIGURE 2.7: Schematic representation of hydrogen recombination during SSC: (a) hydrogen evolution and recombination poisoning near the grain boundaries; (b) preferential absorption of hydrogen on the grain boundaries and intergranular crack under applied tensile stress.

A different theory [95, 96] assumes that hydrosulphide ions (HS^-) adsorb at the surface and promote the direct transfer of hydrogen ions from the electrolyte into the metal (Figure 2.8a). In this case, the role of H_2S is not to weaken the hydrogen recombination, as in the classical theory (i.e. recombination poisoning), but to act as a catalyst for the uptake of hydrogen ions into the metal via direct proton transfer. An alternative model [97] considers that hydrogen entry occurs via a transition state of adsorbed species (Figure 2.8b). Despite the differences proposed to describe H entry mechanism, there is a common agreement that acid environments containing H_2S enhance H absorption into the metal.

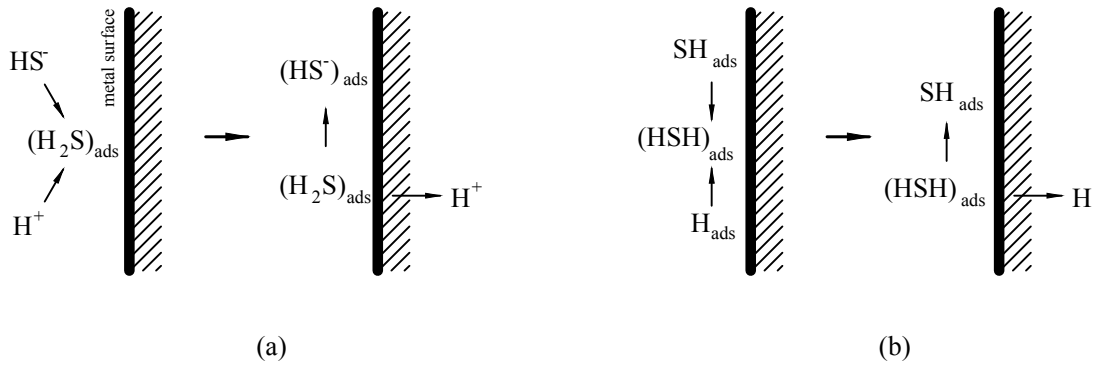

FIGURE 2.8: Models for hydrogen charging if metals in H_2S-containing environments: (a) direct proton transfer; (b) hydrogen absorption through transition state species.

Promising attempts to fully describe the SSC mechanisms of high–strength steels based on holistic approaches incorporating mechanical and metallurgical aspects [98–101] have been recently published. Although no experimental evidence was provided to validate these models, they were helpful in contributing to the current understanding about SSC, particularly on crack initiation from smooth surfaces. These models assume that compressive strains at the early stages of yielding—induced by the Poisson's effect when the material is submitted to tensile loading—and slip dislocations will form cleavage planes perpendicular to the applied tensile stress. According to this theory, hydrogen ions

preferentially occupy these sites and promote lattice expansion until decohesion occurs by the repulsive effect between H^+ and Fe^{2+}.

One important aspect to consider when evaluating cracking in H_2S media is the precipitation of iron sulphide on the metal surface. If stable films are formed, they can provide further protection against corrosion by acting as an additional barrier for the diffusion of ferrous ions [102]. Conversely, if the conditions to mantain a stable film are not sustained, additional sites for localised attack can be formed due to the poor surface coverage. Besides, iron dissolution rate increases when iron sulphide is formed [93]. Systematic investigation [103] on the corrosion of iron exposed to H_2S–saturated solutions indicated that different structures of iron sulphide can be generated. The results revealed that a base layer of mackinawite (tetragonal FeS_{1-x}) was initially formed at the surface by solid–state reaction. Pyrite (cubic FeS_2) and troilite (distorted nickel arsenide–type structure, FeS), were then formed in different proportions depending on the solution pH and time of exposure. Overall, highly acidic conditions led to the formation of weak films, possibly due to the greater solubility of the sulphur species in these environments. In contrast, nearly neutral conditions resulted in the formation of thick protective films. The following pathway was proposed [103]:

$$Fe + H_2S + H_2O \longrightarrow FeSH^-_{ads} + H_3O^+ \tag{2.9}$$

$$FeSH^-_{ads} \longrightarrow FeSH^+_{ads} + 2\,e^- \tag{2.10}$$

where the $FeSH^{+}_{ads}$ species can be directly incorporated to the mackinawite layer (Equation 2.11) or react with water to form dissolved ferrous ion [104].

$$FeSH^{+}_{ads} \longrightarrow FeS_{1-x} + xSH^{-} + (1 - x)H^{+} \tag{2.11}$$

2.2.1.2 Hydrogen embrittlement

Cracking in H_2S environments involves brittle fracture [105] and therefore SSC is often categorised as a form of hydrogen embrittlement (HE), i.e. loss of ductility and/or thoughness due to the presence of hydrogen within the metal [8]. This association is due to clear indications of similarities between both phenomena [106], yet the correspondence is not always adequate. The internal pressure theory of HE, in which hydrogen recombines to form molecular hydrogen and induces localised pressure build–up, for example, is not suitable to explain SSC on high–strength steels, whereas the hypothesis of embrittlement by internal adsorption of hydrogen seem appropriate [107]. During SSC, hydrogen can be generated during corrosion on the crack tip and therefore failure by SSC can involve similar features observed in HE. Relevant HE mechanisms are therefore briefly described in this section.

Cracking involving HE, referred as hydrogen–assisted cracking (HAC), can be classified according to the source of hydrogen as [108]: (i) internal hydrogen embrittlement (IHE), in which pre–existing hydrogen (from fabrication, such as welding and electroplating) accumulates within the microstructure and cracking can occur under applied or residual stress, often below the yield strength of the material; and (ii) hydrogen–environment embrittlement (HEE), in which hydrogen dissociated from gases present in the environment (in this case H_2S) promotes cracking under sustained stress. Hydrogen is then adsorbed on the surface, absorbed into the metal and transported through interstitial positions.

Prominent mechanisms of hydrogen embrittlement relevant to high–strength steels are: hydrogen–enhanced decohesion (HEDE), hydrogen–enhanced localized plasticity (HELP) and adsorption–induced dislocation emission (AIDE). The decohesion model (HEDE), originally proposed in the 1920s [109] and further developed in the 1970s [110], states that solute hydrogen reduces the cohesive force between iron atoms, resulting in reduction of the stress required for crack propagation. This theory says that a crack will propagate if the concentration of hydrogen near the crack tip is sufficiently large to induce stress that exceeds the cohesive strength of the iron lattice (Figure 2.9). Recent review [108] highlighted that decohesion can occur at or ahead of the crack tip. Although the model mainly describes crack propagation, a similar process may be involved in the crack nucleation process [110]. TEM micrographs of fractured specimens [111] provided supporting evidence of decohesion induced by impurities segregated at grain boundaries and similar behaviour could be anticipated for hydrogen [108].

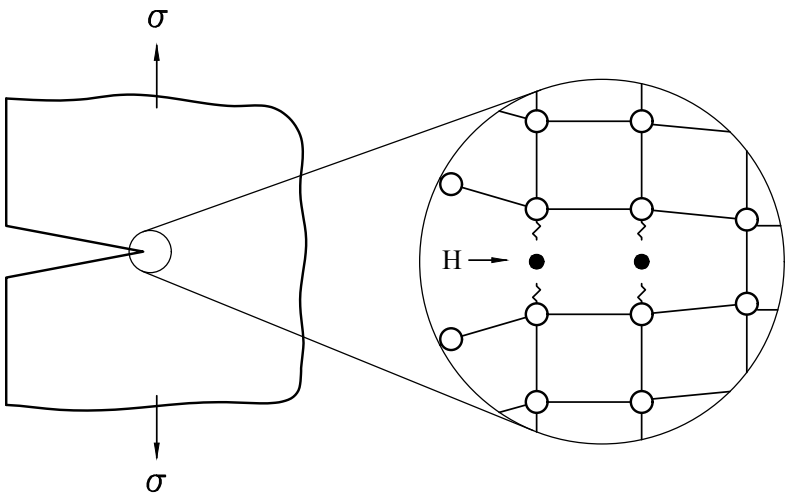

FIGURE 2.9: Schematic representation of the hydrogen–enhanced decohesion (HEDE) model. The zig-zag lines represent decohesion

The HELP theory, first proposed in the 1970s [112], suggests that hydrogen present in

the lattice positions ahead of the crack tip contributes to lowering the stress required for dislocations to move. This model successfully described different fracture modes observed for different levels of stress intensity factor (k) at the crack tip. Observations of fractured surfaces with high k suggested that cracks propagate predominantly by micro void coalescence (Figure 2.10), as previously observed in SCC. As k decreases, the localized plasticity reduces and the cracking mode changes from quasi–cleavage to intergranular cracking and then hydrogen–assisted intergranular cracking. This model was experimentally verified by in situ TEM investigations [113].

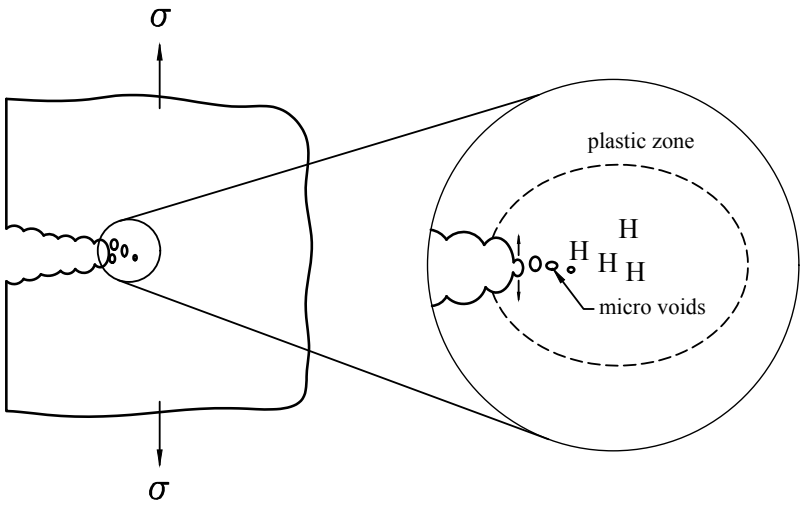

FIGURE 2.10: Schematic representation of the hydrogen–enhanced localized plasticity (HELP) for high stress intensity factor (k)

The AIDE model, proposed in the 1980s [114, 115], suggests that the adsorption of hydrogen facilitates the nucleation of dislocations and its subsequent propagation ahead of the crack tip when a sufficiently high stress is applied. If this stress is sustained, it induces plastic deformation ahead of the crack tip that facilitates the nucleation and growth of micro voids. This model considers that, in addition to the weakening of interatomic bonds promoted by the absorbed hydrogen, the coalescence of micro voids also contribute to the

crack propagation process by re–sharpening the crack. As schematically illustrated in Figure 2.11, before the microvoids coalesce, the crack advances in small increments (Δa) as a result of symmetric slip dislocations (slip planes A and B) at the crack front. Probable evidence supporting this model is based on similarities between AIDE and liquid-metal embrittlement (LME) [108].

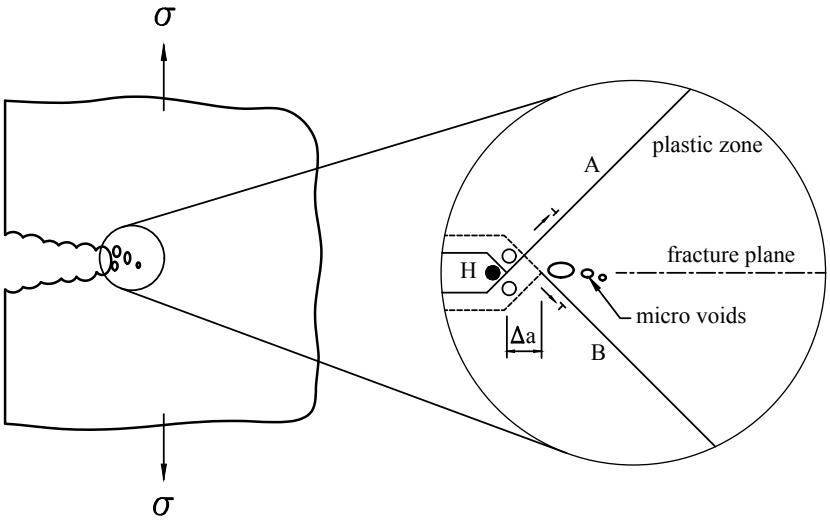

FIGURE 2.11: Schematic representation of the adsorption–induced dislocation emission (AIDE). The crack tip schematic (amplified detail) was adapted from [115]

2.2.1.3 Stress corrosion cracking

Although the predominant mechanism of cracking of high–strength steels submitted to tensile loading is HE, both SCC and HE can occur simultaneously [116]. Contrary to SSC, SCC does not require hydrogen within the microstructure for cracks to nucleate and propagate. But the dissolution model of SCC can be useful in evaluating intergranular cracking tendency in film–forming conditions and therefore a brief review is presented in this section.

As described earlier, SCC is a type of failure that results in crack growth due to the simultaneous action of corrosion and sustained tensile stress [8]. Stress corrosion cracks generally initiate from corrosion pits or discontinuities at the metal surface introduced during manufacturing and from metallurgical defects, such as non-metallic inclusions and grain boundaries [117]. These defects prevent the formation of a continuous passive film and therefore uncovered areas can be subject to localised attack. Either pits or other types of superficial irregularities can become sites of enhanced electrochemical activities where aggressive species, such as chloride ions, can accumulate and damage the passive film [118, 119].

Numerous SCC models have been proposed but no single theory can fully describe all phenomenological aspects of crack growth. Film rupture, also known as slip dissolution, is the main SCC mechanism based on the dissolution model. It assumes that crack grows due to the preferential dissolution of the bare metal at the crack tip once it becomes exposed to the environment when the passive film is locally damaged (Figure 2.12). The film rupture occurs due to the applied stress, which produces plastic deformation at the crack tip. The film tends be reestablished, unless the rate of rupture exceeds the rate of re–passivation [120]. While favourable conditions are maintained, crack advances by subsequent slip steps until complete failure occurs (steps 5 and 6 illustrated in Figure 2.12). According to this model, cracks propagate through active paths formed by chromium depletion along the grain boundaries [121] and therefore it is considered satisfactory to explain intergranular SCC but they fail to describe transgranular SCC.

2.2.2 Assessment of SSC susceptibility

Current practice within the oil and gas industry [88] to assess the SSC susceptibility of specific combinations of materials and environments relies on the detection of cracks after

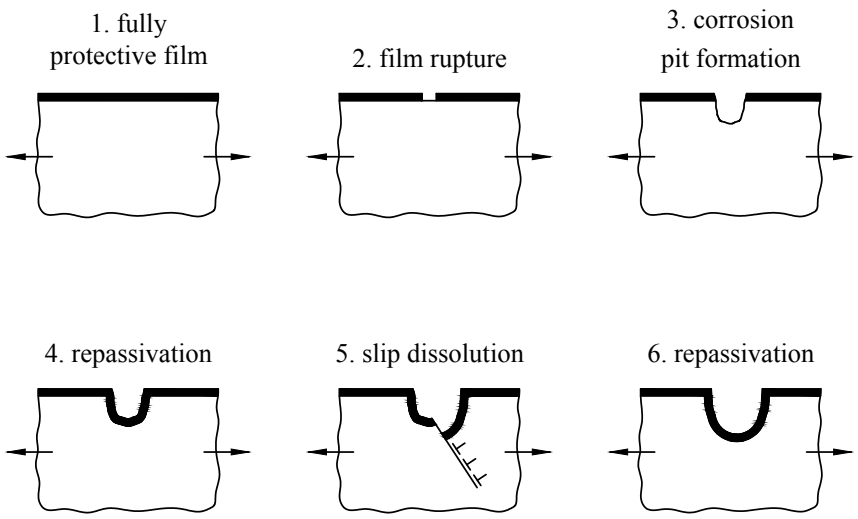

FIGURE 2.12: Schematic representation illustrating the sequence of the main events form the slip dissolution model of SCC. The arrows indicate the directions of the applied tensile stress

the material has been exposed to the environment for a pre–determined time. Failure by SSC occurs if either cracks are identified or the specimens are fractured completely after being exposed to the test solution for at least 720 h. Laboratory–based test methods, briefly described in Table 2.3, are classified as static, e.g. tensile, bent beam, C-ring and double–cantilever beam (DCB) [35, 88], or dynamic, e.g. slow strain rate test (SSRT) [122] and rippled strain rate test (RSRT) [123]. In addition to small–scale specimens [124–129], full sections of pipelines can also be used [130, 131]. Ideally, susceptibility measurements by different methods should be equivalent, although interpretations may be misleading due to specific characteristics of each test—primarily related to different loading approaches and distinct specimen geometries.

TABLE 2.3: Standard test methods to assess the SSC susceptibility

Method	**Procedure**	**Highlights**	**Reference**
Tensile	Tensile specimens are axially loaded to the required level by adjusting the displacement of a proof ring	The threshold stress (σ_{th}) at or below which SSC does not occur can be determined	[35, 88, 124]
Bent-beam	Beams with rectangular cross sections are bended and the target tensile stress is obtained by adjusting the displacement of the outer surface (measured via strain gauge)	Multiple fixtures can be tested simultaneously by using a single vessel	[35, 88, 125, 127]
C-Ring	Analogously to bending, specified stress levels are obtained by tightening the stressing bolt to the corresponding displacement	Convenient alternative to analyse tubing, as specimens can be machined from their transverse sections	[35, 88, 126, 128]
DCB	Susceptibility is determined by the threshold stress intensity factor (K_{ISSC})	Cn be used to characterise the kinetics of crack propagation from pre-existing flaws (Figure 2.13b)	[35, 88]
SSRT	Plane or pre-cracked specimens are continuously elongated at constant strain during exposure	It is commonly used as a screening test and usually complemented by statically loaded and electrochemical techniques	[122, 129]
RSRT	Tensile specimens are axially loaded up to the actual yield strength and cyclic loaded in the plastic regime	Evaluates the effect of plastic straining	[123]
Full-ring	Full sections of pipes are statically loaded and filled with the test solution	It retains full residual stress of pipe sections. Allows online monitoring	[130, 131]

In constant displacement methods (Figure 2.13)—also referred as constant load, even though stress relaxation can occur during crack propagation [132]—specimens are loaded to at least 90% of the actual yield strength (σ_y) of the tested material [16] or to the actual loading conditions expected for the component during service. In dynamic straining techniques (e.g. SSRT) [122], specimens immersed in the test solution are continuously elongated at strain rates varying from 10^{-8} s^{-1} to 10^{-5} s^{-1}. This method is usually combined with prior screening tests to determine the most appropriate strain rate that matches the susceptibility pattern of the material in the tested environment [133]. Overall, larger strain rates accelerate the test and overestimate the loading conditions by applying significant amounts of plastic deformation. Selecting very low strain rates can overcome this effect, but it will result in prolonged and often impractical test durations. Despite the unrealistic loading conditions, the SSRT technique is suitable for evaluating the effectiveness of repassivation of materials in which protective films are formed on the surface, since they can be damaged due to excesisive elongation [134]. More realistic conditions could be simulated by using the loading pattern adopted by the RSRT method [123], since in this case plastic strain is limited to small ranges during the cyclic loading.

Supplementary techniques are often used alongside standard methods to provide further information about the susceptibility to SSC, for example: (i) electrochemical potentiodynamic reactivation (EPR) [135, 136] can be used to determine the sensitisation level (chromium depletion); (ii) cyclic potentiodynamic polarisation techniques can characterise the passivation behaviour and the pitting corrosion resistance [46]; (iii) anodic or cathodic polarisation [50] and analysis of potential and current fluctuations under open circuit conditions [137, 138] can contribute to the understanding of the mechanisms involved in the cracking process; and (iv) hydrogen analysis using electrochemical methods [139],

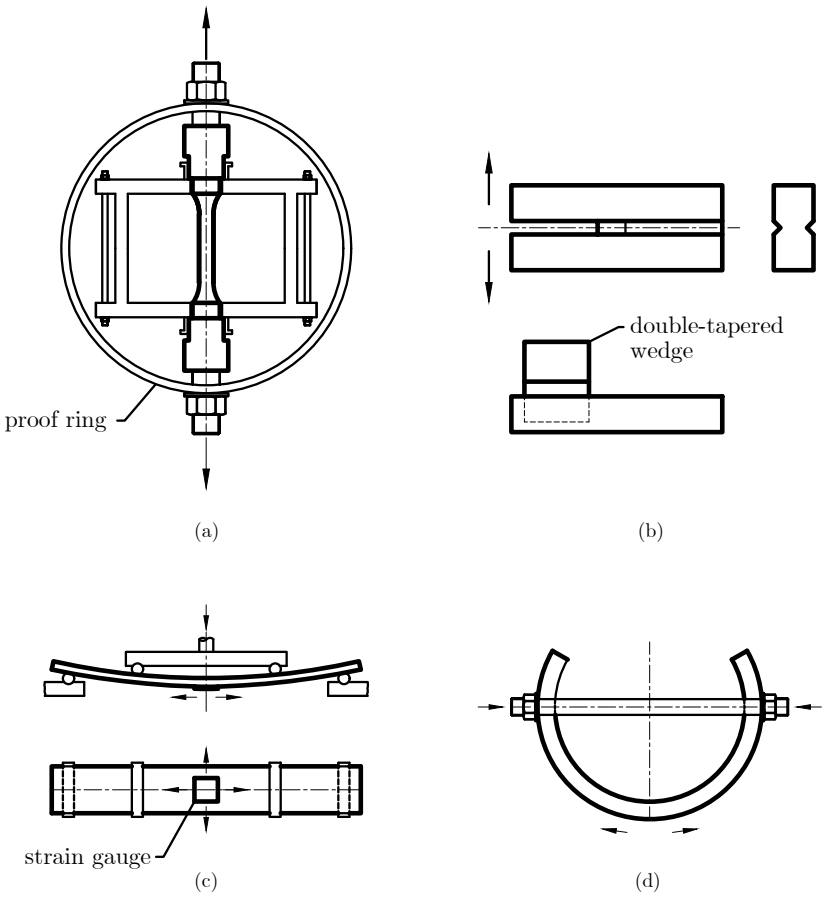

FIGURE 2.13: Main constant–displacement test methods to assess the SSC susceptibility: (a) tensile; (b) double-cantilever beam; (c) bent beam (four-point bend); and (d) C-ring.

hydrogen collection technique [140, 141], melt extraction [142], collecting fluids (glycerine method) [143], thermal desorption spectroscopy techniques, nuclear reaction analysis and Kelvin probe approach [144] can provide information about hydrogen transport and trapping.

For qualification purposes, test solutions must simulate the service environment in terms of gas mixture, pH, dissolved solids and solution chemistry. Since the pH tends to rise during the test in response to the corrosion activity, artificial or natural buffer systems

TABLE 2.4: Standard reference environments to assess SSC susceptibility at room temperautre

Solution	Gas mixture	pH	Buffer system	NaCl	Reference
Solution A	H_2S	2.6 - 2.8	0.5 wt.% CH_3COOH	5.0 wt.-%	TM0177 [88]
Solution B	H_2S	3.4-3.6	2.5 wt.% CH_3COOH 4.1 wt.% $CH_3COOHNa$	5.0 wt.%	TM0177 [88]
Solution C	H_2S/CO_2 (balance)	service	$0.4\,g\,L^{-1}$ $CH_3COOHNa$	service	TM0177 [88]
Produced water	service	4.5	not specified	$165\,g\,L^{-1}$	EFC 17 [35]
Condensed water	service	3.5	not specified	$1\,g\,L^{-1}$	EFC 17 [35]
Type 1	H_2S/CO_2	≥ 4.5	bicarbonate	service	MR0175 [16]
Type 2	H_2S/CO_2 (balance)	service	bicarbonate	service	MR0175 [16]
Type 3	H_2S/CO_2 (balance)	service	CH_3COOH	service	MR0175 [16]

must be added to maintain the required acidity level. Table 2.4 lists recommended buffer systems to be added to the main test solutions used to assess the SSC susceptibility. NACE TM 0177 [88] defines 3 types of environment, namely solution A, B, and C. Solution A is formed by de-aerated, H_2S–saturated distilled or de–ionized water containing $50\,g\,L^{-1}$ of NaCl and $5\,g\,L^{-1}$ of acetic acid (CH_3OOH) to obtain a pH varying from 2.6 to 2.8 after saturation. Solution B is similar to solution A, except that the buffering system is adjusted to maintain the pH within 3.4-3.6. Solution C is composed of H_2S at the same partial pressure as in the intended service and CO_2 as balance gas. In this case, the pH is adjusted by adding hydrochloric acid (HCl) and sodium hydroxide (NaOH). NACE MR0175-3 [16] uses a different terminology and classifies the solutions as type 1, 2 and 3, according to the buffering agent and gas mixture. In these solutions, the NaCl content can be adjusted as in the intended service. Guidelines from EFC Publication 17 [35] recommend reference test solutions representing typical oil and gas production

environments, i.e., produced water ($165\,g\,L^{-1}$ of NaCl and pH 4.5) and condensed water ($1\,g\,L^{-1}$ of NaCl and pH 3.5), respectively.

2.2.3 Main variables affecting SSC

2.2.3.1 Temperature

Temperature has a strong effect on the SSC resistance of high–strength steels [33, 145]. Figure 2.14a shows that the susceptibility of high–strength wires [107] reached a maximum at 25 °C. At 0 °C, the reduced corrosion kinetics and lower diffusion of hydrogen apparently contributed to reduce the time–to–failure and, on heating (above 25 °C and up to approximately 80 °C), the material presented increased resistance to SSC. Similar trends were observed [106] for a different high–strength steel (12% Cr) loaded to different stress levels. As shown in Figure 2.14b, greatest susceptibility—measured by the ratio between the threshold tensile stress for SSC to occur (σ_{th}) and the yield strength (σ_y)—occurred at approximately 25 °C. In the same graph, one result from the 17-4 PH is shown for comparison, demonstrating its high susceptibility to SSC at 25 °C [13], with $\sigma_{th}/\sigma_y = 0.2$. The authors [13] highlighted similarities between these results and the temperature effect on HE, in which the tendency for brittle failure to occur decreases with increasing temperature. Since the temperature dependence in SSC of high–strength steel is well established, standard methods [88] recommend that it shall be maintained within the most susceptible temperature, i.e. (23 ± 2) °C.

2.2.3.2 H_2S concentration and environment pH

The partial pressure of H_2S (pH_2S) and the solution pH are critical variables controlling the SSC behaviour. Extensive laboratory experiments using synthetic solutions and field investigations in different oilfield environments [106] demonstrate that, in general,

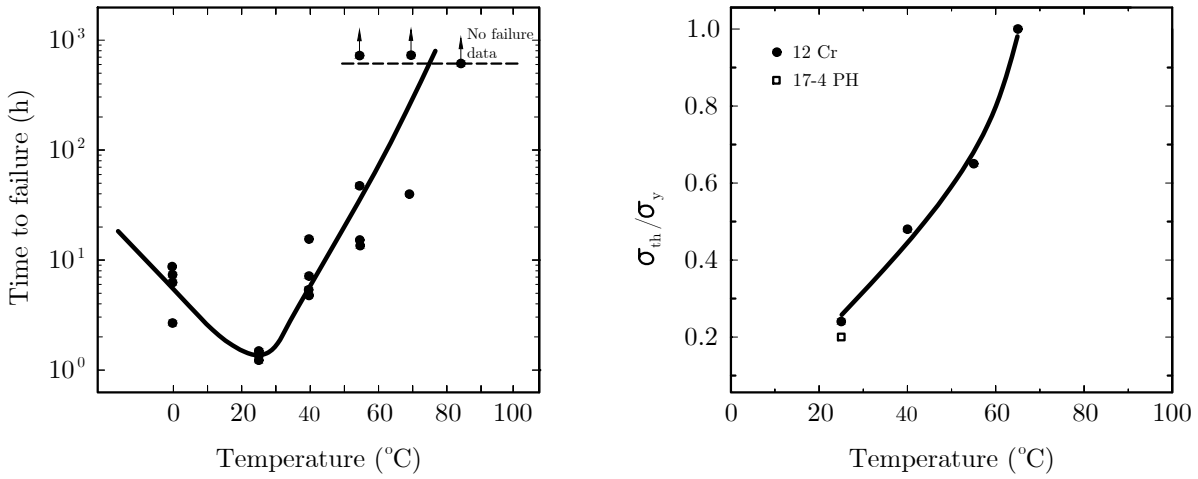

FIGURE 2.14: (a)Effect of temperature on the time-to-failure by SSC of high–strength wires (data from [107]); (b) Data exemplifying the variation of the threshold stress for SSC to occur in high–chromium stainless steels (12% Cr) [106] and in the 17-4 PH [13].

the susceptibility to SSC of various high-strength steels intensifies with increasing the concentration of H_2S. There is also evidence that the environment harshness generally increases with increasing acidity [146]. One of the first documented laboratory reports related to the SSC susceptibility of the 17-4 PH [33] indicated limited resistance in a H_2S-saturated solution containing 0.5 wt.% of acetic acid (pH below 3 at 20-25 °C). In this study, specimens were statically loaded using a flexural device and failed shortly after immersion, rising attention to the high sensitivity of this alloy to SSC when exposed to acid environments.

Likewise, data from several studies employing double precipitation hardened 17-4 PH (H1150D and H1150M) in the past years showed high susceptibility to SSC in severe conditions (Figure 2.15). These results have contributed to determining the application limits for the 17-4 PH, currently defined as pH $\geq$ 4.5 and $pH_2S \leq$ 3.4 kPa [16]. Data summarised in Figure 2.15 confirm that failure by SSC can occur both inside and out this domain. All these experiments were performed at room temperature (from 23 to 25 °C)

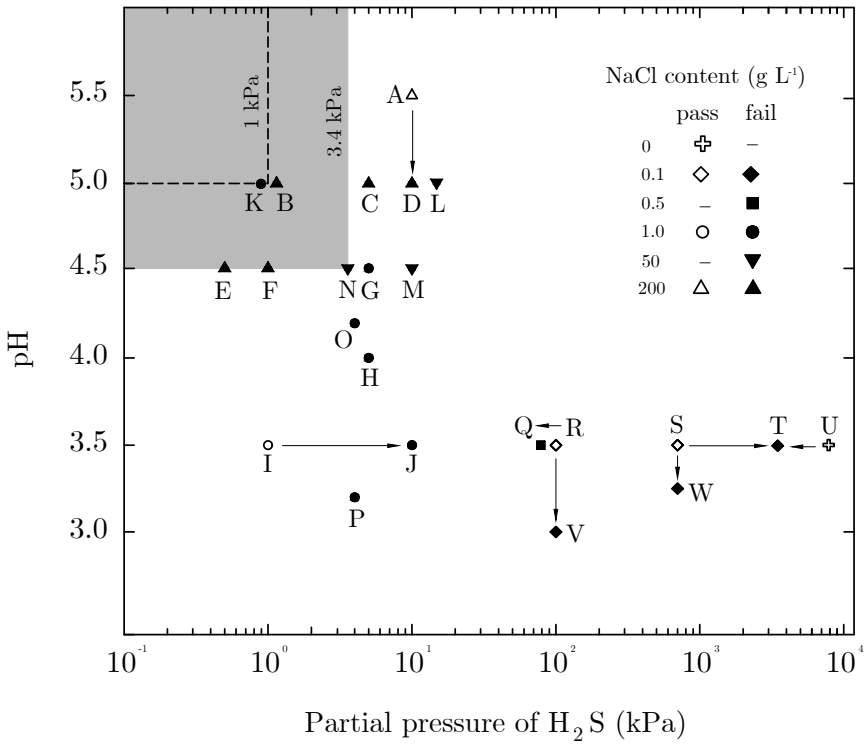

FIGURE 2.15: Summary of results from SSC experiments conducted with the 17-4 PH (H1150D and H1150M conditions) at room temperature, σ/σ_y = 0.9-1.0 and different concentrations of NaCl. Data from: A to J [71]; K to M [147]; N [10]; O and P [82]; Q to W [148]

and with different combinations of pH_2S, pH and chloride content. The exposure time, susceptibility criteria and stress levels (σ/σ_y varying from 0.9 to 1.0, σ_y being the actual yield strength) for all these experiments followed the recommendations from constant displacement methods [88].

The influence of the solution pH on the SSC resistance can be clearly seen in Figure 2.15. Lowering the pH from 3.5 to 3.0 (R $\longrightarrow$ V) [148] at 100 kPa of pH_2S resulted in failure by SSC. Similar effect was observed at 700 kPa of pH_2S (S $\longrightarrow$ W) [148] and at higher sodium chloride (NaCl) content at 10 kPa (A $\longrightarrow$ D) [71]. Studies applying a wider range of pH (from 3.5 to 5.5) [71] suggested that the maximum acceptable pH_2S

should be limited to 1 kPa when the pH is higher than or equal to 3.5, provided that the NaCl content is lower than $0.1\,g\,L^{-1}$. In less acidic environments (pH $\geq$ 5.5), however, the accepted pH_2S could be expanded to 10 kPa and the NaCl threshold increased to $200\,g\,L^{-1}$ (point A). Further attempts [147] to expand the existing limits showed high susceptibility for all tested conditions (from point K to M).

The isolated effect of the H_2S concentration on the SSC resistance can also be observed in Figure 2.15. After increasing the partial pressure from 700 to 1500 kPa (S $\longrightarrow$ T) [148], keeping all other variables unchanged, the material failed by SSC. The same occurred at lower partial pressures (1–10 kPa) for the same pH level (I $\longrightarrow$ J) [71], although the higher NaCl content used in the latter may have contributed to reduce the concentration threshold at which SSC occurred.

2.2.3.3 Chloride content

Chloride ions (Cl^-) are known to have negative impact on the passivity of high-chromium stainless steels. In the presence of H_2S, Cl^- can diminish the stability of the chromium-rich passive film [149] and, as a result, film breakdown can promote localised attack and subsequent cracking. Experiments, dating back to the 1950s [33], suggested that the 17-4 PH was highly susceptible to the effects of Cl^- since it failed by SSC only after the addition of 6 wt.% of NaCl. It was not clear, however, to what extent the Cl^- contributed to cracking. Figure 2.15 shows two examples of the detrimental effect of the Cl^-: the material failed by increasing the amount of NaCl from 0.1 to $0.5\,g\,L^{-1}$ (R $\longrightarrow$ Q) [148] and from 0 to $0.1\,g\,L^{-1}$ (U $\longrightarrow$ T) [148]. Similar investigations [71] about the particular effect of NaCl on the SSC resistance of the 17-4 PH highlighted its negative effect and suggested to restrict the maximum allowable chloride content, taking into account the acidity of the environment. The following limits were proposed [71]: a) maximum $200\,g\,L^{-1}$ NaCl when

pH $\geq$ 5.5 and $H_2S \leq 10\,kPa$; and (b) NaCl content up to $0.1\,g\,L^{-1}$ if pH $\geq$ 3.5 and $pH_2S \leq 1\,kPa$. In spite of that, current standards [16] do not specify maximum chloride content in H_2S-containing environments.

2.2.3.4 Applied and residual stress

As reported in numerous studies on the 17-4 PH, time-to-failure by SSC reduces after increasing the applied tensile stress. Failures on this material can occur at stress levels as low as 20% of its actual yield strength (σ_y), even when the heat treatment requirements and hardness criteria (i.e. hardness must not exceed 33 Rockwell C) are in accordance with the specifications of NACE MR0175 [16]. The failure of a tubing hanger made of 17-4 PH, that fractured after being in service in a H_2S-containing environment for less than one year, called attention to the importance of the loading conditions. After a detailed investigation [13], it was concluded that the threshold stress for SSC to occur was less than 20% of σ_y. Further investigations [73, 82] and systematic analysis of failures involving valve stems [14] confirmed this trend (see Figure 2.16) and highlighted that the guidelines from NACE MR0175, which only recommended limits for pH, H_2S and hardness, were not adequate. Recently, a restriction for the maximum stress was therefore added to the standard [17], based on specific research concentrated on different loading modes [10]. This study recommended to limit 17-4 PH to applications in which the maximum stress does not exceed 50% of the specified minimum yield strength or 380 MPa, whichever is lower, to prevent SSC. This recommendation was supported by additional evidence [147] of failure within the acceptable domain (pH 5 and pH_2S 1 kPa, see Figure 2.15, point K) at elevated stress levels, i.e. 90–100% of σ_y—maximum stress level previously accepted for qualification.

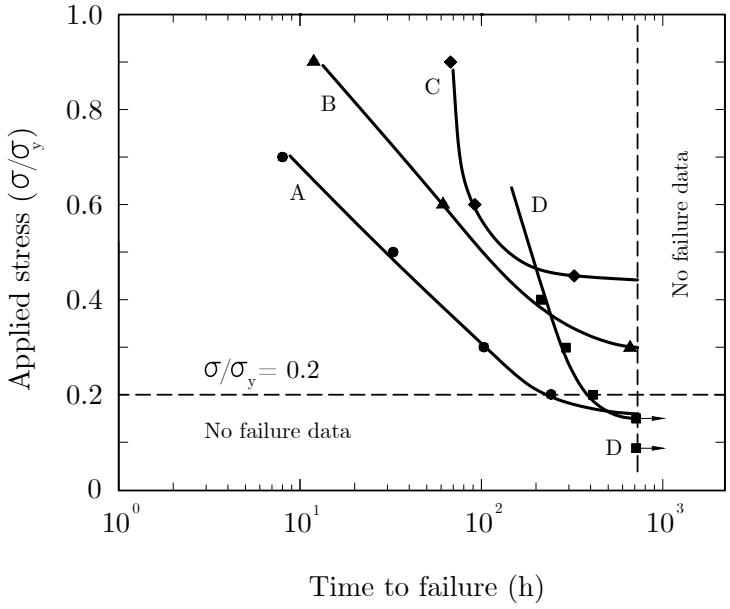

FIGURE 2.16: Effect of the applied stress on the SSC susceptibility (σ/σ_y) of the 17-4 PH (H1150D). Data from: A [14]; B [73]; C [82]; D [13].

2.2.3.5 Metallurgical factors

Current standards do not directly specify microstructure and phase composition. Instead, for the specific case of the 174 PH heat treated to H1150D or H1150M conditions, they recommend that the hardness be maintained equal to or below 33 Rockwell C [16]. This indirectly controls the maximum strength and microstructure, although results from numerous studies indicate that this approach can be misleading. Investigation [82] conducted with three di erent commercially sourced 174 PH highlighted that minor variations in heat treatment can result in an unexpected microstructure, even if the materials meet the hardness condition. These results [82] suggest that the volume per cent of δf errite should be limited to less than 1% and that the austenite content should be higher than 15% to provide better resistance to SSC. The detrimental e ect of large amounts of δf errite on SSC, however, was not fully clarified. Higher corrosion activity could be a possible explanation based on the work carried out to evaluate the SSC resistance of tempered 13%

chromium stainless steel [150] (with low-carbon martensite, similar to the 17-4 PH). The negative effect of the δ-ferrite was presumably related to the chromium-depleted zones promoted by the precipitation of chromium carbides and chromium nitrides (CrN) at grain boundaries of the ferritic structure. Thus, the sensitised areas would be more susceptible to localised corrosion and consequently less resistant to SSC. Similar studies with the 17-4 PH [151] suggested an opposite effect, i.e. higher amounts of ferrite, obtained by increasing the molybdenum content, led to lower passivation currents and higher pitting potential. This resulted in increased resistance to stress corrosion cracking, possibly due to the reduction of the hardness with the increase of the Mo content. Specimens failed when the δ-ferrite content increased, even after reducing the hardness to below 33 Rockwell C.

The role of the austenite (retained and reverted) in the cracking process is contradictory. It is generally accepted that austenite positively affects the impact properties, yet studies with the 17-4 PH [48] suggested that the retained austenite has little effect on the impact toughness. Moreover, since the solubility of hydrogen is greater in face-centred cubic structures compared with that of martensitic substrates [152], it seems reasonable to expect that the greater the austenite content, the higher the susceptibility to brittle cracking after hydrogen charging. However, this assumption is not in agreement with the minimum austenite content (15% in volume) suggested for the 17-4 PH to avoid SSC [82]. In addition to the amount, the size and distribution of austenite grains seem to be relevant aspects. Finely distributed grains are unlikely to affect the cracking [73], while large austenite bands—possibly generated due to improper heat treatment—can cause premature failure [153], even in non-sour environments.

2.2.3.6 Gas mixture (CO_2/H_2S)

CO_2 corrosion of carbon steel involves the formation of a solid layer of ferrous carbonate ($FeCO_3$) with protective characteristics. It can effectively reduce the corrosion rate by acting as a barrier for the diffusion of the corrosion species if a dense layer is formed. Similarly to H_2S, CO_2 is soluble in water and forms carbonic acid (Equation 2.12), which dissociates to form bicarbonate ion (Equation 2.13) and carbonate ion (Equation 2.14) [154]. When the limits of solubility of ferrous and carbonate ions are exceeded, $FeCO_3$ is deposited at the surface (Equation 2.15).

$$CO_2 + H_2O \longrightarrow H_2CO_3 \tag{2.12}$$

$$H_2CO_3 \longrightarrow H^+ + HCO_3^- \tag{2.13}$$

$$HCO_3^- \longrightarrow H^+ + CO_3^{-2} \tag{2.14}$$

$$Fe^{2+} + CO_3^{-2} \longrightarrow FeCO_3 \tag{2.15}$$

Studies with high-chromium stainless steels exposed to environments containing CO_2 [155] indicate that the precipitation of $FeCO_3$ is accompanied by the formation of Cr_2O_3, resulting in different protective characteristics. Below 60°C, the formation of chromium hydroxide $Cr(OH)_3$ prevailed and $FeCO_3$ started to form when further raising the temperature. In H_2S/CO_2 mixed systems, film composition and growth are dictated by the competitive formation of iron sulphide and $FeCO_3$. Studies with carbon steels [156] indicated that both structures were obtained at low H_2S concentration, while iron sulphide

(mackinawite) predominated when the amount of H_2S was further increased.

Overall, the corrosion resistance of stainless steels in H_2S/CO_2 systems is higher than that in pure H_2S and lower than that in CO_2-saturated conditions. Evidence [157] of enhanced corrosion resistance of high-chromium stainless steels in mixed H_2S/CO_2 compared with pure H_2S (at 80°C, irrespective of the pH and chloride content) was attributed to the formation of a passive film of Cr_2O_3. Likewise, similar studies [158] suggested that the lower corrosion resistance in H_2S/CO_2 solutions compared with pure CO_2 environment was related to the preferential formation of iron sulphide—with lower protective characteristics—in the mixed system. In this case, the authors [158] assumed that HS^- and S^{2-} species promoted the formation of soluble corrosion products, thereby preventing the development of an effective barrier for general corrosion.

2.3 Plasma nitriding

Surface engineering technologies, such as nitriding, carburizing and nitrocarburizing, which involve the introduction of nitrogen, carbon or both species simultaneously into the material, respectively, have been extensively used to improve the wear resistance of the 17-4 PH. For specific combinations of process parameters, the corrosion resistance can also be increased. Table 2.5 summarises the main structures (defined in section 2.3.1) obtained after each surface modification, which were carried out in three different atmospheres: liquid (e.g. salt bath nitriding [159]), gas (e.g. gas nitriding [160]) or plasma (e.g. plasma nitrocarburising [61, 69, 161] and plasma nitriding [18, 19, 162, 163]). Overall, all the treatments resulted in increased sliding wear resistance compared to the unmodified 17-4 PH and, in some cases, superior corrosion resistance was also observed. As shown in Table 2.5, plasma-based diffusion treatments were carried out at relatively

low temperatures compared to those conducted in either ammonia or molten salt. In particular, low-temperature plasma nitriding—successfully performed in the 17-4 PH at 420 °C [72] and later at 350 °C [70]—resulted in a modified layer with better corrosion resistance, mostly attibuted to the absence of CrN at low temperatures. In addition, the low-temperature treatment prevents further microstructural transformations during the nitriding process. These aspects, combined with lower environmental impact [164] and better control of the process in industrial scale [165], favour the use of low-temperature plasma nitriding for the 17-4 PH. For this reason, the remaining sections of this chapter will concentrate on this type of treatment.

TABLE 2.5: Typical structure of nitrided layers obtained by different surface modification treatments used to increase wear and corrosion characteristics of the 17-4 PH

Surface modification	**Process parameters**		**Modified layer**		**Ref.**
	T (°C)	**Atmosphere**	**Thickness** (μ**m**)	**Microstructure**	
Salt bath nitriding[a]	610-650	Molten salt	95 - 135	α'_N, γ_N, CrN, γ'-Fe_4N and $(Cr,Fe)_xO_y$	[159]
Plasma nitrocarburizing[b]	430-460	N_2,H_2; C_2H_5OH	up to 60	α'_N, CrN, γ'-Fe_4N	[61, 69, 161]
Gas nitriding[c]	410-570	NH_3	up to 55	α'_N, ε-Fe_3N, CrN and γ'-Fe_4N (490 °C)	[160]
Plasma nitriding[b]	350-500	N_2,H_2	up to 100	α'_N, γ_N (350 °C) γ'-Fe_4N, CrN (>420 °C)	[18, 19, 162, 163]

[a] solution annealed (SA) + precipitation hardened (PH) at 595 °C/4h; [b] SA; [c] SA + PH (200-800 °C/4h).

2.3.1 Background

Plasma nitriding (also known as ion nitriding and glow-discharge nitriding) is a thermochemical process developed in 1932 [166] that involves the introduction of atomic nitrogen into the surface of (mainly) metallic materials to improve their tribological characteristics.

In the industry, plasma can be obtained by ionising a gas by the application of an electric field at low pressure. Typical gaseous mixtures comprise different concentrations of nitrogen and hydrogen or argon as balance gas, hydrogen being preferred due to its hability to enhance the diffusion of nitrogen by neutralising the detrimental effects of oxygen—a common contaminant in the chamber—adsorbed on the surface [167]. Due to the greater energy of the particles in the ionised atmosphere compared to those in the gaseous state, plasma is considered the fourth state of the matter [168]. Typical nitrogen-rich structures comprise an outer compound layer and an inner diffusion zone with structures and thicknesses depending primarily on the process parameters and metallurgical aspects of the base material.

During plasma nitriding of iron-based alloys, nitrogen ions are accelerated towards the target surface and associated with sputtered iron atoms to form iron nitrides [166]. The mechanisms involved in plasma nitriding, according to the Koelbel's model [169, 170], can be described by the following reactions, schematically illustrated in Figure 2.17: (i) electrons are attracted with high energy to anode (furnace wall) an collide with nitrogen molecules generating nitrogen ions and nitrogen atoms; (ii) sputtering, in which Fe atoms are removed from the surface (contaminants and oxides are also removed); (iii) sputtered Fe atoms combine with N to form FeN; (iv) breakdown of Fe into ε-Fe_2N, ε-Fe_3N, γ'-Fe_4N and α-Fe due to continuous bombardment.

The solubility of nitrogen in iron is temperature-dependent and varies in each structure, as shown in the metastable Fe-N diagram in Figure 2.18. In typical nitriding temperature (e.g. 500 °C), the γ'-Fe_4N structure can accommodate up to 19-20 at% of N and, beyond this concentration, the phase ε-Fe_3N starts to stabilise. These structures are formed on the top of nitride layer (compound layer) and are usually referred as 'white layer' due to their bright appearance after etching. They are often 10-20 µm thick and

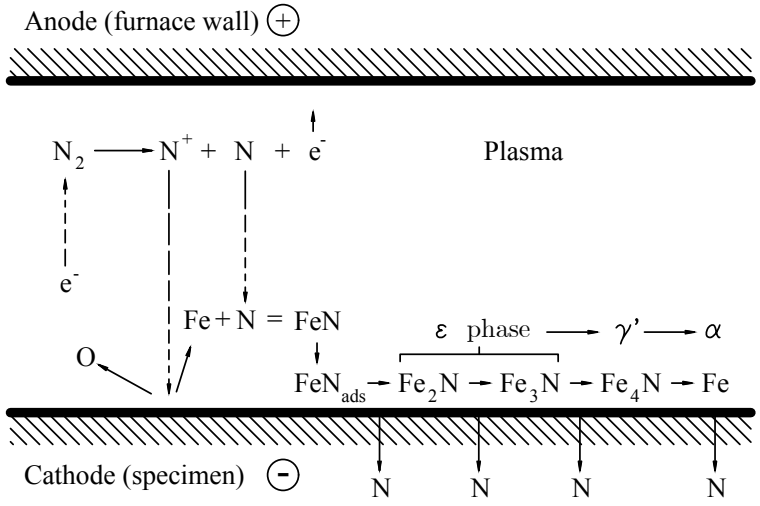

FIGURE 2.17: Schematic representation of the plasma nitriding mechanisms, according to the Koelbel's model. Adapted from [169, 170]

consists of either mixed γ'-Fe_4N and ε-$Fe_{2\text{-}3}N$ or single γ'-Fe_4N [171]. The discontinuity and residual stress produced by the coexistence of these two forms of nitride increase the probability of spalling during service [172] and therefore some applications require adjustments of the nitriding parameters to control the proportions of each phase. The homogeneous structure of the single-phase γ'-Fe_4N has higher ductility and thus better fatigue resistance and tribological properties compared to mixed layers [173].

Beneath the compound layer, a diffusion zone with lower nitrogen content is formed. In martensitic substrates, this region is formed by expanded martensite [175], α'_N, with nitrogen occupying octahedral interstitial positions and inducing lattice expansion. The N solubility is this structure is very low, as in α-Fe, i.e. approximately 0.4 at.% at 590 °C (Figure 2.18). Analogously, austenitic structures can form expanded austenite, γ_N [176], and therefore any retained or reverted austenite in the diffusion zone is expected to be in this form. During nitriding, dissolved nitrogen can precipitate as CrN, although other forms of nitride are possible if nitrogen combines with other nitride-forming elements

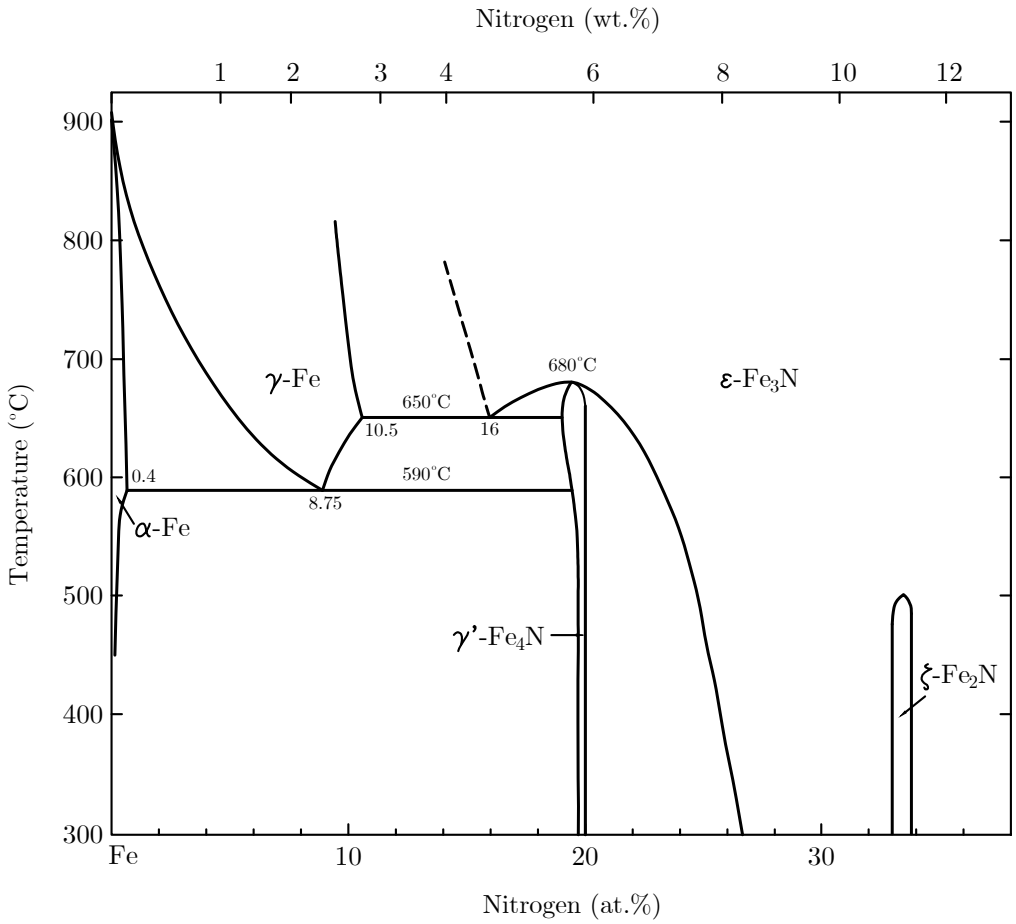

FIGURE 2.18: Metastable iron-nitrogen phase diagram. Redrawn from [174]

such as aluminium, niobium and manganese. In the 17-4 PH, CrN can be formed at elevated temperatures ($> 420\,°C$, Table 2.5) and are known to have a detrimental effect on corrosion resistance (see section 2.3.3).

2.3.2 Plasma nitriding techniques

In conventional or DC (direct current) plasma nitriding (DCPN), electric potential is applied between the wall of the furnace (anode) and the component (cathode), as illustrated in Figure 2.19a. In this technique, plasma is formed directly on the surface of the material being treated and there are many disadvantages associated with this approach, as highlighted in recent literature reviews [177, 178]: (i) since high potential are applied to the cathode, the surface of the component can be damaged due to the formation of electric arcs; (ii) hollow cathode effect, which is the increase on the nitriding kinetics [179] in specific geometries (e.g. cavities and gaps) resulting in overheating and thereby non-uniform nitriding; (iii) edge effect, which also results in non-uniform nitriding due to variations of the strength of the electric field near sharp edged. Pulsed DC plasma nitriding can provide improved process control compared to the DC technique, but the inhomogeneities discussied earlier are not elimnated [177].

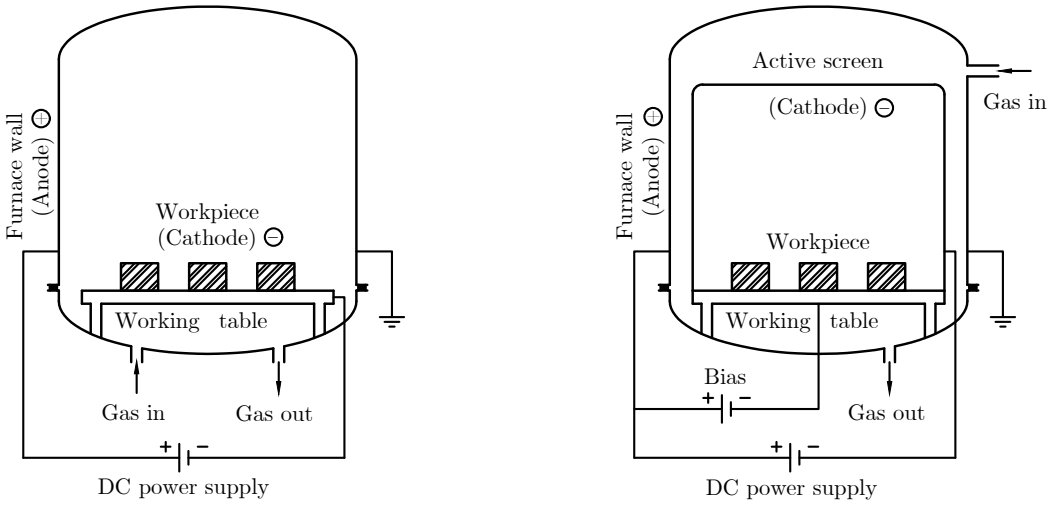

FIGURE 2.19: Schematic representation of (a) direct current (DCPN) and (b) active screen plasma nitriding (ASPN) systems. Adapted from [178]

Active screen plasma nitriding (ASPN), also referred as through cage or post discharge, is a technology developped in the 1990s to overcome the main problems associated with conventional DCPN [180, 181]. In the ASPN system (Figure 2.19b), electric potential is applied between a metallic screen (cathode) and the furnace wall (anode). Plasma is therefore formed on the screen—the workpiece is maintained at floating potential—and part of the active species are directed to the surface of the sample. To maintain uniform plasma conditions, an auxiliary cathodic potential (bias) is often applied to the worktable. With the ASPN configuration, the issues discussed earlier (i.e. arcing, hollow and edge effects) are eliminated. Many investigations on ASPN [182–186] conducted with different materials provided supporting evidence for the superior results obtained by using this method and highlighted further remarkable advantage of ASPN over DCPN: the possibility to perform treatments in batches using workpieces with varied geometries. This is possible since the temperature is more uniform inside the furnace and it can be finely adjusted by varying the current applied to the screen.

2.3.3 Corrosion and SSC resistance

There seems to be no reference in the literature to the corrosion resistance of plasma nitrided 17-4 PH in H_2S-containing environments and limited data are available in non-sour environments. In standard aerated brines (3.5% NaCl), there are indications [18, 19] of improved corrosion resistance when plasma nitriding is performed at sufficiently low temperatures (420 °C) and the treatment time is relatively short ($<$ 10 h). The results from these investigations [18, 19] showed that the formation of thick compound layers of γ'-Fe_4N increased the corrosion resistance, yet the greater temperatures required to obtain a thicker structure had a detrimental effect. The main downside related to applying elevated temperatures is associated with chromium depletion from the grain

boundaries to form chromium nitride, thereby lowering the resistance to intergranular corrosion. The authors [19] concluded that the optimum treatment parameters providing balanced corrosion and wear resistance on the 17-4 PH (solution annealed condition) consisted in plasma nitriding at 420 °C for 10 h in a gas mixture containing 25% N_2 and 75% H_2. Systematic characterisation of plasma nitrided 17-4 PH [187] provided additional evidence on the formation of CrN only when the temperature exceeds 420 °C or at 420 °C for more than 10 h.

As noted in recent review [188], the mechanisms involved in the enhanced corrosion resistance of plasma nitrided structures still unclear. Studies performed with plasma nitrided iron [189] suggested that further protection against corrosion was provided by a thin passive layer of oxide which was spontaneously formed on the top of the nitrided layer after it has been exposed to air at room temperature. A passivation mechanism was also proposed for a martensitic stainless steel (AISI 4140) [192], in which oxygen from the atmosphere was absorbed into the pores of the γ'-Fe_4N and ε-$Fe_{2\text{-}3}N$ structures and formed Fe_3O_4, which presubably acted as a barrier for the corrosion of the underlying substrate. Many reseachers [190–192] attribute the superior resistance to pitting corrosion of nitrided layers to the local increase on the pH inside the pits due to the formation of NH_4^+.

Concerning the SSC resistance of plasma nitrided 17-4 PH, a recent investigation [20] showed that the material (solution annealed and precipitation-hardened at 595 °C for 4 h) exhibited high susceptibility after being surface modified by an oxy-nitriding treatment, i.e. plasma nitriding at 450 °C for 4 h in 50 vol.% H_2 / 50 vol.% N_2 and an oxidising stage at 450 °C for 30 min in 50 vol.% O_2 and 50 vol.% Ar. By using the tensile method with $\sigma/\sigma_y = 0.6$, plasma nitrided specimens failed (complete fracture) within 12-25 h of exposure to H_2S-saturated environment (Solution A, see Table 2.4 for details). This

time-to-failure, in spite of being greater than that of the unmodified material (i.e. 2.5 h), was lower than those obtained for unmodified 17-4 PH in other studies (see Figure 2.15). The authors [20] attributed the delayed time-to failure to the greater corrosion resistance of the nitrided layer, but the electrochemical measurements were performed in non-sour environment and this aspect was not fully clarified.

2.4 Summary

This section reviewed data published in the past decades demonstrating the high susceptibility of the 17-4 PH (H1150D) to SSC in typical oilfield environments. The data highlighted that the limits recommended by NACE MR0175/ISO 1515-6 (i.e. pH $\geq$ 4.5 and $pH_2S \leq 3.4$ kPa) to qualify this material for use in H_2S-containing environments was not sufficient to prevent failure by SSC. Based on observations that failures consistently occurred at low stress levels (as low as 20% of the yield strength), detailed investigations on the effect of the amplitude of the applied load on SSC was performed and an additional restriction was therefore recently added to the standard. In the revised version, the maximum permitted stress reduced to about 50% of the yield strength. The data also highlighted that the hardness criteria (maximum 33 HRC) can be misleading, suggesting that strict control on the metallurgical conditions are required to reduce the chances of failure by SSC.

This review also presented strong evidence that plasma nitriding can be effectively used to modify the surface of the 17-4PH, without being detrimental to its corrosion performance. It became apparent that corrosion behaviour is primarily associated with the structure of the modified layer, which is in turn related to the treatment parameters (time, temperature and gas composition). The data presented in this chapter indicated

that treatment conditions that minimise the precipitation of CrN are essential to reduce chromium depletion from the structure and therefore avoid the poor resistance to intergranular corrosion associated with this phenomenon. There are indications that the best combination of corrosion and wear resistance in brine can be obtained by limiting the treatment temperature to 420 °C for no longer than 10 hours. To date, there are no references in the literature to the corrosion resistance of plasma nitrided 17-4 PH in environments containing H_2S.

A recent reference on the resistance of oxy-nitrided 17-4 PH to SSC showed that the modified material fractured after one day of exposure to the test environment, indicating greater susceptibility when compared with results of unmodified 17-4 PH from similar experiments.

Despite the unclear nature of the SSC mechanism, it became evident that the primary driving force for the formation of brittle cracks is associated with hydrogen absorption and transport within the microstructure. An additional review on this topic is presented in Chapter 6, along with detailed background on the residual stress induced by plasma nitriding and its effect on SSC.

.

Chapter 3

Materials characterisation and plasma nitriding

This chapter presents the characterisation of the unmodified and plasma nitrided 17-4 PH. Plasma nitriding was conducted at two di erent temperatures, referred to as low-temperature plasma nitriding (LTPN) and high-temperature plasma nitriding (HTPN). The complete set of experiments carried out in this work is summarised in Figure 3.1, highlighting the topics covered in this specific chapter.

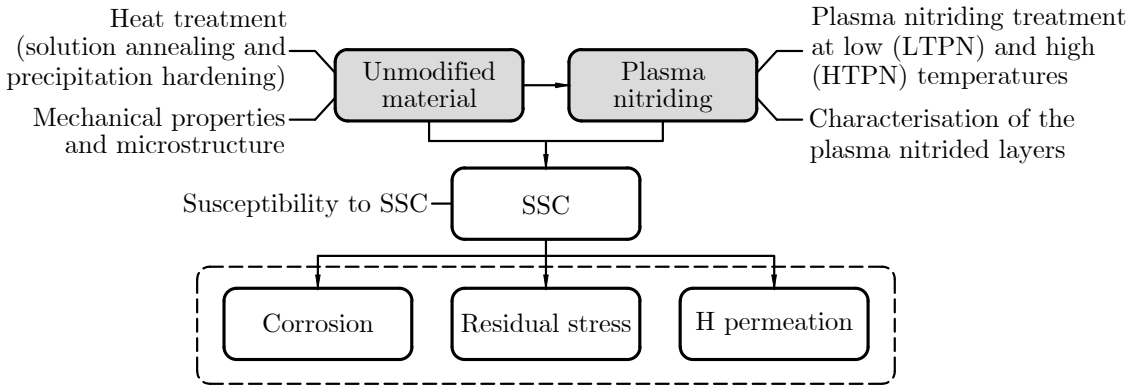

FIGURE 3.1: Schematic diagram summarising the topics covered in this chapter (highlighted in grey) within the complete experimental context of this work.

3.1 Experimental

3.1.1 Unmodified material

3.1.1.1 Chemical composition and heat treatment

The material investigated in this study is the ASTM A-564, grade 630 (UNS S17400, 17-4 PH or DIN 1.4542) martensitic precipitation hardening stainless steel with the following chemical composition (wt.%): 0.035% C, 15.20% Cr, 4.47% Ni, 3.03% Cu, 0.20% Si, 0.41% Mn, 0.020% P, 0.0006% S, 0.19% Mo, 0.280% Nb, 0.002% Ta. Wrought 17-4 PH was supplied as a cross-hot-rolled plate of 500 × 800 × 12 mm, heat treated as follows (see Figure 2.4): solution-annealed at 1040 °C for 30 minutes and air cool to below 32 °C, followed by two consecutive precipitation hardening stages at 620 °C (for four hours each) and air cool to below 32 °C. This sequence corresponds to the H1150D condition (described in section 2.1.2.2), specified by NACE MR0175 [16] for oilfield components exposed to H_2S.

3.1.1.2 Mechanical properties

Standard monotonic tension test method (ASTM E8/E8M) [193] was carried out at room temperature to determine the actual yield strength (σ_y) and the percent elongation of the unmodified material. Standard round tension specimens (with threaded ends and gauge section 4 mm in diameter and 20 mm in length) were submitted to controlled uniaxial loading until complete rupture and the elongation was recorded by a contact extensometer attached to the gauge section. Before the tests, the specimens were manually ground with 600 grit SiC (P1200). The microhardness was determined using a Mitutoyo MVK-H1 tester with the load set to 25 g.

3.1.1.3 Microstructure characterisation

The microstructure of the unmodified material was characterised by combining scanning electron microscopy (SEM) and X-ray diffraction (XRD) techniques. For the SEM examination, selected specimens—cut from different positions on the source material—were prepared as follows: (i) degreased with neutral detergent, (ii) wet grinded with successively finer abrasive papers (up to 600 grit SiC or P1200); (iii) polished with successively finer diamond suspensions (up to 1 µm) and acidic alumina suspension; (iv) etched by immersion in Vilella's reagent (1 g of picric acid, 5 mL of hydrochloric acid and 100 mL of ethanol) for 5 seconds and (v) ultrassonically cleaned with acetone for 5 minutes and dried with an air blower. For the samples submitted to XRD measurements, the surface finish was kept similar to that used in the SSC and corrosion experiments, i.e. 600 grit SiC (P1200). In all the analysis of the XRD data, the b.c.t. structure of martensite was approximated as a b.c.c. structure. This assumption, as discussed earlier (section 2.1.2.2), is reasonable in this particular case due to the low carbon content in the 17-4 PH, which makes the diffraction lines of martensite and ferrite to nearly coincide.

The total austenite content (retained after solution annealing, γ_{ret}, and reverted during precipitation hardening, γ_{rev}) was determined by XRD, following the procedures from ASTM E975 [84]. Its volume percent was estimated from the proportions of integrated intensities of the peaks obtained experimentally by XRD—or, equivalently, the area under the diffraction curve after subtracting background signals—and the corresponding theoretical intensities of peaks of austenite and martensite. The diffraction data were obtained with a Bruker D8 advanced diffractometer with a CuK_α radiation (λ= 0.154056 nm) equipped with a nickel filter. Scanning was performed at 0.8 seconds per step with a step size of 0.01°, with 2θ varying from 30° to 120°. The integrated intensities were obtained by fitting the experimental profile using a commercial software package (Match!)

for analysing XRD data. The lattice parameters of both austenitic (f.c.c.) and martensitic (b.c.t.) structures were determined by extrapolating the results obtained for each reflection line against a particular function of the diffraction angle.

Calculation of the austenite content assumes that martensite and austenite are the only phases present in the microstructure ($c_{\alpha'} + c_{\gamma} = 1$); for details see Appendix A. In summary, by considering n_{γ} reflections of austenite and $n_{\alpha'}$ reflections of martensite, the ratio between the volume fraction of each phase, $c_{\gamma}/c_{\alpha'}$, was obtained by [194]

$$\frac{c_{\gamma}}{c_{\alpha'}} = \frac{\frac{1}{n_{\gamma}} \sum_{0}^{n_{\gamma}} \left(\frac{I_{\gamma}}{R_{\gamma}} \right)}{\frac{1}{n_{\alpha'}} \sum_{0}^{n_{\alpha'}} \left(\frac{I_{\alpha'}}{R_{\alpha'}} \right)} \tag{3.1}$$

in which I_{γ} and $I_{\alpha'}$ are the integrated intensities of the diffracted peaks of each phase. Their corresponding theoretical intensities are represented by R_{γ} and $R_{\alpha'}$.

3.1.2 Plasma nitriding

3.1.2.1 Selection of the nitriding method

Plasma nitriding was selected as a surface modification technique used in this work due to the positive aspects presented in Chapter 2 (section 2.3). A remarkable advantage of plasma nitriding is that it can be successfully carried out at low temperatures (from 350-420 °C), thereby retarding or avoiding the precipitation of chromium nitrides and their negative impact on the corrosion performance. Similar structure can be obtained by low-temperature gas nitriding different stainless steel grades [195], although precipitation of chromium nitride was reported for the 17-4 PH at temperatures as low as 410 °C (section 2.3). For precipitation-hardening stainless steels, particularly the 17-4 PH heat treated

to the H1150D specification, nitriding at low temperature is essential to avoid undesirable microstructural transformations (e.g. further coarsening of copper precipitates and increase of the reverted austenite content) that could otherwise occur if the treatment temperature exceeds a certain limit. For example, as discussed in section 2.1.2.2, if the nitriding temperature is close to A_{c1}—temperature at which austenite starts to form on heating (slightly above 620 °C, in this case)—more fresh austenite can be formed during the treatment and retained after cooling.

The newly developed active screen plasma nitriding (ASPN) was selected as the method to be used in this work due to the advantages highlighted in section 2.3.2. With this configuration, most of the technical problems that arise from conventional methods (i.e. DC and pulsed plasma nitriding) such as arcing, edge and hollow cathode effects are addressed and a uniform modified layer is obtained.

3.1.2.2 Identification of the nitriding parameters

The main plasma nitriding parameters (i.e. temperature, time and gas mixture), summarised in Table 3.1, were selected based on previous results obtained for the 17-4 PH. As indicated in section 2.3.3, plasma nitriding this material at 420 °C for 10 h resulted in optimum combination of corrosion and wear resistance in seawater (3.5 wt.% NaCl). It was, therefore, anticipated that the nitrided layer obtained by these conditions would provide improved resistance to sulphide stress cracking (SSC), considering that SSC susceptibility decreases with increasing resistance to localised corrosion, and that the superior tribological characteristics imply enhanced resistance to crack initiation. A second condition (i.e. 500 °C for 10 h), representative of typical treatment temperature used in conventional nitriding, was selected for comparison. The same nitrogen-hydrogen ratio (25% N_2 - 75% H_2) was used in all the treatments.

TABLE 3.1: Main process parameters used for plasma nitriding at low temperature (LTPN) and at high temperature (HTPN)

Treatment	**Temperature**	**Time (h)**	**Gas mixture (vol.%)**	**Bias (%)**
LTPN	420 °C	10	25 N_2 + 75 H_2	5
HTPN	500 °C	10	25 N_2 + 75 H_2	5

3.1.2.3 Plasma nitriding procedures

Plasma nitriding was carried out in an industrial scale unit (AS Plasma Metal) with an active screen (ASPN) configuration (see schematic diagram in Figure 3.2a and the photograph in Figure 3.2d-e) with 75 kV A power supply between the cathode (metallic screen made of carbon steel) and the anode (furnace wall). An auxiliary cathodic potential—or electrical bias, set to 5% of the power input—was applied between the furnace wall and the worktable to guide active species to the workpieces being treated. Since in the ASPN method sputtering is more intense on the surface of the screen than on the surface of the samples, the temperature surrounding the workpieces is more uniform, which allowed the treatments to be performed in batches.

Figure 3.2c illustrates that tensile specimens (used on SSC experiments, Chapter 4) and corrosion coupons for electrochemical measurements (Chapter 5) were treated simultaneously. For each batch, the specimens were symmetrically arranged on the worktable (see Figures 3.2b and d) and the tensile specimens were placed on the upright position with their threaded ends masked with stainless steel coupling nuts. Prior to the treatment, the specimens were degreased, ultrassonically cleaned with acetone and dried with an air blower. Screening treatments were performed to confirm homogeneity of the modified layer.

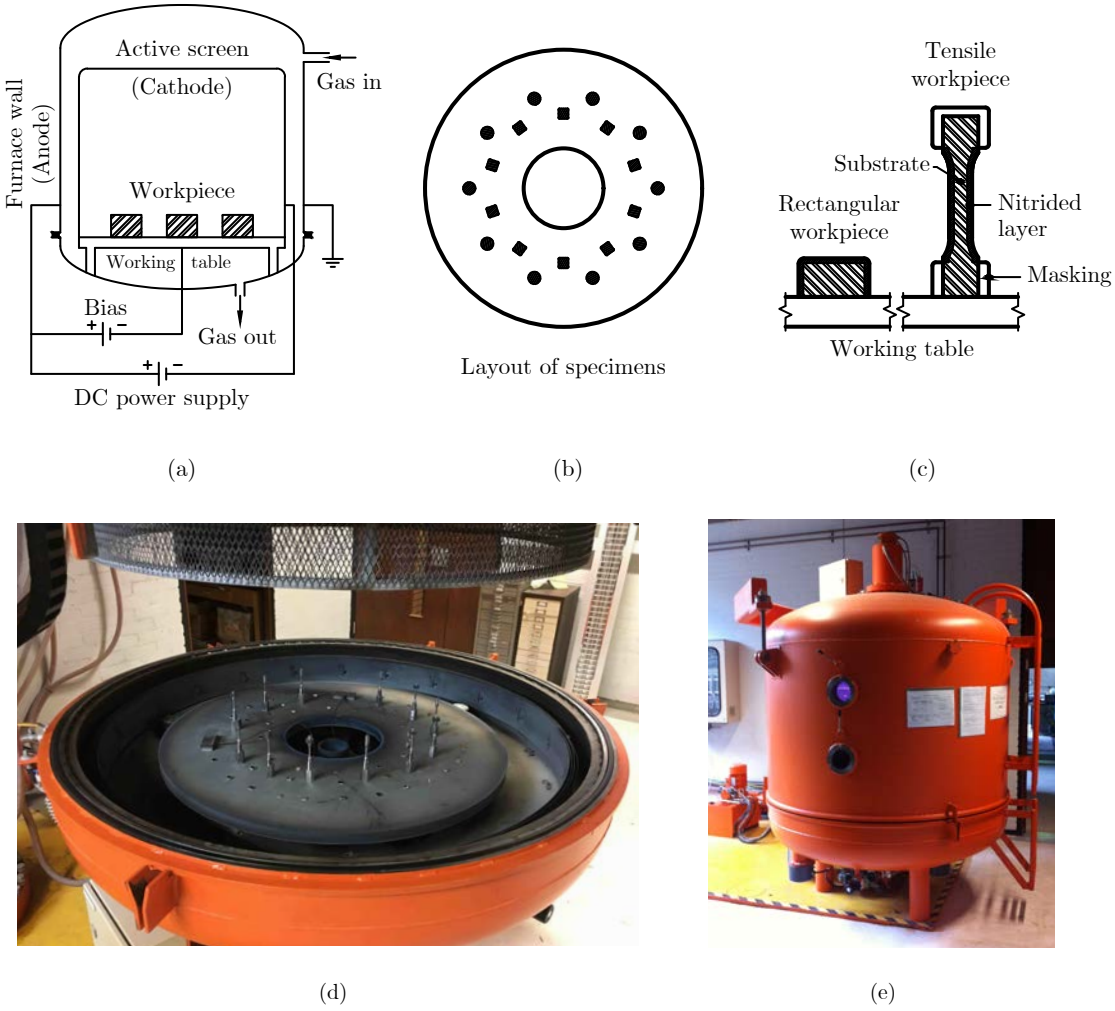

FIGURE 3.2: Active-screen plasma nitrided (ASPN) furnace: (a) schematic; (b) layout of specimens in the worktable; (c) detail (cross-section) of the specimens; (d-e) photos of the ASPN unit.

The plasma nitriding cycle is schematically illustrated in Figure 3.3. The chamber was first evacuated at room temprature (T_r) until its internal pressure reached 0.75 mbar and, at this point, hydrogen gas was introduced and glow discharge started on the surface of the active screen. The power was automatically increased gradually until an intermediate temperature (T_i) was achieved (T_i was set to 350 °C for the LTPN and 420 °C for the HTPN). This condition was maintained for 1 minute for stabilisation and then a gas

mixture (25 vol.% N_2 + 75 vol.% H_2) was provided and maintained at a constant flow rate. The 5% electrical bias was applied gradually until it reached the set point. When the treatment temperature (T_n) was reached (T_n was 420 °C for the LTPN and 500 °C for the HTPN), the plasma nitriding treatment effectively started. After 10 h at T_n, the plasma source was switched off and the chamber was naturally cooled to the room temperature (T_r). During the cooling stage, the vacuum was maintained inside the furnace to avoid the formation of oxides on the surface of the specimens.

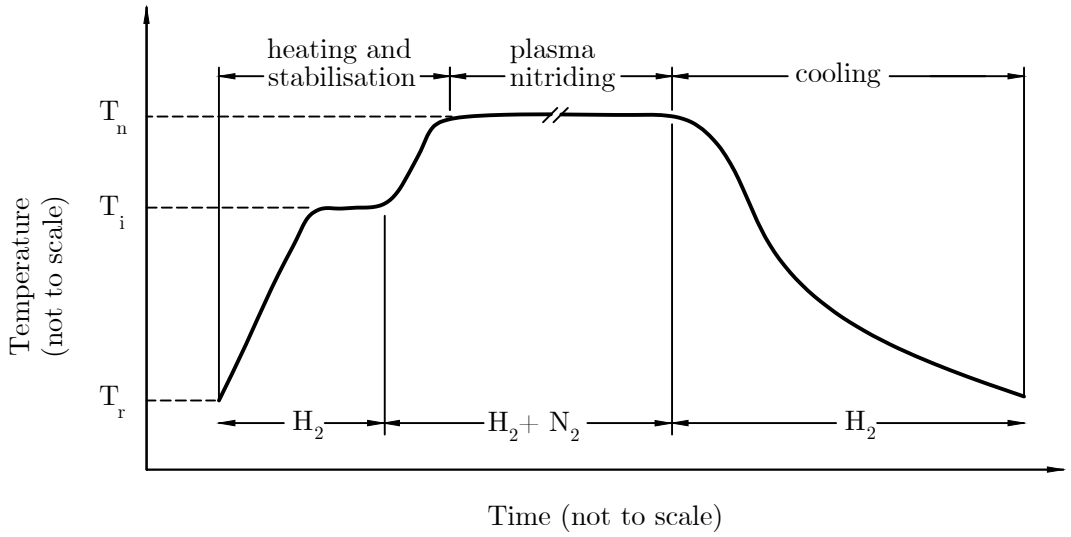

FIGURE 3.3: Schematic diagram of the plasma nitriding treatment

3.1.2.4 Characterisation of the nitrided cases

After plasma nitriding, the samples were cross-sectioned, degreased, ground with successively finer abrasive papers (up to 600 grit SiC or P1200), polished with diamond suspension (from 9 - 1 µm) and acidic alumina, ultrassonic cleaned with acetone, dried with air, etched with Vilella's reagent for 5 s and examined using SEM. The characterisation of the nitrided cases were complemented by a phase composition depth profiling

using XRD. Specimens exposing different depths of the nitrided layer (up to 20 µm deep with respect to the original outer surface, with 5 µm increments) were prepared by manual grinding with fine abrasive paper (1200 grit SiC or P4000). The diffraction patterns from each position were obtained with a Bruker D8 Advanced diffractometer equipped with a CuK_α radiation source ($\lambda = 0.154\,056$ nm) and a nickel filter. The scans were performed with a glancing angle of 7°, step size of 0.01° and a scan speed of 0.8 seconds per step from 2θ varying from 35° to 55°. This range was selected after a screening measurement of a wider interval, in which it was observed that most of the diffraction lines of interest were located within these positions.

The hardness depth profiling was conducted by using a Mitutoyo MVK-H1 microhardness tester with the load set to 25 g. Measurements were taken on the top surface (0 µm) and at different depths of cross-sectioned specimens (from 7.5 to 65 µm). For each depth, micro hardness was measured in five different positions, spaced at least 15 µm.

The concentration depth profile of nitrogen was obtained by glow discharge optical emission spectroscopy (GDOES) with a GDA 65 0HR (Spectruma) instrument.

3.2 Results and discussion

3.2.1 Unmodified material

3.2.1.1 Mechanical properties

The nominal stress-strain curves of three specimens heat treated to the H1150D condition, shown in Figure 6.5a, indicate that the material has an actual yield strength of (773 ± 12) MPa at 0.2 % offset strain (Figure 6.5b) and 22 % elongation, suggesting ductile behaviour and high fracture toughness. These results are in agreement with the required mechanical properties specified for this material, i.e. minimum yield strength of

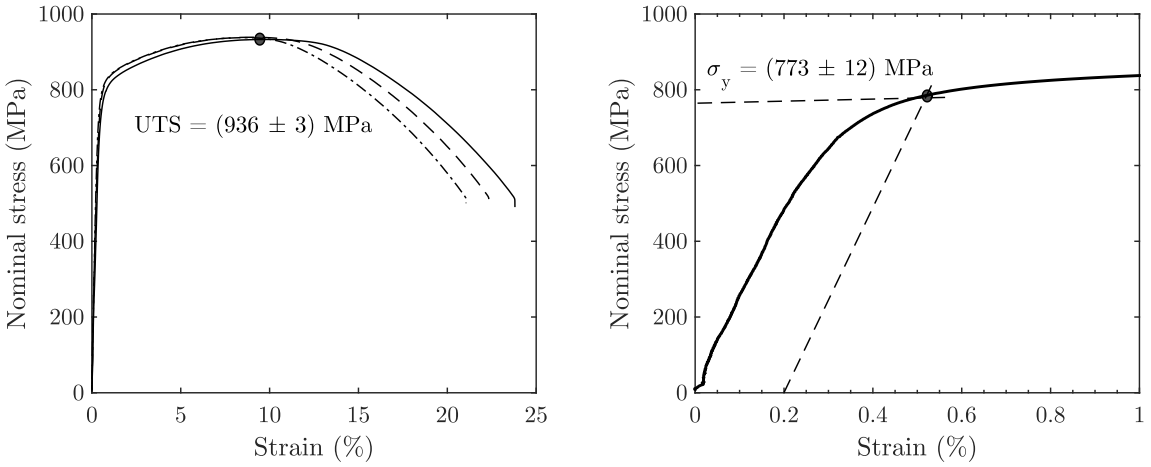

FIGURE 3.4: (a) Stress-strain curve of unmodified 17-4 PH at the H1150D condition; (b) Detail of the linear section (0.2% offset strain method used to determine the yield strength)

725 MPa and minimum elongation of 16 % (see Table 2.2 in Chapter 2). The fractured specimens presented a cup-and-cone feature (Figure 3.5a) with micro voids and dimples (Figure 3.5b), characteristic of ductile fracture. The low carbon (0.035 wt.%) and the high chromium content (15.2 wt.%) of this grade, combined with the partial reversion of martensite into austenite during precipitation hardening, apparently contributed to the enhanced toughness and ductility, as detailed in section 2.1.2.2.

3.2.1.2 Microstructure

The microstructure of the 17-4 PH, heat treated to the H1150D condition (Figure 3.6a), is mainly composed of a matrix of low-carbon (or lath) martensite—obtained after cooling from the annealing temperature and preserved after precipitation hardening, as detailed later in this section. As can be seen in the SEM micrograph (Figure 3.6a), the boundaries of prior-austenite grains (brighter phase), equiaxially distributed and with an average size of approximately 20 µm, were revealed after etching. Besides, nearly-parallel stringer-like

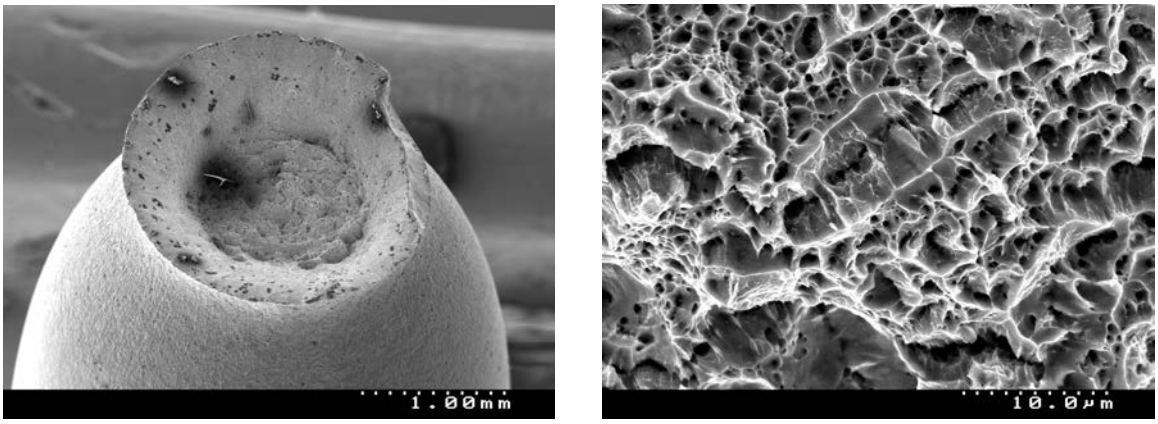

(a) (b)

FIGURE 3.5: (a) Cup-and-cone feature of the fractured tensile specimen of unmodified 17-4 PH (H1150D); (b) Morphology of the fractured surface.

features were also observed in the interior of each grain, supporting the formation of typical crystallographic features of lath martensite (i.e. packets, blocks and lath boundaries, as previously illustrated in Figure 2.2). Reverted austenite, δ–ferrite, ε–copper precipitates and carbides are also important features in this microstructure and will be discussed in the following paragraphs.

Low-carbon martensite

When the material was cooled from the annealing temperature (1040 °C) to below 32 °C, low-carbon (or lath) martensite (α') was obtained, in agreement with previous observations [55, 68, 85, 196, 197]. Typical martensite laths, as indicated in the TEM (transmission electron microscopy) micrograph in Figure 3.6b, are approximately 300 nm wide. This microstucture can be justified by analysing the kinetics of phase transformations during the heat treatment. Upon cooling from annealing, martensite starts to form at M_s (martensite start temperature) and its fraction progressively increases as cooling proceeds. If the final temperature is below M_f (martensite finish temperature), the microstructure at this

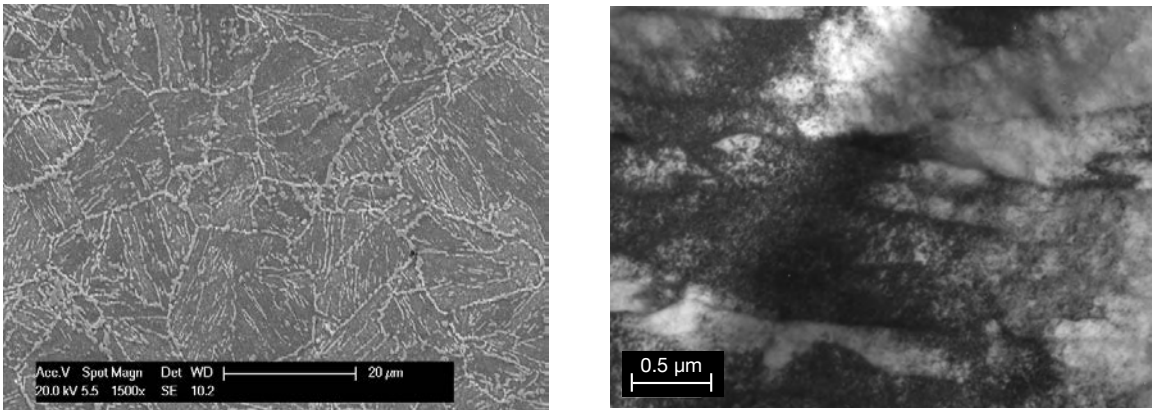

(a) (b)

FIGURE 3.6: (a) Microstructure (SEM) of the unmodified 17-4 PH (H1150D); (b) TEM micrograph showing nearly parallel laths of martensite of the 17-4 PH at the annealing condition. TEM image from [196]

point will be virtually all martensite. By considering the chemical composition of the 174 PH used in this work (section 3.1.1.1), M_s ranges from 247 to 320 °C—estimated from classical empirical formulae (Eqs. 2.1 and 2.2)—and M_f is just above room temperature (32 °C) [82].

Retained and reverted austenite

The X-ray diffraction pattern shown in Figure 3.7a confirms the presence of austenite after double precipitation hardening (H1150D), evidenced by the planes $(111)_\gamma$, $(200)_\gamma$, $(220)_\gamma$ and $(311)_\gamma$, corresponding to a f.c.c. structure (according to the ICDD reference pattern 00-033-0397)—in addition to the diffraction lines related to martensite (ICDD 00-035-1375), namely $(110)_{\alpha'}$, $(200)_{\alpha'}$, $(211)_{\alpha'}$ and $(202)_{\alpha'}$. The austenite content, obtained as described in the section 3.1.1.3, was (9.6 ± 0.4) % in volume. This total value comprises retained austenite (γ_{ret}), obtained after annealing, and reverted austenite (γ_{rev}), obtained after precipitation hardening. The γ_{ret} was considered negligible because it is typically lower than 1% in volume [46, 48] and in some cases not even detected for this material

[68, 198]. Typical X-ray diffraction pattern of the 17-4 PH at the annealing condition, shown in Figure 3.7b (data from [198]), exemplify the absence of peaks corresponding to austenite at this stage of the treatment. Based on these observations, it was considered that the austenite determined in the present work was mostly reverted during precipitation hardening.

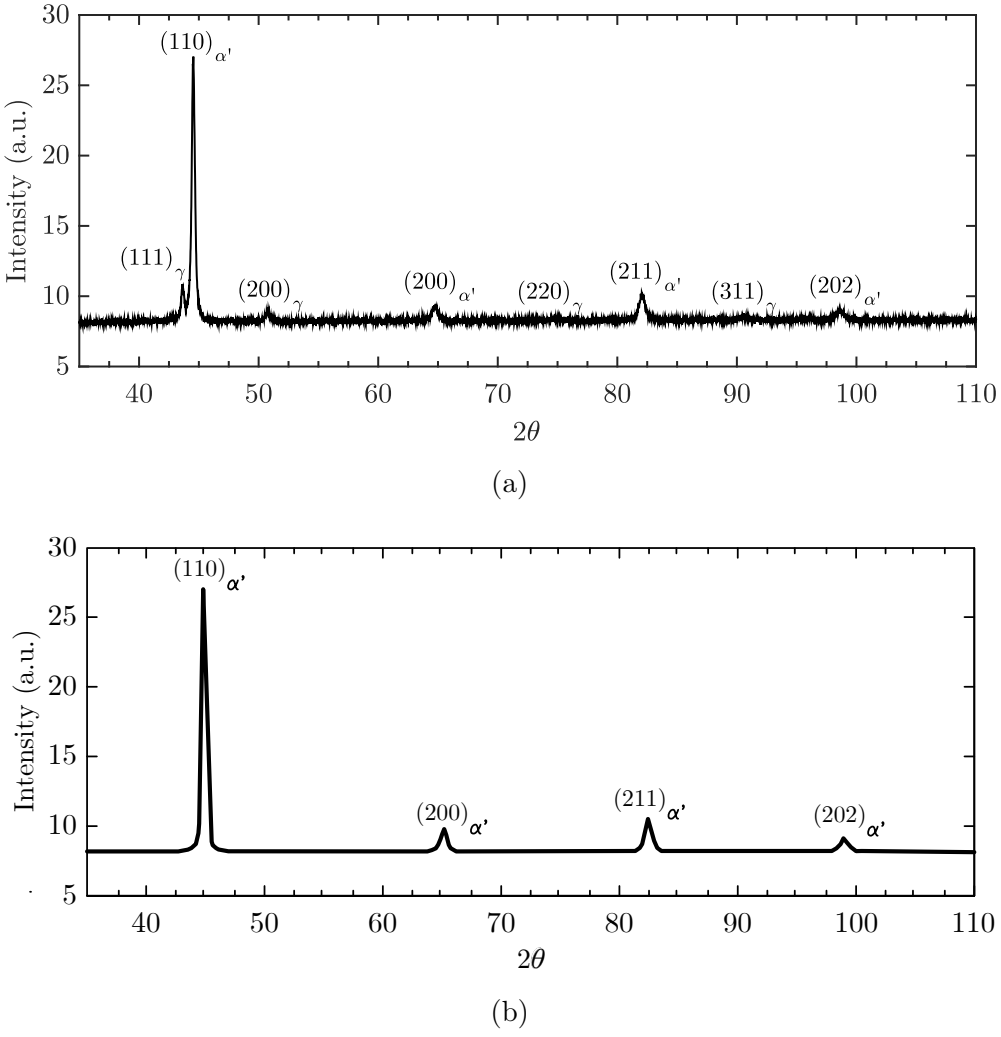

FIGURE 3.7: X-ray diffraction data of the 17-4 PH: (a) SA (solution annealing) and precipitation hardening (H1150D); (a) SA (data of SA from [198]) included for reference

The formation of reverted austenite ($\alpha' \rightarrow \gamma_{rev}$) during precipitation hardening was expected, since the material was heated twice to 620 °C and this temperature is close to that at which austenite starts to form on heating, estimated to be 614–620 °C [60, 83]. Once the material was cooled to below 32 °C after the first harening cycle, the reverted austenite was not converted back into martensite and remained stable at room temperature. A possible explanation for this stability is the drop of M_s to below the room temperature due to segregation of austenite stabilizers—mainly cooperr ich precipitates—along the martensite laths [68]. Similar e ect occured during the second hardening, in which further stable austenite was formed.

The lattice parameters of martensite ($a_{\alpha'}$) and austenite (a_γ), obtained by the extrapolation method described in section 3.1.1.3 and detailed in Appendix A, are shown in Figure 3.8.

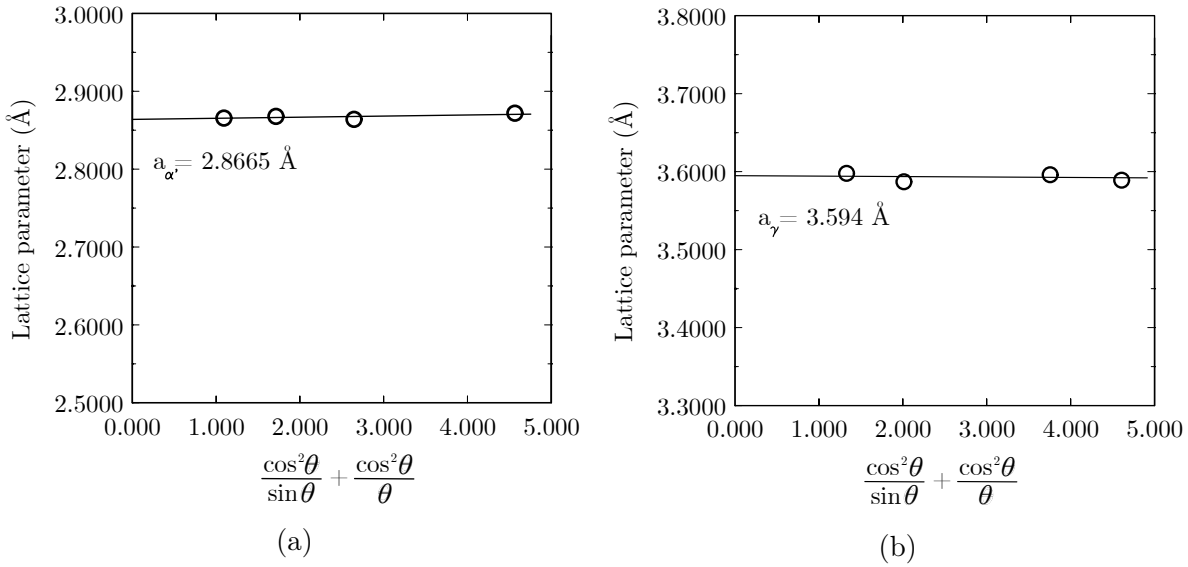

FIGURE 3.8: Extrapolation of lattice parameters (obtained from the experimental diffraction data) against $\left(\cos^2\theta\right)/(\sin\theta)+\left(\cos^2\theta\right)/(\theta)$: (a) martensite (b) austenite

δ–ferrite

The metastable Fe-Cr phase diagram of low carbon steels (0.05 wt.% C), shown in Figure 2.6a, predicts that δ–ferrite will be formed at high temperatures if the chromium content is sufficiently high. Analogously, this phase is expected to be formed in the 17-4 PH, favoured by the low carbon (0.035 wt.% C) combined with the high chromium content (> 15 wt.% Cr)—a ferrite stabilizer. The presence of δ–ferrite in this material, considering the effects of its main alloying elements, can also be predicted by the Schaeffler diagram shown in Figure 2.6b. As can be seen, by using the chromium equivalent (Cr_{eq}) and nickel equivalent (Ni_{eq}) numbers, the phase composition lies within the (α' + δ) domain. Despite the particular limitations of both diagrams, they were able to successfully anticipate the presence of δ–ferrite in the microstructure of the 17-4PH. In fact, few δ–ferrite stringers, as shown in Figure 3.9, were identified. Its volume fraction, however, was negligible, since only isolated stringers were observed by metallographical examination of selected samples.

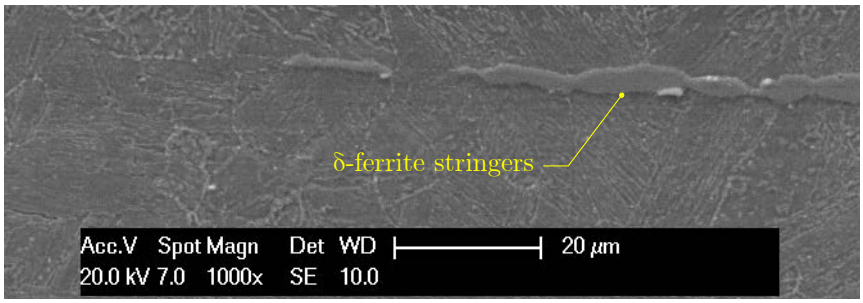

FIGURE 3.9: Schematic diagram of the plasma nitriding treatment

ε–Cu precipitates

Copper-rich precipitates are key features on the precipitation hardening process of the 17-4 PH [11]. It is, however, outside the scope of this work to perform a complete characterisation of this phase. Instead, this section briefly describes the precipitation stages that presumably occured on the particular condition being investigated. This analysis is based on earlier observations, which provided evidence of the formation of copper precipitates in this material [51, 55, 68, 199]. All these studies used TEM for characterisation, since the precipitates are too small (20–30 nm) to be resolved by SEM.

During solution annealing at 1040 °C, temperature at which the limit of solubility of copper in iron is approximately 7.4 wt.% (estimated from Fe-Cu systems [200]), copper is fully dissolved in the austenitic phase. A supersaturated condition is achieved upon cooling due to the reduced solubility and the limited mobility of copper in the martensitic structure at lower temperatures [200]. In the particular case of the 17-4 PH (H1150D), precipitation of copper occurs when the material is subsequently heated twice to 620 °C for 4 hours. During each cycle, copper atoms diffuse to form coherent copper-rich clusters, inducing lattice strain of the martensitic matrix [197]. As noted in previous studies, when the 17-4 PH was precipitation-hardened at 620 °C, peak hardening was achieved after approximately 30 minutes [55]. A further increase in the treatment time resulted in loss of coherence, i.e. mismatch at the precipitate-matrix interface, which resulted in reduced lattice micro strain and coarsening of copper-rich precipitates (now arranged in an f.c.c. structure). As discussed earlier, these transformations were accompanied by softening, as indicated in Figure 2.5. It can therefore be inferred that similar process occurred when the 17-4 PH was heat treated to the H1150D condition, in which precipitation hardening was performed at 620 °C for more than 30 minutes. It is important to note that the formation of reverted austenite and recovery could also have contributed to softening, specially after

double precipitation hardening.

Carbides

Both prolonged precipitation hardening (i.e. oveargeing for 9 to 12 months) of the 17-4 PH at relatively low temperature (350 °C) [85] and precipitation hardening at elevated temperature (500 to 620 °C) [82] can promote precipitation of chromium carbides ($M_{23}C_6$, M being Fe, Cr). The interfaces between the fine precipitates (approximately 50 nm) and the martensitic matrix can become additional sites for the nucleation of reverted austenite [82]. The fine structure of $M_{23}C_6$ can be identified by TEM [85], although detailed characterisation is beyond the scope of this work.

3.2.2 Plasma nitriding

Figures 3.10a and 3.11a show cross sections of the nitrided layers obtained by LTPN and HTPN. As can be seen, modified layers with different structures and thicknesses were obtained by varying the nitriding temperature. These structures are discussed in terms of their morphology, microhardness profile and microstructure.

3.2.2.1 Morphology

As can be seen in the cross section shown in Figure 3.10a, a well-defined layer of approximately 15 µm was formed on the surface of specimens modified by LTPN. The morphology of this region—clearly less attacked by the etchant when compared with the substrate (implying superior corrosion resistance)—is similar to that observed in earlier studies in which the 17-4 PH was plasma nitrided with comparable conditions [18, 19, 70, 162, 187]. The micrograph in Figure 3.10a also shows few darker lines, apparently coinciding with the prior austenite grain boundaries, as indicated in Figure 3.10b.

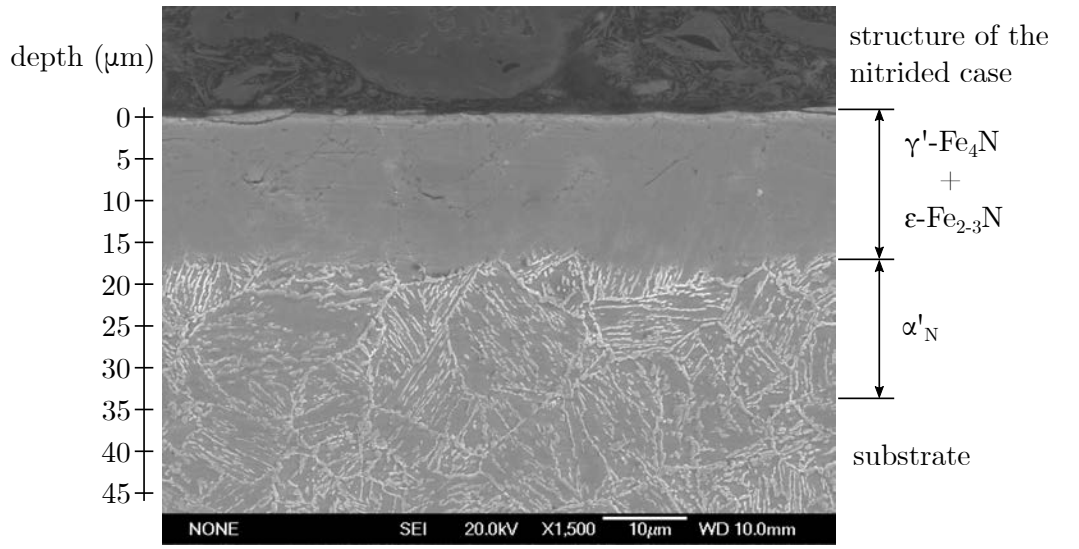

(a)

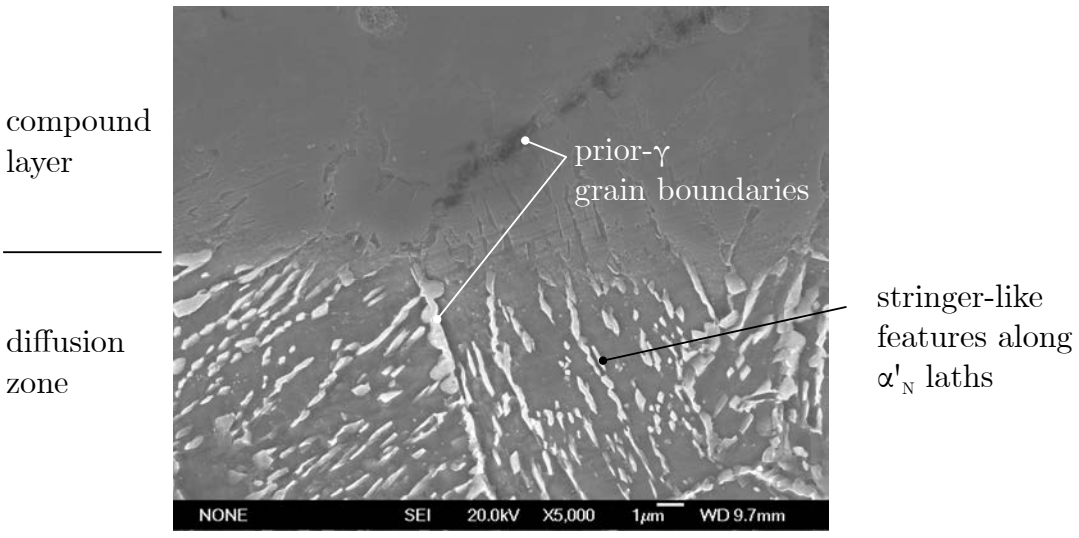

(b)

FIGURE 3.10: SEM micrographs showing the morphology of the nitrided layer after plasma nitriding at 420 °C for 10 h: (a) cross section; (b) detail from the compound layer/diffusion zone interface

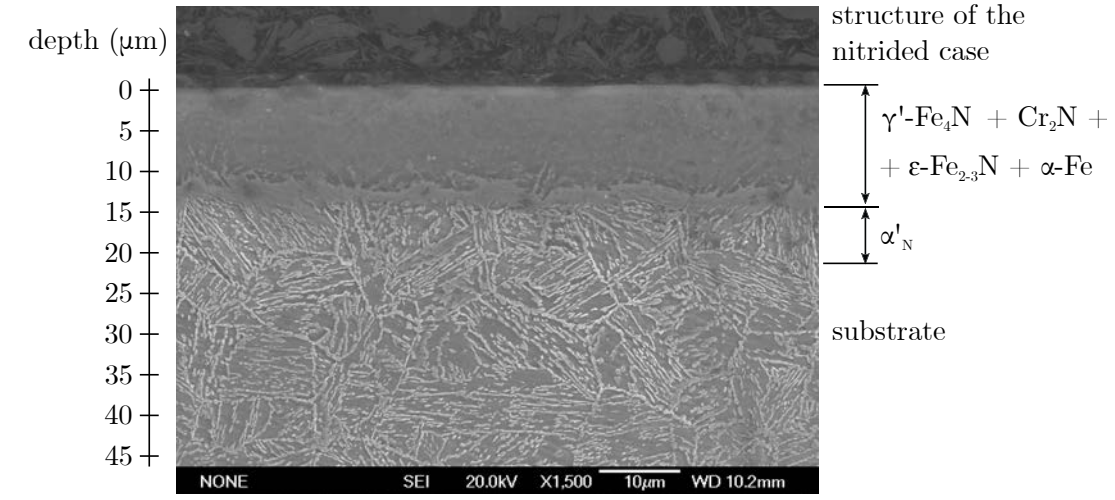

(a)

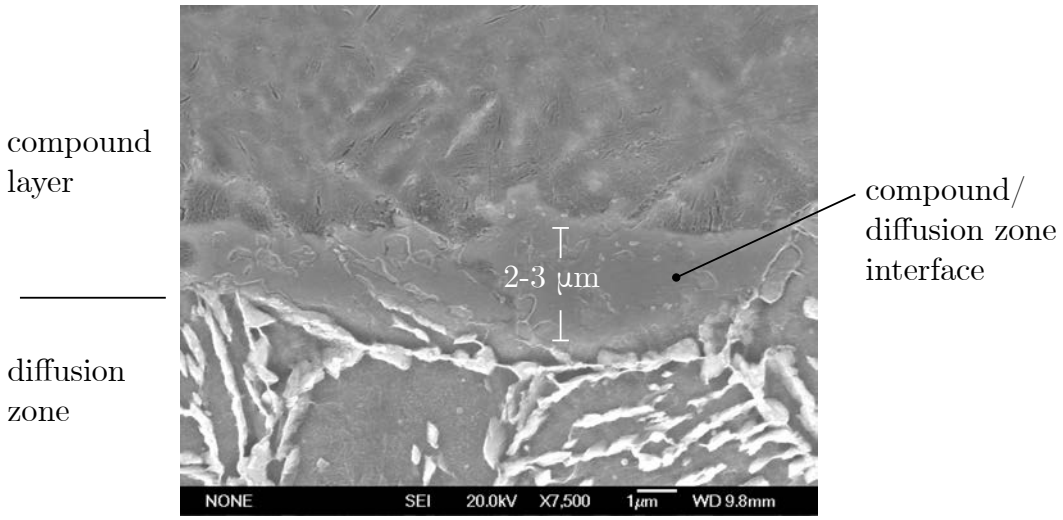

(b)

FIGURE 3.11: SEM micrographs showing the morphology of the nitrided layer after plasma nitriding at 500 °C for 10 h: (a) cross section; (b) detail from the compound layer/diffusion zone interface

The compound layer obtained by HTPN is composed of two distinct regions (Figure 3.11): a thicker portion on the top (10–12 µm) and a thinner layer near the substrate (2–3 µm). The morphology of the latter (Figure 3.11b) resembles the morphology of the nitrided layer obtained by LTPN (Figure 3.10b) while the top section is apparently less resistant to etching as it clearly revealed precipitates more intensely (Figure 3.11b).

Contrary to earlier observations [19, 70], higher temperature resulted in thinner layer (15 µm on HTPN compared to 20 µm on LTPN —see Figures 3.10 and 3.11). A possible qualitative explanation for this result is the precipitation of chromium nitride (CrN or Cr_2N), which is favoured at the elevated temperatures due to the higher mobility of chromium. As a consequence, the diffusion of nitrogen is reduced, as suggested in studies with Fe-Cr alloys [201]. In this case, the kinetics of nitrogen trapping to substitutional chromium, which would allow nitrogen to further diffuse quickly to the next available trap (and consequently increase the thickness of the nitrided layer), was presumably diminished due to the preferential precipitation of CrN or Cr_2N. In fact, the presence of this type of precipitates in the HTPN condition was confirmed by X-ray diffraction (see section 3.2.2.4).

3.2.2.2 Nitrogen composition profile

By analysing the nitrogen composition profiles of both LTPN and HTPN conditions (Figure 3.12a), it can be seen that the nitrogen content is maximum at the surface[1] and reduces towards the substrate in three different modes. It falls abruptly in the first 2–3 µm, decreases gradually until it reaches 8-10 µm and continues to drop with a higher

[1] A fraction of the N atoms sputtered during the erosion process (ion bombardment) is redeposited on the surface and result in N build up near the surface (first 1-2 µm)

concentration gradient until it reaches the substrate. At any point, up to approximately 18–20 µm from the surface (see an amplified view in Figure 3.12b), the concentration of nitrogen exceeds its solubility limit in martensite (about 0.05 wt.% within the range 420-500 °C, estimated from the Fe-N phase diagram in Figure 2.18), suggesting that a supersaturating condition was achieved and the phases γ'–Fe_4N and ε–$Fe_{2\text{-}3}N$ (typical structures comprising the compound layer, as presented in section 2.3.1), with greater nitrogen solubility (20 to 25 at.%), were formed near the surface. As the nitrogen content (in both LTPN and HTPN) exceeded its solubility in these structures, a supersaturation condition was achieved. The occurrence of these structures in each condition (LTPN and HTPN), including the precipitation of chromium nitrides (CrN or Cr_2N) at high temperature, was analysed in conjunction with the X-ray diffraction data (section 3.2.2.4) and the micro hardness profiles (section 3.2.2.3).

3.2.2.3 Micro hardness profile

Case-hardening by low-temperature plasma nitriding is mainly due to the excessive nitrogen in solid solution [30] and the resultant compressive residual stress induced by supersaturation [162]. For conventional plasma nitriding of alloying steels containing nitride formers such as Cr, Al and Mo, precipitation hardening predominate. The micro hardness profiles (Figure 3.13) of both structures indicate that the hardness is maximum at the surface and decreases towards the substrate, corresponding with the nitrogen concentration profiles (Figure 3.12a). The noticeable difference in strenghtening observed between HTPN and LTPN suggests the formation of different structures, as confirmed by the X-ray diffraction data (section 3.2.2.4).

As shown in Figure 3.13, the hardness of the substrate (363 ± 6 HV in LTPN and 353 ± 6 HV in HTPN) slightly increased compared to the unmodified material (332 ± 15

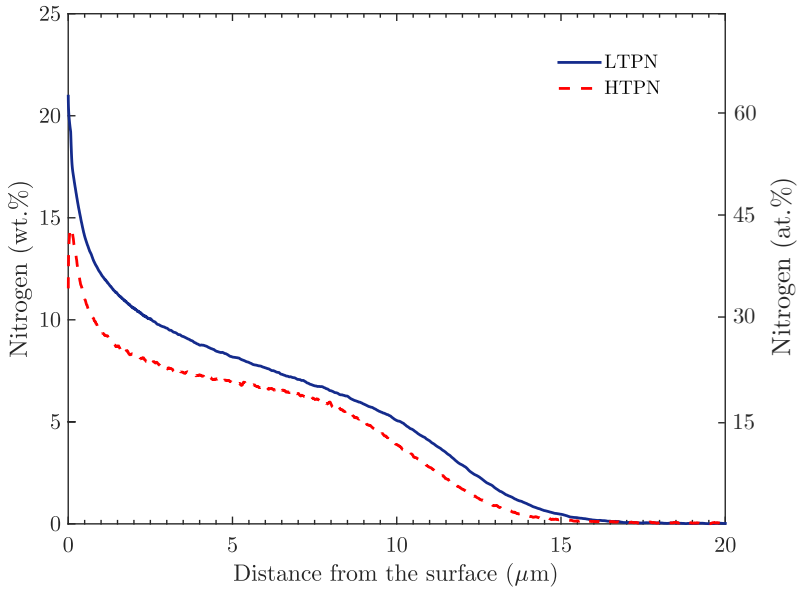

(a)

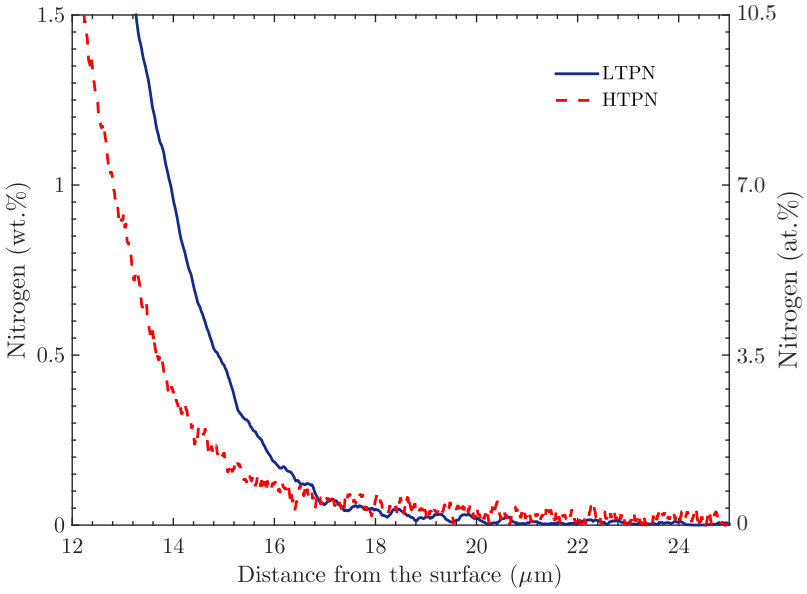

(b)

FIGURE 3.12: Nitrogen composition profile (a) throughout the nitrided case and (b) near the substrate (amplified)

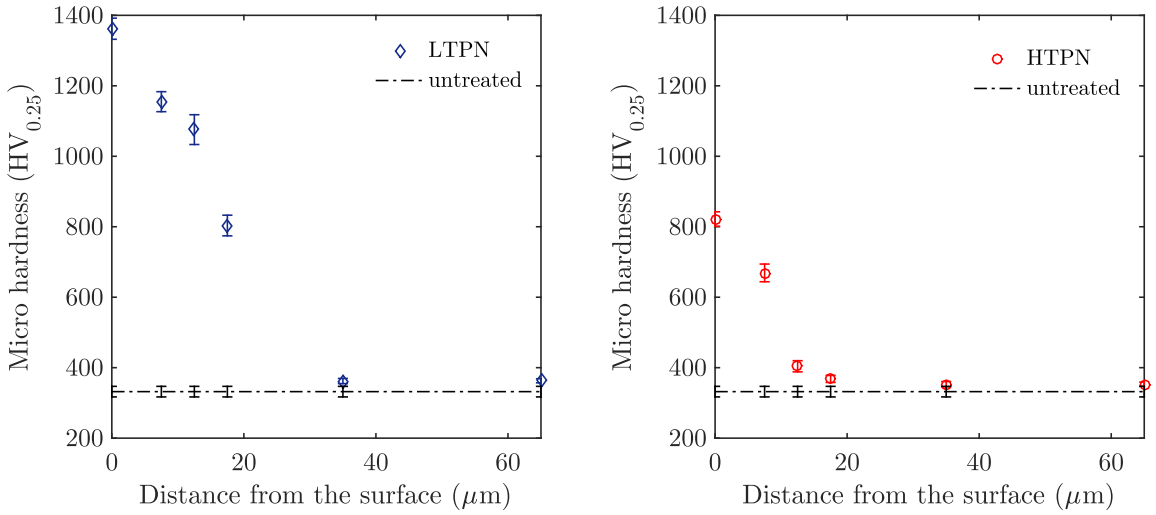

FIGURE 3.13: Micro hardness profile of (a) LTPN and (b) HTPN. Data from the unmodified (untreated) material was included for comparison.

HV) after the treatment. These results indicate that further microstructural transformations occurred in the substrate during plasma nitriding. Since copper is the main hardening element in the 17-4 PH, it was assumed that heating the material to 420-500 °C during nitriding favoured the formation of further coherent Cu precipitates.

3.2.2.4 X-ray diffraction

Low-temperature plasma nitriding

The X-ray diffraction pattern of the LTPN condition (Figure 3.14) shows the phase changes of the nitrided case from the surface (0 µm) to up to 20 µm, with 5 µm increments. At the surface, both γ'–Fe_4N and ε–$Fe_{2\text{-}3}N$ iron nitrides were formed. The experimental data matched the following: plane $(111)_{\gamma'}$ at $2\theta = 41.223°$ and plane $(200)_{\gamma'}$ at $2\theta = 47.969°$ corresponding to the γ' phase (ICDD reference pattern 01-083-0875 [202]) and

the peaks $(110)_\varepsilon$ at $2\theta = 37.531°$, $(002)_\varepsilon$ at $2\theta = 40.894°$ and $(\bar{1}\bar{1}1)_\varepsilon$ at $2\theta = 42.945°$ relative to the ε–type iron nitride (ICDD 01-072-2125). From 5 µm to 15 µm (Figure 3.14), the peaks of γ' became less intense while ε, particularly the $(002)_\varepsilon$, predominated. Near the interface between the compound layer and the substrate material (20 µm), the peaks corresponding to martensite and reverted austenite, i.e. planes $(110)_{\alpha'}$ at $2\theta = 44.647°$ (ICDD 00-035-1375) and $(111)_\gamma$ at $2\theta = 43.583°$ (ICDD 00-033-0397), became apparent.

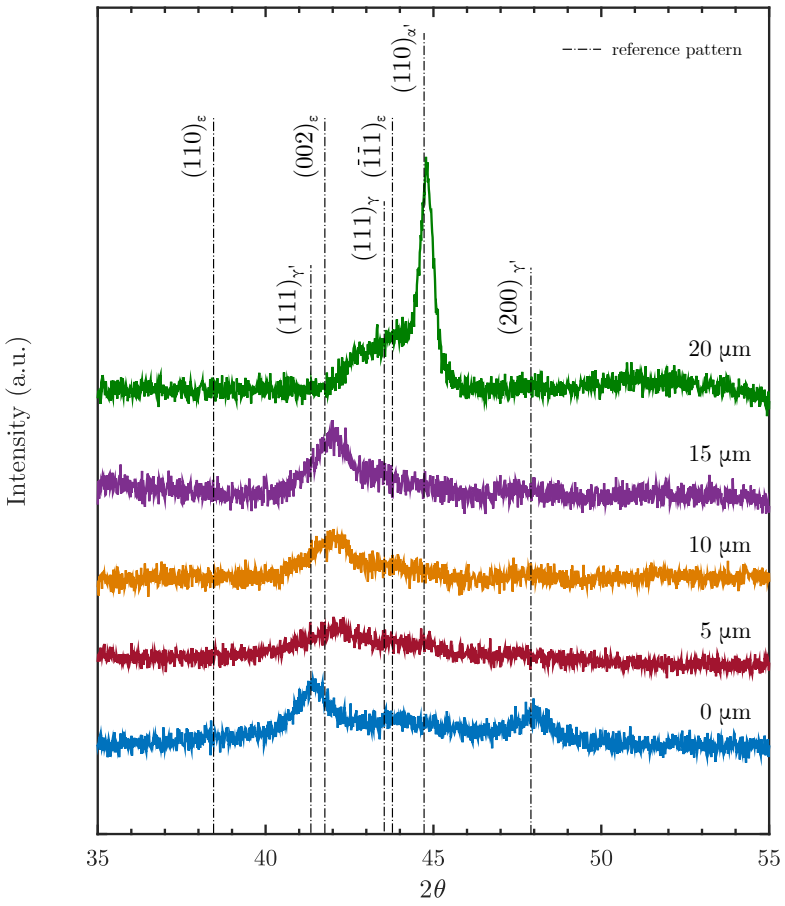

FIGURE 3.14: X-ray diffraction pattern of the 17-4 PH (H1150D) plasma nitrided at 420 °C for 10 hours

The formation of a thin compound layer (approximately 15 µm) at the top of the

surface is in agreement with previous craracterisation of the 17-4 PH [18, 187] using XRD. In fact, studies with pure iron [203] indicate that iron nitrides are formed on the surface during the early stages of plasma nitriding due to the combination of nitrogen with sputtered iron atoms, as previously illustrated in Figure 2.17. Since the peaks relative to the γ' phase were more pronounced near the surface and became less intense over the subsequent layers—while opposite effect was observed for the ε phase—it is possible to assume that the compound layer was formed by γ' on the top while the portion underneath was predominantly composed by the ε phase. The XRD results suggests that the γ' phase is less than 5 µm deep, although its precise dimension was not determined as there were no clear variations on the morphology with varying the depth (Figure 3.10a). The formation of a mixed structure, with different ε/γ' ratios, is also plausible.

In agreement with previous characterisations of the 17-4 PH at 420 °C [18, 187, 198], the section underneath the compound layer was mainly composed of a matrix of martensite with nitrogen in solid solution (α'_N), referred to as 'expanded martensite' when a supersaturation condition is achieved—in this case accompanied by lattice distortion. The XRD results did not provide alone sufficient evidence of lattice expansion of the martensitic phase, since the peak $(110)_{\alpha'}$ obtained at 20 µm from the surface did not shift to lower diffraction angles with respect to the equivalent peak from the unmodified material. Nonetheless, the microhardness profile (Figure 3.13b) showed a transition region (from 20 µm to 30 µm) in which the micro hardness was greater than that of the substrate, suggesting the formation of a harder layer due to the presence of nitrogen in solid solution. Still, the nitrogen concentration (Figure 3.12a) below the compound layer does not seem to exceed its solubility limit in martensite (estimated to be lower than 0.05 wt.% according to iron-nitrogen systems [204]). Likewise, earlier investigations on the microstructure of the plasma-nitrided 17-4 PH [187] suggests that fine grains of reverted austenite can

form expanded austenite (γ_N) after nitriding. In the present study, however, this was not possible to verify by XRD due to the superposition of the plane $(111)_\gamma$ with adjacent peaks of iron nitrides and martensite.

High-temperature plasma nitriding

The possible candidates for the phases present in the nitrided case formed after plasma nitriding at high temperature are shown in Figure 3.15. The data (from 0 µm to up to 20 µm) indicate considerable superposition of diffraction lines. At the surface, the data best match the following phases: γ' –Fe_4N, ε–$Fe_{2\text{-}3}N$, Cr_2N and α'. Similar indexing was observed from 5 µm to 15 µm, with some variations in the peak intensities. At 20 µm, stronger peaks corresponding to the substrate were observed (martensite and reverted austenite).

Similarly to the LTPN, the XRD data revelaled two peaks of γ'–Fe_4N on the top surface of the HTPN specimens (Figure 3.15): plane $(111)_{\gamma'}$ at $2\theta = 41.187°$ and plane $(200)_{\gamma'}$ at $2\theta = 48.104°$) corresponding to the γ' phase (ICDD reference pattern 00-003-0958). They became less intense with increasing the depth whereas the peaks corresponding to the ε–$Fe_{2\text{-}3}N$ phase, i.e. $(110)_\varepsilon$ at $2\theta = 37.547°$, $(002)_\varepsilon$ at $2\theta = 40.798°$ and $(\bar{1}\bar{1}1)_\varepsilon$ at $2\theta = 42.937°$ (ICDD 01-073-2102), had no noticeable change in intensity throughout the layer. In addition to the γ' and ε phases, the XRD results indicated the precipitation of Cr_2N-type chromium nitride—as expected when the 17-4 PH is plasma nitrided at temperatures above 420 °C [19, 187].

At 20 µm from the surface (Figure 3.15), peaks corresponding to the substrate, i.e. $(110)_{\alpha'}$, $(111)_\gamma$ and $(200)_\gamma$, were revealed. As in the LTPN, it can be inferred—based on the microhardness and nitrogen concentration profiles (Figures 3.13b and 3.12a)—that a

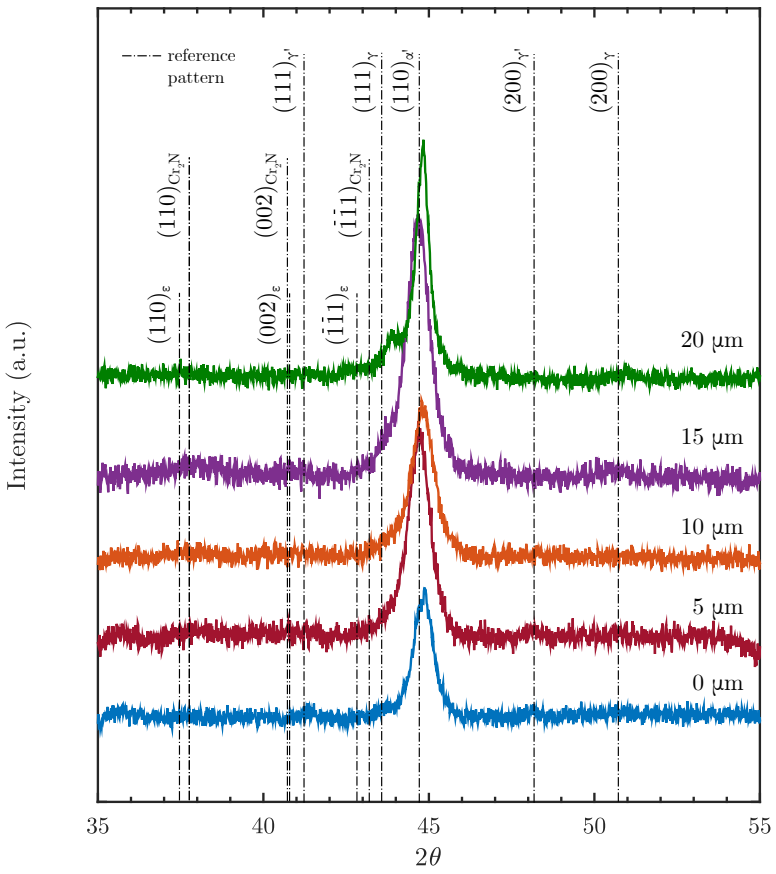

FIGURE 3.15: X-ray diffraction pattern of the 17-4 PH (H1150D) plasma nitrided at 500 °C for 10 hours

diffusion zone (from 15 µm to approximately 20 µm) was formed beneath the compound layer after the HTPN treatment.

3.3 Summary and conclusions

This chapter presented the main mechanical properties and relevant aspects of the microstructure of unmodified and plasma nitrided 17-4 PH. The characterisation was performed by combining microscopic examination (SEM) and analysis of the X-ray diffraction

data, microhardness and nitrogen composition profiles.

3.3.1 Unmodified 17-4 PH (H1150D)

The microstructure of the unmodified 17-4 PH, heat treated to the H1150D condition (annealed at 1040 °C followed by two consecutive precipitation hardening at 620 °C and cooled to below 32 °C after each stage), comprised a matrix of low-carbon (lath) martensite (formed after annealing and preserved after precipitation hardening) with (9.6 ± 0.4) % in volume of reverted austenite (mostly formed during the precipitation hardening cycles) and traces of δ-ferrite.

The yield strength (σ_y) and elongation percent, i.e. (773 ± 12) MPa and 22 %, respectively, are in agreement with current requirements.

3.3.2 Plasma nitrided 17-4 PH (H1150D)

Plasma nitriding at both low temperature (420 °C) and high temperature (500 °C) for 10 h resulted in the formation of a complex structure (compound layer) comprising γ'–Fe_4N and ε–$Fe_{2\text{-}3}N$ phases, varying from 10 to 15 µm. At high temperature, Cr_2N was also observed. Underneath the compound layer, both structures comprised a diffusion zone (mostly martensite with interstitial nitrogen, α'_N). Based on the X-ray diffraction analysis in conjunction with the SEM micrographs, microhardness and nitrogen concentration profiles, the following structure was formed after plasma nitriding at different temperatures, keeping all other treatment parameters (gas mixture, time, pressure) unchanged:

- Low-temperature plasma nitriding (420 °C): compound layer (approximately 15 µm deep) predominantly comprising ε–$Fe_{2\text{-}3}N$-type iron nitride (with γ'–Fe_4N near the surface) followed by a difusion zone (approximately 10 µm deep) comprising mostly nitrogen-containing martensite (α'_N).

- High-temperature plasma nitriding (500 °C): compound layer (approximately 10 µm deep) comprising mixed ε–$Fe_{2\text{-}3}N$ and γ'–Fe_4N iron nitrides and Cr_2N precipitates followed by a difusion zone (approximately 10 µm deep) comprising mostly nitrogen-containing martensite (α'_N).

Chapter 4

Sulphide stress cracking (SSC)

This chapter presents the results from the sulphide stress cracking (SSC) experiments conducted with low–temperature plasma nitrided (LTPN) and high–temperature plasma nitrided (HTPN) 174 PH (heat treated to the H1150D condition). Although it is recognised that the unmodified material has low resistance to SSC, this condition was evaluated here to determine the actual susceptibility of the substrate material and its threshold stress of failure by SSC. The complete set of experiments carried out in this work is summarised in Figure 4.1, highlighting the topics covered in this specific chapter.

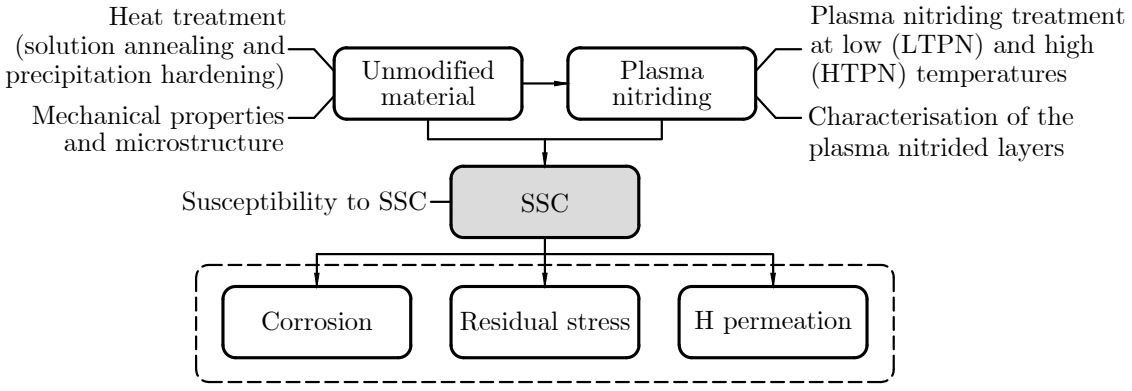

FIGURE 4.1: Schematic diagram summarising the topics covered in this chapter (highlighted in grey) within the complete experimental context of this work.

4.1 Experimental design

4.1.1 Objective of the SSC experiments

The objective of this experiment was to evaluate the resistance to SSC of the 17-4 PH (H1150D) modified by plasma nitriding (Chapter 3) at both low (LTPN; 420 °C) and high temperature (HTPN; 500 °C) when exposed to typical oilfield environments. The susceptibility was determined for the particular case of exposure to simulated produced water typically found in oil production systems.

4.1.2 Selection of the test parameters

As summarised in Chapter 2, the 17-4 PH is highly susceptible to SSC. Current recommendation from NACE MR0175/ISO 15156-3 [16] specifies the following for the use of the 17-4 PH (heat treated to the H1150D condition) in H_2S–containing environments: partial pressure $pH_2S \leq 3.4\,kPa$ and pH $\geq$ 4.5. The threshold lines of this domain, i.e. $pH_2S = (3.4 \pm 0.1)\,kPa$ and pH $= 4.5 \pm 0.2$—the most agressive condition that the unmodified material can be exposed—were selected as the main parameters used in this work.

The operating temperature of oilfield components typically made with 17-4 PH (e.g. tubing hangers and valve stems used in offshore production systems) ranges from room temperature up to 60 °C [36]. Since the greatest susceptibility of high–strength steels to SSC is close to room temperature (see section 2.14), all the experiments were conducted at $(23 \pm 2)\,°C$. This is in accordance with the guidelines from NACE TM0177 [88] and EFC Publication 17 [35] used for qualification of corrosion-resistant alloys exposed to H_2S environments. All the tests were conducted at ambient pressure.

NACE MR0175/ISO 15156-3 [16] does not list specific levels of sodium chloride (NaCl) to be used when evaluating the SSC resistance of the 17-4 PH. Thus, the concentration was

selected based on typical NaCl content found in the intended service, i.e. produced water. The guidelines from EFC–Publication 17 [35] recommend that this type of environment should contain 165 g L^{-1} of NaCl ($\approx$ 100 g L^{-1} of dissolved chloride) and pH 4.5. Typical produced water also contains CO_2 (section 2.1.1) and therefore this was selected as the balance gas in all the experiments.

4.1.3 Selection of the test method

There are a variety of standardised test methods used to assess the susceptibility to SSC, of which the most prominent have been briefly descibed in the literature review chapter (section 2.2.2). In this work, since the objetive was to evaluate the resistance to SSC after plasma nitriding an otherwise susceptible unmodified substrate, the use of a test with standard configuration—that has been frequently used in the industry—seemed adequate for comparison and validation purposes. In the last decade, according to recent statistical investigations [133], nearly 35% of the published reports on stress corrosion cracking used standard static loading methods. In the same period, approximately 20% used corrosion fatigue and 45% applied dynamic straining techniques. These data showed that dynamic straining has been the most used technique, in spite of its severity—strain rates are usually excessively high when compared with the loading conditions experienced by actual components in the field. In this work, however, static loading (the second most used technique [133]) was chosen because dynamic straining are frequently used as screening tests and are best applied in combination with other SSC methods. Alternative loading configurations can be used for future investigations, as suggested in Chapter 8.

Static loading is classified as constant total strain (or constant displacement) and constant (or sustained) load. The main test configuration selected for this work is the standard tensile (classified as constant total strain), in which specimens are uni axially

loaded and the level of stress is controlled by adjusting the strain in the loading direction, keeping it within the elastic limit. Even though stress relaxation can occur once cracking starts, the load is nearly constant throughout the test when calibrated proof rings are used—and these rings are simpler and least costly than strictly constant–load devices (e.g. spring–loaded rigs or dead–weight apparatus). In addition to uni axially loaded, bent–beam specimens (also classified as constant total strain) are used as an alternative method for selected specimens. This method was chosen because of its simpler configuration—it uses flat specimens bent in a restrained rig—and the possibility to test multiple specimens simultaneously in a larger test vessel.

4.1.4 Summary

The schematic diagram in Figure 4.2 present a summary of the main parameters and test procedures used on the SSC experiments. This diagram is a convenient way to emphasize that SSC only occurs when these three factors are present simultaneously: (i) susceptible material, (ii) corrosive environment and (iii) tensile stress.

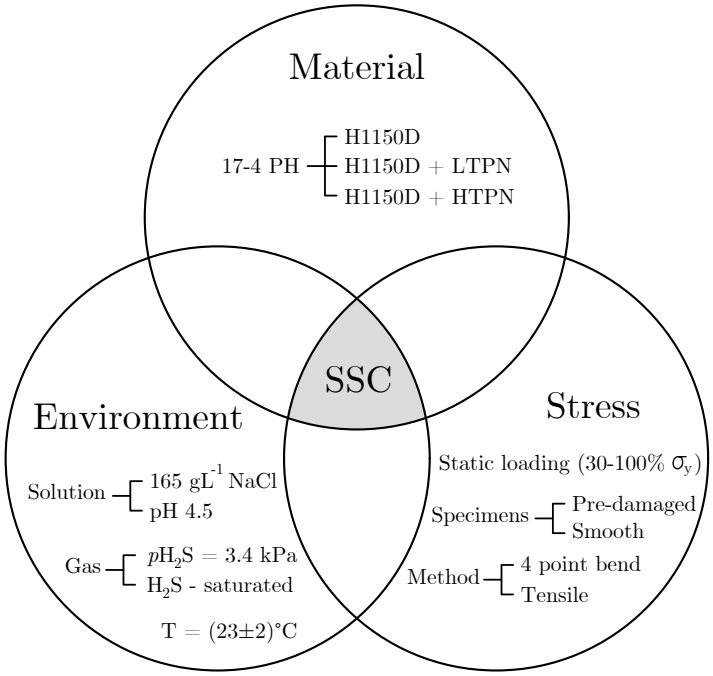

FIGURE 4.2: Summary of the main parameters used on the SSC experiments. H1150D: double precipitation–hardened at 620 °C for 4 hours each; LTPN and HTPN: low and high–temperature plasma nitriding, respectively; σ_y: yield strength of the unmodified material

4.2 Experimental procedures

4.2.1 Uniaxial tensile

Overview

The experimental design to determine the SSC resistance is shown in Table 4.1. In summary, specimens of the 17-4 PH at the H1150D (unmodified) condition and plasma nitrided at both 420 °C (LTPN) and 500 °C (HTPN) for 10 hours were statically loaded from 30 to 90 % of their yield strength (σ_y) and exposed to the test environment for up

to 720 h. In addition to the main test methods and parameters described previously, further analysis on the response of pre-damaged specimens (LTPN and HTPN) to SSC were conducted to determine the susceptibility after exposing the bare metal to the corrosive environment.

TABLE 4.1: Overview of the SSC experiments conducted at $(23 \pm 2)\,°C$ and atmospheric pressure in produced water ($165\,g\,L^{-1}$ of NaCl and pH 4.5 ± 0.2) with mixed H_2S/CO_2 and pure H_2S (SSC Tensile).

Test gas	**Surface condition**	**Condition (stress level as % of σ_y[a])**
H_2S (3.4 kPa) / CO_2 (balance)	Smooth	UN[b] (30, 50, 70 and 90)
		LTPN[c] (70 and 90)
		HTPN[d] (70 and 90)
	Pre-damaged	LTPN (70 and 90)
		LTPN (70 and 90)
H_2S	Smooth	LTPN (70 and 90)

[a]yield strength (unmodified material); [b]unmodified material; [c]low–temperature plasma nitrided; [d]high–temperature plasma nitrided

Specimens

Blocks with rectangular cross section $(13 \times 15)\,mm$ and 125 mm long were cut from a $(500 \times 800 \times 13)\,mm$ plate with a waterjet cutting machine and machined according to the specification from NACE TM0177 [88], as illustrated in Figure 4.3: 25.4 mm–long gauge section with 6.35 mm of diameter and threads on both ends. Unmodified specimens were ground with successively finer abrasive papers (up to 600 grit SiC or P1200), degreased,

cleaned with acetone and dried with in air blower. Plasma nitrided (both LTPN and HTPN) specimens were prepared following the procedure described in section 3.1.2.3. Prior to loading, the shaft sections (space between the threads and the radiused corner of the gauge section) were masked with an epoxy resin to avoid crevice corrosion when the specimens are connected to the test vessel. The actual diameter of the gauge section of each specimen was measured in 3 different positions with a calliper with a precision of 0.01 mm. The average surface roughness (Ra) was 0.20-0.25 µm for all the specimens, determined with a portable surface roughness tester.

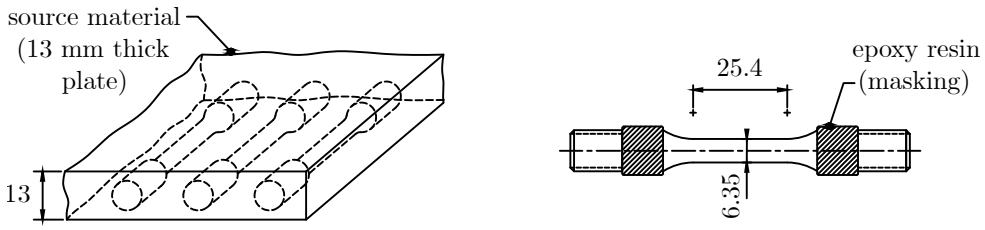

FIGURE 4.3: Schematic representation of the SSC specimens (position cut from the source material, geometry and dimensions) used on the tensile method. Dimensions in mm.

To investigate the effect of exposing the substrate material to the test solution, the surfaces of LTPN and HTPN specimens were impressed by a Vickers indenter (pre-damaged specimens) with different loads (up to 50 kg), as exemplified in Figure 4.4. By analysing the SEM micrograph in Figure 4.4a, it was noticed that plastic deformation occurred in the ductile substrate whereas brittle fracture was observed in the outer layer of the nitrided case. The distribution of the impressions in the SSC tensile specimens is schematically illustrated in Figure 4.4b. The different morphology on the base of the impression (Figure 4.4a) suggests that, for some of the indents, the bottom part was exposed to the environment.

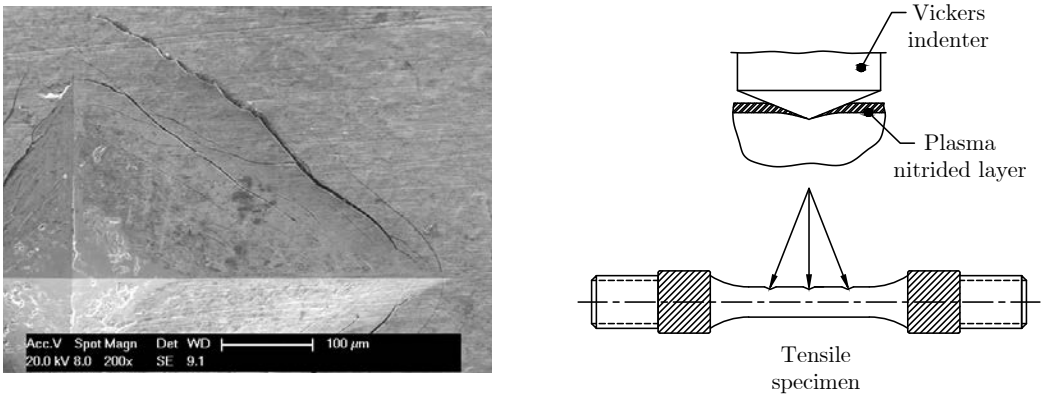

(a) (b)

FIGURE 4.4: Pre-damaged specimens used on SSC tensile experiments: (a) SEM of typical Vickers impression and (b) schematic representation of the distribution of impressions

Loading

The SSC specimens were connected to acrylic test vessels as shown in Figure 4.5c and illustrated in Figure 4.5a. Different stress levels (from 30 to 90% of the yield strength) were set indirectly by tightening the straining nuts and adjusting the displacement of calibrated proof rings (Figure 4.5b). Each frame had a well-defined linear elastic response to the applied load and the stress was readily obtained from the corresponding displacement and the actual cross sectional area. Once the target displacement was achieved (measured with a dial gauge with a precision of 0.001 mm mounted to one end of the frame, Figure 4.5d), the specimens were left for 10 minutes and the measurement was repeated to check for load relaxation. If two consecutive readings differed by more than 1%, the process was repeated until a stable value was obtained.

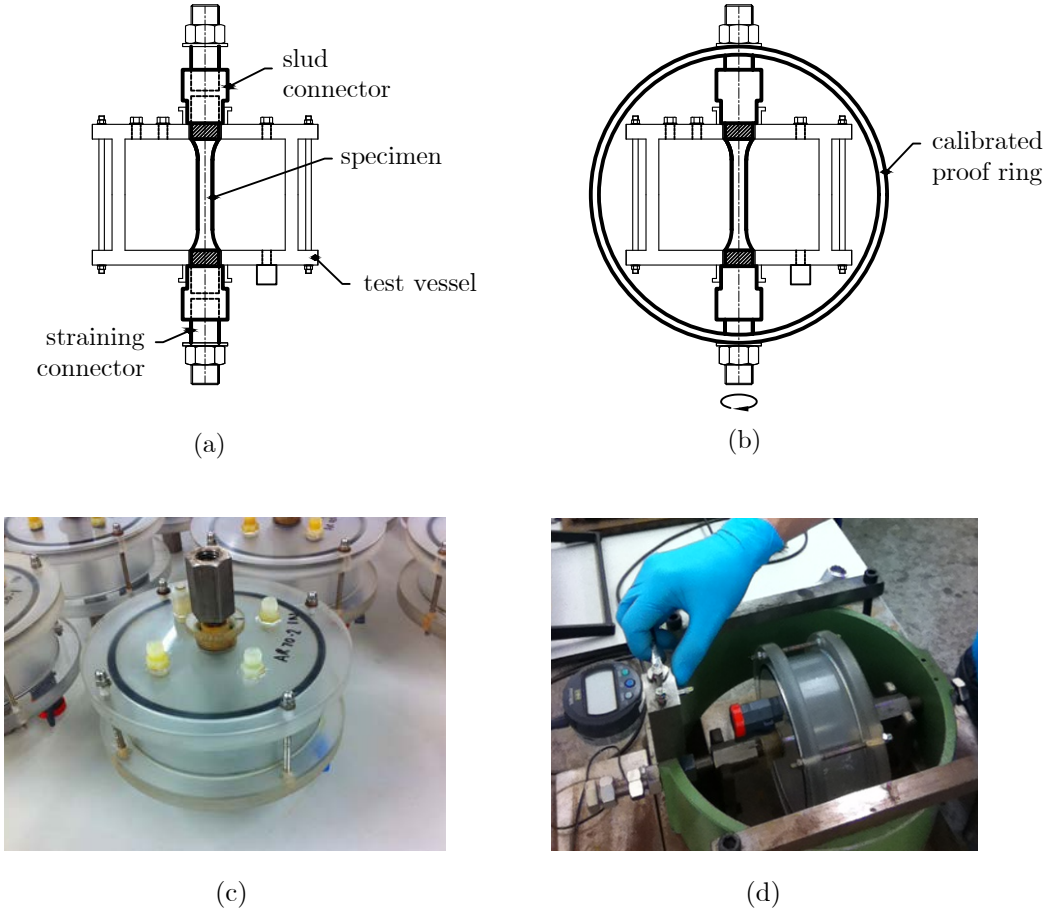

FIGURE 4.5: Loading of tensile specimens: (a) tensile specimen connected to the test vessel; (b) specimen connected to the calibrated proof ring; (c-d) corresponding pictures

Test procedure

For each set of experiments, the test solution was prepared at $(23 \pm 2)\,^{\circ}\mathrm{C}$ in a 10 L glass vessel by dissolving NaCl ($165\,\mathrm{g\,L^{-1}}$) in deionized water. After complete homogenisation, CO_2 gas was continuously purged through the mixture for 60 minutes and the pH adjusted by adding sodium bicarbonate ($NaHCO_3$). The solution was then transferred to a glass vessel fitted with an oxygen analyser (Orbisphere Model 410), in which nitrogen was continuously purged until the concentration of oxygen was below 5 parts per billion. The

deaerated solution was then transferred to individual 600 mL vessels containing the loaded tensile specimens. Before transferring, the vessels and the tubing were also deaerated by back purging the system with nitrogen. As shown in Figure 4.6, the vessels were placed in an acrylic box with nitrogen continuously circulating to prevent accumulation of leaked H_2S. After each vessel was filled, nitrogen gas was purged for 30 minutes at a constant flow rate (2 L per minute). The test gas (H_2S with CO_2 as balance or pure H_2S) was then switched on[1] and flowed through the solution for 30 minutes for saturation. The gas flow was reduced to a few bubbles per minute and the test effectively started at this point. The temperature was continuously recorded during the test.

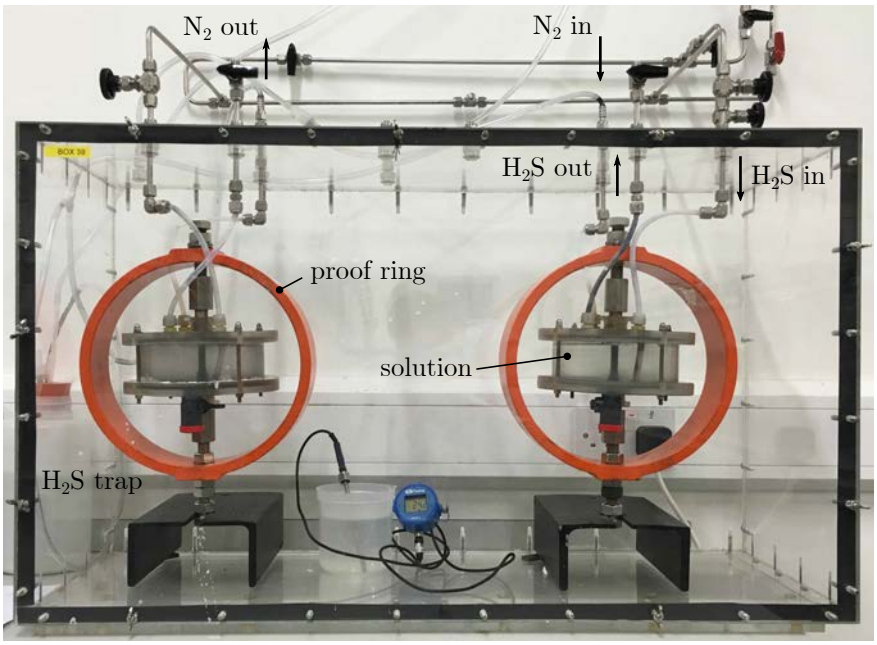

FIGURE 4.6: Picture of the SSC setup (tensile method)

[1]Hydrogen sulphide (H_2S) gas is toxic and flammable (CAS Number 7783-06-4). It has a characteristic rotten egg odour and can cause severe health effects (eyes, nose and throat irritation, loose of the sense of smell, unconsciousness and death). Exposure limits are 5 ppm (8-hour time-weighted average (TWA)) and 10 ppm (15-minute TWA). Refer to http://www.hse.gov.uk for safety guidelines.

During the experiment, the surface of the specimens were visually inspected and the formation of visible cracks was recorded. The test terminated upon total failure (complete separation) or after the time limit (720 h) was reached. After whichever occurs first, 20 mL of solution was collected from the vessel and the pH was measured. The H_2S gas was turned off and nitrogen purged for 30 minutes. The samples were then unloaded, removed from the vessels, immediately cleaned with acetone, dried with air and stored in a desiccator. The surface was examined with SEM and cross sections were prepared for detailed analysis of the cracks. Cross sectional specimens were mounted, ground, polished and etched.

The concentration of H_2S after the test was determined for selected specimens by iodometric titration (Equations 4.1 and 4.2). In this procedure, the concentration of H_2S was determined indirectly by the total volume of sodium thiosulphate ($Na_2S_2O_3$) that reacted with iodine (I_2). A sample of 100 mL was collected from the test solution after the end of the experiment and iodine (normality $N_\mathrm{I} = 0.1$ N) was added in excess ($v_\mathrm{I} = 25$ mL) to the sample so that the H_2S content could be calculated (Eq. 4.3), considering the volume of sodium sulphate (v_t) that reacted with iodine—drops of $Na_2S_2O_3$ ($N_\mathrm{t} = 0.1$ N) were added until the solution changed the colour, indicating that the reaction had completed.

$$\mathrm{H_2S + I_2 \longrightarrow 2\,HI + S} \tag{4.1}$$

$$\mathrm{Na_2S_2O_3 + I_2 \longrightarrow Na_2S_4O_6 + 2\,NaI} \tag{4.2}$$

$$[\mathrm{H_2S}] = \frac{v_\mathrm{I} \times N_\mathrm{I} - v_\mathrm{t} \times N_\mathrm{t}}{100\ \mathrm{mL}} \tag{4.3}$$

4.2.2 Four-point bend

Specimens

Blocks with rectangular cross section (13×15) mm and 125 mm long were cut from the source material with a waterjet cutting machine and machined according to the final dimension (following ASTM G39 [125]): flat strips of rectangular cross section measuring $(5 \times 15 \times 115)$ mm (Figure 4.7), with the test surface coinciding with that used to machine the tensile specimens, i.e. same position across the thickness. Unmodified specimens were ground with successively finer abrasive papers (up to 600 grit SiC or P1200), degreased, cleaned with acetone and dried with air. Plasma nitrided (LTPN only) specimens were prepared following the procedure described in section 3.1.2.3. The average surface roughness (Ra) was 0.20-0.25 µm for all specimens.

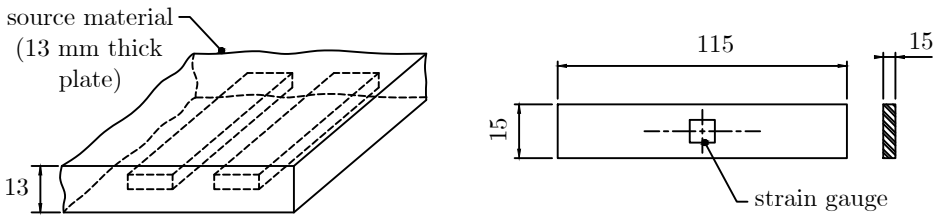

FIGURE 4.7: Schematic representation of the SSC specimens (position cut from the source material, geometry and dimensions) used on the four-point bend method. Dimensions in mm.

Loading

In a four-point bend configuration (Figure 4.8), the region between the inner rolls $(4L/10)$ is submitted to pure bending—the momentum $M(x)$ being constant and the shear $V(x)$ being equal to zero. In this portion of the beam, the stress $\sigma_x(z)$ is constant along the

x–axis and varies with z so that below the neutral axis, or neutral plane, $\sigma_x(z) > 0$ (tension) and above the central axis $\sigma_x(z) < 0$ (compression). The maximum deflection of the beam, $\delta_{\max}$ (Equation 4.5)—obtained from its elastic curve (Equation 4.4), was used to determine the thickness of the beam, t, based on the applied load (P), the modulus of elasticity of the material (E), the moment of inertia I with respect to the y axis and the distance between the inner rolls (L). The calculations, assuming a plane state of stress—considering that $t \ll L$ and that $w \ll L$ (w being the width of the beam), are detailed in Appendix B.

$$y(x) = \frac{P}{2EI}\left[\frac{1}{3}x^3 - \frac{1}{3}\langle x - \frac{3L}{10}\rangle^3 - \frac{1}{3}\langle x - \frac{7L}{10}\rangle^3 - \frac{21L^2}{100}x\right] \tag{4.4}$$

$$y\left(\frac{L}{2}\right) = \delta_{\max} = -\frac{33PL^3}{1000EI} \tag{4.5}$$

The loading was carried out as follows: the four–point bend specimens were fitted in stressing jigs (Figures 4.8a) and the target stress (from 30 to 90 % of the yield strength of the material, σ_y) was indirectly obtained by adjusting the strain of the deflected beam. The specimens were deflected by pressing the stressing bolt until the target strain (measured with a strain gauge attached in the middle of the sample) was achieved. Prior to applying the strain gauges, the work surface was degreased with a detergent–based cleaner and cleaned with a water–based alkaline solution (stabilizer) with a cotton bud and dried with an air blower. The strain gauges were then aligned and fixed with adhesive in the middle of the working surface. The readings were automatically obtained by a strain indicator and recorder device (Figures 4.8b).

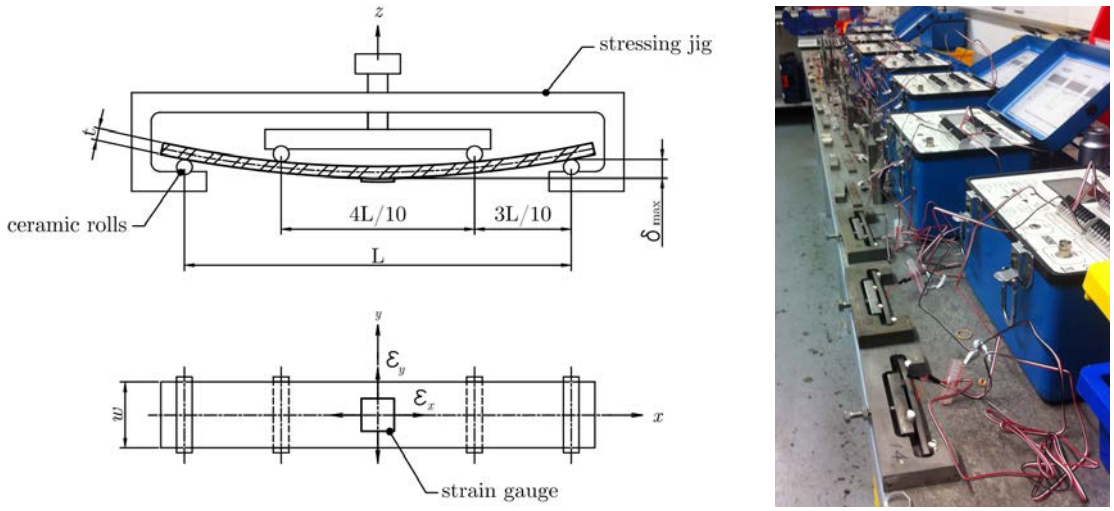

(a) (b)

FIGURE 4.8: Loading of four point bend specimens: (a) specimen fitted to the stressing jig; (b) loading setup

The target strain (ε_T) corresponding to each required stress was obtained from the stress–strain curves of the unmodified material. Assuming a two–dimensional state of stress with the directions of the principal stresses corresponding to the x and y axis (see Figure 4.8a), the equivalent uniaxial strain ε_u was determined by

$$\sigma = \frac{E}{1-\nu^2}\left(\varepsilon_x + \varepsilon_y\right) \tag{4.6}$$

where $\nu = 0.272$ [205] is the Poisson's ratio, ε_x and ε_y are the readings from the strain gauge (longitudinal and transversal strain, respectively) and the principal stress in the longitudinal direction given by $\sigma = \varepsilon_u E$. The deflection was adjusted so that the difference between the equivalent uniaxial strain obtained experimentally was not more than 10 % off the target strain. The readings were monitored for 10 minutes and

the process repeated until stable readings were obtained, indicating that relaxation was minimised.

Test procedure

The test solution (produced water with $165\,\mathrm{g\,L^{-1}}$ of NaCl dissolved in deionised water) was prepared following the same procedure described in section 4.2.1. CO_2 gas was continuously purged through the mixture for 60 minutes and the pH adjusted to 4.5 ± 0.2 by adding sodium bicarbonate ($NaHCO_3$). The solution was then purged with nitrogen to reduce the level of oxygen to below 5 parts per billion. The deaerated solution was then transferred to a glass vessel containing all the loaded specimens (Figure 4.9) and a second deaeration stage was performed by purging the solution with nitrogen for 60 minutes at a constant flow rate (1 L per minute). The test gas (H_2S/CO_2) was then switched on at 1 L per minute for 90 minutes for saturation and the flow was reduced to a few bubbles per minute once the test started. The temperature was recorded throughout the experiment.

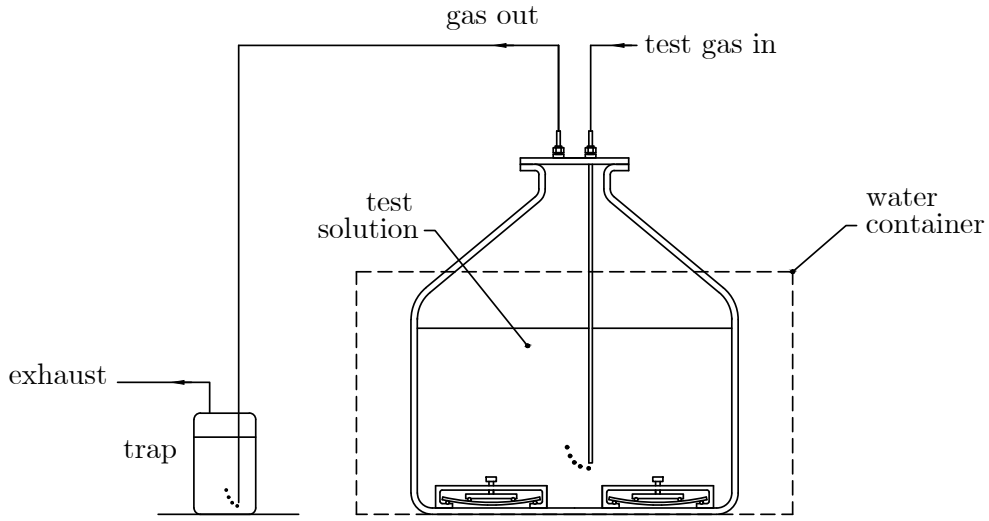

FIGURE 4.9: Schematic representation of the four point bend SSC setup

After 720 hours of exposure to the test environment, the pH was measured and the test gas switched off, followed by 60 minutes of nitrogen purge to reduce the concentration of H_2S and safely remove the specimens. After the test, all the samples were removed from the vessels, immersed in acetone for 2 minutes to remove the strain gauges, unloaded and dried with an air blower. The test surfaces were examined with SEM and cross sections were prepared for detailed analysis of the cracks. Cross sectional specimens were mounted, ground, polished and etched.

4.3 Results and discussion

In this section, the numbering scheme presented in Figure 4.10 is used to identify the specimens used in the SSC experiments. Unless otherwise specified, the specimens have smooth surfaces. Particular cases (i.e. pre-damaged surfaces, PD) are clearly identified.

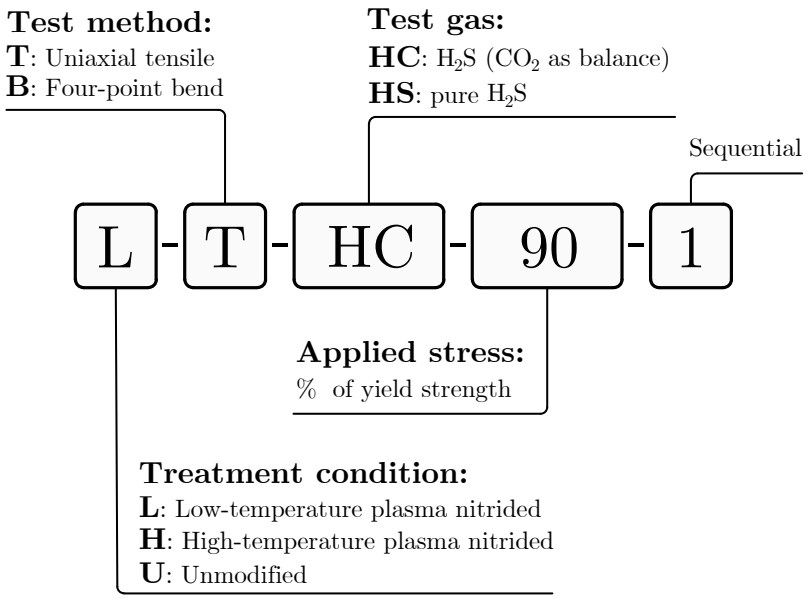

FIGURE 4.10: Numbering scheme used to identify the samples used in the SSC experiments

4.3.1 Uniaxial tensile

Unmodified material

Table 4.2 shows the loading data of unmodified specimens submitted to tensile SSC experiments in produced water ($165\,\mathrm{g\,L^{-1}}$ NaCl and pH 4.5 ± 0.2) with $p\mathrm{H_2S} = (3.4 \pm 0.1)\,\mathrm{kPa}$ and CO_2 as balance. The data include the average diameter (d) of the specimens, applied stress—measured as a percentage of the yield strength of the material (σ/σ_y)—and the corresponding uniaxial loads. It also shows readings of the initial (before SSC) and final deflections (after the SSC) and the parameters obtained after calibration of the loading frames used for setting the stress level, i.e slope (a) of the curves obtained by plotting displacement against load and their respective y-intercepts (b). The yield strength, σ_y, used as reference (section 3.2.1.1) for all the specimens, was $(773 \pm 12)\,\mathrm{MPa}$.

Table 4.2: Loading data and final deflection of unmodified 17-4 PH (H1150D) submitted to SSC tensile in produced water ($165\,\mathrm{g\,L^{-1}}$ NaCl and pH 4.5 ± 0.2) with mixed H_2S ($p\mathrm{H_2S} = (3.4 \pm 0.1)\,\mathrm{kPa}$ and CO_2 as balance).

Specimen ID	d **(mm)**	**Applied stress** (σ/σ_y)	**Load** (kN)	**Loading frame**			
				a ($\mu\mathrm{m\,kN^{-1}}$)	b (µm)	**Initial deflection** (µm)	**Final deflection** (µm)
U-T-HC-30-1	6.32 ± 0.03	0.3	7.2 ± 0.1	396.8	-617.2	2251 ± 18	2228 ± 18
U-T-HC-30-2	6.30 ± 0.02	0.3	7.3 ± 0.1	397.7	-520.6	2373 ± 27	2352 ± 27
U-T-HC-50-1	6.30 ± 0.02	0.5	12.2 ± 0.1	145.3	-55.6	1711 ± 21	1627 ± 20
U-T-HC-50-2	6.33 ± 0.03	0.5	12.0 ± 0.1	153.2	-114.4	1735 ± 20	1710 ± 19
U-T-HC-70-1	6.30 ± 0.04	0.7	17.0 ± 0.3	123.6	-82.8	2015 ± 33	—
U-T-HC-70-2	6.32 ± 0.03	0.7	16.9 ± 0.3	116.4	-73.1	1890 ± 33	—
U-T-HC-90-1	6.33 ± 0.04	0.9	21.7 ± 0.4	121.6	-105.8	2532 ± 42	—
U-T-HC-90-2	6.30 ± 0.02	0.9	21.9 ± 0.4	116.7	-126.0	2329 ± 49	—

By comparing the initial and final deflections of the specimens loaded to 30 and 50% of σ_y, the percentage variation of the deflection was $\approx 2\%$, in average. This indicated that

stress relaxation was not significant and that the load was nearly constant during the 720 hours of exposure. For the specimens loaded to 70 to 90% of σ_y, the final deflection was not measured since partial or complete fracture occurred before the end of the experiment.

Time–to–failure by SSC of unmodified specimens—characterised by either the presence of cracks on the surface after the end of the test or fracture (complete separation) of the specimens—are presented in Figure 4.11.

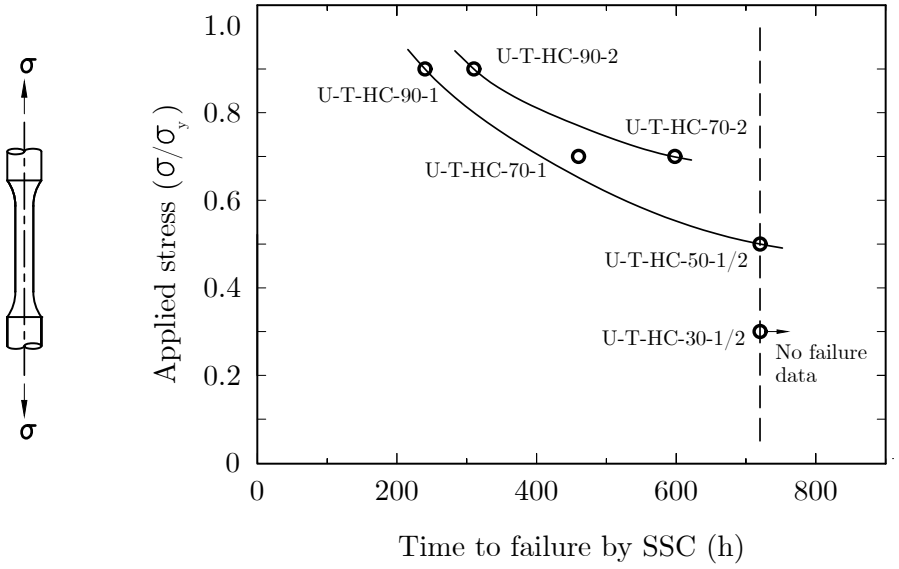

FIGURE 4.11: Time–to–failure by SSC of unmodified 17-4 PH (H1150D) submitted to SSC tensile in produced water ($165\,\mathrm{g\,L^{-1}}$ NaCl and pH 4.5 ± 0.2) with mixed H_2S ($pH_2S = (3.4 \pm 0.1)\,\mathrm{kPa}$ and CO_2 as balance).

The results (Figure 4.11) showed that unmodified specimens, except those stressed to $\sigma/\sigma_y = 0.3$, failed by SSC. The average time for complete rupture of the specimens loaded to 90% (U-T-HC-90-1/2) and 70% of σ_y (U-T-HC-70-1/2) were 274 and 529 hours, respectively. When loaded to 50% (U-T-HC-50-1/2), cracks were detected on the surface of both specimens (by microscopic examination) after the end of the exposure period—time–to–failure, in this case, was 720 h. Conversely, the specimens loaded to 30%

(UT H C3 01 /2) resisted to SSC since no cracks were detected on their surfaces after the end of the exposure period. Therefore, the threshold stress (σ_{th}) at which SSC does not occur for the tested conditions was within $0.3\ \sigma_y < \sigma_{th} < 0.5\ \sigma_y$. This clearly poses a limitation for the application of this material in environments containing H_2S, since failures occurred when the stress was far below the yield strength, even keeping the pH and pH_2S within the acceptable domains (i.e. pH $\geq$ 4.5 and maximum pH_2S of 3.4 kPa [16]). Recognizing this limitation, the maximum permitted stress was recently reviewed [10, 17] and, according to that, it must not exceed the lowest value between (i) 50% of the minimum specified yield strength of the material, i.e. 50% of 725 MPa[44] and (ii) 380 MPa. Thus, the results from the present work provide additional data to support the loading criteria.

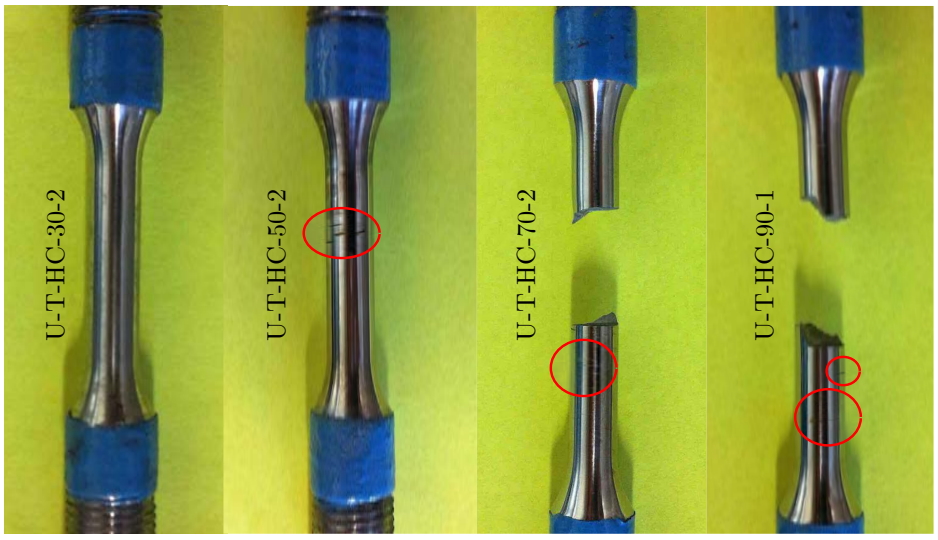

FIGURE 4.12: Macroscopic view of the test surfaces of unmodified 17-4 PH (H1150D) after the SSC tensile experiment in produced water (165 g L^{-1} NaCl and pH 4.5 ± 0.2) with $pH_2S = (3.4 \pm 0.1)$ kPa and CO_2 as balance.

Figure 4.12 shows macroscopic views of the test surfaces after the SSC experiment, indicating the positions (red circles) of cracks visually observed after the specimens were

removed from the vessel. In all the specimens—except for U-T-HC3-01/2—cracks were concentrated near the middle of the gauge section. On the specimens U-T-HC7-01/2 and U-T-HC9-01/2, secondary cracks were also observed in addition to the main cracks that caused complete rupture of these samples—also located near the centre of the specimens.

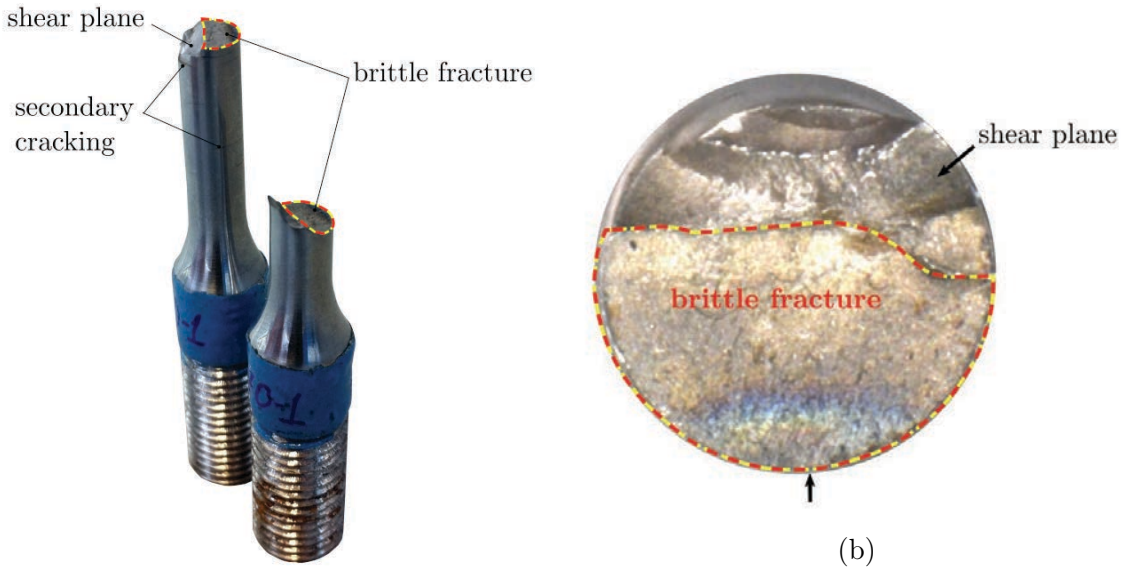

FIGURE 4.13: Fractured surfaces of unmodified 17-4 PH (H1150D) after the SSC tensile experiment in produced water ($165\,\mathrm{g\,L^{-1}}$ NaCl and pH 4.5 ± 0.2) with $p\mathrm{H_2S} = (3.4 \pm 0.1)\,\mathrm{kPa}$ and $\mathrm{CO_2}$ as balance (sample U-T-HC-70-2): (a) overview; (b) amplified view from the top.

A closer view of typical fracture surface is shown in Figure 4.13 (specimen U-T-HC7 0-2). As indicated in Figure 4.13a, the fractured area comprises a flat surface perpendicular to the applied tensile stress and a smaller region corresponding to fast overload fracture. These two regions are separated by a shear plane inclined 45°—the direction of maximum shear stress—with respect to the loading axis. The absence of deformation and the bright appearance of the flat region confirmed the occurrence of brittle fracture. As can be seen in Figure 4.13b, the brittle section accounts for $\approx 60\%$ of the cross sectional area. Similar

features were observed in specimens loaded to 90 %, the brittle area being smaller in this case (between 30 and 40%) due to greater overloading. The arrow in Figure 4.13b indicates the crack initiation site.

Figure 4.14, taken from the brittle fracture sites (perpendicular to the applied stress) provides additional evidence of brittle cracking. As can be seen, sulphide stress cracks propagated in both intergranular (propagation path coincide with prior austenite grains, Figure 4.14a) and transgranular manner (cracks propagate through prior–austenite grains, as in Figure 4.14b), with no signs of plastic deformation. These cracking modes were also observed in the crosss ectional micrographs.

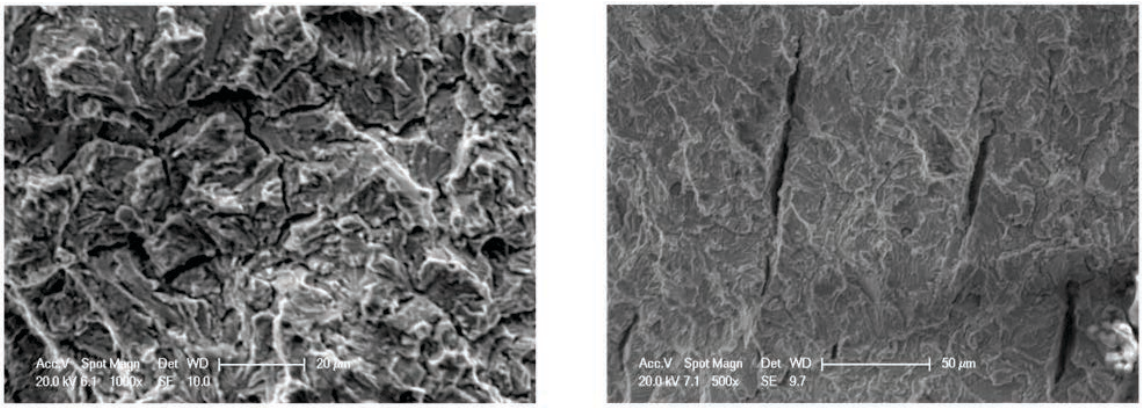

(a) (b)

FIGURE 4.14: SEM micrographs taken from the brittle fracture sites indicated in Figure 4.13 (specimen U-T-HC-70-2): (a) Intergranular and (b) transgranular cracking.

Figures 4.15 and 4.16 show cross sections (SEM micrographs) of cracks that propagated from the surfaces of unmodified specimens loaded to 50, 70 and 90 % of σ_y. Apparently, the fracture mode was independent of the applied stress, since all cracks exhibit both intergranular (IGS SC) and transgranular (TG-SSC) cracking. Detailed analysis for each stress level is presented in the following paragraphs.

Cracks formed on the specimens loaded to 50% of σ_y are shown in Figure 4.15. It appears that the crack shown in Figure 4.15a initiated from a corosion pit, similar to what occured in earlier observations [33], whereas the crack presented in Figure 4.15b did not require a surface defect to initiate. Figures 4.15c and 4.15d, taken from different positions away from the surface, revealed further details about the failure. It showed that cracks, up to 200 µm long, propagated in both transgranular and intergranular modes and, in some parts, secondary cracks deviated from the main path and propagated simultaneously in different directions (i.e. crack branching, Figure 4.15c).

In tempered martensitic structures, brittle intergranular cracks can occur due to segregation of impurities (e.g. phosphorous [52] and sulphur[79]) within the prior–austenite grain boundaries, which reduces the cohesion of iron atoms. In agreement with this observation, 4.1 wt.% of sulphur was detected by EDS (spectrum 1 in Figure 4.15f, taken from the specimen U-T-HC-50-2) near the crack (darker area). This quantity is above that obtained away from the crack (spectrum 2, brighter area), which was similar to the background content of this element (maximum 0.03 wt.%) within the microstructure. Besides, the presence of sulphur in the grain boundaries can indicate precipitation of iron sulphide, which can increase the rate of hydrogen permeation into the substrate, increasing the probability of failure by intergranular SSC [79].

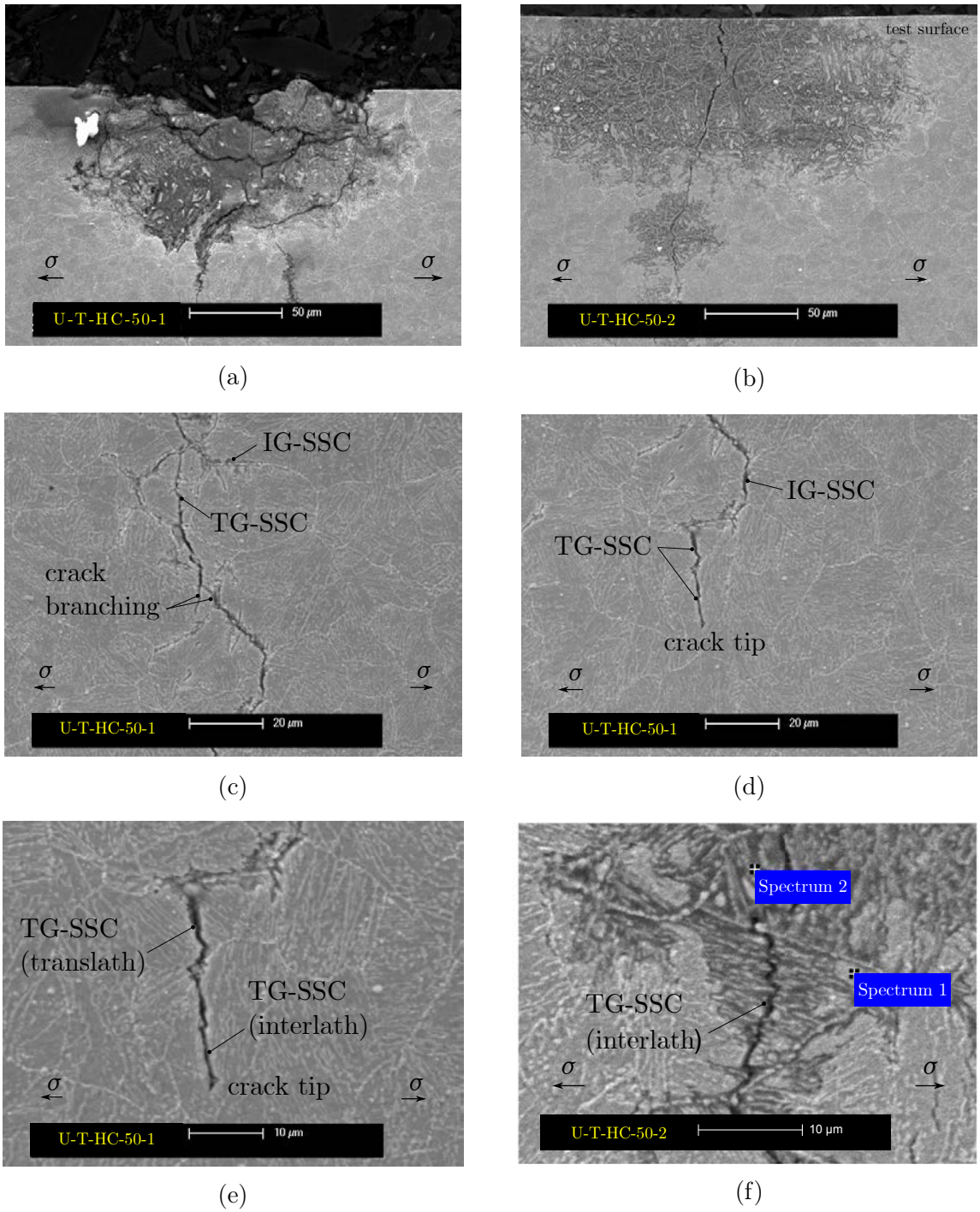

FIGURE 4.15: SEM micrographs (cross sections) of (a-e) unmodified 17-4 PH (H1150D)—loaded to 50% of σ_y—after the SSC tensile experiment in produced water ($165\,\mathrm{g\,L^{-1}}$ NaCl and pH 4.5 ± 0.2) with $p\mathrm{H_2S} = (3.4 \pm 0.1)\,\mathrm{kPa}$ and CO_2 as balance; (f) U-T-HC-70-2 (used for EDS).

Tempered martensite can also undergo transgranular cracking when the segregation of impurities at the grain boundaries (e.g. P, S) is low. It occurs in two different modes: following the lath structure (interlath) or across the laths (translath), as indicated in Figures 4.15e and 4.15f. Transgranular cracking involves low anodic dissolution and typically occurs in non–sensitized structures. The occurence of both IG-SSC and TG-SSC has been reported in the literature for high–strength steels exposed to H_2S, being predominantly intergranular [206] or mostly transgranular [14]. For the 17-4 PH, specifically, faliure analysis [66] has shown that, in fact, mixed cracking mode occurs in this material—predominantly transgranular, as noted in some studies [14, 56].

The greater concentration of sulphur near the cracks (e.g. 4.1 wt.%, Figure 4.15f) suggests that segregation of these species contributed to SSC. As reviewed in Chapter 2, the classical SSC mechanism involves enhanced absorption of hydrogen promoted by preferential segregation of sulphur species along the grain boundaries—hydrogen adsorbed at the surface is absorbed by the metal rather than recombine to form H_2 (known as recombination poisoning). This mechanism can explain crack advance through prior–austenite grain boundaries and through lath contours of the martensitic structure, but is not sufficient to describe transgranular propagation. It was assumed, therefore, that other forms of hydrogen embrittlement took place concurrently, e.g. hydrogen-enhanced localized plasticity (HELP) and adsorption-induced dislocation emission (AIDE)—a brief description of each mechanism is provided in section 2.2.1.2. Besides, it is generally accepted that, although cracking of high strength steels in H_2S environments arise mostly out of hydrogen embrittlement mechanisms, it can also involves features of stress corrosion cracking (SCC). Overall, the failures showed characteristics of both SSC (e.g. crack initiation from a sooth surface) and SCC (e.g. branching and crack initiation from surface defects, i.e corrosion pits). A fully comprehensive evaluation, however, is required to determine the

exact mechanism. A list of recommendations for future investigations is presented in Chapter 8.

Cross sections of specimens loaded to 70% of σ_y (Figures 4.16a and 4.16b) displayed similar features as those observed in specimens loaded to 50%, e.g. crack branching (intensified due to the higher stress) and mixed IG-SSC/TG-SSC cracking. These similarities suggest that their mechanisms were equivalent. Secondary cracks, nucleated from the fractured surface, was also observed (Figure 4.16c). In this case, nucleation and propagation (nearly perpendicular to the loading direction) occurred due to the uneven stress distribution (notch effect) induced by the opening of the main crack that caused rupture of the specimen. Figure 4.16d shows earlier stages of cracking, apparently propagating through a prior–austenite grain and following martensite laths. For the specimens loaded to 90% of σ_y (Figures 4.16e and 4.16f), crack opening was wider (up to 50 µm) and crack penetration was deeper (> 1 mm) due to the larger stress. Mixed intergranular/transgranular cracking, branching and secondary cracking were also observed in these specimens.

The pH after the test (for all the loading conditions) was nearly constant (increased less than 0.2 units compared to the initial pH, which lies within the specification limits, i.e. 4.5 ± 0.2), suggesting low corrosion activity. This variation was reflected in the concentration of H_2S, also verified at the end of the test by iodometric titration: the concentration reduced from $(78 \pm 1)\,\mathrm{mg\,L^{-1}}$ (initial concentration) to $(74 \pm 1)\,\mathrm{mg\,L^{-1}}$ (immediately before the test gas was switched off).

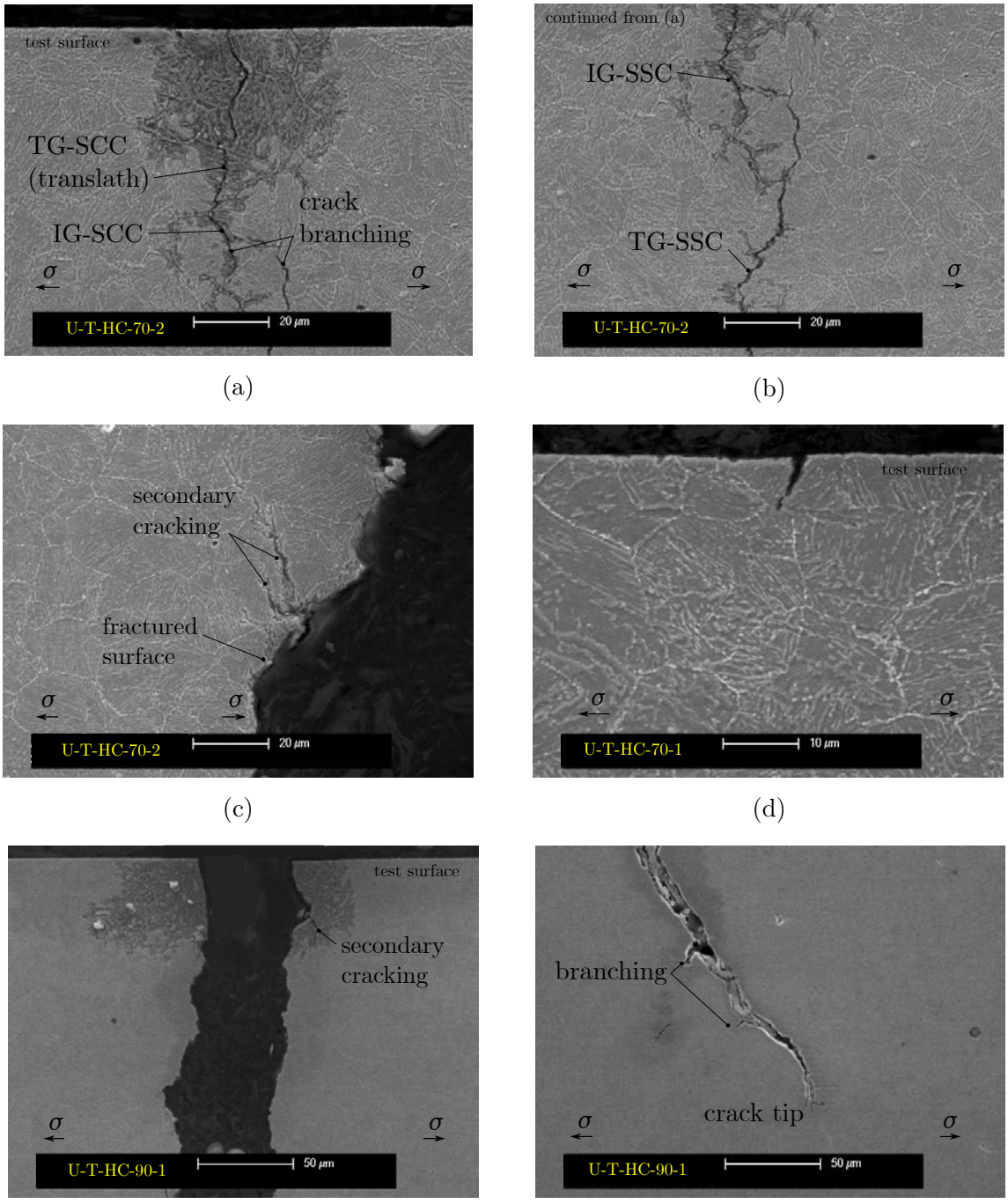

FIGURE 4.16: Cross sections of unmodified 17-4 PH (H1150D)—loaded to (a-d) 70% and (e-f) 90% of σ_y—after the SSC tensile experiment in produced water (165 g L^{-1} NaCl and pH 4.5 ± 0.2) with pH_2S = (3.4 ± 0.1) kPa and CO_2 as balance.

LTPN

Table 4.3 shows loading data of low–temperature plasma nitrided (LTPN) specimens submitted to tensile SSC experiments in produced water ($165\,\mathrm{g\,L^{-1}}$ NaCl and pH 4.5 ± 0.2) with $p\mathrm{H_2S} = (3.4 \pm 0.1)\,\mathrm{kPa}$ and CO_2 as balance (L-T-HC-70 and L-T-HC-90 and one pre-damaged specimen L-T-HC-90-PD) and with pure H_2S (specimens L-T-HS-70 and L-T-HS-90). Similarly to what occurred for the unmodified material, stress relaxation was negligible since the final deflection measured after the end of 720 h was no greater than 1% for all the specimens. The assumption of constant stress was, therefore, validated.

TABLE 4.3: Loading data and final deflection of LTPN specimens submitted to SSC tensile in produced water ($165\,\mathrm{g\,L^{-1}}$ NaCl and pH 4.5 ± 0.2) with $p\mathrm{H_2S} = (3.4 \pm 0.1)\,\mathrm{kPa}$ and CO_2 as balance and pure H_2S

Specimen ID	d **(mm)**	**Applied stress** (σ/σ_y)	**Load** (kN)	**Loading frame**			
				a ($\mu\mathrm{m\,kN^{-1}}$)	b (µm)	**Initial deflection** (µm)	**Final deflection** (µm)
L-T-HC-70-1	6.30 ± 0.02	0.7	16.9 ± 0.2	122	-110	1952 ± 28	1928 ± 27
L-T-HC-70-2	6.34 ± 0.02	0.7	17.1 ± 0.2	118	-109	1912 ± 26	1884 ± 26
L-T-HC-70-3	6.32 ± 0.02	0.7	17.0 ± 0.2	121	-66	1992 ± 27	1962 ± 26
L-T-HC-90-1	6.30 ± 0.04	0.9	21.7 ± 0.4	122	-106	2532 ± 49	2506 ± 49
L-T-HC-90-2	6.30 ± 0.04	0.9	21.7 ± 0.4	116	-73	2451 ± 49	2410 ± 48
L-T-HC-90-3	6.33 ± 0.04	0.9	21.9 ± 0.4	124	-83	2622 ± 50	2630 ± 50
L-T-HS-70-1	6.31 ± 0.02	0.7	16.9 ± 0.1	120	-66	1963 ± 11	1974 ± 11
L-T-HS-90-1	6.28 ± 0.02	0.9	21.6 ± 0.4	115	-73	2409 ± 41	2431 ± 41
L-T-HC-90-PD[(a)]	6.31 ± 0.02	0.9	21.9 ± 0.4	119	-124	2474 ± 14	2727 ± 15

[a] pre-damaged specimen (impressions with Vickers indenter).

As shown in Figure 4.17, none of the LTPN specimens (loaded to 70 and 90% of σ_y) failed by SSC when exposed to produced water with $p\mathrm{H_2S} = (3.4 \pm 0.1)\,\mathrm{kPa}$ and CO_2 as balance. During the experiment, the samples were monitored by visual inspection and no signs of crack initiation were identified on their surfaces—including the pre-damaged

specimen. Similarly to the unmodified specimens, the pH level was maintained within 4.5 ± 0.2 throughout the experiment and the concentration of H_2S immediately before the end of the test was $(77 \pm 1)\,\mathrm{mg\,L^{-1}}$, in this case closer to the initial value—indicative of different corrosion activity compared to the unmodified material, although the concentration on the bulk solution may not be representative of the local concentration at the metal/electrolyte interface.

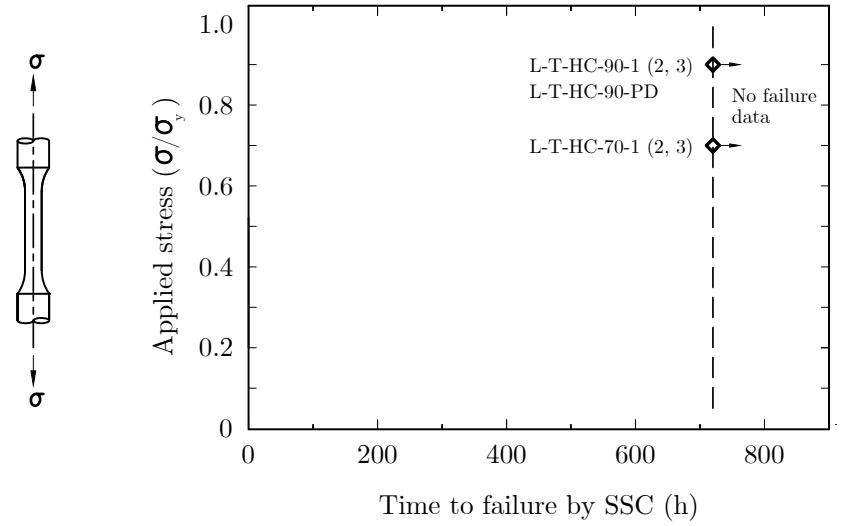

FIGURE 4.17: Time–to–failure by SSC of LTPN 17-4 PH (H1150D) submitted to SSC tensile in produced water ($165\,\mathrm{g\,L^{-1}}$ NaCl and pH 4.5 ± 0.2) with $p\mathrm{H_2S} = (3.4 \pm 0.1)\,\mathrm{kPa}$ and CO_2 as balance

Figure 4.18 shows the appearance of selected specimens (L-T-HC-70-1, L-T-HC-90-1 and L-T-HC-90-PD) after being removed from the vessel, cleaned and dried. Preliminary examination of the surface with optical microscope and SEM confirmed that cracks were not formed. Elemental analysis (Figure 4.19) of the test surface for all specimens indicated the presence of sulphur (varying from 4.6 to 9.7 wt.%), which suggests the formation of a thin film of iron sulphide (FeS_2) on the surface.

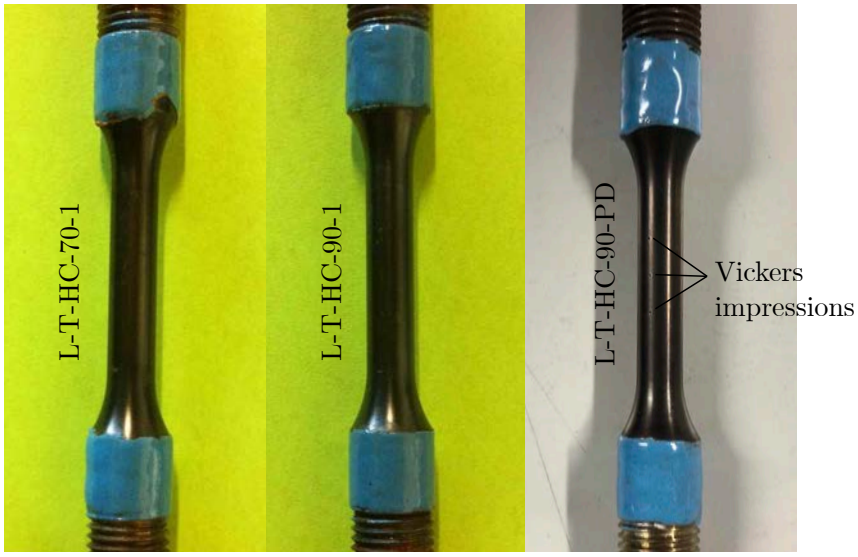

FIGURE 4.18: Macroscopic view of the surfaces of LTPN 17-4 PH (H1150D) specimens after being submitted to SSC tensile in produced water ($165\,\mathrm{g\,L^{-1}}$ NaCl and pH 4.5 ± 0.2) with $p\mathrm{H_2S} = (3.4 \pm 0.1)\,\mathrm{kPa}$ and $\mathrm{CO_2}$ as balance

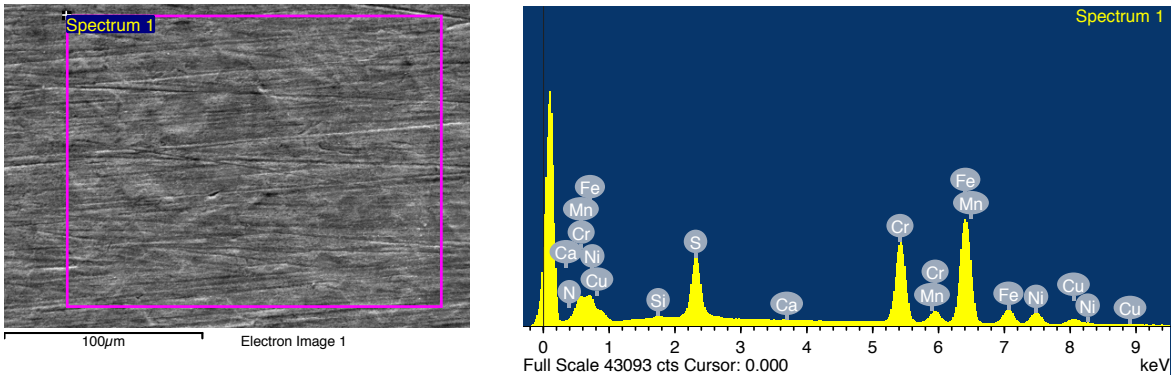

(a) (b)

FIGURE 4.19: Typical elemental composition of the surfaces of the samples L-T-HC-70-1, L-T-HC-90-1 and L-T-HC-90-PD after SSC: (a) SEM image; (b) EDS spectrum.

Cross sectional SEM micrographs (typical images are shown in Figure 4.20) provided additional evidence of the absence of SSC cracks perpendicular to the loading direction. For the specimens loaded to 70% of σ_y, the morphology of the nitrided layer (Figure 4.20a) preserved the main features identified before the SSC experiment (see Figure 3.10a

in Chapter 3), with the prior-austenite grain boundaries preferentially attacked after etching (see an amplified view in Figure 4.20b). Similar features were identified in the specimens loaded to 90% of σ_y (Figure 4.20c). A distinct phenomenon, i.e. delamination–like effect, was observed in the outer section of some specimens. As shown in Figure 4.20d, spalling occurred near the surface. A closer examination of SEM images obtained before and after the SSC experiments, including not etched specimens (Figure 4.20e) confirmed that this effect was also noticeable before the experiment (Figure 4.20f). A possible cause for the superficial spalling is the compressive residual stress within the compound layer, associated with the high concentration of nitrogen near the surface. Since these defects were only present in cross section images—they were not identified when examining the top of the surfaces—it can be assumed that they occurred due to stress redistribution during sample preparation (grinding and cutting).

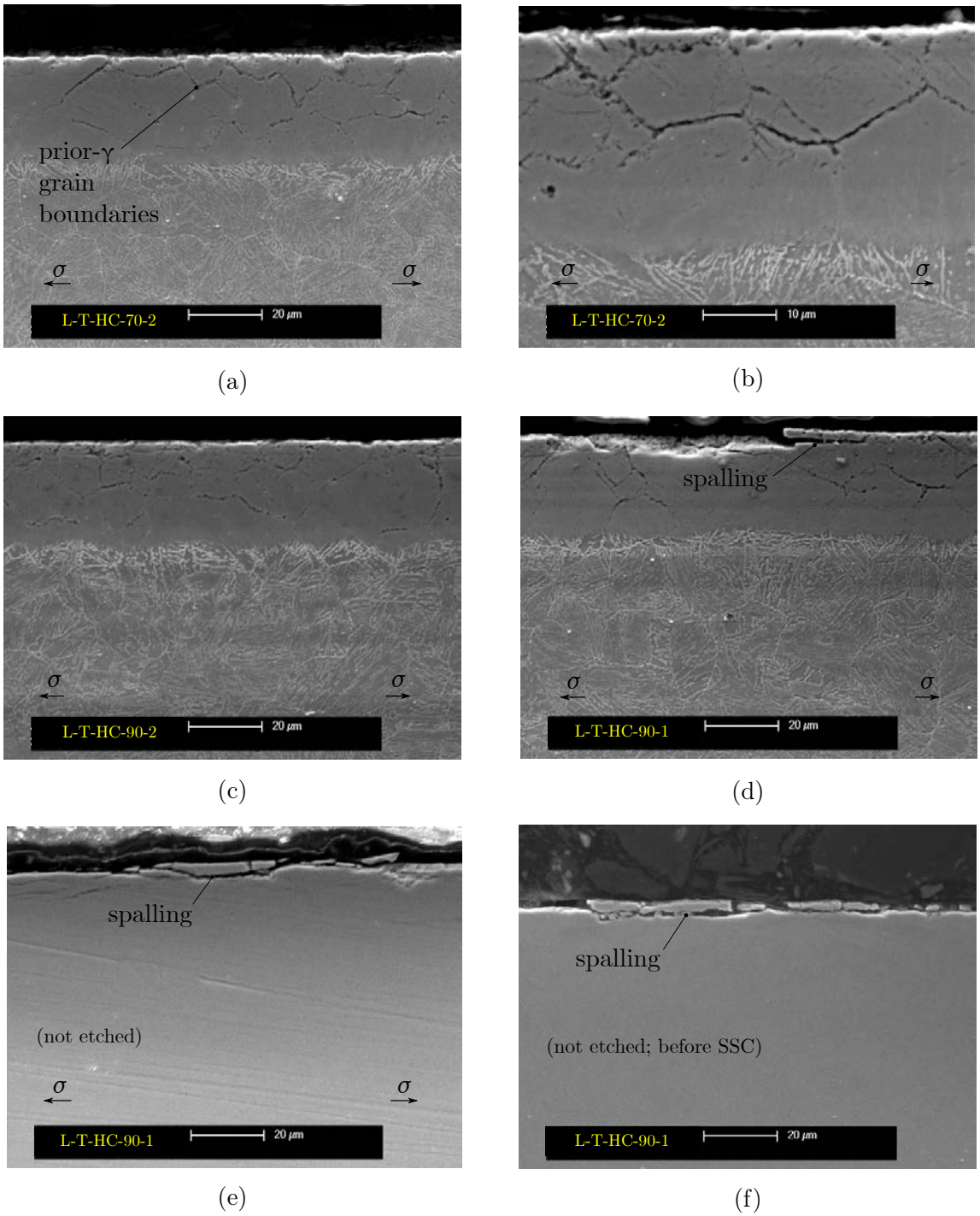

FIGURE 4.20: Cross sections of LTPN 17-4 PH (H1150D) specimens loaded to (a-b) 70% of σ_y and (c-f) 90% of σ_y after being submitted to SSC tensile in produced water ($165\,g\,L^{-1}$ NaCl and pH 4.5 ± 0.2) with pH_2S = (3.4 ± 0.1) kPa and CO_2 as balance.

The pre-damaged specimen (L-T-HC-90-PD, Figure 4.21), in which the substrate was exposed to the electrolyte—by either on the bottom of the Vickers impressions or through the brittle cracks surrounding the top of the indent—also resisted to SSC. In this case, the pH of the bulk solution increased from 4.5 (beginning of the test) to 4.8 (after 720 hours of immersion), but the complex reactions taking place near the surface and the buffer effect of CO_2 made it difficult to determine the causes for that increase.

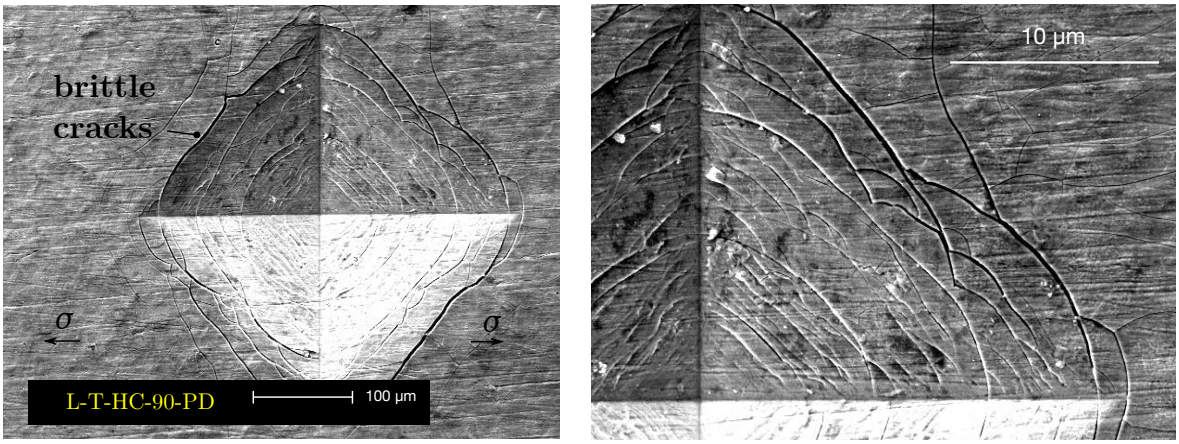

(a) (b)

FIGURE 4.21: Top view of pre–damaged LTPN 17-4 PH (H1150D) specimen loaded to 90% of σ_y after being submitted to SSC tensile in produced water ($165\,g\,L^{-1}$ NaCl and pH 4.5 ± 0.2) with $pH_2S = (3.4 \pm 0.1)\,kPa$ and CO_2 as balance: (a) overview and (b) amplified view.

For the LTPN specimens loaded to 70 and 90% of σ_y and exposed to pure H_2S (L-T-HS-70-1 and L-T-HS-70-2), no cracks were observed on their surfaces after the end of the experiment. The general appearance of the specimens after being removed from the test vessels were similar to that when exposed to mixed H_2S/CO_2 (Figure 4.18). It also appears that a film of iron sulphide was formed on the surface of both specimens, since the EDS measurements indicated the presence of more than 2 wt.% of sulphur—the spectrum was similar to that in Figure 4.19.

A closer examination of the surfaces with SEM revealed superficial damage on the specimen loaded to 90%. Figure 4.22a shows localised attack that occurred near the centre of the gauge section and the amplified view (Figure 4.22b) indicates that the outer section of the plasma nitrided layer was dissolved. In spite of that, no cracks nucleated from this location. The pH, as in the pre-damaged specimens, increased from 4.5 to 4.8.

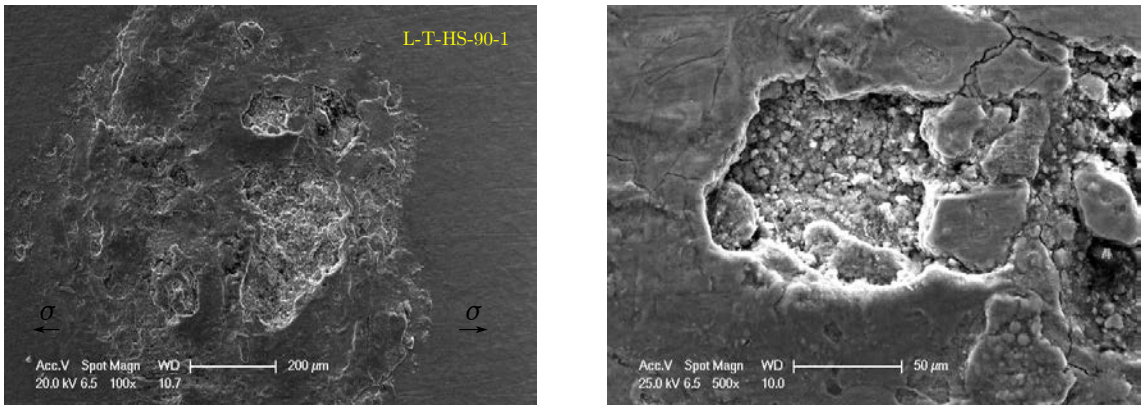

(a) (b)

FIGURE 4.22: Top view (a-b) of the surfaces of LTPN 17-4 PH (H1150D) specimens after being submitted to tensile SSC in produced water (165 g L^{-1} NaCl and pH 4.5 ± 0.2) saturated with pure H_2S: (a) overview and (b) amplified view.

HTPN

Loading data for the HTPN specimens are shown in Table 4.4. Similar to the unmodified and LTPN, stress relaxation—estimated by the percentage difference between the initial and final deflection of the loading ring—was negligible and the load was therefore approximately constant throughout the experiment.

TABLE 4.4: Loading data and final deflection of HTPN specimens submitted to SSC tensile in produced water ($165\,g\,L^{-1}$ NaCl and pH 4.5 ± 0.2) with $pH_2S = (3.4 \pm 0.1)$ kPa and CO_2 as balance.

Specimen ID	d **(mm)**	**Applied stress** (σ/σ_y)	**Load** (kN)	**Loading frame**			
				a ($\mu m\,kN^{-1}$)	b (μm)	**Initial deflection** (μm)	**Final deflection** (μm)
H-T-HC-70-1	6.29 ± 0.02	0.7	16.8 ± 0.2	118	-91	1896 ± 26	1883 ± 26
H-T-HC-70-2	6.27 ± 0.02	0.7	16.7 ± 0.2	123	-114	1948 ± 28	2111 ± 30
H-T-HC-90-1	6.32 ± 0.03	0.9	21.8 ± 0.4	123	-93	2585 ± 46	2587 ± 46
H-T-HC-90-2	6.34 ± 0.03	0.9	22.0 ± 0.4	120	-106	2524 ± 46	2667 ± 48
H-T-HC-90-PD[a]	6.32 ± 0.02	0.9	22.0 ± 0.4	117	-253	2304 ± 17	2406 ± 18

[a] pre-damaged specimen (impressions with Vickers indenter).

Time–to–failure of HTPN specimens loaded to 70% and 90% of σ_y, Figure 4.23, shows that failure by SSC did not occur. No signs of cracking was identified by examination of the test surfaces with SEM after 720 h of exposure, although significant amount of corrosion deposits was observed on the surface of the pre-damaged specimen H-T-HC-90-PD and to a lesser extent (only dispersed deposits) on the specimens H-T-HC-70-1/2 and H-T-HC-90-1/2.

Figure 4.24a shows typical cross section of HTPN specimens (H-T-HC-90-1, with similar morphology was observed for H-T-HC-70-1/2) after the SSC experiment, confirming the absence of cracks. Contrary to what was observed on LTPN specimens, no delamination (spalling) was observed on the top of the nitrided layer, possibly due to the lower compressive residual stress, associated with the lower nitrogen content near the surface (section 3.2.2.2). By examining the top surface with SEM (Figure 4.24b), only dispersed scales—presumably $FeCO_3$, due to the high concentration of oxygen obtained by EDS—were identified. Elemental analysis also revealed that the surface was covered by a thin film of iron sulphide (FeS_2), since the sulphur content was about 12 wt.%. The final pH of the bulk solution was 4.8.

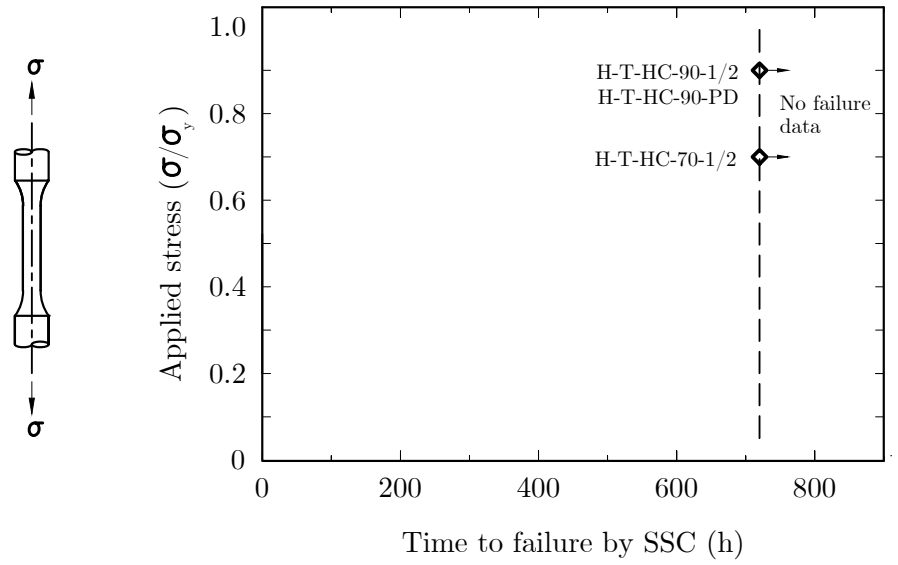

FIGURE 4.23: Time–to–failure by SSC of HTPN 17-4 PH (H1150D) submitted to SSC tensile in produced water ($165\,\mathrm{g\,L^{-1}}$ NaCl and pH 4.5 ± 0.2) with $p\mathrm{H_2S} = (3.4 \pm 0.1)\,\mathrm{kPa}$ and CO_2 as balance

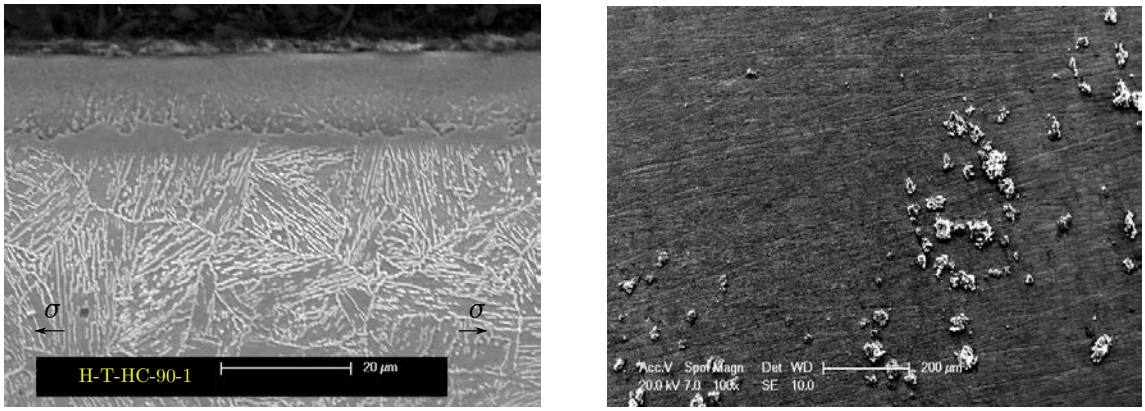

(a) (b)

FIGURE 4.24: SEM micrographs of HTPN 17-4 PH (H1150D) specimens loaded to 90% of σ_y after being submitted to SSC tensile in produced water ($165\,\mathrm{g\,L^{-1}}$ NaCl and pH 4.5 ± 0.2) with $p\mathrm{H_2S} = (3.4 \pm 0.1)\,\mathrm{kPa}$ and CO_2 as balance: (a) cross section; (b) top view.

For the pre–damaged specimen (H-T-HC-90-PD), it was noticed that the surface was

covered with corrosion scale after two weeks of immersion. This was identified by visually inspecting the specimen inside the transparent acrylic vessel. Figure 4.25 shows the SEM micrograph (after 720 h of immersion) of the top surface near one of the Vickers impressions, confirming deposition and thereby intense corrosion activity on these regions. Due to the poor corrosion resistance of the plasma nitrided layer obtained at elevated temperature, attributed to the precipitation of chromium nitride (section 3.2.2.4), the galvanic effect formed between unmodified substrate (cathode) and the nitrided layer (anode) was a major driving force for the increased corrosion. This occurred because, as with the pre-damaged LTPN specimen, the substrate was exposed to the electrolyte either on the bottom of the impression or through the brittle cracks formed on the nitrided layer.

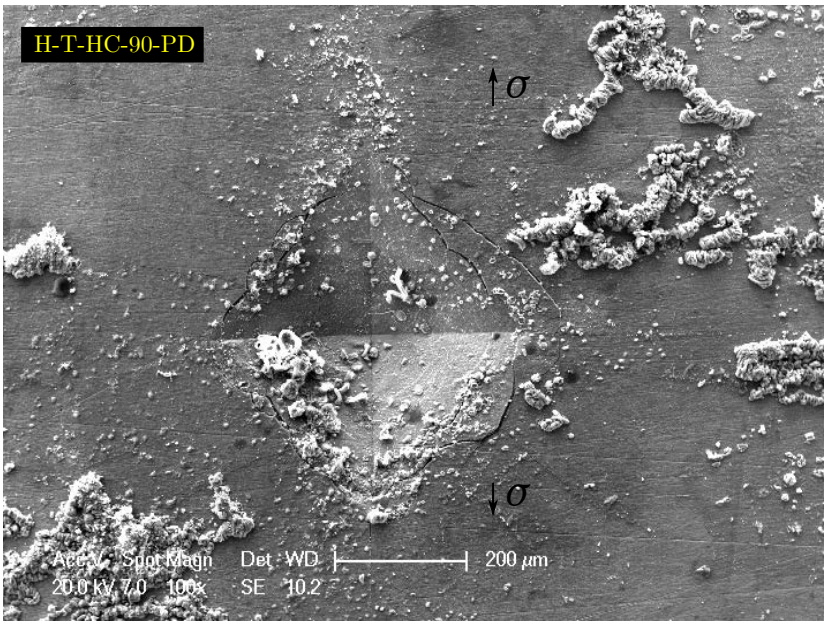

FIGURE 4.25: SEM micrograph (top view) of pre–damaged HTPN 17-4 PH (H1150D) specimen loaded to 90% of σ_y after being submitted to SSC tensile in produced water ($165\,g\,L^{-1}$ NaCl and pH 4.5 ± 0.2) with pH_2S = (3.4 ± 0.1) kPa and CO_2 as balance.

The corrosion scale covered great part of the surface exposed to the environment,

including regions away from the impressions, as shown in Figure 4.26b. Elemental composition—obtained by EDS (Figure 4.26)—indicated that about 3.6 wt.% of sulphur was present in areas not covered by the corrosion scales, which suggests the formation of FeS_2. EDS alone, however, was not sufficient to determine the nature of the corrosion scales.

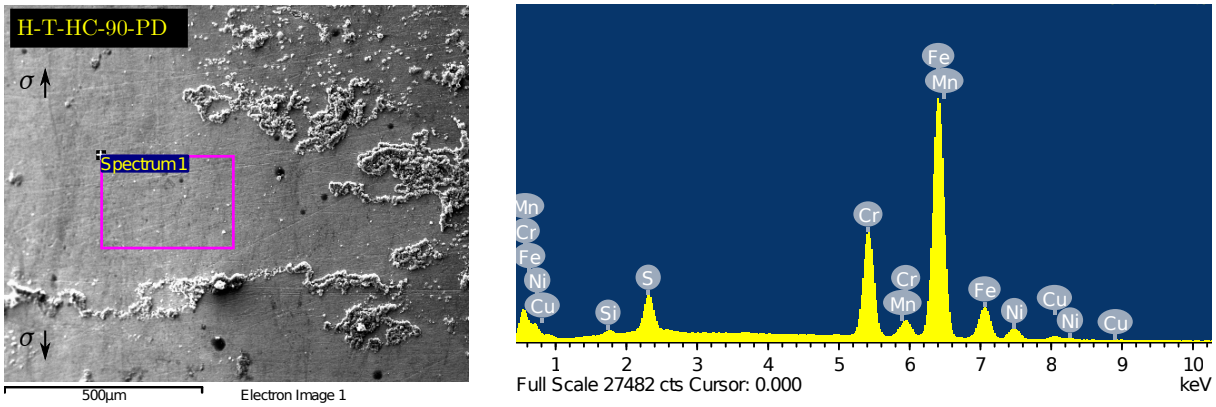

(a) (b)

FIGURE 4.26: Typical elemental composition of the surface of the pre-damaged HTPN specimen (H-T-HC-90-PD): (a) SEM image; (b) EDS spectrum.

4.3.2 Four-point bend

Table 4.5 shows selected loading data of unmodified and LTPN specimens used in the four-point bend experiment (two repeats for each condition). The target stresses, σ/σ_y, were the same as those used on SSC tensile (from 30 to 90 % of the yield strength), but actual stresses were larger for higher stress levels (i.e $\sigma/\sigma_y = 0.8$ and 1.0 rather than 0.7 and 0.9), due to the difficulty to obtain stable readings from strain gauges (longitudinal strain, ε_x, and transversal strain, ε_y) by manually adjusting the load to reach the target strain. These actual stress levels, although some not being the same as those used in the uniaxial tensile experiment, were maintained and provided supplementary information to

evaluate the effect of stress on SSC. As mentioned earlier, the SSC resistance of HTPN was not evaluated with the four-point bend method.

TABLE 4.5: Loading data of unmodified and LTPN 17-4 PH (H1150D) specimens used in four–point bend SSC in produced water ($165\,\mathrm{g\,L^{-1}}$ NaCl and pH 4.5 ± 0.2) with $p\mathrm{H_2S} = (3.4 \pm 0.1)\,\mathrm{kPa}$ and $\mathrm{CO_2}$ as balance.

Specimen ID	Target stress (σ/σ_y)	Target strain ($\mu\varepsilon_\mathrm{T}$)	Longitudinal strain ($\mu\varepsilon_\mathrm{x}$)	Transversal strain ($\mu\varepsilon_\mathrm{y}$)	Equivalent uniaxial strain ($\mu\varepsilon_\mathrm{u}$)	Actual stress ($\sigma'/\sigma_\mathrm{y}$)
U-B-HC-30-1	0.3	1177	1251	-366	1243	0.3
U-B-HC-50-1	0.5	2021	2135	-666	2110	0.5
U-B-HC-70-1	0.7	2853	3112	-927	3088	0.8
U-B-HC-90-1	0.9	3950	4029	-1247	3985	1.0
L-B-HC-50-1	0.5	2021	2082	-608	2070	0.5
L-B-HC-70-1	0.7	2853	2988	-885	2967	0.8
L-B-HC-90-1	0.9	3950	3988	-1212	3951	1.0

Figure 4.27 shows photo macrographs of representative test surfaces after the end of the experiment (720 h of immersion). For the unmodified material loaded to $\sigma'/\sigma_\mathrm{y} = 1.0$ and 0.8, cracks up to 7 mm wide were observed in the pure bending section, i.e. region between the inner rolls (indicated by circles 1,3,4,5,6) and beneath the inner rolls (circles 2 and 7). The latter was formed possibly due to the friction between the ceramic roll and the test surface. It was noticed that some of the cracks extended towards the edge of the specimens and this can be attributed to the anticlastic bending effect, i.e. transversal contraction of the beam [207]. No cracks were detected on the surface of unmodified specimens loaded to $\sigma/\sigma_\mathrm{y} = 0.3$ and 0.5. Likewise, no cracks were observed in plasma

nitrided specimens after detailed examination (optical microscope and SEM) of the test surfaces.

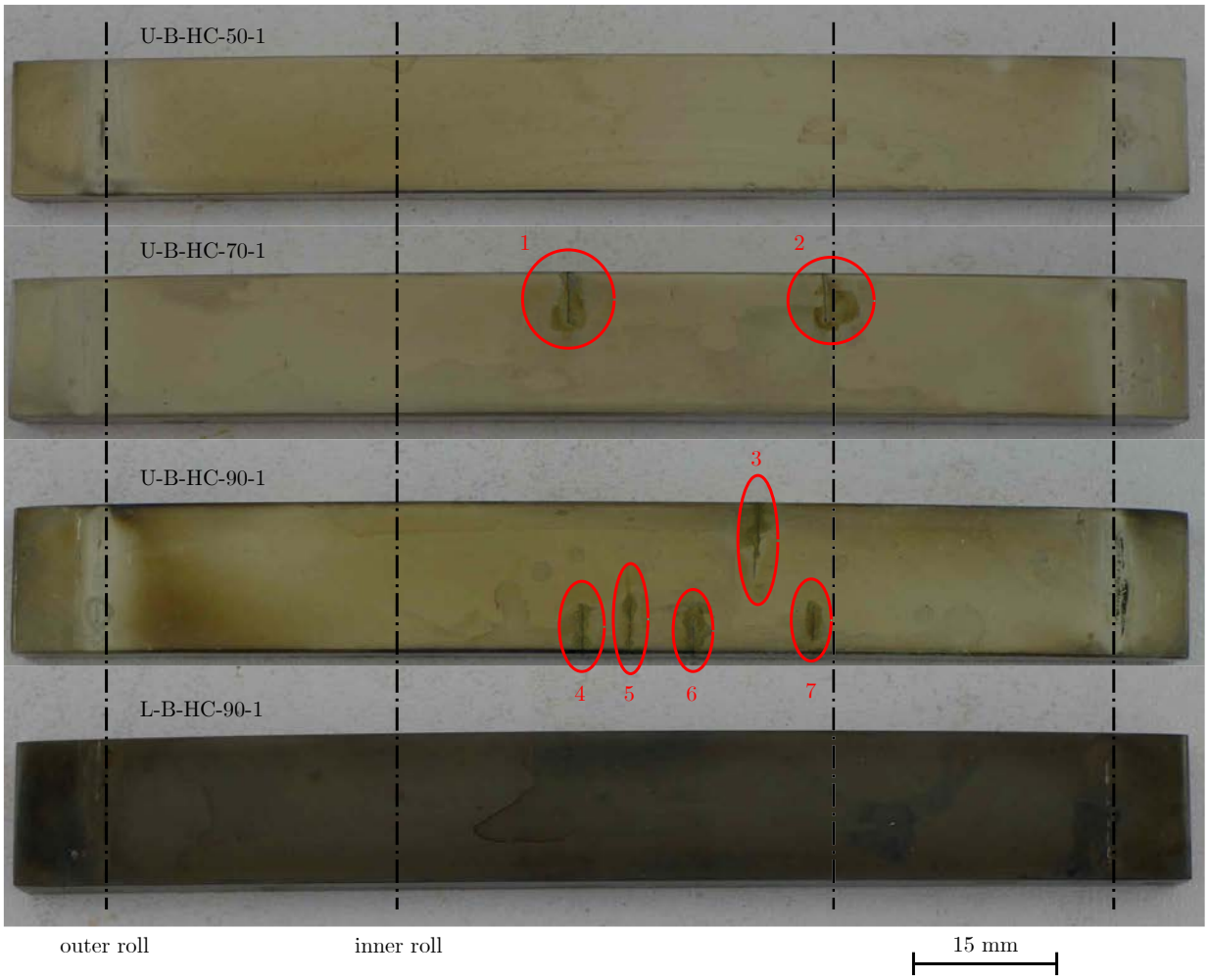

FIGURE 4.27: Macroscopic view of unmodified and LTPN 17-4 PH (H1150D) specimens after being submitted to four–point bend SSC in produced water (165 g L^{-1} NaCl and pH 4.5 ± 0.2) with pH_2S = (3.4 ± 0.1) kPa and CO_2 as balance.

Figure 4.28 shows cross sectional micrographs of typical cracks formed on the surface of unmodified specimens. Crack propagation, as shown in Figure 4.28a (specimen loaded to 90% of σ_y), was mixed intergranular and transgranular (interlath and translath). As

in the uniaxial tensile method, crack branching was also observed. Figure 4.28b (optical micrograph) shows a 1 mmd eep crack that apparently initiated from a corrosion pit (specimen loaded to 70% of σ_y).

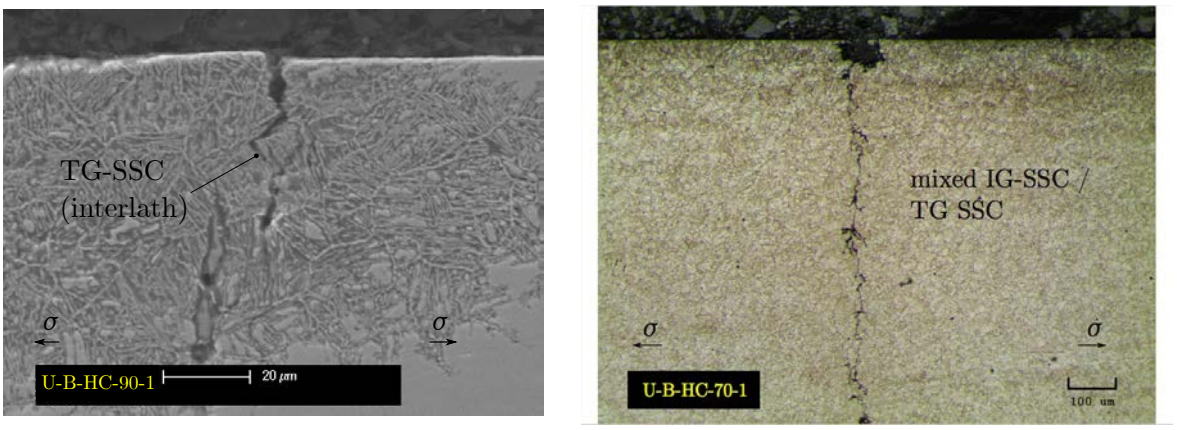

(a) (b)

FIGURE 4.28: Cross sections of unmodified 17-4 PH (H1150D) after being submitted to four–point bend SSC in produced water (165 g L^{-1} NaCl and pH 4.5 ± 0.2) with $pH_2S = (3.4 \pm 0.1)$ kPa and CO_2 as balance: (a) U-B-HC-90-1 (SEM); (b) U-B-HC-70-1 (optical microscope).

Overall, the results from the four–point bend are comparable to those of tensile SSC, except that the samples loaded to 50% of σ_y did not fail in the bending method. Besides, the uneven stress distribution across the thickness—the tensile stress is maximum at the test surface and gradually reduces towards the center line—can explain why the bending specimens did not fracture completely as occurred on SSC specimens loaded to or above 70% of σ_y. Time–to–failure was not possible to determine, since all the specimens were removed from the vessel only after the 720 hours of immersion was completed.

4.3.3 Environmental factors affecting SSC susceptibility

Sodium chloride

As discussed in section 2.2.3.3, NaCl can reduce the stability of the passive film in high–chromium stainless steels exposed to H_2S environments [149], causing localised attack and subsequent cracking. This was observed on unmodified specimens—some cracks apparently initiated from corrosion pits—but localised attack was not evident in plasma nitrided specimens, except for LTPN loaded to 90% of σ_y and exposed to H_2S–saturated solution. In this case, the high content of NaCl ($165\,g\,L^{-1}$) may have accumulated near these sites and prevented complete repassivation—passivity on these conditions is related to the stability of the film of iron sulphide [41] deposited on the surface.

4.3.3.1 Environment pH and partial pressure of H_2S

At the pH tested (4.5 ± 0.2), H_2S_{aq} is stable at $(23 \pm 2)\,°C$, according to potential/pH diagrams at room temperature [92]. Therefore, a direct reduction of H_2S_{aq} to form $H_{2(g)}$ and HS^- may have occured near the surface [208] in addition to hydrogen–ion dissociation reactions. This is expected for acidic and nearly–neutral environments. Section 2.2.3.2 presents examples of the effect of pH on SSC demonstrating that lower pH increases SSC susceptibility. The initial pH was not varied in this work and therefore its effect was not evaluated.

When the partial pressure of H_2S was increased from 3.4 kPa to $\approx$ 100 kPa (pure H_2S) to further investigate the response of LTPN specimens exposed to more severe environment, localised attack was observed and, therefore, considering that cracking could potentially nucleate from these sites, it is reasonable to conclude that the tendency to SSC increased with increasing the concentration of H_2S, in agreement with the observations presented in section 2.2.3.2.

Gas mixture

In environments containing H_2S, iron sulphide can precipitate on the metal surface [41] and CO_2—used as balance gas—tends to form Cr_2O_3 [157] and $FeCO_3$ scales [43]. In mixed H_2S/CO_2 systems, the kinetics of scale formation dictates the predominant species [156]. These scales are known to have significant influence on the corrosion resistance, but no evidence of their influence on SSC was observed in this chapter. When CO_2 was used as balance gas, no deposits of $FeCO_3$ were identified on the surface. In fact, studies [209] have shown that the temperature should be greater than 60 °C to result in supersaturation and precipitation of CO^{3-} and Fe^{2+}. Besides, in mixed H_2S/CO_2, iron sulphide is preferentially precipitated [156]. Although FeS_2 was detected on the surface of specimens after 720 h of exposure, no direct correlation between the formation of these deposits and susceptibility to SSC was observed. In pure H_2S, however, the localised corrosion observed on LTPN specimens could have been caused by insufficient coverage of the film on specific sites. In chapter 5, electrochemical investigations with mixed and pure gases are performed as an attempt to determine the role of each gas on the corrosion process.

Loading

In unmodified specimens, the effect of the load on SSC was clear: SSC susceptibility—quantified by the time to failure—increased with increasing the stress level. The results provided additional data supporting the maximum stress criteria adopted by current standard. For the modified conditions (both LTPN and HTPN), it was not possible to determine a threshold stress since none of these failed by SSC for the tested conditions. Compressive residual stresses, however, had a positive effect on SSC since it prevented cracking due to the reduced net tensile stress, as discussed in section 7.2.2.

4.4 Summary

This chapter demonstrated, by using constant–load standard test methods (uniaxial tensile and four-point bend), that the unmodified 17-4 PH (H1150D) is susceptible to SSC in typical produced water ($165\,\mathrm{g\,L^{-1}}$ of NaCl and pH 4.5 ± 0.2) with $p\mathrm{H_2S} = (3.4 \pm 0.1)\,\mathrm{kPa}$ and CO_2 as balance gas at $(23 \pm 2)\,^{\circ}\mathrm{C}$ and ambient pressure. For elevated applied stresses (70 and 90% of σ_y), unmodified specimens ruptured in less than 720 h and cracks were detected on the surface of the specimens loaded to 50%, the threshold stress for SSC to occur being therefore within 30-50% of its actual yield strength. After modifying the surface by plasma nitriding at both low and high temperature, failure by SSC did not occur for the same conditions. Likewise, no signs of failure by SSC were detected on the surface of LTPN specimens in pure H_2S, except for localised corrosion when the material was loaded to 90% of σ_y. In mixed H_2S/CO_2, HTPN exhibited lower corrosion resistance compared to LTPN, evidenced by the presence of corrosion scales on the surface—more pronounced on pre–damaged specimens.

Detailed discussion on the causes for the superior resistance to SSC after plasma nitriding, particularly for LTPN specimens, is presented in Chapter 7. In summary, the increased resistance to SSC was attributed to three main factors, further discussed in subsequent chapters: (i) localised corrosion and surface defects can be potential sites for crack initiation; (ii) plasma nitrided layer acted as a barrier that presumably reduced hydrogen uptake by the substrate; (iii) the compressive residual stress induced by the plasma nitrided treatment prevented crack nucleation and propagation.

Chapter 5

General and localised corrosion

This chapter presents the results of the general and localised corrosion resistance of the unmodified and plasma nitrided 17-4PH (H1150D). The complete set of experiments carried out in this work is summarised in Figure 5.1, highlighting the topics covered in this specific chapter.

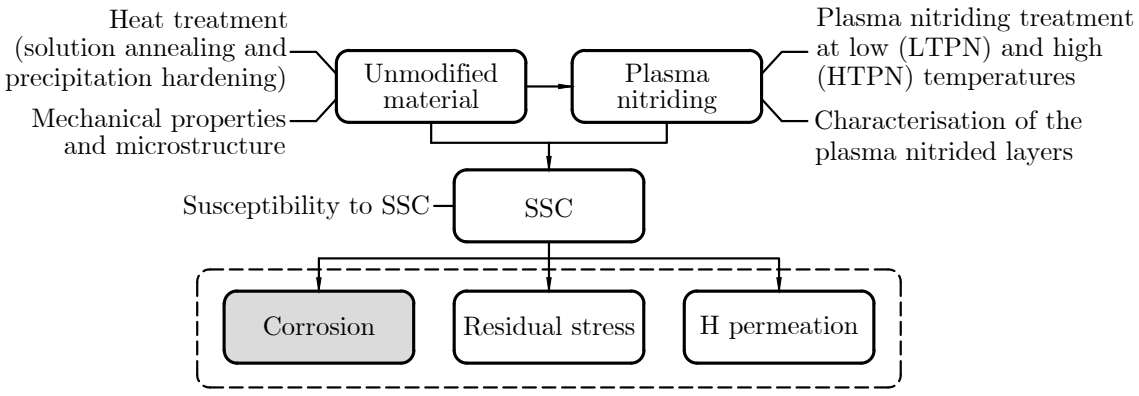

FIGURE 5.1: Schematic diagram summarising the topics covered in this chapter (highlighted in grey) within the complete experimental context of this work.

5.1 Experimental design

5.1.1 Objective of the corrosion experiments

Previous chapter demonstrated that the 17-4 PH at the H1150D condition is highly susceptible to SSC and that plasma nitriding at low temperature can effectively prevent SSC for the tested conditions. The resistance to general and localised corrosion was identified as one of the factors influencing the SSC susceptibility and electrochemical techniques were used to further investigate it, exposing the material to the same environments used on the SSC tests.

5.1.2 Selection of the test parameters

The material was exposed to the same test solution (simulated produced water with $165\,\mathrm{g\,L^{-1}}$ NaCl and pH 4.5 ± 0.2) and gas mixture ($p\mathrm{H_2S} = (3.4 \pm 0.1)\,\mathrm{kPa}$ with $\mathrm{CO_2}$ as balance and pure $\mathrm{H_2S}$) used in SSC experiments. The temperature and pressure were also maintained, i.e. $(23 \pm 2)\,^{\circ}\mathrm{C}$ and atmospheric pressure. Additional measurements with $\mathrm{CO_2}$–saturated solution were used as an attempt to determine the role of $\mathrm{CO_2}$ on the corrosion process. Moreover, an additional investigation into low-temperature plasma nitrided specimens was carried out, to further understand the corrosion mechanisms.

5.1.3 Selection of the test method

One of the elctrochemical methods selected to evaluate the corrosion resistance was the cyclic potentiodynamic polarisation technique. This is one of the most used techniques to characterise localised corrosion response of metals in aqueous solutions [210]. It consists of measuring the current density in response to applied potentials varying from slightly below the open circuit potential (OCP) until a predetermined current density is reached.

In a given electrolyte, OCP is continuously measured and the electrochemical readings are taken after a steady-state condition is established.

Figure 5.2 shows a typical potentiodynamic scan of stainless steels susceptible to localised (pitting) corrosion identifying the main regions and points of interest. In this case, the horizontal axis is the logarithm of the current density and the vertical axis is the potential. From A to B, the material is polarised cathodically until the corrosion potential E_{corr} is reached (point B)—at this point the rate of the cathodic reaction (e.g. hydrogen ions being consumed at the surface to form hydrogen gas: $2\,H^+ + 2\,e^- \longrightarrow H_2$) equals the rate of the anodic reaction (e.g. oxidation of iron to form ferrous ion: $Fe \longrightarrow Fe^{2+} + 2\,e^-$). The interception between the anodic and cathodic curves (it requires extrapolation, as shown in the experimental procedures section), corresponds to the corrosion current density, i_{corr}, which can be used to estimate the corrosion rate of the metal.

From B to C (Figure 5.2), the material undergo anodic dissolution (general corrosion) and the corrosion rate increases until it reaches the passivating potential E_{pp} (point C), corresponding to the critical current i_{pp}. From this point, a further increase in potential does not affect the current density and therefore the corrosion rate is negligible. This effect—typical in stainless steels—is due to the formation of passive film of chromium oxide that acts as a barrier for the corrosion species.

Passivation (from point C to point D in Figure 5.2) is compromised when the protective film is locally damaged and the substrate material is exposed to the electrolyte, resulting in pitting corrosion. Rapid dissolution, i.e. rapid increase on the corrosion current density, occurs from the onset of pitting at E_{p}, the pitting corrosion potential (point D), until the pre determined limiting (or vertix) current density (point E) is reached. Before continuous growth, metastable pitting can occur due to repeated nucleation and repassivation of small pits [211]. This effect is reflected on fluctuations of the potential and current density

near E_{p}. Once the vertix current is achived, the scan can be reverted—starting from E, forming an hysteresis loop closing at F—and it can be used to obtain information about the repassivation behaviour. When the reverse sweep intersects the forward scan (point F, referred as re-passivation potential, E_{rp}, or protection potential, E_{rp}), re-passivation occurs. This potential is often used as a design parameter, assuming that stable passivation will occur if the potential is kept below this point. But there are controversies in adopting E_{rp} a protective criteria, as indicated in the literature [212], since repassivation is associated with many conditions necessary to maintain an aggressive electrolyte inside the pits, which are linked with, for example, pit geometry and scan rate. Therefore, the reverse scan is not performed in some studies.

Potentiodynamic polarisation is an accelerated test and has limitations, mostly related with the proper determination of film breakdown. Despite that, the electrochemical parameters obtained from the polarisation sweep are good indicators of localised corrosion tendency (quantified by critical potentials) for particular metal/environment systems and therefore this technique was considered appropriate for the purpose of this work.

A second method selected to further investigate the corrosion of low-temperature plasma nitrided specimens is the electrochemical impedance spectroscopy (EIS), or AC (alternating current) impedance. This is a technique that determines the response from an electrochemical system to small amplitude sinusoidal perturbations on the potential and it is based on the relationship between current and voltage—approximated as linear (pseudo linear) due to the small amplitude of the signal, typically from 5-10 mV. It is sensible, non-destructive technique that can be used to provide information about complex systems, such as coated metals [213]. This was found to be particularly useful in this work because when the material is exposed to H_2S–CO_2–NaCl systems, different corrosion products can be formed resulting in additional corroding interfaces. Equivalent

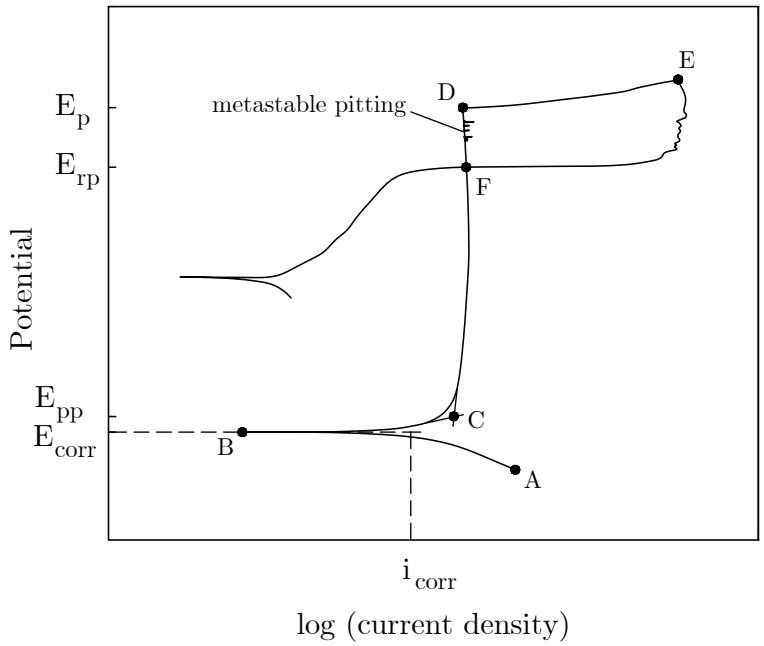

FIGURE 5.2: Schematic representation of typical cyclic potentiodynamic scan of stainless steels susceptible to pitting corrosion.

electrical circuits are often used as a tool to interpret the data, provided that adequate correspondence is made between the elements in the circuit and the physical system being investigated.

Analogously to the Ohm's law for an ideal resistor, the impedance $Z(\omega)$—which measures the effective resistance of the element considering the effects of applied alternating current—can be expressed by the ratio between the time–dependent potential $E(t)$ with amplitude E_0 and the corresponding time–dependent current $i(t)$ with amplitude i_0, in which $\omega = 2\pi f$ is the radial frequency of the signal (f being the frequency) and ϕ is the phase shift between $E(t)$ and $i(t)$ [214]:

$$Z(\omega) = \frac{E_0 \sin(\omega t)}{i_0 \sin(\omega t + \phi)} \tag{5.1}$$

Due to the complexity of the response to an alternating signal, it is convenient to express the impedance as [214]:

$$Z(\omega) = Z'(\omega) + \mathrm{j}Z''(\omega) \tag{5.2}$$

where $Z'(\omega)$ is the real part, $Z''(\omega)$ is the imaginary part (following standard terminology [215]) and j is the imaginary number ($\mathrm{j}^2 = -1$). These quantities are plotted using a rectangular coordinate system (complex plane) in which the impedance for each frequency is represented by a vector oriented with an angle ϑ with the real axis, the so-called Nyquist plot, schematically represented in Figure 5.3a—the arrow indicates the direction of increasing frequency. In this example, which represents the corrosion of a surface exposed to an electrolyte, a single impedance arc was formed in the Nyquist plot, indicating that only one corroding interface is involved, i.e. the system has only one time constant. The equivalent electric circuit that can represent this system is shown in Figure 5.3c. It consists of a resistor R_s representing the resistance of the electrolyte, a capacitor C_dl with capacitance C and impedance $Z(\omega) = -1/\mathrm{j}\omega C$ representing the capacitance at the electrolyte/metal interface (double-layer capacitance) and the charge-transfer resistance of the metal, R_t (assuming that mass transfer is negligible). By associating these elements, the impedance of the system can be obtained.

The Nyquist plot (Figure 5.3a) do not display the frequency dependency for each impedance and therefore Bode plots ($\log |Z|$ and ϕ versus $\log f$) are used to complement the analysis. From these plots it is possible to determine the frequency domains that are being dominated by resistive or capacitive behaviours. At high frequencies (considering the hypothetical plot shown in Figures 5.3b and 5.3c), the current flows through the capacitor C_dl and the impedance is dominated by R_s ($\omega \to \infty$, $\phi \to 0$ and $|Z| = R_\mathrm{s}$). At

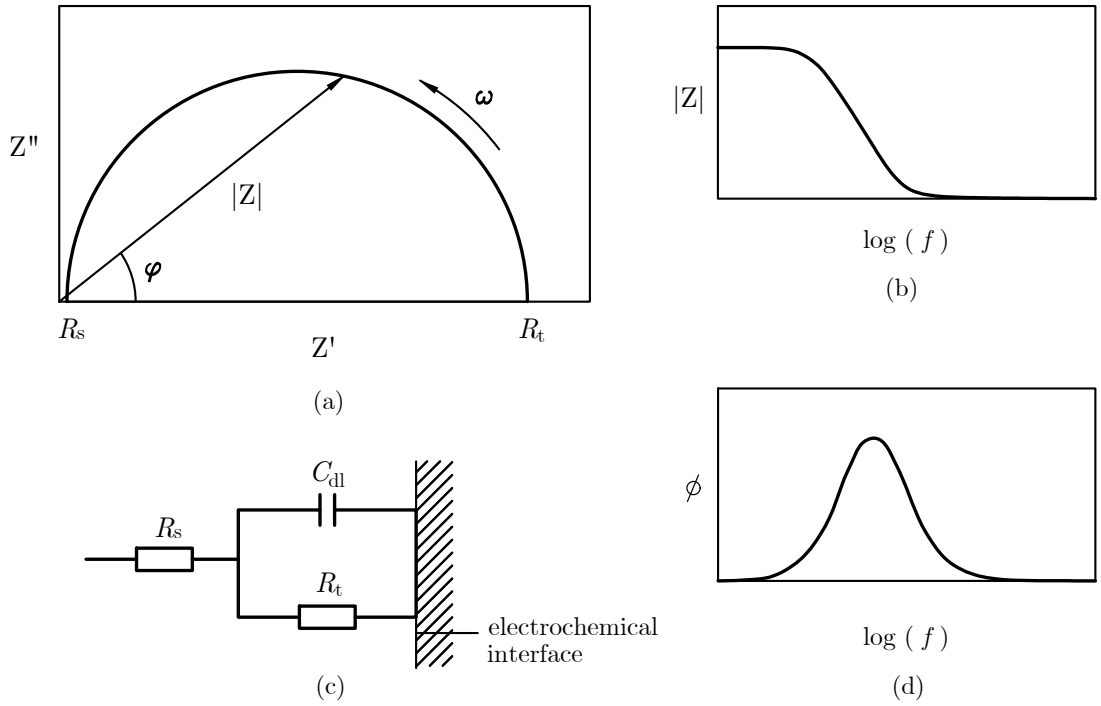

FIGURE 5.3: Schematic representation of typical (a) Nyquist plot, (b and d) Bode plots and (c) equivalent electrical circuit used to analyse electrochemical impedance spectroscopy data.

low frequencies, current flows through R_s and R_t and the capacitance is real and equal to $|Z| = R_s + R_t$ ($\omega \to 0$, $\phi \to 0$). A capacitive behaviour is observed in the intermediate frequency range, characterised by a slope of $\log |Z|/\log f$ = - 1 (assuming that it is purely capacitive) and a phase shift approaching ± 90°.

The polarisation resistance, that characterises the resistance of the metal, can then be determined from the difference between the impedance at low frequency $Z(\omega \to 0) = R_s + R_t$ and at high frequency Z_s ($\omega \to \infty$) = R_s. Large semicircles represent larger polarisation resistance and therefore higher corrosion resistance (lower i_{corr} and thereby lower corrosion rate). In coated samples, other elements may be considered and multiple semi circles can be seen. More details about fitting the experimental data to equivalent

electrical circuits is shown in the results section.

5.1.4 Overview of the experiments

Table 5.1 shows an overview of the experiments conducted in this chapter, with all the parameters—as detailed in section 5.1.2—being the same as those used to evaluate SSC. Potentiodynamic polarisation scans were carried out on unmodified and plasma-nitrided specimens (low-temperature plasma nitrided, LTPN, and high-temperature plasma nitrided, HTPN) immersed in mixed H_2S/CO_2 ($pH_2S = (3.4 \pm 0.1)$ kPa with CO_2 as balance), pure H_2S—except for the HTPN—and pure CO_2. Electrochemical impedance spectroscopy was carried out on LTPN specimens for different times of exposure to mixed H_2S/CO_2 with the same partial pressures used in the polarisation experiments.

TABLE 5.1: Overview of the experiments conducted to evaluate the corrosion resistance of the unmodified and plasma nitrided (LTPN and HTPN) 17-4 PH (H1150D).

Condition	**Potentiodynamic polarisation**			**Impedance spectroscopy**
	H_2S/CO_2	CO_2	H_2S	H_2S/CO_2
Unmodified (H1150D)	✓	✓	✓	-
LTPN	✓	✓	✓	✓
HTPN	✓	✓	-	-

5.2 Experimental procedures

5.2.1 Potentiodynamic Polarisation

Specimens

Coupons with $(15 \times 15 \times 5)$ mm were cut from a $(500 \times 800 \times 13)$ mm plate, as illustrated in Figure 5.4, so that the test surface coincided with that used on the SSC experiments. Unmodified specimens were ground with successively finer abrasive papers (up to 600 grit SiC or P1200), degreased, cleaned with acetone and dried with air. Plasma nitrided (both LTPN and HTPN) specimens were prepared following the procedure described in section 3.1.2.3. The surfaces of the working electrodes were covered with an epoxy resin and 1 cm^2 was left uncoated on the test face. A copper wire was spot welded to one side of each electrode and fitted in a plastic or glass tube. Careful was taken when applying the resin to avoid crevice corrosion—specimens were left for 24 hours with the test face upwards for complete settlement of the paint.

Experimental procedure

All the corrosion measurements were performed by using a Gill AC potentiostat (ACM Instruments) connected to a three-electrode electrochemical cell (2 L glass vessel) containing one working (specimen), one counter (platinum-plated niobium electrode) and one reference (standard calomel – SCE) electrode, as illustrated in Figure 5.5a. The working electrode was connected to the vessel via a salt bridge filled with 1M potassium chloride solution and closed in one end with agar. For the impedance spectroscopy measurements, due to the low current (below 1 µA) and high frequency signals, a Faraday cage was designed to reduce the power-line noise. To avoid leaking, thread sealant was

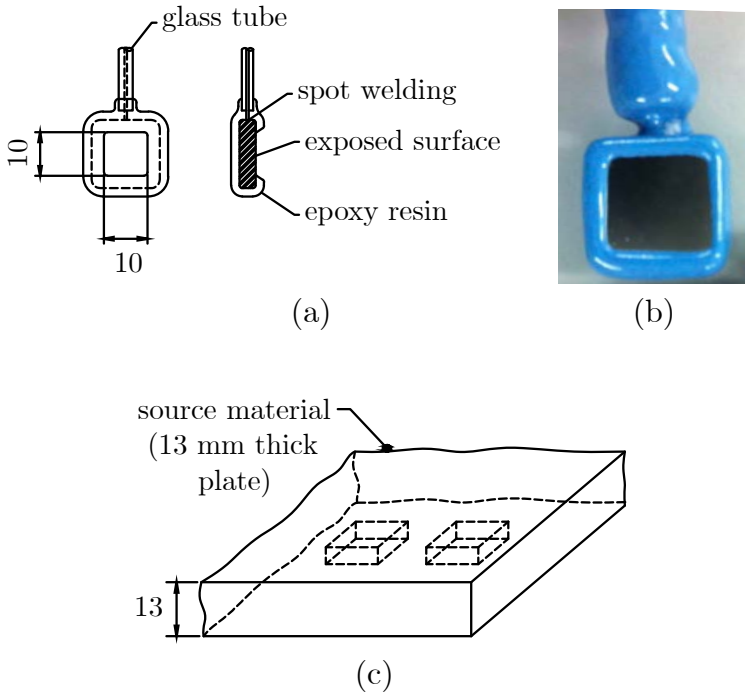

FIGURE 5.4: Corrosion coupons used on electrochemical experiments: (a) schematic; (b) picture of typical electrode; (c) cut positions from the source material. Dimensions in mm.

applied in all threaded joints and H_2S–resistant rubber seals were fitted in the lid and pressed into the top of the vessel. Prior to each test, the glass cell was degreased.

In both potentiodynamic scans and EIS, the test solution ($165\,\mathrm{g\,L^{-1}}$ of NaCl in deionised water) was prepared following the same procedure described in section 4.2.1. CO_2 gas was continuously purged through the mixture for 60 minutes and the pH adjusted to 4.5 ± 0.2 by adding sodium bicarbonate ($NaHCO_3$). The test vessel was then sealed and a leak test was performed. The solution was de-aerated with nitrogen for 90 minutes at a constant flow rate (specify) and the test gas (H_2S, CO_2 or mixed H_2S/CO_2) was switched on at 1 L min for 60 minutes (saturation stage) and the flow was reduced to a few bubbles per minute.

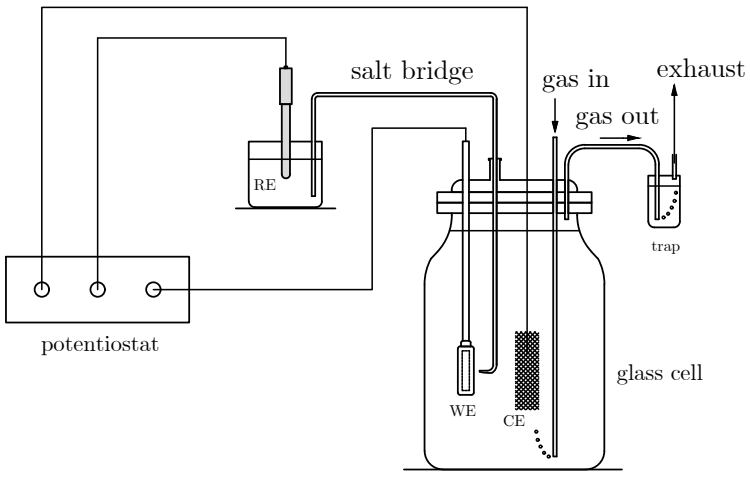

FIGURE 5.5: Schematic diagram of the setup used on the electrochemical measurements. The Faraday cage is not represented.

In the potentiodynamic test, the open circuit potential was continuously measured during the de-aeration stage with N_2 and during the 20 hours of exposure to the test gas—this time frame was selected for being sufficiently long to achieve a nearly steady–state condition. After stabilisation, the forward scan (positive direction of the potential) started from $-50\,\mathrm{mV}$ offset relative to the open circuit potential and progressed at $0.16\,\mathrm{mV\,s^{-1}}$ (typical scan rate recommended for cyclic potendiodynamic measurements [216]) until the current density reached $5 \times 10^{-2}\,\mathrm{mA\,cm^{-2}}$. Additional readings were taken with larger limiting currents ($1 \times 10^{-1}\,\mathrm{mA\,cm^{-2}}$ and $1\,\mathrm{mA\,cm^{-2}}$).

The corrosion rate was determined from the potentiodynamic sweeps by using the polarisation resistance technique. Due to the semi-log linearity between the applied potential and the rate of reaction (expressed by the current density through the working electrode), the slopes of the curves E (potential) versus i (current density) were used to approximate the corrosion kinetics, following the mixed–potential theory. It was assumed that the corrosion is activation–controlled (mass transport is negligible) by either

cathodic or anodic charge transfers in the vicinity of the corrosion potential. The slope of the curves near the linear portion (±20 mV from the corrosion potential), assuming a corroding condition, is given by [217]:

$$\left.\frac{d\eta}{di}\right|_{i\to 0} = \frac{\beta_a \beta_b}{(2.3)\,(i_{corr})\,(\beta_b + \beta_a)} \tag{5.3}$$

where η is the charge transfer overpotential (difference between the polarisation potential E and the corrosion potential E_{corr}), β_a and β_b are the Tafel slopes (anodic and cathodic portion, respectively) and i_{corr} is the corrosion current. The left side of Equation 5.3 represents the polarisation resistance, R_p, following the Ohm's law. R_p, β_a and β_c were determined experimentally from the polarisation curves, as illustrated in Figure 5.6—at least one decade of current was considered for determining the Tafel slopes. Since i_{corr}—current density at the equilibrium (open circuit) potential—cannot be directly measured, it was estimated by using Equation 5.3.

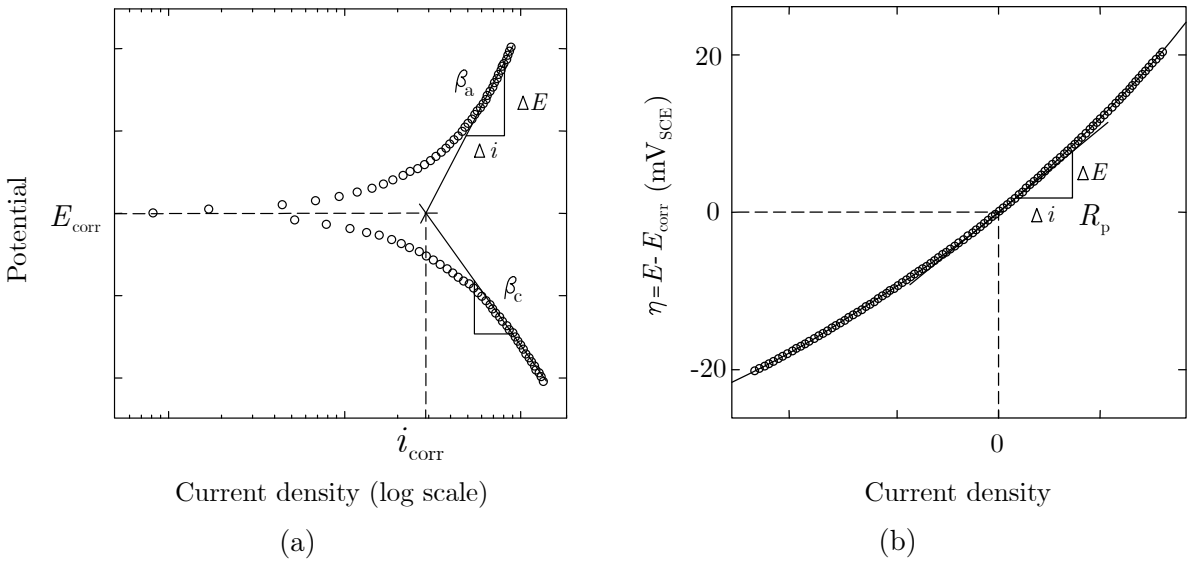

FIGURE 5.6: Schematic representation of the procedure used to obtain: (a) Tafel slopes β_a and β_c and (b) polarisation resistance R_p.

The corrosion rate, CR (in mm per year) was then estimated by using Equation 5.4 [218], based on Faraday's law, which states that the electrochemical dissolution of one gram equivalent weight of metal involves the charge transfer of one Faraday ($\approx$ 96,487 Coulombs). In this equation, K_1 is a constant ($3.27 \times 10^{-3}\,\mathrm{mm\,g\,\mu A^{-1}\,cm^{-1}}$ per year) that represents the mass loss per unit of current and unit of area considering one year of charge transfer, ρ is the density in $\mathrm{g\,cm^{-3}}$ and EW is the equivalent weight of the alloy, calculated as follows: $EW = 1/\left(\sum nf/W\right)$, n being the valence, f the mass fraction and W the atomic weight of each element (only elements with more than 1 percent in mass were considered, following standard practice [218]: Cr, Ni, Cu and Fe). The use of penetration rate may not be adequate for materials that exhibit a passive behaviour due to localised corrosion, although this is an useful parameter recommended by ASTM G102 [218] for most engineering alloys that makes the results from different work comparable.

$$CR = K_1 \frac{i_{\mathrm{corr}}}{\rho} EW \tag{5.4}$$

In EIS experiments, the amplitude of the AC signal was set to 10 mV rms with respect to the open circuit potential and the frequency spectrum applied to the cell varied from 10 kHz to 1 mHz. These values were selected based on screening tests with different amplitudes (from 5 to 15 mV), frequencies (from 0.1 mHz to 100 kHz) and on the guidelines from technical reports [219, 220]. The readings were taken at different times of exposure (from 5 to 21 hours). The open circuit potential was continuously measured during the intervals of the EIS scans, which lasted $\approx$ 4 hours when the number of readings per test was set to 50.

5.3 Results and discussion

In this section, the numbering scheme presented in Figure 5.7 is used to identify the specimens used in the electrochemical experiments. Particular cases (i.e. alternative limiting currents) are clearly identified.

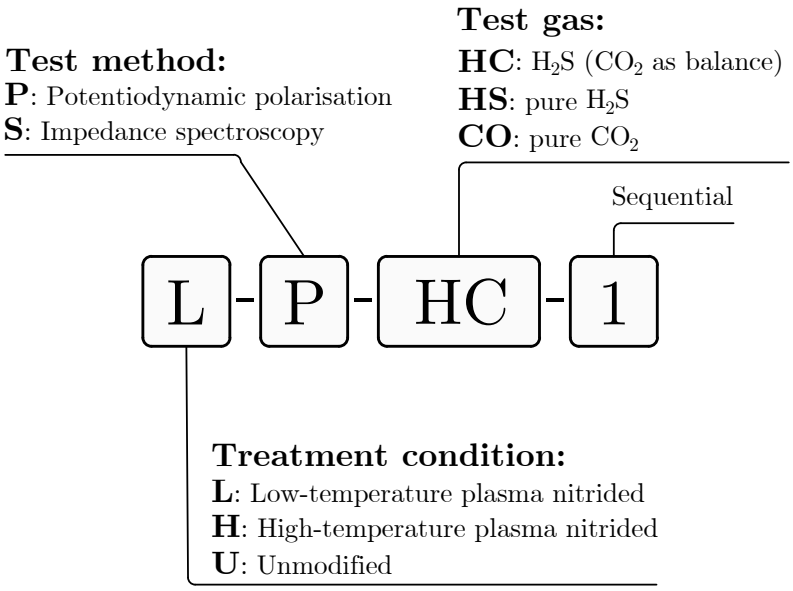

FIGURE 5.7: Numbering scheme used to identify the samples used in the electrochemical experiments

The following sections present the results from potentiodynamic scans in each tested environment. A summary of the electrochemical data is shown in Table 5.2 (section 5.3.4).

5.3.1 Potentiodynamic polarisation (H_2S/CO_2)

Unmodified specimens

Figure 5.8 shows the variations of the open circuit potential with immersion time when the unmodified material (specimen U-P-HC-3) was exposed for 21 hours to simulated produced water with $pH_2S = (3.4 \pm 0.1)$ kPa and CO_2 as balance. During the deaeration stage with N_2, the open circuit potential continuously dropped towards less noble potential, implying lower corrosion resitance associated with the reduction of the concentration of oxygen. This decay, also observed in studies investigating the effects of oxygen on the passivity of Fe-Cr alloys [221], suggests that the loss of the protective characteristics of the chromium oxide film with decreasing the concentration of oxygen could be due to a change in the film composition and it does not involve film breakdown. After the dearation was completed, the H_2S gas was turned on (immersion time = 0), and the potential increased abruptaly towards more positive potential, suggesting that a passive layer of iron sulphide was instantly formed (as previously observed [222]) and affected the potential at the metal/solution interface. After reaching a peak at -475 mV in 30 minutes of immersion, the potential decreased monotonically in two stages: a rapid drop of 50 mV in 45 minutes followed by a slow decrease towards a potential plateau (quasi-equilibrium condition) of -545 mV. The reduction on the potential suggests that the film of iron sulphide is unstable and not sufficient to maintain a passive condition, possibly due to poor surface coverage.

The polarisation scan (specimen U-P-HC-3), taken after 21 hours of immersion is shown in Figure 5.9. Three distinct regions can be identified by analysing the data: an active region (from E_{corr} to point A), a passive zone (from A to B) and breakdown of the protective film (from B, the pitting potential E_p, until the maximum current was reached). In the active stage, the corrosion rate (expressed by the current density) first

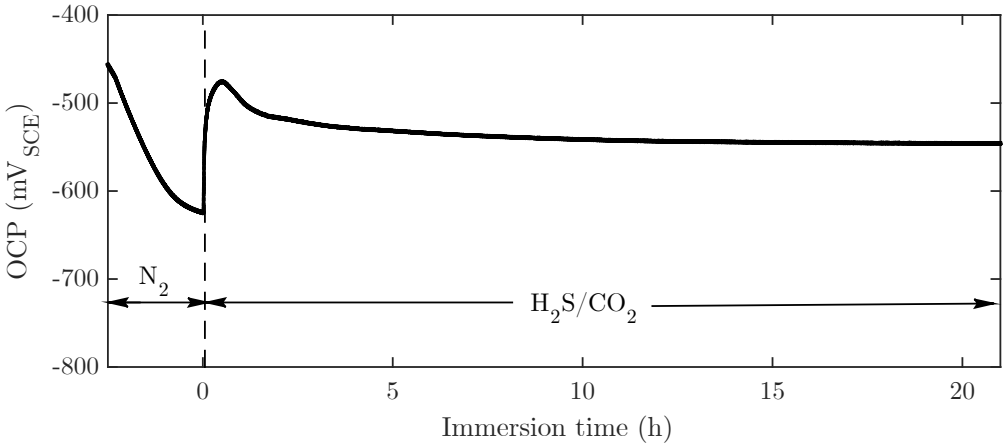

FIGURE 5.8: Variations of the open circuit potential with immersion time (up to 21 hours) for the unmodified 17-4 PH (H1150D) immersed in produced water (165 g L^{-1} NaCl and pH 4.5 ± 0.2) with pH$_2$S = (3.4 ± 0.1) kPa and CO_2 as balance. Specimen U-P-HC-3.

increased linearly with increasing the potential and reached a maximum at the inflection point (A) separating the active from the passive state (from ≈ -510 mV to ≈ -375 mV), in which the current did not change notably with increasing the voltage. Breakdown of the passive film occurred when the potential reached ≈ -510 mV (inflection point B), corresponding to the onset of pitting corrosion. By further increasing the potential, the current density—and thereby the corrosion rate—increased linearly until the reverse current density (5×10^{-2} mA cm^{-2}) was reached and the scan terminated. This behaviour can also be an indicative of crevice corrosion, observed in selected electrodes—especially when the limiting current was increased.

Additional readings were taken with larger limiting current density (1×10^{-1} mA cm^{-2}), resulting in polarisation curves with similar shape as in Figure 5.9, except for the extended dissolution after film breakdown until the new limit was reached. Reverse scan, performed on selected specimens (Figure 5.13b), resulted in positive hysteresis loops (current density of the reverse scan is higher than that of the forward scan for every anodic potential until

it repassivates—interception of the reverse scan with the forward scan), which is indicative of pitting corrosion. The polarisation resistance and the Tafel slopes were determined as described in the experimental procedures, section 5.2.1.

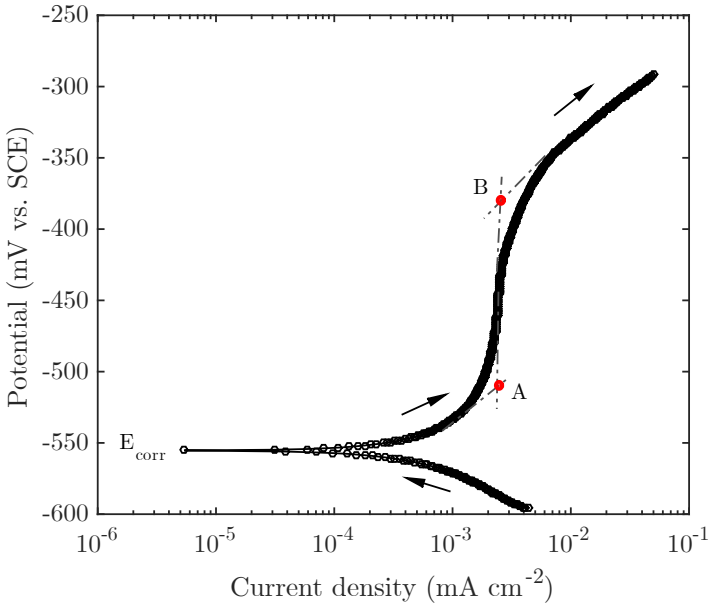

FIGURE 5.9: Potentiodynamic polarisation scan of unmodified 17-4 PH (H1150D) taken after 21 hours of immersion in produced water ($165\,\mathrm{g\,L^{-1}}$ NaCl and pH 4.5 ± 0.2) with $p\mathrm{H_2S} = (3.4 \pm 0.1)\,\mathrm{kPa}$ and $\mathrm{CO_2}$ as balance. Specimen U-P-HC-3.

After the polarisation sweep (with limiting current density of $5 \times 10^{-2}\,\mathrm{mA\,cm^{-2}}$), shallow circular pits (5 to 100 µm wide) were observed near the centre of the working electrodes (specimens U-P-HC-1,2 and 3). These pits were presumably generated by a film breaking mechanism due to accumulation of chloride ions on their bases, which inhibited further repassivation and allowed them to grown. Although being difficult to provide supporting evidence for that mechanism since the specimens were immediately cleaned after the tests (comprehensive investigation requires in situ observations), this assumption seems reasonable because NaCl deposits were identified in deeper pits (e.g. in pure $\mathrm{CO_2}$, Figure

5.18a), even after cleaning. As discussed in the next paragraphs, it seems that deposits of FeS_2 contributed to nucleation and growth of some of the pits.

Figure 5.10a shows typical circular pits with approximately 40 µm. A closer look at the bottom of the pit (Figure 5.10b) implied that the chromium oxide film was removed and features from the corroding substrate were revealed: grain boundaries and nearly-parallel laths of martensite.

When the limiting current was increased to $1 \times 10^{-1}\,\mathrm{mA\,cm^{-2}}$, the morphology of the pits changed and crevice corrosion was observed at the resin/metal interface of some specimens. Perforated pits (Figure 5.10c), typical of stainless steels, were formed at the centre of the specimen U-P-HC-1 by the following mechanism [223]: (i) at an early stage, passive film breaks and pit grows with a hemispherical shape; (ii) repassivation occurs near the mouth of the pit (opening at the top surface) where the concentration of Fe^{++} is low whereas further dissolution occurs on the side walls; (iii) preferential dissolution on the sides then develops an undercut (the width of the pit is larger than the mouth) while the cover (on the top of the pit) remains partially passivated, giving this porous appearance—the top film can break when a critical size is achieved and the bottom of the pit is covered with salt, which acts as a barrier for the diffusion of corrosion species. In this case, the barrier was enhanced by the accumulation of FeS_2 on the centre of the pit, as the sulphur content was elevated on this position (16 wt.%, obtained by EDS, Figure 5.10e). This effect was experimentally verified in recent studies [224]. For those pits with an annular shape (Figure 5.10d), a deposit of FeS_2 possibly acted as an initiation site—in this case, the sulphur content on the centre of the pit was 14 wt.%, according to the EDS spectrum in Figure 5.10f. This observation agrees with previous findings [225, 226].

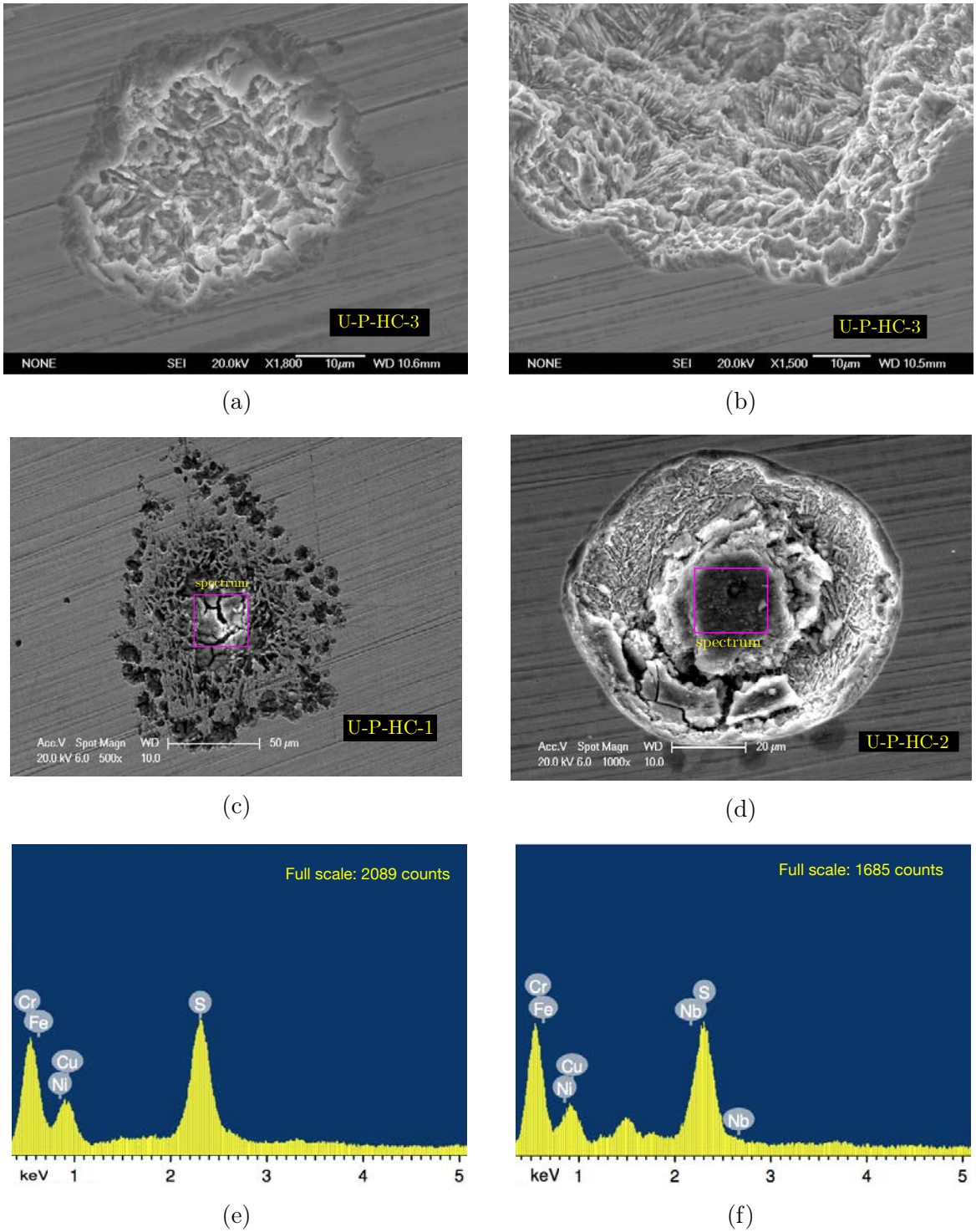

FIGURE 5.10: SEM micrographs (top view) of the unmodified 17-4 PH (H1150D) after the potentiodynamic scans taken following 21 hours of immersion in produced water with $pH_2S = (3.4 \pm 0.1)$ kPa and CO_2 as balance: (a-b) specimen U-P-HC-3 (limiting current density of 5×10^{-2} mA cm^{-2}) and (c-d) specimens U-P-HC-1 and 2 (limiting current 1×10^{-1} mA cm^{-2}); (e) EDS spectrum of U-P-HC-1; (f) EDS spectrum of U-P-HC-2.

HTPN and LTPN specimens

The open circuit potentials of low and high-temperature plasma nitrided specimens (L-P-HC-1 and H-P-HC-1), immersed for 21 hours in simulated produced water with $pH_2S = (3.4 \pm 0.1)$ kPa and CO_2 as balance, are shown in Figure 5.11. Similar to the unmodified condition, the potential of both HTPN and LTPN continuously decreased during deaeration and increased shortly after the test gas was turned on (time = 0). In both cases, the potential was nearly constant after approximately 2 hours of immersion and reached stable values of −675 mV (HTPN) and −585 mV (LTPN) after 21 hours of exposure. The potential of the HTPN condition shifted towards less noble potential, suggesting lower corrosion resistance compared to the LTPN. Comparing these potentials with that of the unmodified material (−475 mV), both plasma nitrided electrodes seemed to be less thermodynamically stable, thereby more susceptible to corrosion—both had less noble OCP, HTPN having the lowest stability.

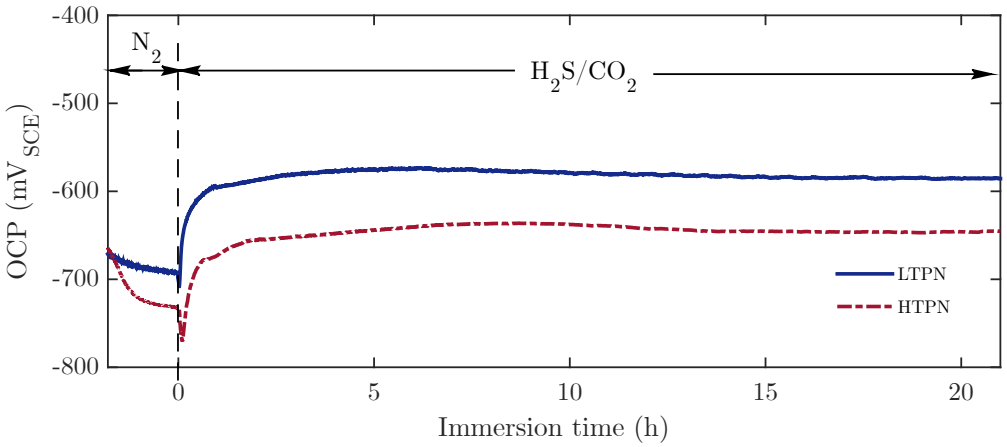

FIGURE 5.11: Variations of the open circuit potential with immersion time for the high (HTPN, specimen L-P-HC-1) and low–temperature plasma nitrided (LTPN, specimen L-P-HC-1) 17-4 PH (H1150D) exposed to produced water with $pH_2S = (3.4 \pm 0.1)$ kPa and CO_2 as balance for 21 hours.

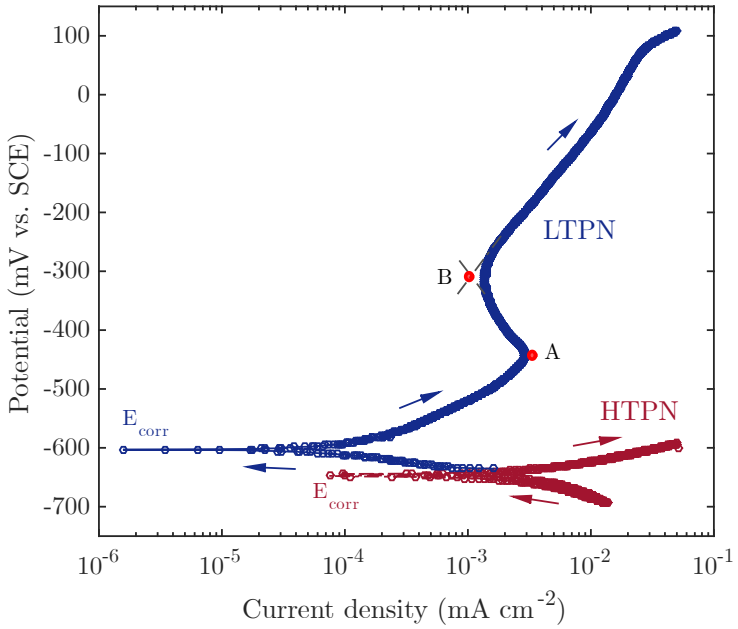

FIGURE 5.12: Potentiodynamic polarisation scans of high (HTPN, specimen H-P-HC-1) and low–temperature plasma nitrided (LTPN, specimen L-P-HC-1) 17-4 PH (H1150D) taken after 21 hours of immersion in produced water with $pH_2S = (3.4 \pm 0.1)$ kPa and CO_2 as balance.

The shapes of the potentiodynamic curves, shown in Figure 5.12 (specimens L-P-HC-1 and H-P-HC-1), indicated different responses when the material was plasma nitrided at high and low temperature: HTPN specimens did undergo anodic dissolution with no passivation whereas LTPN showed a passive behaviour. The absence of passive region on the HTPN condition suggested that a protective film was not formed at the surface after the plasma nitrided treatment and therefore general dissolution occurred—rather than localised corrosion—until the limiting current (5×10^{-2} mA cm^{-2}, Figure 5.12) was reached. Besides, when the scan was reverted, it followed nearly the same path of the forward scan, i.e. the current densities in both directions nearly coincided for any anodic potential, implying absence of localised attack as no hysteresis loop was formed.

For the LTPN condition, anodic dissolution reached a maximum at -450 mV (point

A in Figure 5.12). From this point, the current decreased with increasing the potential, resulting in a passive state from −450 mV to −300 mV (point B). The short passive region can be due to the formation of a weak film (presumably iron sulphide or a nitrogen-rich layer near the surface) not capable of sustaining the protective characteristics (with increasing the potential) due to the small thickness and low surface coverage. By further increasing the potential to beyond the pitting potential (point B), anodic dissolution occurred at a rate similar to that of the unmodified material.

Based upon the results from the potentiodynamic scans, the LTPN condition is less susceptible to pitting corrosion compared to the unmodified material due to its higher pitting potential ($E_p = -300$ mV, Figure 5.12) compared with −375 mV of the unmodified material (Figure 5.9). Besides, when the reverse scan—performed on selected specimens (see typical curves shown in Figure 5.13)—is included in the analysis, the repassivation potential of the LTPN specimens ($E_{rp} = -350$ mV, Figure 5.13a) is higher than that of the unmodified material (< -450 mV, Figure 5.13b). The point A indicated in both graphs corresponds to the reverse current.

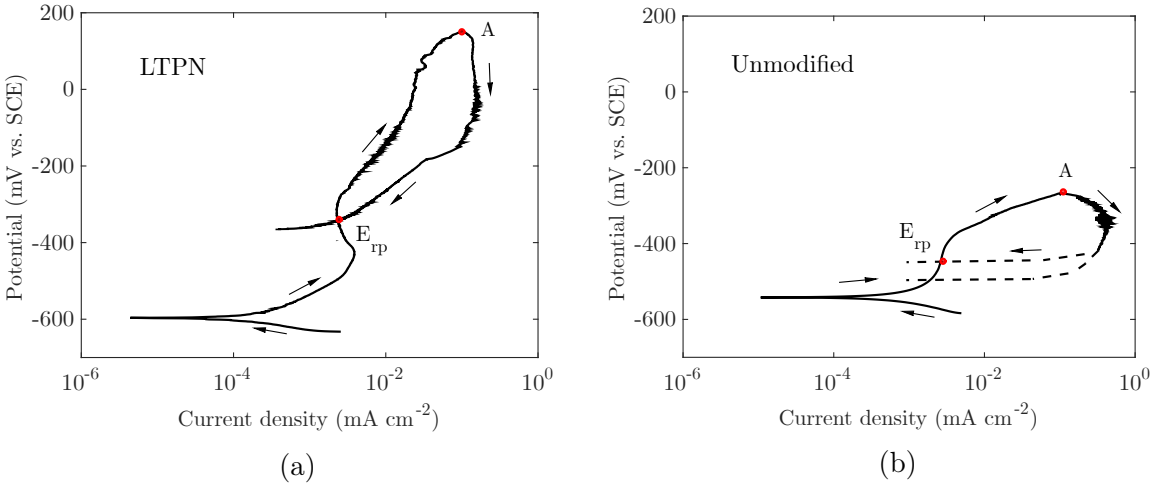

FIGURE 5.13: Reverse potentiodynamic polarisation scans of (a) LTPN and (b) unmodified 17-4 PH (H1150D) taken after 21 hours of immersion in produced water with $pH_2S = (3.4 \pm 0.1)$ kPa and CO_2 as balance.

Even though the corrosion potential, E_{corr}, of the LTPN material was less noble than that of the unmodified (suggesting lower corrosion resistance), the corrosion current was lower on the LTPN electrodes ($i_{\text{corr}} = 0.9 \times 10^{-4}\,\text{mA}\,\text{cm}^{-2}$, 4 times lower than the unmodified, see Table 5.2). The passivating current (i_{pass}, point A in Figures 5.9 and 5.12), however, was slightly higher on the unmodified material and the same occurred for their corresponding passivating potentials i_{pass} (Table 5.2). This makes it difficult to define the material with superior corrosion characteristics (LTPN or unmodified), although the best resistance to pitting corrosion seems to be a positive aspect in favour of the LTPN, as localized attack could be potential site for crack initiation. To clarify this, the morphologies of the surfaces were examined.

Figure 5.14 shows the SEM images (top view) of the exposed surfaces of the working electrodes after 21 h of immersion in the test environment. All the images agree with the potentiodynamic polarisation results, as described in the next paragraphs.

Typical micrograph from HTPN specimens (Figure 5.14a) shows that general corrosion occurred on the surface, as no pits were identified. EDS analysis revealed different sulphur contents in the darker (1.6 wt.%) and brighter (0.6 wt.%) areas, indicating poor surface coverage of FeS_2—insufficient to provide passivation, in agreement with the potentiodynamic scans. By analysing the size and distribution of the darker areas, it appears that iron sulphide formed preferentially along prior austenite grain boundaries, approximately 20 µm wide.

As predicted in the potentiodynamic scans, localized corrosion ocurred on the centre of LTPN electrodes, as shown in Figure 5.14b. A closer look with higher magnification (Figure 5.14c) showed a darker area (1-2 µm wide) covered with FeS_2—the concentration of sulphur in this region was about 2 wt.% (determined by EDS). The bright circular areas, visible at higher resolution, correspond to iron nitride (γ'–Fe_4N), typical morphology when

plasma nitriding is performed using the active screen method [227]. This agrees with the XRD data from LTPN (section 3.2.2.4).

To induce pit growth in LTPN and analyse its morphology, the limiting current density was increased to 1×10^{-1} mA cm^{-2} for selected specimens and resultant images are shown in Figure 5.14d-f. Typical pit (50 µm–wide) formed at the centre of the working electrode is shown in Figure 5.14d. The image indicates that the outer section of the compound layer (γ'–Fe_4N and ε–$Fe_{2\text{-}3}N$) was locally dissolved, exposing its underlying portions. At the bottom of the pit—more clearly seen in Figure 5.14e, a wider localised attack—there were signs of intergranular corrosion. Brittle cracks were also observed on the top layer, next to some of the pits (Figure 5.14f). Overall, these images suggest that the compound layer is more resistant to corrosion than the unmodified material, since the areas of localised attack were shallower (less than 10 µm) than typical hemispherical pits (Figure 5.10b).

Examination of the bottom of the pits on LTPN specimens at higher resolution (Figure 5.15), provided additional evidence of the superior resistance of the compound layer compared to the unmodified material. The structure on the bottom of the pit (Figure 5.15a) is typical of mixed γ'–Fe_4N and ε–$Fe_{2\text{-}3}N$, confirming that only the outer part of the compound layer—predominantly γ'–Fe_4N, according to the XRD analysis (section 3.2.2.4)—was dissolved. Figure 5.15b shows an amplified view of the bottom of the pit, indicating the occurrence of brittle transgranular cracking.

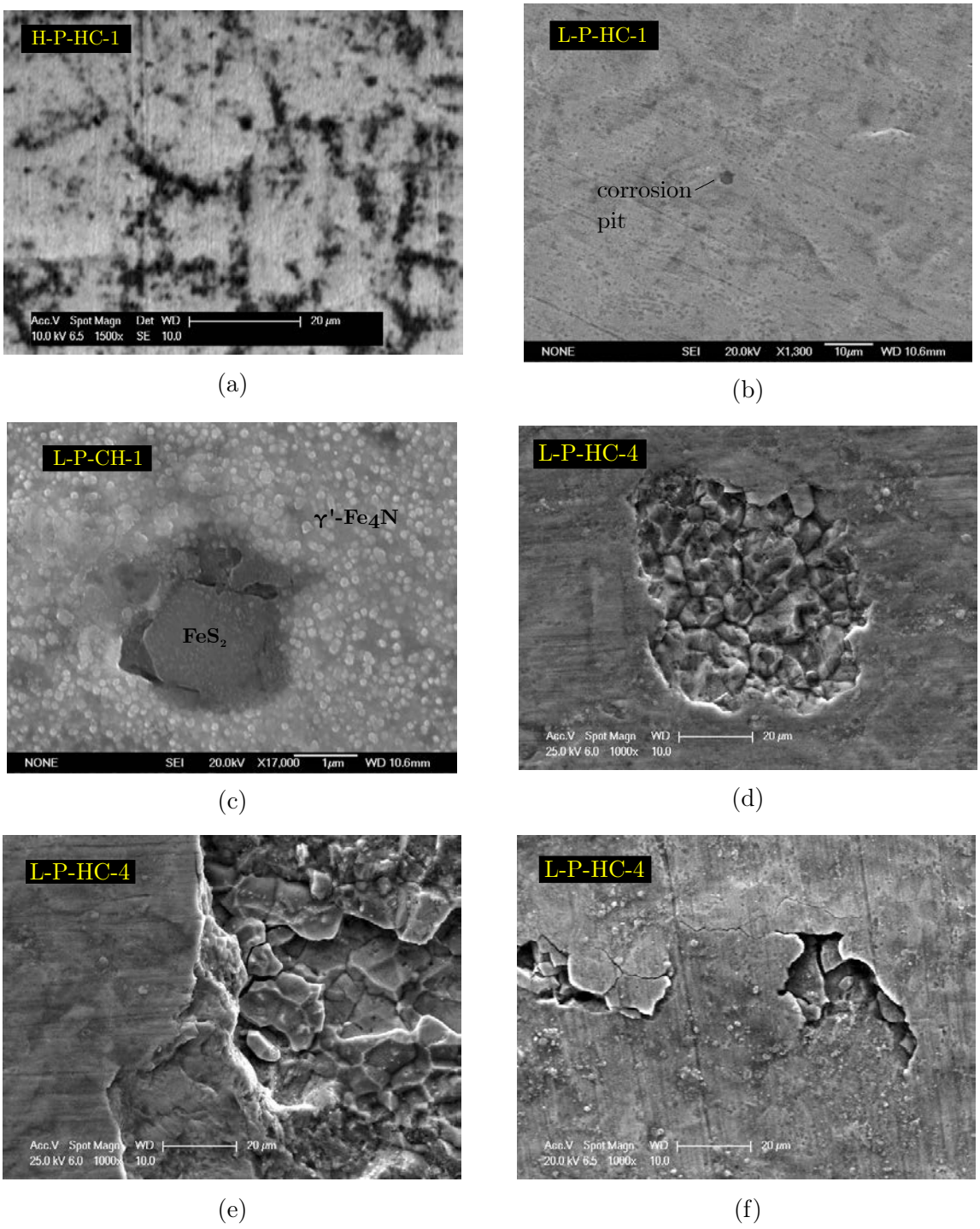

FIGURE 5.14: SEM micrographs of high (HTPN) and low–temperature plasma nitrided (LTPN) 17-4 PH (H1150D) after the potentiodynamic scans taken following 21 hours of immersion in produced water with $pH_2S = (3.4 \pm 0.1)$ kPa and CO_2 as balance: (a) HTPN; (b-c) LTPN; (d-f) LTPN with increased limiting current density (1×10^{-1} mA cm^{-2}).

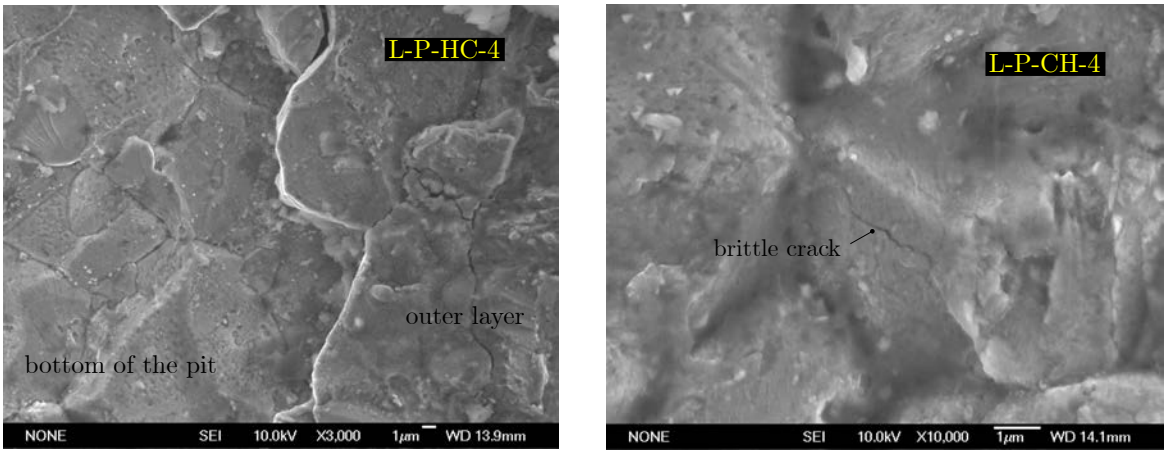

(a) (b)

FIGURE 5.15: SEM micrographs of low–temperature plasma nitrided (LTPN) 17-4 PH (H1150D) after the potentiodynamic scans taken following 21 hours of immersion in produced water with $pH_2S = (3.4 \pm 0.1)\,kPa$ and CO_2 as balance and limiting current density of $1 \times 10^{-1}\,mA\,cm^{-2}$: (a) outer layer and bottom of the pit; (b) brittle crack on the bottom of the pit.

5.3.2 Potentiodynamic polarisation (CO_2)

Unmodified specimens

Representative open-circuit potential of unmodified specimens (U-P-CO-1) immersed in produced water with $165\,g\,L^{-1}$ NaCl and pH 4.5 ± 0.2 saturated with pure CO_2 is shown in Figure 5.16. Similar to what occurred with mixed H_2S/CO_2, the potential went up quickly when the deaeration was finished and the test gas started to flow in the vessel. In the time frame evaluated (21 h of immersion), the potential reached $(-433 \pm 21)\,mV$. The potential gradually increased during the immersion period, indicating corrosion inhibition due to growth of corrosion scales—mainly ferrous carbonate $FeCO_3$, which may have formed due to the high concentration of CO_2. But, at room temperature, the formation of a dense film $FeCO_3$ is not favoured (see section 4.3.3.1) and therefore disperse deposits may have contributed to the potential increase.

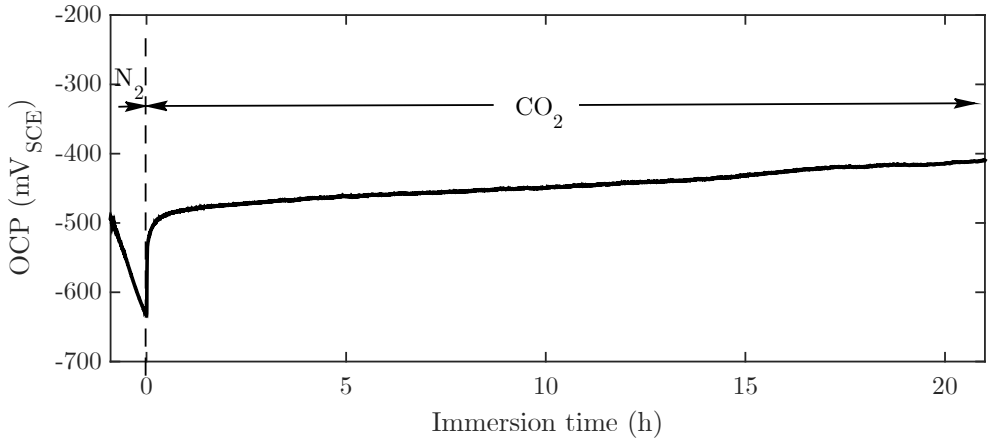

FIGURE 5.16: Variations of the open circuit potential with immersion time of unmodified 17-4 PH (H1150D) specimen exposed to produced water saturated with CO_2 for 21 hours.

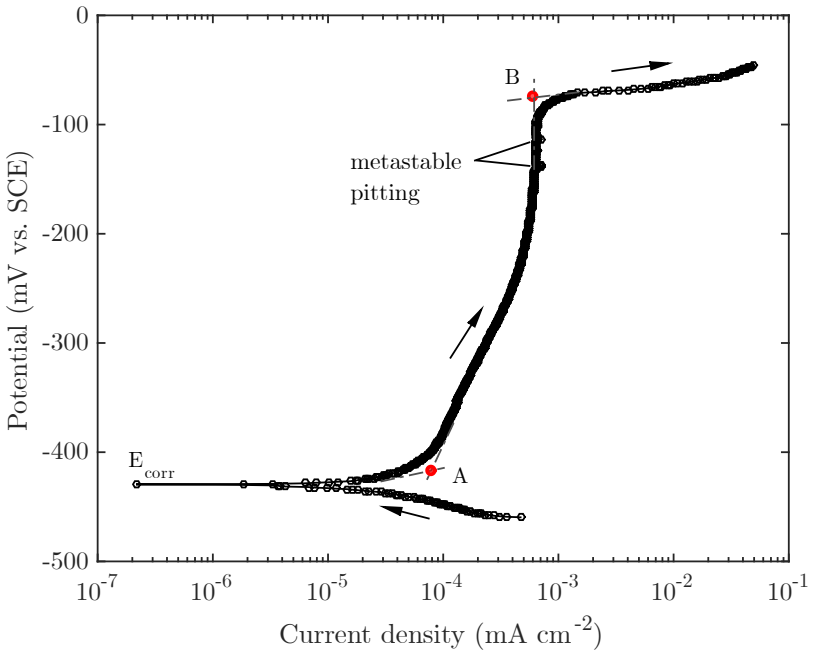

FIGURE 5.17: Potentiodynamic polarisation scans of unmodified 17-4 PH (H1150D) taken after 21 hours of immersion in produced water saturated with CO_2

The potentiodynamic scan (Figure 5.17), obtained after 21 h of immersion, indicates

a passivating behaviour. From the inflection point A ($\approx -410\,\mathrm{mV}$), the rate of increase of the current density reduced significantly and reached a fully passive condition at $\approx -200\,\mathrm{mV}$. From this point, further increase of the potential resulted in metastable pitting, subsequent breakdown of the protective film (point B, pitting potential E_p) and rapid dissolution until the limiting current was reached ($5 \times 10^{-2}\,\mathrm{mA\,cm^{-2}}$). The passive behaviour was due to the film of chromium oxide (Cr_2O_3).

After the potentiodynamic scans, examination of the surfaces with SEM revealed a few dark spots (less than 1 µm wide) on the surface. To allow pits to further grow so that their morphology could be analysed, additional scans were performed with larger limiting current ($1 \times 10^{-1}\,\mathrm{mA\,cm^{-2}}$, Figure 5.22). Typical pit formed at the centre of the working electrode—with an hemispherical shape, 150 µm wide—is shown in Figure 5.18a, in which corrosion scale and deposits of NaCl can also be identified. Figure 5.18b shows an augmented view of the bottom of the pit, in which intergranular and interlath corrosion can be seen.

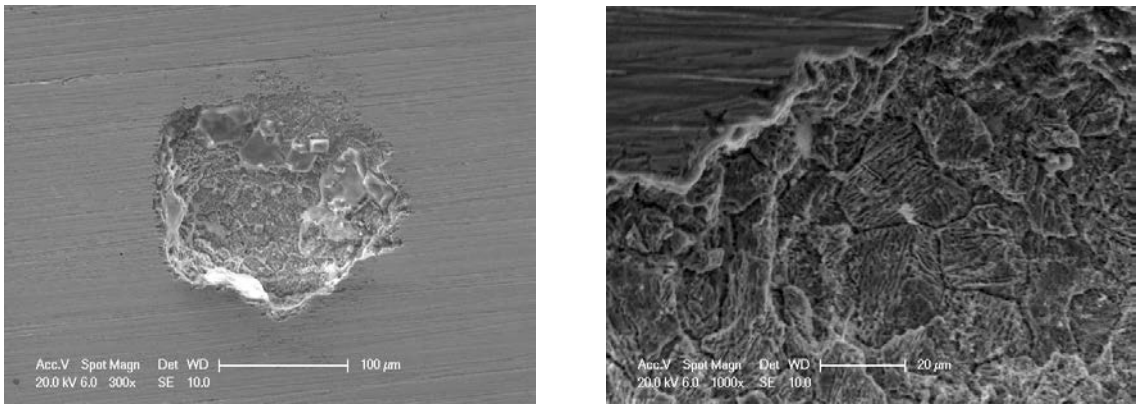

(a) (b)

FIGURE 5.18: SEM micrographs of unmodified 17-4 PH (H1150D) after the potentiodynamic scans taken following 21 hours of immersion in produced water saturated with CO_2: (a) typical corrosion pit; (b) amplified view of the bottom of typical pit

HTPN and LTPN specimens

The open circuit potentials of plasma nitrided specimens (L-P-CO-1 and H-P-CO-1) in pure CO_2 are shown in Figure 5.19. After deaeration with N_2, the potential of both HTPN and LTPN increased when the test gas was turned on (time = 0) and followed different paths with increasing the immersion time. For the HTPN condition, the potential first increased abruptly and, after reaching a peak of $-630\,\text{mV}$), decreased monotonically until a plateau of $(-664 \pm 5)\,\text{mV}$ was established after 5 hours of exposure. For the LTPN, the potential increased from$-640\,\text{mV}$ to $-590\,\text{mV}$ in the first 90 minutes and continue to rise linearly at a low rate ($\approx 0.8\,\text{mV}$ per hour) until it reached $(-576 \pm 3)\,\text{mV}$ at the end of the 21 hours of exposure. As in mixed H_2S/CO_2, the potential in pure CO_2 was less noble for the HTPN compared to both LTPN and unmodified conditions.

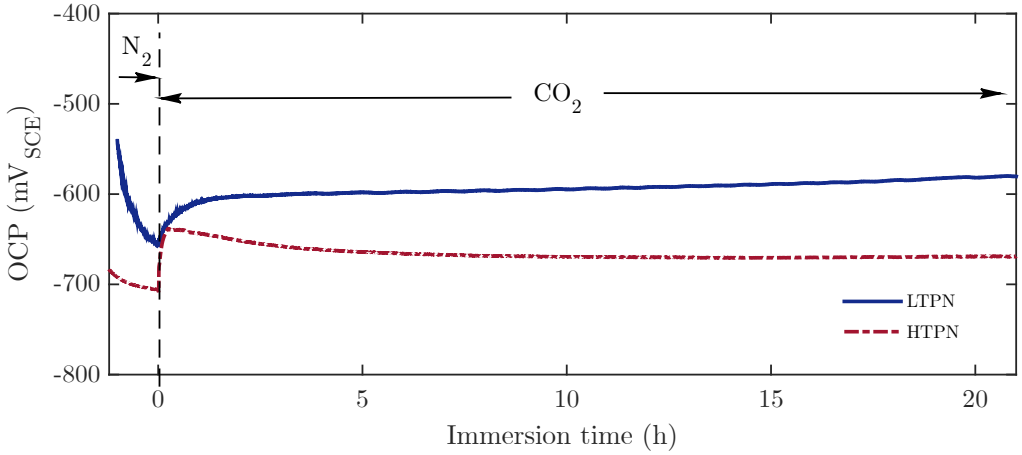

FIGURE 5.19: Variations of the open circuit potential with immersion time for the high (HTPN) and low–temperature plasma nitrided (LTPN) 17-4 PH (H1150D) exposed to produced water with pure CO_2 for 21 hours.

The potentiodynamic scans presented in Figure 5.20 show that, for the limiting current of $5 \times 10^{-2}\,\text{mA cm}^{-2}$, none of the plasma nitrided specimens had passivating behaviour

in pure CO_2. The more noble corrosion potential and the lower corrosion current of the LTPN specimens confirmed its superior corrosion resistance compared with the HTPN.

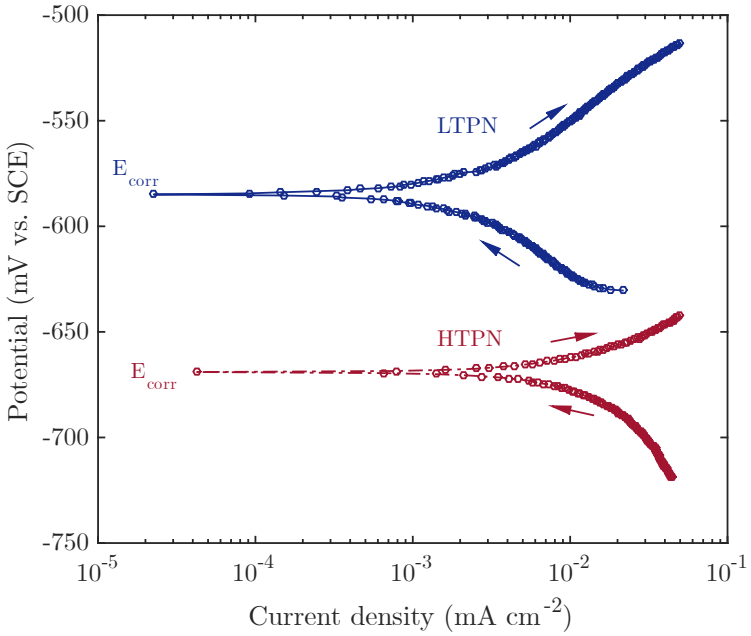

FIGURE 5.20: Potentiodynamic polarisation scans of high (HTPN) and low–temperature plasma nitrided (LTPN) 17-4 PH (H1150D) taken after 21 hours of immersion in produced water with pure CO_2.

Examination of the surfaces of the HTPN and LTPN after immersion (Figures 5.21a-b) confirmed that no pits were formed in pure CO_2 for both conditions (with the maximum current set to 5×10^{-2} mA cm^{-2}). For the HTPN condition, corrosion scales—as exemplified in Figure 5.21a—were identified on the surface. These deposits (randomly distributed on the surface of the working electrodes) were characterised as $FeCO_3$, since the EDS spectrum showed increased amount of oxygen (21 wt.%) compared to that of the uncovered surface (5 wt.%). Similar morphology was observed on the LTPN specimens: Figure 5.21b shows an overview of the surface at lower magnification.

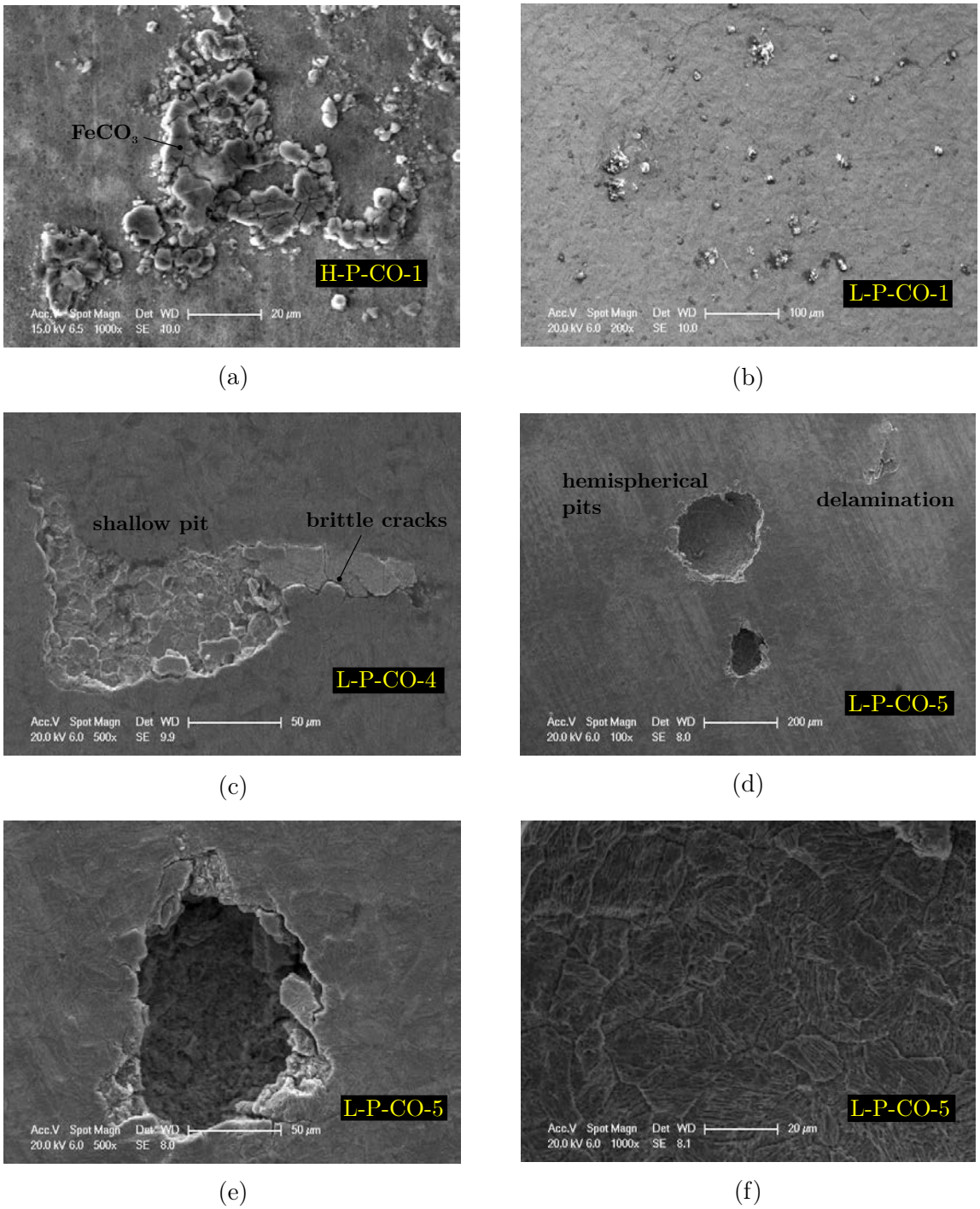

FIGURE 5.21: SEM micrographs of HTPN and LTPN 17-4 PH (H1150D) after the potentiodynamic scans taken following 21 hours of immersion in produced water with pure CO_2: (a) HTPN (limiting current density $5 \times 10^{-2}\,\mathrm{mA\,cm^{-2}}$; (b) LTPN ($5 \times 10^{-2}\,\mathrm{mA\,cm^{-2}}$; (c) LTPN with increased limiting current density ($1 \times 10^{-1}\,\mathrm{mA\,cm^{-2}}$); (d-f) LTPN with increased limiting current density ($1\,\mathrm{mA\,cm^{-2}}$)

The maximum current was increased ($1 \times 10^{-1}\,\mathrm{mA\,cm^{-2}}$ and above) and the scan repeated to analyse pit tendency of LTPN specimens. The material passivated when the current density was $i_{\mathrm{pass}} = 2 \times 10^{-1}\,\mathrm{mA\,cm^{-2}}$ and breakdown of the passive film occurred when the potential reached $E_{\mathrm{p}} = (-120 \pm 20)\,\mathrm{mV}$ (Figure 5.22a). For this condition, two types of localised attack were observed: (i) shallow pits (limiting current set to $1 \times 10^{-1}\,\mathrm{mA\,cm^{-2}}$, Figure 5.21c), in which only the outer portion of the compound layer was dissolved, as in mixed H_2S/CO_2 and (ii) round, hemispherical pits (limiting current set to $1\,\mathrm{mA\,cm^{-2}}$), up to 200 µm–wide (Figure 5.21d). In the latter case, the nitrided layer was completely dissolved and the bottom of the pit revealed the martensitic structure of the substrate (Figure 5.21f). Brittle cracks (Figure 5.21c and 5.21e) and delamination–like defect (Figure 5.21d) were also observed.

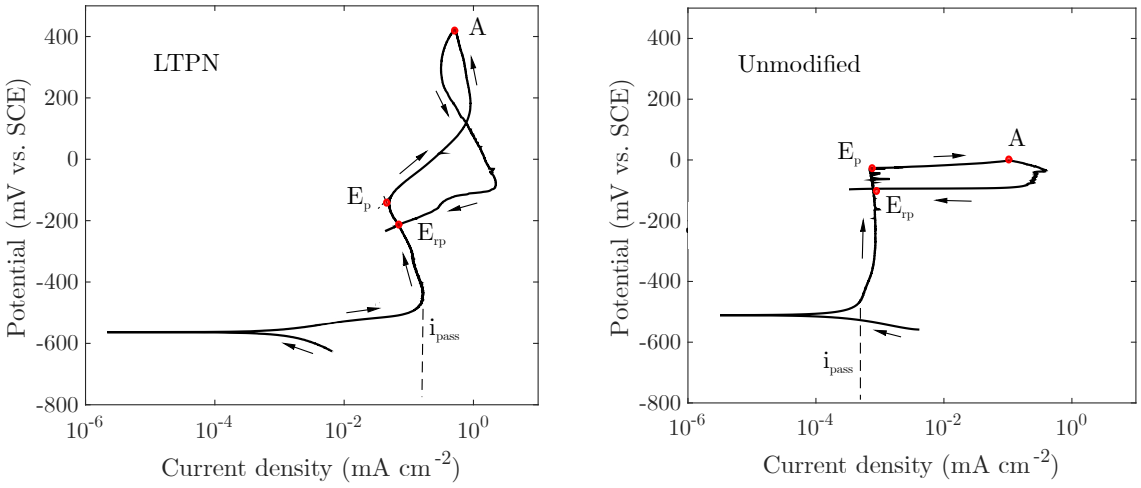

FIGURE 5.22: Representative reverse potentiodynamic polarisation scans of (a) low–temperature plasma nitrided (LTPN) and (b) unmodified 17-4 PH (H1150D) taken after 21 hours of immersion in produced water with pure CO_2

5.3.3 Potentiodynamic polarisation (H_2S)

Unmodified and LTPN specimens

Open circuit potential of unmodified and LTPN specimens exposed to H_2S–saturated produced water is shown in Figure 5.23. The shape of the curves and the potentials obtained for unmodified specimens in pure H_2S were similar to those when the material was exposed to mixed H_2S/CO_2 (see Figure 5.8). This suggests that, for both gas mixtures, the corrosion scales were not sufficiently stable to provide passivity since the potential dropped after reaching a peak value. LTPN specimens followed a different trend after deaeration: the potential dropped and increased rapidly, reaching a peak of $-600\,\text{mV}$, after which a sudden drop of about $20\,\text{mV}$ occurred before the potential started to grow towards a stable plateau (after about 10 hours of immersion) of $(-381 \pm 7)\,\text{mV}$. This potential rise suggests that the corrosion deposits (iron sulphide) are providing further protection against corrosion and a passive state could be formed due to the larger surface coverage owing to the high concentration of H_2S.

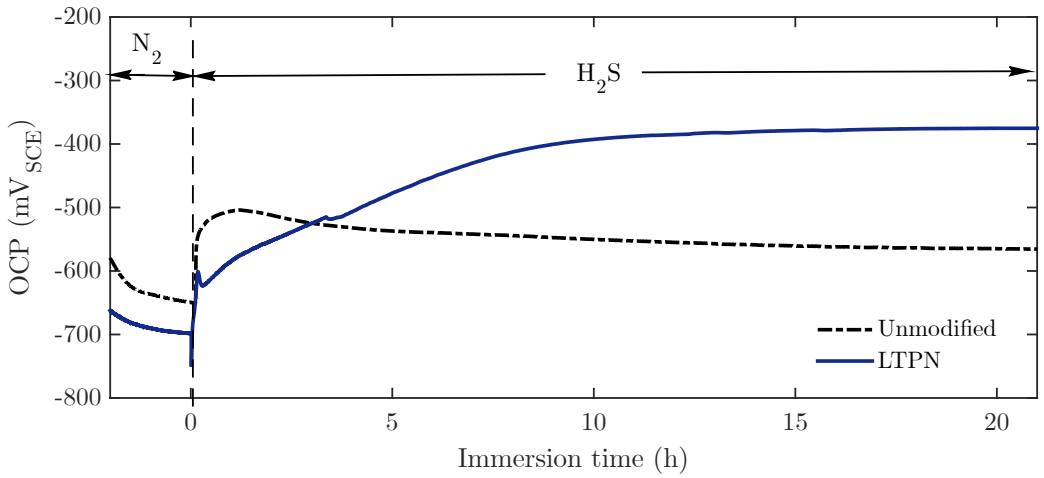

FIGURE 5.23: Variations of the open circuit potential with immersion time for the LTPN and unmodified 17-4 PH (H1150D) exposed to produced water with pure H_2S for 21 hours.

The potentiodynamic scans (Figure 5.24) showed that the unmodified material had a short passive region (from point C to D). After the onset of pitting (−420 mV), anodic dissolution occurred at a faster rate: approximately one decade of current density per 100 mV of potential increase. For the LTPN specimens (Figure 5.24), anodic dissolution occurred at different rates (it increased after passing point A) and passivation started ahead of point B.

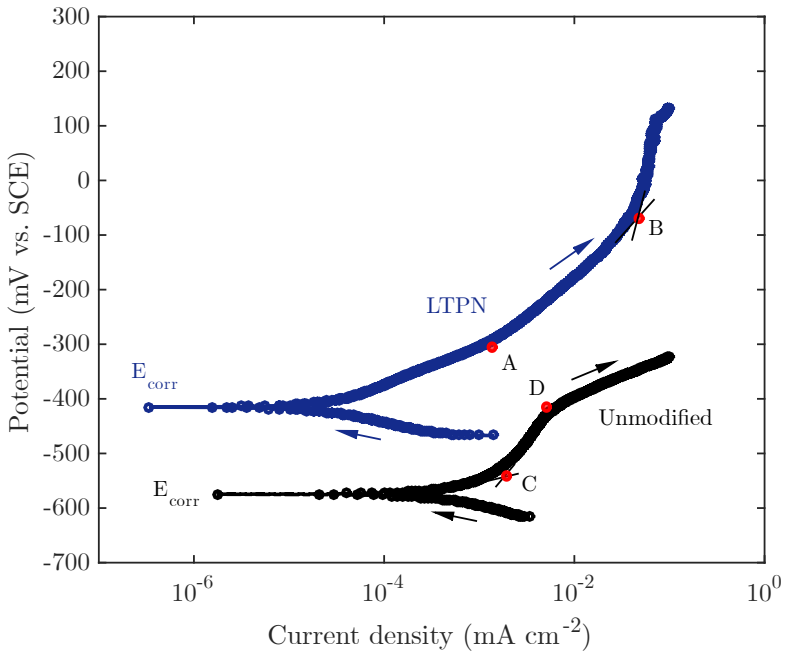

FIGURE 5.24: Potentiodynamic polarisation scans of low–temperature plasma nitrided (LTPN) and unmodified 17-4 PH (H1150D) taken after 21 hours of immersion in produced water with pure H_2S.

The SEM micrographs shown in Figure 5.25 provide further insights into the corrosion behaviour of both conditions. Figure 5.25a shows typical round pit located near the centre of the unmodified electrode, confirming that the material was susceptible to localised attack due to the chromium–rich film formed on the surface—iron sulphide was not identified on the surface by EDS for this condition. When the scan was forced to

run until a higher limiting current ($1 \times 10^{-1}\,\mathrm{mA\,cm^{-2}}$), however, deposits of FeS_2 near the centre of the electrode (Figure 5.25b) were identified—the concentration of sulphur on these darker regions were nearly 30 wt.%, obtained by EDS (Figure 5.25e). These deposits precipitated near corrosion pits (about 100 µm wide) since the limit of solubility of iron sulphide in the electrolyte was exceeded due to the enhanced corrosion activity.

The LTPN electrodes, after the scan shown in Figure 5.24 was completed, were almost deposit–free, having only few dark circular spots (Figure 5.25c) indexed by EDS as FeS_2 (S content of 0.5 wt.%). These are presumably deposits formed on the early stages of pitting and they would be expected to grow, as in the unmodified specimens, if dissolution had continued—that was not the case since the scan (Figure 5.24) was interrupted shortly after pitting potential was reached (point E). To investigate pit growth, the maximum current density was set to $1 \times 10^{-1}\,\mathrm{mA\,cm^{-2}}$ and intense precipitation of FeS_2 around regions of localised attack were identified (Figure 5.25d). The concentration of sulphur was nearly 30 wt.% on these regions (Figure 5.25f). EDS spectrums, obtained in different parts of the surface away from these locations, showed lower sulphur content (from 1 to 5 at.%), suggesting that a thin film of iron sulphide covered the surface of the electrode—this agrees with earlier observations [228], in which iron sulphide was formed by an inner, uniform thin layer and an outer layer composed by deposits.

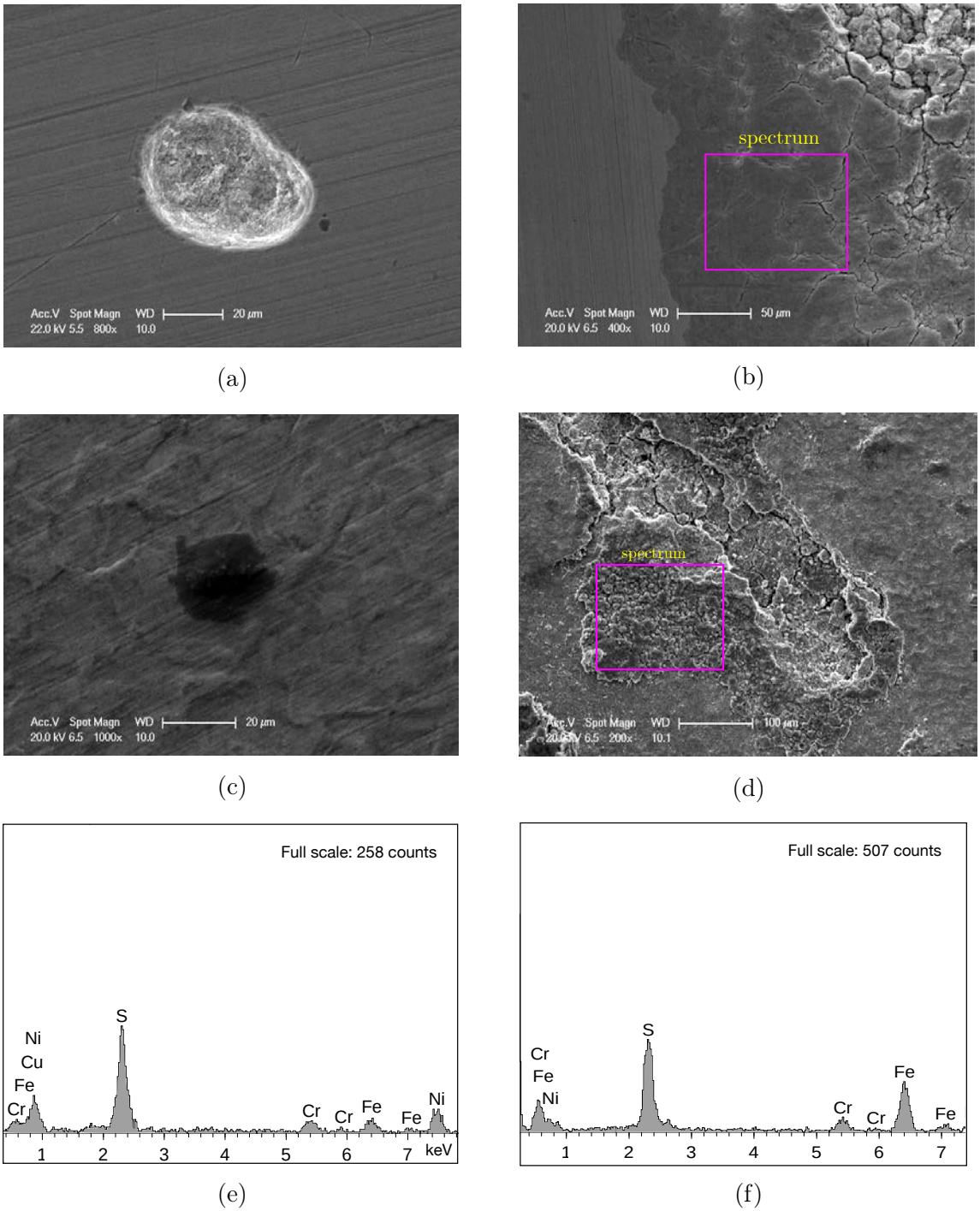

FIGURE 5.25: SEM micrographs of unmodified and LTPN 17-4 PH (H1150D) after the potentiodynamic scans taken following 21 hours of immersion in produced water with pure H_2S: (a) unmodified (limiting current density $5 \times 10^{-2}\,\mathrm{mA\,cm^{-2}}$; (b) unmodified ($1 \times 10^{-1}\,\mathrm{mA\,cm^{-2}}$); (c) LTPN ($5 \times 10^{-2}\,\mathrm{mA\,cm^{-2}}$); (d) LTPN ($1 \times 10^{-1}\,\mathrm{mA\,cm^{-2}}$); (e) EDS spectrum from (b); (f) EDS spectrum from (d).

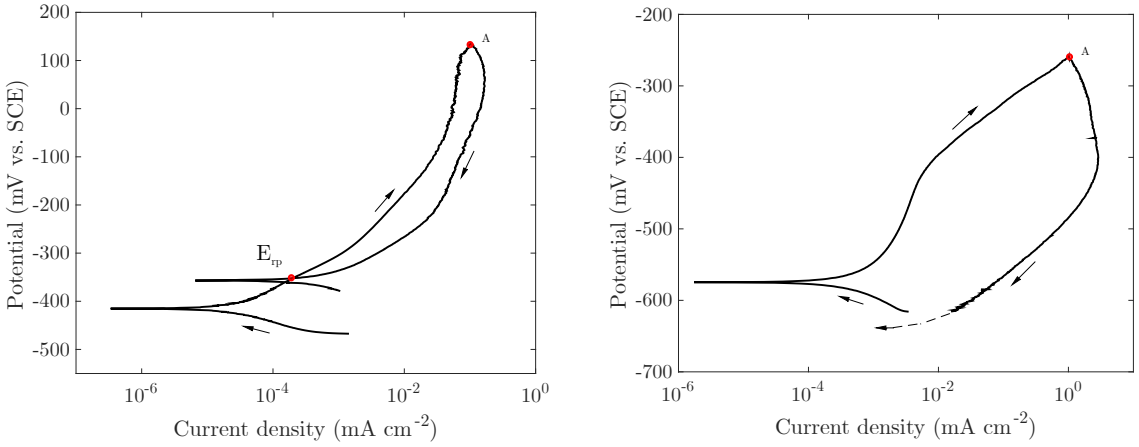

FIGURE 5.26: Representative reverse potentiodynamic polarisation scans of (a) low–temperature plasma nitrided (LTPN) and (b) unmodified 17-4 PH (H1150D) taken after 21 hours of immersion in produced water with pure H_2S.

Figure 5.26 presents typical reverse scans of unmodified and LTPN specimens. The large positive hysteresis loop on the unmodified material (Figure 5.26b) indicates that this condition is highly susceptible to pitting—the path followed by the reverse scan suggests that passivation would occur at a potential below E_{corr} and, in this case, pitting can occur even when the material is freely corroding at the corrosion potential. Conversely, repassivation of LTPN occurred above E_{corr} (Figure 5.26a).

5.3.4 Potentiodynamic polarisation (Summary and discussion)

The electrochemical data, extrapolation parameters and corrosion rates obtained from the potentiodynamic polarisation scans taken after 21 h of immersion in produced water (165 g L^{-1} NaCl and pH 4.5) with mixed H_2S/CO_2, pure H_2S and pure CO_2 are presented in Tables 5.2 and 5.3. The uncertainties were quantified by the standard deviation, considering at least three repeats for each condition. The results, discussed in detail in

the previous sections, showed that the resistance to general corrosion—quantified by the corrosion rate (Table 5.3)—in mixed H_2S/CO_2 increased (compared to the unmodified material) after plasma nitriding at low temperature (LTPN) and decreased after plasma nitriding at high temperature (LTPN). LTPN also exhibited superior resistance to pitting corrosion compared to the unmodified material, attributed to the greater corrosion resistance of the compound layer. In spite of both pitting E_p and the repassivating E_{rp} potentials being similar to that of the unmodified condition, SEM images indicated that only shallow pits were formed on the surface rather than typical hemispherical pits observed in unmodified specimens. By evaluating the corrosion response in pure H_2S and pure CO_2, as an attempt to understand the role of each gas on the corrosion process, the following was observed: LTPN had superior resistance (general and localised corrosion) in H_2S while the unmodified material performed best in CO_2, HTPN having the lowest resistance in the latter. In the following paragraphs, the results obtained for each test gas are further discussed.

Pure H_2S

As briefly reviewed in Chapter 2, when H_2S in the gas state is mixed with H_2O, it dissolves into aqueous H_2S, i.e. $H_2S_{(g)} \xrightarrow{K_{H_2S}} H_2S_{(aq)}$, $K_{H_2S} = c_{H_2S}/pH_2S$ being the solubility constant (reported to be from 0.097 to $0.103\,mol\,L^{-1}\,bar^{-1}$ in distilled water at 25 °C [229]) and c_{H_2S} is the concentration of H_2S. Addition of NaCl slightly decrease the solubility [230]). Similar expressions are obtained for solubility constants on each subsequent dissociation step ($H_2S_{(aq)} \xrightarrow{K_1} H^+ + HS^-$ and $HS^- \xrightarrow{K_2} H^+ + S^{2-}$). As noted by [231], these sulphur species are stable at high pH levels (pH≥6) whereas dissolved H_2S is stable at lower pH. Since the pH in all the electrochemical measurements in this work was kept within 4.5 ± 0.2, $H_2S_{(aq)}$ was predominant.

TABLE 5.2: Electrochemical data obtained from the potentiodynamic scans after 21 h immersion in produced water (165 g L^{-1} NaCl and pH 4.5 ± 0.2) with different gas mixtures at (23 ± 2) °C and atmospheric pressure

Test gas	**Condition**	E_{corr} mV_{SCE}	i_{corr} $mA\,cm^{-2}$	E_p mV_{SCE}	E_{pass} mV_{SCE}	i_{pass} $mA\,cm^{-2}$	E_{rp} mV_{SCE}
H_2S/CO_2	UN[a]	-547 ± 4	$(0.41 \pm 0.09) \times 10^{-3}$	-383 ± 14	-518 ± 16	$(1.53 \pm 0.46) \times 10^{-3}$	≈ -500
	HTPN[b]	-646 ± 5	$(1.82 \pm 0.40) \times 10^{-3}$	—	—	—	—
	LTPN[c]	-595 ± 5	$(0.10 \pm 0.02) \times 10^{-3}$	-305 ± 5	-430 ± 9	$(3.60 \pm 0.53) \times 10^{-3}$	-358 ± 8
CO_2	UN	-451 ± 22	$(0.07 \pm 0.04) \times 10^{-3}$	-67 ± 14	-430 ± 20	$(0.15 \pm 0.05) \times 10^{-3}$	-103 ± 6
	HTPN	-655 ± 4	$(11.40 \pm 5.25) \times 10^{-3}$	—	—	—	—
	LTPN	-566 ± 17	$(1.17 \pm 0.32) \times 10^{-3}$	-150 ± 5	-472 ± 10	$(1.77 \pm 0.25) \times 10^{-1}$	-207 ± 8
H_2S	UN	-556 ± 23	$(0.22 \pm 0.13) \times 10^{-3}$	-388 ± 23	-550 ± 9	$(0.90 \pm 0.17) \times 10^{-3}$	< -556
	LTPN	-412 ± 9	$(0.03 \pm 0.01) \times 10^{-3}$	125 ± 15	-308 ± 14[d]	$(1.50 \pm 0.50) \times 10^{-3}$[d]	-367 ± 29

[a]unmodified; [b]high-temperature plasma nitrided; [c]low-temperature plasma nitrided; [d]values taken from the first inflection point (forward scan) after the corrosion potential.

TABLE 5.3: Extrapolation parameters, polarisation resistances and corrosion rates obtained from the potentiodynamic scans after 21 h immersion in produced water ($165\,g\,L^{-1}$ NaCl and pH 4.5 ± 0.2) with different gas mixtures at $(23 \pm 2)\,°C$ and atmospheric pressure

Test gas	**Condition**	β_a mV/decade	β_c mV/decade	R_p $k\Omega\,cm^2$	CR mmyear^{-1}
H_2S/CO_2	UN	44 ± 3	32 ± 2	20.0 ± 4.0	$(4.31 \pm 0.91) \times 10^{-3}$
	HTPN	29 ± 1	37 ± 3	4.1 ± 1.0	$(1.82 \pm 0.40) \times 10^{-3}$
	LTPN	31 ± 7	33 ± 4	72.0 ± 13.0	$(0.91 \pm 0.43) \times 10^{-3}$
CO_2	UN	52 ± 12	29 ± 2	150.0 ± 90.0	$(0.75 \pm 0.44) \times 10^{-3}$
	HTPN	31 ± 3	43 ± 5	0.8 ± 0.5	$(1.20 \pm 0.60) \times 10^{-1}$
	LTPN	31 ± 3	42 ± 2	7.0 ± 1.7	$(12.41 \pm 3.45) \times 10^{-3}$
H_2S	UN	42 ± 4	32 ± 2	48 ± 3	$(2.35 \pm 1.34) \times 10^{-3}$
	LTPN	34 ± 8	23 ± 9	220 ± 150	$(0.34 \pm 0.11) \times 10^{-3}$

In H_2S-H_2O systems, complex reactions take place at the metal surface simultaneously, as briefly reviewed in Chapter 2, the net reaction being $Fe + H_2S \overset{H_2O}{\rightleftharpoons} FeS + 2\,H$. In addition to the anodic dissolution of iron ($Fe \longrightarrow Fe^{2+} + 2\,e^-$) and adsorption of corrosion species, precipitation of iron sulphide occurs when its limit of solubility is exceeded, resulting in corrosion inhibition if the immersion time in the electrolyte is sufficiently long—more than 2 h, as noted by some studies[102]. Among various structures of iron sulphide, metastable mackinawite (tetragonal FeS_{1-x}, x varying from 0 to 0.11) has been reported as the first corrosion product to form at 25 °C [229] and subsequently transformed into more stable forms, such as pyrite FeS_2 and cubic FeS. The latter can be excluded, since it has been shown that it cannot be formed in the presence of NaCl [229], and therefore all the corrosion deposits in pure H_2S were characterised as pyrite (FeS_2, confirmed by EDS). Its corrosion inhibition effect was clearly observed in the LTPN condition (the open circuit potential shifted to more noble potential during immersion), in which corrosion scales accumulated near sites of localised attack (Fe^{2+} being more intensely released from the surface) after the potentiodynamic scans rather than form a uniform thin film on the

surface of the electrode. Similar effects occurred on the surface of the unmodified specimens, but corrosion inhibition was not observed. This could be because the unmodified is more susceptible to pitting, which favoured the kinetics of growth of the FeS film and regions not covered by FeS became anodic to the larger and more frequent FeS deposits, resulting in higher dissolution. This can explain the higher corrosion rate observed in the unmodified specimens (Table 5.3).

Pure CO_2

Similarly to H_2S, CO_2 dissolves in water ($CO_{2(g)} \xrightarrow{K_{CO_2}} CO_{2(aq)}$) and an iron carbonate scale can be formed if the limits of solubility of CO^{3-} and Fe^{2+} are exceeded (supersaturation). This layer can become a barrier for the corrosion species and slow down the corrosion process or can be porous and increase the susceptibility to localised attack. In this study, none of these cases occured as only few deposits of $FeCO_3$ were identified. This is in agreement with previous studies [209], which have shown that $FeCO_3$ has low adherence to the surface when the temperature is lower than 60 °C, since supersaturation of CO^{3-} and Fe^{2+} is not achieved on these temperatures. Besides, the pH used in this work (4.5 ± 0.2) increases the solubility of iron carbonate, thus supersaturation and thereby the scaling tendency are decreased—previous study [232] indicated the tendency of the formation of a compact and protective film only when the pH of the environment was larger than 6. Furthermore, saturation of iron carbonate is also decreased by increasing the ionic strength of the environment, which is high due to the high NaCl content used in this work.

According to the potentiodynamic scans and SEM micrographs, localised corrosion occurred in both unmodified and LTPN electrodes while general corrosion was dominant

on HTPN. The latter had the lowest corrosion resistance—as expected due to the formation of CrN—and corroded at a rate one to a few orders of magnitude faster than LTPN and unmodified specimens. Due to the high chromium content, pitting occurred by a film breaking mechanism (chromium oxide) in the unmodified condition and a passivity–like behaviour of the LTPN was due to the higher corrosion resistance of the outer nitrogen–rich layer compared with the underlying layers of the nitrided case. The unmodified material has lower corrosion rate, higher pitting potential and lower passivating current, indicating that this condition has superior resistance to both localised and general corrosion in pure CO_2.

Mixed CO_2/H_2S

When both H_2S and CO_2 are present in solution, it is expected that both iron carbonate and iron sulphide scales precipitate on the surface and that different H_2S/CO_2 ratio would result in different proportions of $FeCO_3$/FeS. Studies with carbon steels [156] exposed to these environments confirmed that both scales compete and that the partial pressure of H_2S is an important aspect controlling the precipitation. According to their findings, with small amounts of H_2S (about 1 kPa), both scales are formed whereas the precipitation of iron sulphide predominates when the concentration of H_2S increases. But, as the precipitation of $FeCO_3$ is not favoured in the conditions evaluated in this work, as indicated in previous section, iron sulphide would therefore be the predominant corrosion scale in mixed H_2S/CO_2. To support this, previous studies [233] have demonstrated that when the ratio of partial pressures (pCO_2/pH_2S) is less than 500 (it is approximately 28 in the present work), the formation of iron sulphide predominates. The sulphur content on the surface, however, was lower than 2 wt.% in specific regions and this could be because HS^- and S_2^- species could had interacted with the growing film and promoted the formation

of soluble corrosion products, thereby preventing the development of an effective barrier for general corrosion, in agreement with previous observations [158].

Contrary to previous studies [222, 234, 235], which showed that the addition of H_2S to CO_2 reduced the corrosion rate of steels in acidic conditions when the immersion time was longer than 2 hours [235], the unmodified material had lower corrosion resistance in mixed H_2S/CO_2 compared to pure CO_2. This confirms that a protective film of iron sulphide was not sustained for the conditions tested in this work. Similarly, there was no evidence of formation of a protective film on the surface of LTPN specimens—apart from isolated deposits with higher sulphur content compared to the uncovered areas. Despite the absence of an uniform film, iron sulphide appeared to have covered the porous structure of the outer compound layer (γ'–Fe_4N) and slowed the corrosion process—both general and localised corrosion resistance increased in mixed gas. As in pure H_2S and in pure CO_2, HTPN had the lowest corrosion resistance due to the presence of CrN in its structure.

5.3.5 Electrochemical impedance spectroscopy

As discussed earlier, electrochemical impedance spectroscopy analysis was used only to evaluate the LTPN condition. In the first part of this section, major trends of the experimental data were analysed. In the second part, an equivalent electric circuit was used to describe the system and the the physical interpretation of each parameter was discussed.

5.3.5.1 Experimental data

Figure 5.27 shows the Nyquist plots, i.e the negative of the imaginary impedance Z"(ω) against the real impedance Z'(ω), obtained for LTPN specimens immersed in produced water with $pH_2S = (3.4 \pm 0.1)$ kPa and CO_2 as balance. Electrochemical readings were

taken for different immersion times, from 5 to 21 h. Overall, except for the increase in the first hours (from 5 to 9 h), the size of the impedance arcs decreased with increasing the immersion time and reached a stable size after 17 h. From 9 h to 17 h, the magnitude of the electrochemical impedance of the system—represented by a vector from the origin to the impedance arc ($|\mathrm{Z}(\omega)| = \left[(\mathrm{Z'})^2 + (\mathrm{Z''})^2\right]^{1/2}$)—is reducing for the entire frequency spectra (more visible at lower frequencies) as the immersion time increases. This indicates that the polarisation resistance of the system—determined by the difference between the impedance at high and low frequency, i.e. $R_\mathrm{p} = |Z(\omega)_{\omega\to\infty}|$ - $|Z(\omega)_{\omega\to 0}|$—is reducing and thereby the corrosion rate is increasing, possibly due to the dissolution of the thin film of iron sulphide initially formed on the surface. Quantitatively, however, the variations of impedance with the immersion time were negligible, as detailed in the next section. This is reflected on the minor variation of the cell potential: from -573 (9 h) to $-577\,\mathrm{mV}$ (21 h), which agrees with the readings of the open circuit potential in the same period (Figure 5.8). In pure N_2, the impedance was slightly higher than that in mixed gas and the impedance arc was longer (almost completing a semi-circle). The partial arcs (not extended to the low frequency spectra) obtained for the mixed gas is typical of metallic surfaces forming porous films (in this case iron sulphide) with high capacitance.

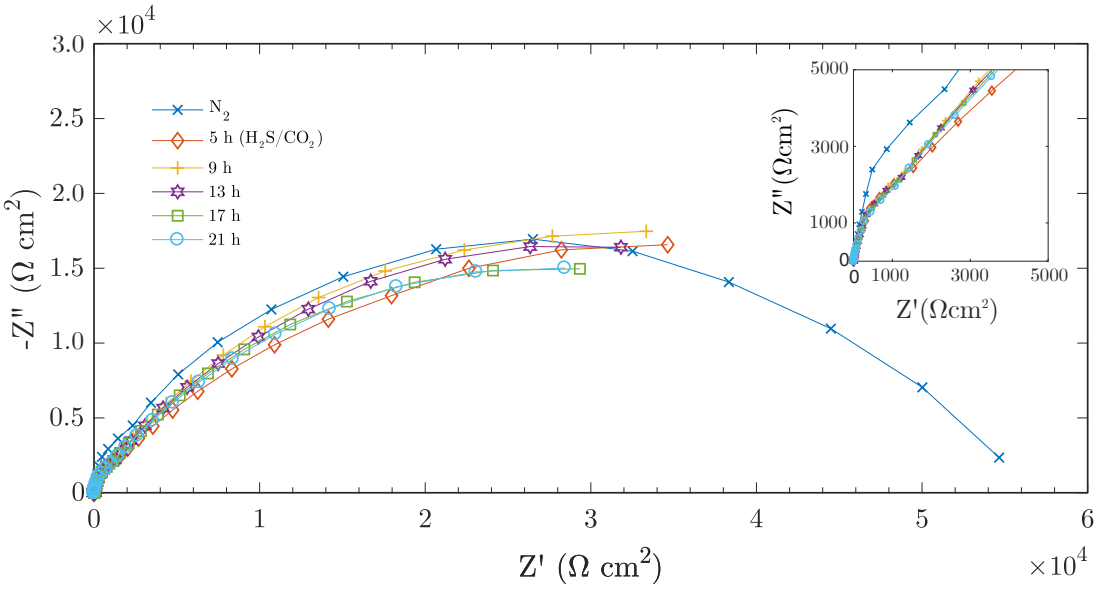

FIGURE 5.27: Nyquist plots of low–temperature plasma nitrided (LTPN) specimens taken after deaeration with N_2 and at different times of immersion (up to 21 hours) in produced water with $pH_2S = (3.4 \pm 0.1)$ kPa and CO_2 as balance. Insert: amplified view at high frequency.

A closer look at the shapes of the arcs (see insert in Figure 5.27) indicates that they are formed by two semicircles. This suggests that there are two rate–determining paths for the corrosion process, i.e. two different interfaces corroding simultaneously. A discussion about these interfaces is presented in the next section.

The corresponding Bode (phase) plots (phase angle ϕ against frequency) are shown in Figure 5.28a. The overlapping of two waves confirms that there are two major electrochemical interfaces. In mixed H_2/CO_2, phase angle dropped for all immersion times (about 20 degrees) when the frequency reached about 10^{-1} Hz, which shows a deviation from a fully capacitive behaviour—characterised by a plateau near 90°, which would indicate high corrosion resistance (e.g. passivity due to a compact, non-porous film on the surface). The non–ideal response (deviation from ideal capacitor) suggests that the resistance to minor faults on the surface (e.g. superficial defects or narrow pores exposed to

the electrolyte) became detectable on the low–frequency range. The shape of the curve in pure N_2 followed a similar trend from high to intermediate frequencies, with the phase angle shifted (about 2°) towards 90 degrees, indicating higher corrosion resistance. On the lower side of the frequency spectra, however, the phase angle dropped (from just above 10^{-2} to 1 mHz to near 0° and it suggests the presence of larger or more frequent pores at the surface (implying lower corrosion resistance).

The features observed in the Bode (phase) plots can also be identified in the Bode (magnitude) plots (module of impedance $|Z|$ against frequency) shown in Figure 5.28b. At high frequency, characteristics of the electrolyte were revealed: for all the specimens, the impedance of the electrolyte was about $2\,\Omega\,cm^2$—this confirms the high ionic strength of the electrolyte due to the high concentration of NaCl. From frequencies below 10^2 Hz, a straight line with slope $\Delta|Z|/\Delta f \approx$ -1 indicates capacitive behaviour (slope equal to 1) and the slope became higher ($>$ -1) when the frequency was lower than 10^{-1} Hz, confirming the deviation from a fully capacitive behaviour at low frequencies. In pure N_2 the impedance deviated from a straight line in the low frequency side of the graph (below $\approx 10^{-2}$ Hz), also an indicator of deviation from purely capacitive behaviour due to the formation of a porous structure or flaws on the surface. This effect was less pronounced in mixed H_2S/CO_2.

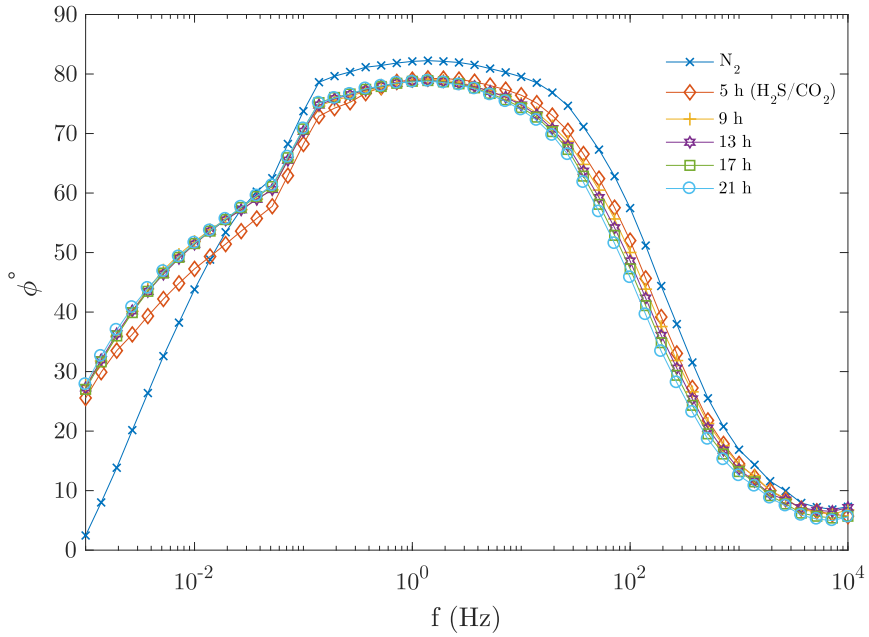

(a)

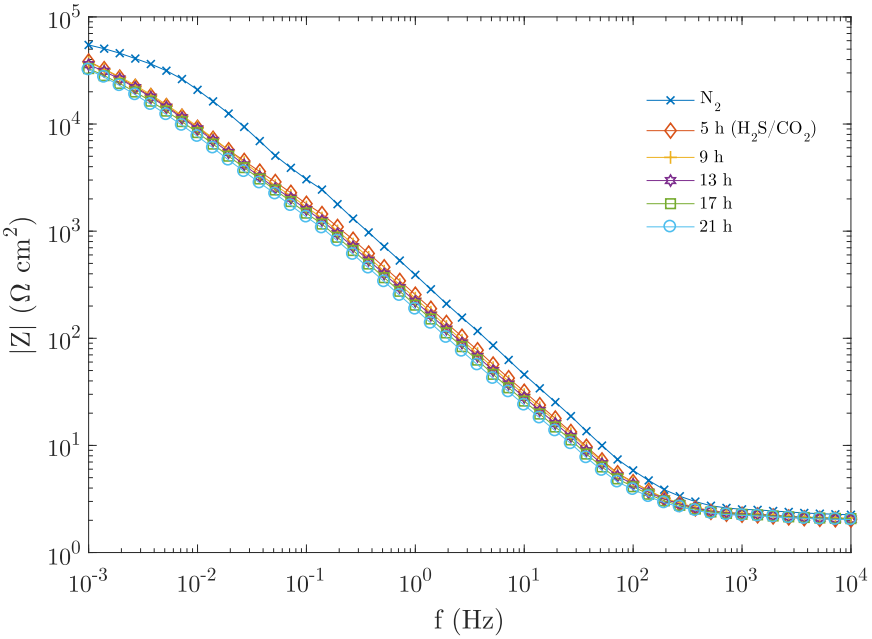

(b)

FIGURE 5.28: Bode plots of low–temperature plasma nitrided (LTPN) specimens taken after deaeration with N_2 and at different times of immersion (up to 21 hours) in produced water with $pH_2S = (3.4 \pm 0.1)$ kPa and CO_2 as balance: (a) Bode (phase angle); (b) Bode (magnitude)

5.3.5.2 Equivalent circuit

A useful approach to help interpret the EIS data is to fit it to an equivalent electrical circuit which best represents the processes taking place in the electrochemical cell being investigated. Although useful, this needs to be used with caution because there are many possible circuits that can describe the system. The complexity increases when many reactions are taking place, such as the formation and grown of passive films and corrosion products (the kinetics of formation of iron sulphide deposits involves its solubility in the test environment and the rate that this is being formed at the surface). A fully comprehensive investigation of this is not part of the scope of this project. Rather, the circuit was used to assist the understanding of the main features of the corroding interfaces to evaluate the corrosion resistance of the plasma nitrided layer when exposed to the test environment.

A possible circuit that can be used to fit the experimental data is shown in Figure 5.29. This is typical circuit used to describe metallic substrates protected by non-conductive porous coatings [213] or by conductive passive films [158, 210]. The corroding interfaces in contact with the electrolyte were modelled as a two–layer system: the top section represents the outer portion of the compound layer (predominantly γ'–Fe_4N, 3-5 µm deep) and the inner portion represents the substrate, i.e. the underlying portions of the compound layer. The pores of the γ'–Fe_4N structure or flaws on its surface are modelled as narrow channels connecting the electrolyte with the underlying γ'–Fe_4N/ε–$Fe_{2\text{-}3}N$ structure. In Figure 5.29, R_s is the ohmic resistance of the electrolyte (between the reference and working electrode), R_c is the resistance of the outer layer, which measures the resistance to the passage of the electrolyte through the microscopic channels (pores) and R_t is the charge–transfer resistance at the interface electrolyte/inner layer. Q_c and Q_t (double layer capacitance) represent the capacitances of the outer and inner layer, respectively.

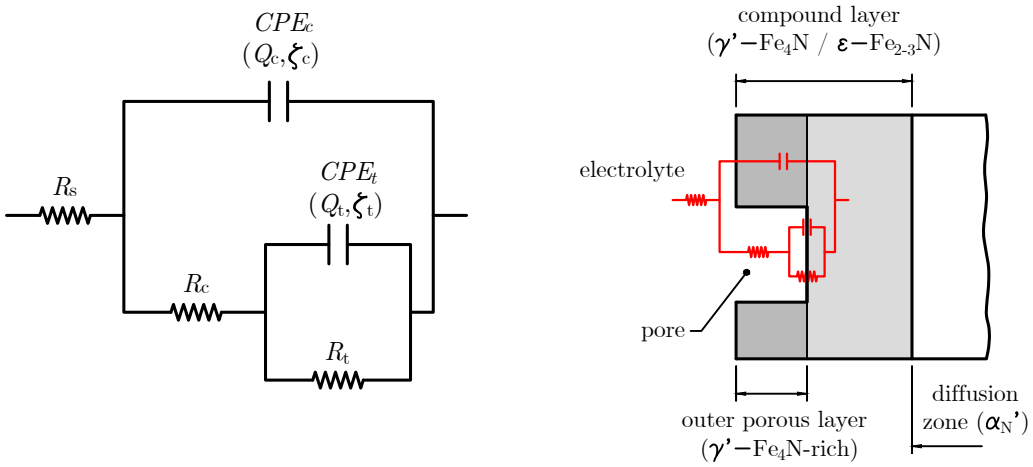

FIGURE 5.29: (a) Equivalent electric circuit used to model the experimental data; (b) schematic representation of the corroding interfaces (cross section)

As the semicircles on the complex plane (Figure 5.27) are flattened, i.e. depressed semi-circular arcs, constant–phase elements (CPE) were used to represent non–ideal capacitors. This behaviour, as discussed earlier, is due to inhomogeneities on the surface and complex reactions taking place near the interface (e.g. adsorption). In this case, the impedance is given by [210]

$$Z_{\mathrm{CPE}}(\omega) = \frac{1}{Q(\mathrm{j}\omega)^{\zeta}} \tag{5.5}$$

in which ω is the angular frequency ($\omega = 2\pi f$, where f is the frequency), j is the imaginary unit ($\mathrm{j} = \sqrt{-1}$) and ζ is a parameter related to the depression angle (rotation of the semi circle with respect to the real axis) which varies from 0.5 to 1. When $\zeta = 1$, the element acts as an ideal capacitor with capacitance equal to Q. The impedance of an ohmic resistor when a sinusoidal voltage is applied is its resistance, R, and the impedance of a

capacitor is given by

$$Z_{\mathrm{C}}(\omega) = \lim_{\zeta \to 1} Z_{\mathrm{CPE}}(\omega) = \frac{1}{\mathrm{j}\omega C} \tag{5.6}$$

By arranging the elements as indicated in the circuit (Figure 5.29) and using equations 5.7 and 5.6, the total impedance of the system is given by

$$Z(\mathrm{j}\omega) = R_s + \frac{R_c + R_t + (\mathrm{j}\omega)^{\zeta_t} R_c R_t Q_t}{(\mathrm{j}\omega)^{\zeta_c} \left[Q_c (\mathrm{j}\omega)^{\zeta_t} R_c R_t Q_t + R_c + R_t \right] + (\mathrm{j}\omega)^{\zeta_t} R_t Q_t + 1} \tag{5.7}$$

5.3.5.3 Fitting results

The parameters obtained after fitting the experimental data to the equivalent circuit shown in Figure 5.29 are summarised in Figure 5.30 and Table 5.4. Selected Bode (magnitude and phase) plots exemplify the fitting results (Figure 5.32). The low χ^2 (Table 5.4), used to determine the goodness of fit, indicates that the selected circuit is adequate to describe the experimental data—ideally, $\chi^2 \to 0$ [236]. Besides, the Kramers–Kronig (K-K) transform [237, 238] was used to verify the consistency of the experimental data—this model connects real and imaginary parts of the impedance and evaluate causality, linearity, stability and finiteness—and the resulting impedance curve was similar to that obtained experimentally, as shown in Figure 5.32. The following relations were used:

$$Z'(\omega) = Z'(\infty) + \left(\frac{2}{\pi}\right) \int_0^\infty \frac{x Z"(x) - \omega Z"(\omega)}{x^2 - \omega^2} dx \tag{5.8}$$

$$Z\text{"}\,(\omega) = -\left(\frac{2\omega}{\pi}\right)\int_0^{\infty}\frac{Z'\,(x) - Z'\,(\omega)}{x^2 - \omega^2}dx \tag{5.9}$$

in which $Z'(\omega)$ and $Z\text{"}\,(\omega)$ are the real and imaginary parts of the impedance (respectively), ω is the frequency and x is the variable of integration.

Figure 5.30 show the variations of R_{s}, R_{c}, R_{t} and R_{p} with immersion time. The ohmic resistance of the electrolyte, $R_{\mathrm{s}} = (2.2 \pm 0.1)\,\Omega \cdot \mathrm{cm}^2$, remained constant during the exposure and its small value is due to the high conductivity of the electrolyte (high content of NaCl). The polarisation resistance, R_{p}, dropped from $(4.5 \pm 0.5) \times 10^4\,\Omega \cdot \mathrm{cm}^2$ (pure N_2) when the electrode was immersed in the test gas, reaching $(3.8 \pm 0.4) \times 10^4\,\Omega \cdot \mathrm{cm}^2$ after 5 hours. It continued to decrease after reaching a peak (9 hours) and, in 21 hours of exposure, R_{p} was about 11 % lower, i.e. $(3.4 \pm 0.4) \times 10^4\,\Omega \cdot \mathrm{cm}^2$ compared to the first reading in the mixed gas. This indicates that, overall, the material is becoming less corrosion resistance with increasing the immersion time in H_2S/CO_2. To investigate the possible mechanisms involved in this process, the variations of their components (R_{c} and R_{t}) are discussed in the next paragraphs.

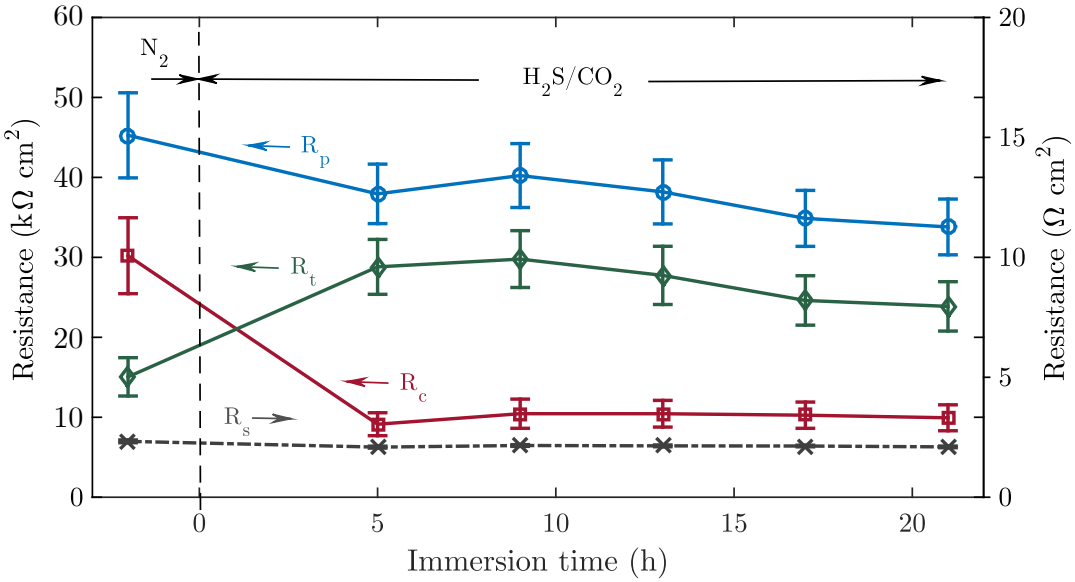

FIGURE 5.30: Electrochemical data (polarisation resistance, R_p; ohmic resistance of the outer layer, R_c; ohmic resistance of the inner layer, R_t; and electrolyte resistance, R_s) of low–temperature plasma nitrided (LTPN) specimens taken after deaeration with N_2 and at different times of immersion (up to 21 hours) in produced water (165 g L^{-1} NaCl and pH 4.5) with mixed H_2S (3.5 kPa) and CO_2 (as balance)

By analysing the results from Figure 5.30, it is evident that the polarisation resistance was dominated by the resistance of the outer layer (R_c) in pure N_2 and that the charge–transfer resistance of underlying interface of the compound layer (R_t) became the main contributor in H_2S/CO_2—R_t accounting for about 70 % of R_p. This suggest that, when H_2S was present in solution, iron sulphide preferentially deposited on the bottom of these pores—as indicated by EDS, see Figure 5.31—and slowed down the corrosion process taking place locally. As a result, the charge–transfer resistance of the inner interface, i.e. bottom of the pores, increased. With increasing immersion time, however, it seemed that these deposits partially dissolved resulting in reduction of R_t until a nearly steady condition was reached (between 17 and 21 hours), R_t being $(2.4 \pm 0.3) \times 10^4\,\Omega \cdot cm^2$ at the end of this period.

In the potentiodynamic experiments, it was noticed that the outer part of the compound layer formed on LTPN specimens was dissolved after the scan was completed whereas the inner portion was still present in the structure, as can be seen in Figure 5.15. This is in agreement with the EIS results obtained in this section, which suggest that the inner layer is more resistant to corrosion.

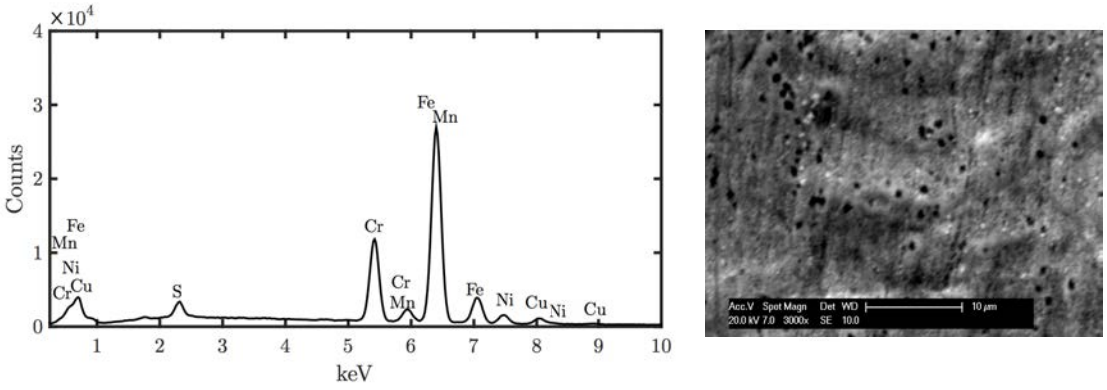

FIGURE 5.31: EDS scan of dark spots on the surface of selected LTPN specimen after EIS readings; 21 hours of immersion in produced water with mixed H_2S/CO_2 (as balance). SEM included for reference (after potentiodynamic scan).

The capacitance of the outer layer (Q_c), often used as a measure of water permeability into coatings [213], increased with increasing the immersion time in H_2S/CO_2 (Table 5.4). This implies that the top layer is becoming more permeable after longer exposure, although it cannot be used to indicate its degradation since R_c remained nearly constant during the period. For the double–layer capacitance (Q_t), no clear trend was observed due to the highly scattered data (Table 5.4).

TABLE 5.4: Parameters obtained after fitting the experimental data to the selected equivalent circuit: LTPN specimen deaerated in pure N_2 and immersed (up to 21 hours) in produced water with mixed H_2S/CO_2 (as balance)

Gas	**Immersion time (h)**	Q_c $10^2\,\mu F\,cm^2$	ζ_c	Q_t $10^2\,\mu F\,cm^2$	ζ_t	χ^2
N_2	-	4.6 ± 0.1	0.93	11.9 ± 6.3	0.99	0.031
	5	7.4 ± 0.2	0.91	10.5 ± 3.7	0.90	0.017
	9	8.2 ± 0.2	0.90	8.6 ± 3.2	0.89	0.012
H_2S/CO_2	13	8.7 ± 0.2	0.90	9.5 ± 3.9	0.89	0.013
	17	9.4 ± 0.2	0.90	11.5 ± 4.6	0.91	0.012
	21	9.9 ± 0.2	0.90	13.1 ± 5.4	0.92	0.013

5.4 Summary

The results from the electrochemical measurements showed that LTPN can be successfully applied to the 17-4 PH (H1150D) to obtain superior corrosion resistance in mixed H_2/CO_2 compared to the unmodified and HTPN materials. These results were attributed to the formation of a compound layer of mixed γ'–Fe_4N/ε–$Fe_{2\text{-}3}N$, the inner section being more corrosion resistant. Moreover, deposits of FeS_2 in the porous structure of the compound layer contributed to slow down the corrosion process. In pure gases, different responses were observed: unmodified material exhibited greater resistance in pure CO_2 and LTPN had superior performance in pure H_2S. In the latter, enhanced corrosion resistance was provided by the formation of FeS_2 on the surface. HTPN had the lowest corrosion resistance in all the environments, attributed to the presence of chromium nitrides in its structure.

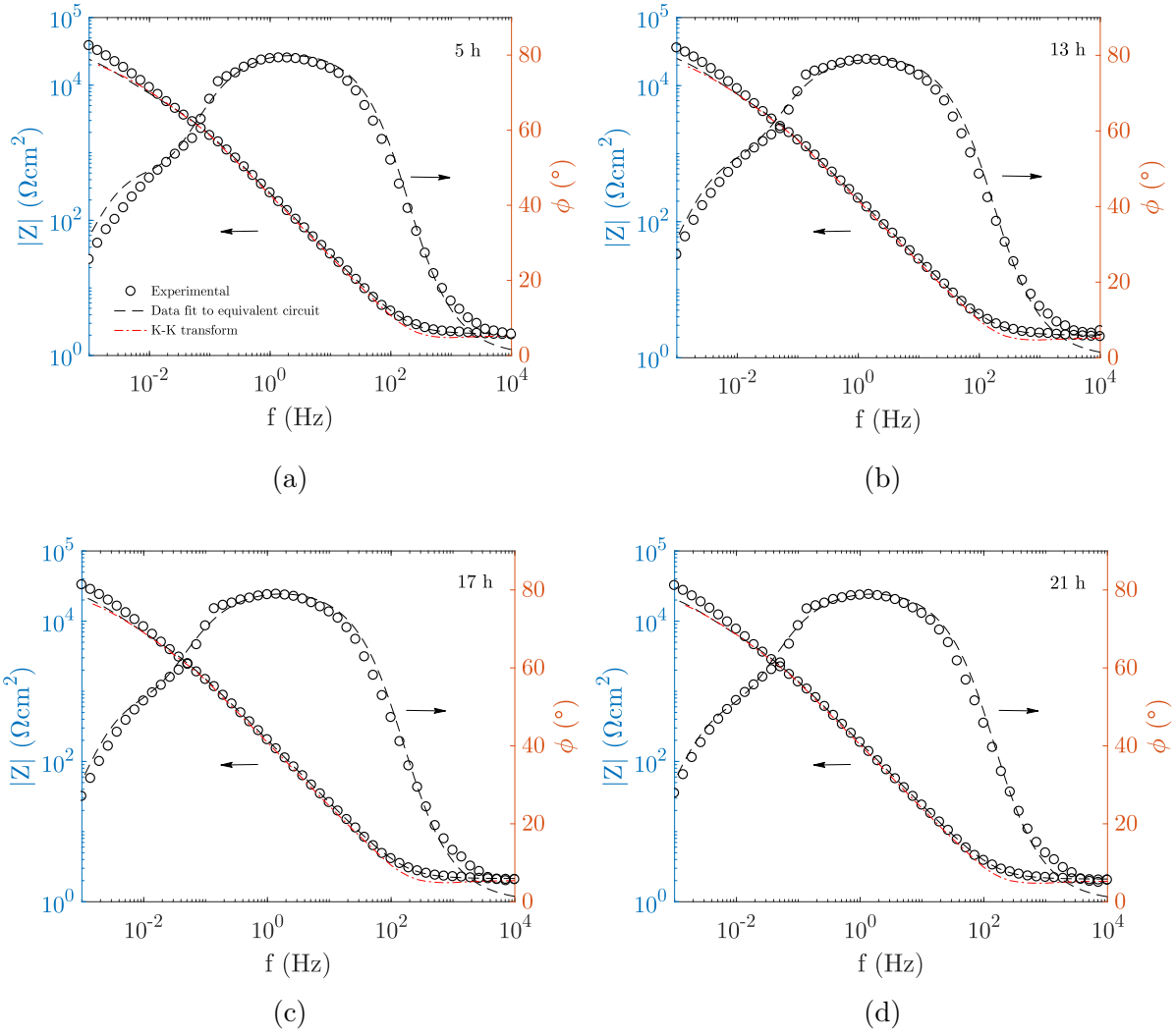

FIGURE 5.32: Bode (magnitude and phase angle) plots illustrating data fit using the selected equivalent circuit: (a)5 h; (b) 13 h; (c) 17 h; (d) 21 h

Chapter 6

Residual stress and hydrogen permeation

This chapter presents experimental and theoretical analysis on the role of the residual stress and hydrogen permeation (barrier effect) on the sulphide stress cracking (SSC) resistance of the plasma nitride layer observed in Chapter 4. The macro residual stress was determined for the low–temperature plasma nitrided (LTPN) condition and an attempt was made to determine the barrier effect of the plasma nitrided layer experimentally by using the hydrogen collection technique. This chapter also presents additional background information and discussions on hydrogen transport in different structures of the plasma ntrided layer to support the analysis of the barrier effect. The complete set of experiments carried out in this work is summarised in Figure 6.1, highlighting the topics covered in this specific chapter.

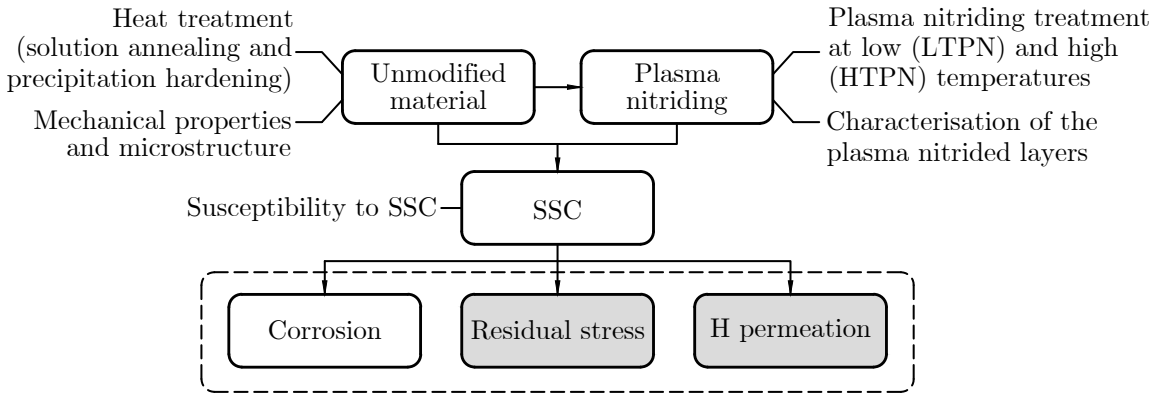

FIGURE 6.1: Schematic diagram summarising the topics covered in this chapter (highlighted in grey) within the complete experimental context of this work.

6.1 Residual stress

6.1.1 Background

Compressive residual stress can develop during plasma nitriding process, due to the following main factors [30]: (i) lattice expansion caused by nitrogen in solid solution, (ii) volume misfit between precipitates (carbides and nitrides) and the matrix, (iii) thermal stress and (iv) stress relaxation. This is of great interest to the industry since the high compressive residual stress can provide increased wear resistance [18] and fatigue strength [239] of mechanical components. The treatment parameters (e.g. time, temperature and gas mixture) and alloying elements—in general, the larger the amount of nitride–forming elements, such as chromium, aluminium and titanium, the higher the residual stress—are the main factors controlling the state of residual stress. If compound layers with mixed ε–$Fe_{2\text{-}3}$ and γ'–Fe_4N nitrides are formed, tensile (outer layer) and compressive (inner layer) stresses can arise [239]. In the diffusion zone, the residual stress is compressive and

it varies according to the concentration of nitrogen—the greater the concentration, the greater the stress, limited by the maximum solubility of nitrogen in the microstructural phase. It is expected, therefore, that this compressive state of stress will prevent crack initiation and propagation at the surface (compound layer) and subsurface (diffusion zone and substrate) since it can surpass or reduce the net tensile stress.

Figure 6.2 illustrates the macro residual stress developed in a plasma nitrided metal and shows a schematic representation of the structure of the substrate/nitrided interface. The latter, although being simplified, is convenient to demonstrate that the compressive stress is generated when the unexpanded lattice of the substrate restricts lattice expansion, caused by nitrogen in solid solution. Previous studies [240–244] have shown that peak compressive residual stress on nitrided steels can range from -500 MPa to above -2 GPa.

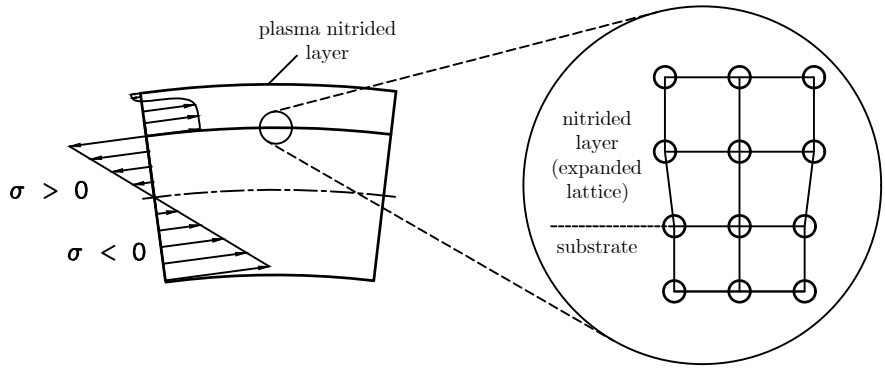

FIGURE 6.2: Schematic representation of the macro residual stress developed in a plasma nitrided metal and the structure of the substrate/nitrided interface.

Some studies have shown that there is a correlation between micro hardness and residual stress profiles of plasma nitrided steels [241, 245, 246]. Overall, as illustrated in Figure 6.3, the compressive residual stress increases with increasing the microhardness. It was noticed, for example, that abrupt decrease of the microhardness was accompanied

by an abrupt decrease of the residual stress. Some authors [245] demonstrated that the position of maximum compressive residual stress could be determined by deriving the microhardness profile with respect to depth.

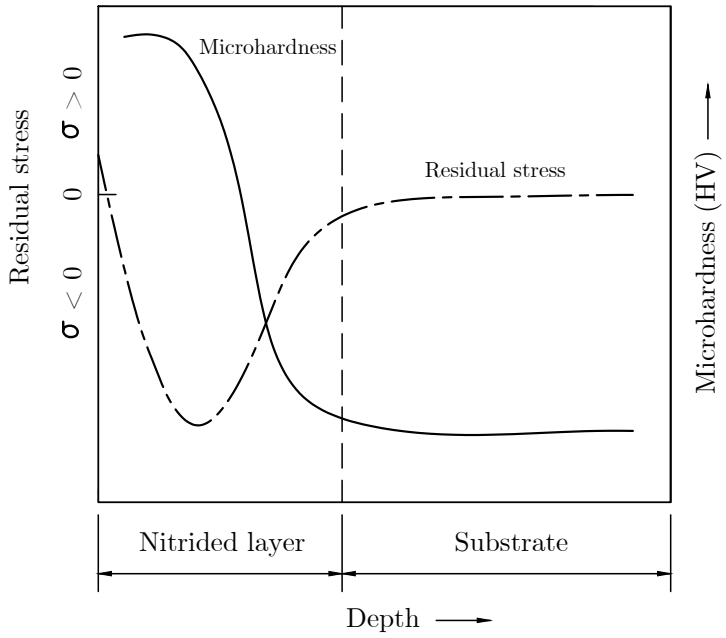

FIGURE 6.3: Schematic representation of the correlation between micro hardness and residual stress profiles on plasma nitrided steels.

Different methods have been used to quantify the residual stress of plasma nitrided materials, such as X-ray diffraction (XRD) [240, 246, 247], hole drilling [245], micro slit milling [240] and stress differential technique [242]. The XRD method [248] is a non–destructive technique that measures the strain of crystal lattices orientated along known directions relative to the surface and, assuming a linear elastic behaviour, the stress associated with the deformed lattice can be determined. To construct the residual stress depth profile, material must be successively removed from the surface, generally by electropolishing—corrections are often necessary to compensate for changes on the state of stress caused by the material removal process. Hole drilling [249] is a destructive technique

that measures the strain that corresponds to stress relaxation after a hole is machined on the surface. Micro slit milling [240] uses a similar principle, but instead of a strain gauge, it uses a scanning electron microscope (SEM) to measure the displacement of a milled slit (obtained by focused ion beam milling) after stress relaxation. The displacement is then associated with the residual stress. Similar methods, e.g. micro ring core [243], use focused ion beam milling in conjunction with imaging (SEM). In the stress differential technique [242], stress–strain curves of plasma nitrided and unmodified specimens are compared and the shift of stress in the plastic region is used to estimate the residual stress.

In many industrial applications it is common practice to induce compressive residual stress on the surface of components (e.g. by shot peening [250–253]) to prevent stress corrosion cracking (SCC). After an extensive search in the literature, it was noticed that there are no publications about the use of the apparent beneficial effects of the compressive stress developed in plasma nitrided steels to specifically overcome SCC or sulphide stress cracking (SSC). Despite that, there are recent publications [254–257] investigating the fatigue behaviour of nitrided structures and their main findings are summarised in the next paragraph. Although these studies were conducted with different loading conditions (cyclic loading) than those used on SSC experiments (constant loading), they are useful in illustrating the fracture mode of the nitrided layer.

Studies conducted to investigate the fatigue behaviour of plasma nitrided steel with tempered martensitic structure [254] showed that the nitrided layer—composed by a compound layer with mixed ε–$Fe_{2\text{-}3}N$ / γ'–Fe_4N nitrides and diffusion zone—was very sensitive to brittle fracture. By applying constant amplitude loading (about 80% of the yield strength of the material), numerous cracks nucleated on the surface and complete

fracture occurred after less than 1000 cycles. The authors attributed this detrimental effect—plasma nitrided showed lower resistant compared with the unmodified material—to the relaxation of the compressive residual stress on nitrided specimens, although the reason for this phenomenon was not clarified. When specimens of the plasma nitrided material were submitted to standard uniaxial tensile test until rupture, cracking with spiral pattern was observed on the surface due to the brittle characteristic of the compound layer. SEM micrographs revealed that cracks initiated from pores on the nitrided structure. It was also noticed that the thin nitrided layer did not affect significantly the tensile strength compared with the unmodified material (about 2% increase after nitriding), but the ductility was compromised (reduced by approximately 60% after nitriding).

Similar studies [255, 257] have shown that fatigue crack growth limits of a high strength alloy steel improved after plasma nitriding under constant amplitude loading. The compressive residual stress (up to -1 GPa) was considered the main contributor to the increase of the fatigue life. SEM images [255] revealed that fracture occurred predominantly by transgranular cracking for specimens plasma nitrided at relatively low temperatures whereas transgranular cracking dominated when nitriding was performed at elevated temperatures (600 °C).

6.1.2 Experimental

Selection of the test method

Since it was out of the scope of this project to perform a fully comprehensive investigation of the compressive residual stress developed by plasma nitriding, a simple technique (curvature method) was used to quantify it, although it was recognised that the methods described in section 6.1.1 would provide more reliable and detailed results. Those techniques, specially XRD, are therefore recommended for future investigations (Chapter

8). Macro residual stress was experimentally determined only on specimens treated by low–temperature plasma nitriding (LTPN) and, by using correlations of the residual stress with hardness profiles, the compressive stress on specimens treated by high–temperature plasma nitriding (HTPN) was evaluated by comparison.

Due to lattice expansion, nitrided layers on thin strips or discs are stretched and cause the substrate to bend and, by measuring the curvature, it is possible to determnine the corresponding residual stresses. The classic Stoney equation [258], originally developed to quantify the stress generated during metallic film deposition, was used to determine the compressive residual stress on plasma nitrided specimens. To account for biaxial deformation, the Poisson's ratio was included [259] and the formula became

$$\sigma_{\mathrm{N}} = \frac{E_{\mathrm{s}} t_{\mathrm{s}} \kappa}{6 t_{\mathrm{N}} \left(1 - \nu_{\mathrm{s}}\right)} \tag{6.1}$$

where σ_{N} is the compressive residual stress in the nitrided layer with thickness t_{N} and E_{s}, t_{s} and ν_{s} are the elastic modulus, thickness and Poisson's coefficient of the substrate, respectively, and κ is the curvature (reciprocate of the radius of curvature ρ, Figure 6.4). The main following assumptions were considered: (i) the plasma nitrided layer and the substrate have uniform thickness; (ii) the plasma nitrided layer is thin compared with the substrate and with the radius of curvature; (iii) both materials (film and substrate) are homogeneous, isotropic and deformation occurs within their elastic limits.

Procedure

A disc with 90 mm diameter and 12 mm thick was cut from the source material with a water-jet cutting machine and submitted to low–temperature plasma nitriding (420 °C for 10 h in 25 vol.% N_2 + 75 vol.% H_2 using the active screen method) following the same

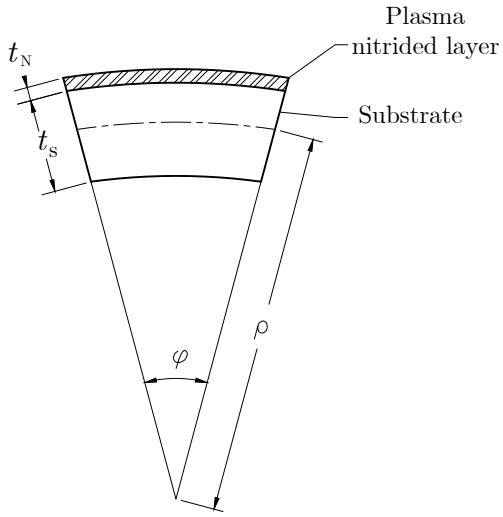

FIGURE 6.4: Schematic representation of bending the LTPN disc.

procedures used for SSC and corrosion specimens (section 3.1.2.3). After nitriding, the thickness of the disc was reduced to approximately 1 mm by wire–cut electrical discharge machining (EDM) and polishing.

The deflection of the disc ($\delta = \rho\,[1 - \cos\,(R/\rho)]$, R being the radius of the disc) was measured from images (lateral view) taken from six different orientations. By using CAD software, the curvature was geometrically determined, as illustrated in Figure 6.4, and Eq. 6.1 was used to determine the residual stress.

The stress differential technique [242] was also used to estimate the residual stress in LTPN. A standard monotonic tension test method was used to deform round tension specimens (gauge diameter of 4 mm and gauge length of 20 mm, manually grinded to 600 grit SiC or P1200) until complete rupture. The shift of stress ($\Delta\sigma$) in the plastic region of LTPN with respect to unmodified material, was used to estimate the average residual stress σ_N by [242]

$$\sigma_N =\approx \Delta\sigma \frac{S_s}{S_N} \tag{6.2}$$

where S_s and S_N are the cross sectional areas of the substrate and plasma nitrided layer, respectively. The images taken after rupture were used to analyse the behaviour of the nitrided case under overloading conditions.

6.1.3 Results and discussion

The macro compressive residual stress on LTPN specimens, determined by the curvature method, was -(1.0 ± 0.1) GPa. This value suppresses the maximum tensile stress of (773 ± 12) MPa applied in the SSC experiments and may have prevented crack nucleation and propagation. Assuming that SSC occurs by the mechanism described in section 7.2.1, there is no driving force (tensile stress) for decohesion of the iron lattice—that would occur due to the repulsive effect of hydrogen—and thereby cracking is prevented.

The average residual stress estimated by the stress differential approach was approximately -1.6 GPa. The stress strain curves are shown in Figure 6.5. The yield strength after plasma nitriding was approximately 3% greater ($\approx$ 800 MPa) compared to the substrate (773 MPa). It can also be noticed a small reduction in ductility after plasma nitriding (18% compared with 22% in the unmodified material). These results showed that the mechanical response of surface–modified specimens is dominated by the substrate material.

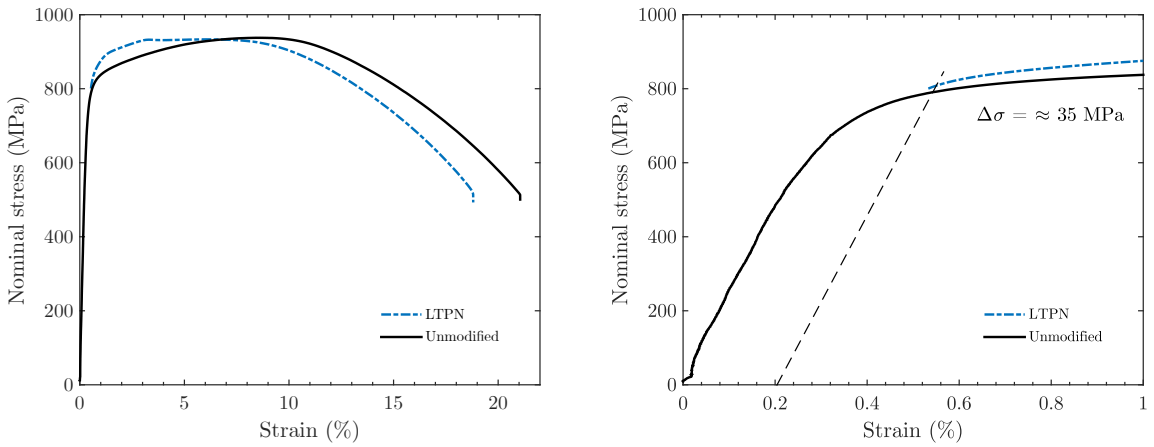

FIGURE 6.5: (a) Stress-strain curve of unmodified and LTPN and (b) amplified view.

Figure 6.6 shows SEM images of the surface of plasma nitrided specimens after rupture. The brittle behaviour of the nitrided layer can be clearly noticed. Along the surface, numerous cracks were formed perpendicular to the applied stress and this indicates that the outer layer was not capable of sustaining the substantial plastic deformation of the substrate. It is also observed that the nitrided layer re accommodated in the circumferential direction due to the different mechanical responses to transversal deformation (Poisson's effect). As a result, it seems that fracture also occurred following the direction of maximum shear stress of the ductile substrate, i.e 45° with respect to the axial direction, since the nitrided layer still attached to the core. In fact, a pattern with fractures at 45° can be seen along the surface (Figure 6.6a and 6.6b). These results demonstrate the brittle nature of the plasma nitrided layer and further analysis are recommended in Chapter 8 to identify maximum overloading conditions that can be sustained without cracking.

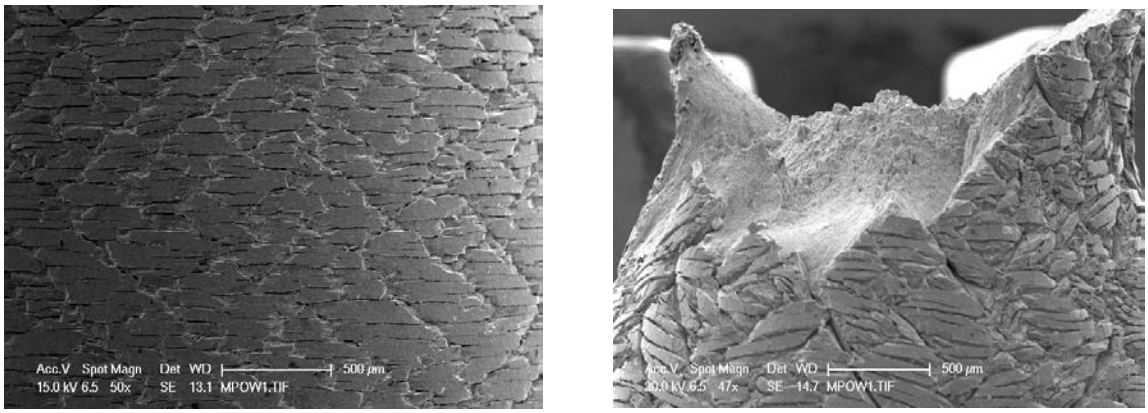

(a) (b)

FIGURE 6.6: SEM images of LTPN specimens after being ruptured in the tensile test (a) overview of the surface and (b) view of the fractured surface.

The residual stress on HTPN material was not quantified, but it is possible to infer that its magnitude was lower than that of LTPN by comparing their nitrogen composition (Figure 3.12) and microhardness (Figure 3.13) profiles—considering that these quantities are correlated, as observed earlier [241, 245, 246]. Comparing with LTPN, the microhardness was about 40% lower and the nitrogen composition was more than 20% lower near the surface. Since no cracking was observed on HTPN specimens during the SSC experiments, it is also possible to conclude that the compressive residual stress, even being smaller than that of LTPN, was able to neutralise or reduce the net tensile stress to a level sufficiently low to avoid cracking.

6.2 Hydrogen permeation

6.2.1 Literature review and background

There has been very little research on the entry and transport of hydrogen in martensitic stainless steel modified by plasma nitriding. Therefore, in addition to martensitic structures, this section briefly reviews studies conducted on the hydrogen permeation of pure iron, carbon steel and austenitic stainless steel after being modified by different nitriding techniques. Correspondences with martensitic structures are made where appropriate.

In most cases referenced in this section, hydrogen permeation measurements were performed with standard or modified versions of Devanathan–Stachurski (D-S) electrochemical cells [260], schematically illustrated in Figure 6.7. The basic configuration comprises two electrochemical cells separated by a metallic membrane, made from the material being investigated. In one cell (entry side), hydrogen—generated by cathodic polarisation at a constant current density—is adsorbed at the surface, absorbed into the metal and diffuses through the membrane. On the opposite surface (exit side), hydrogen is oxidised and the recorded anodic current is used to determine the flux of hydrogen through the membrane by using Faraday's law.

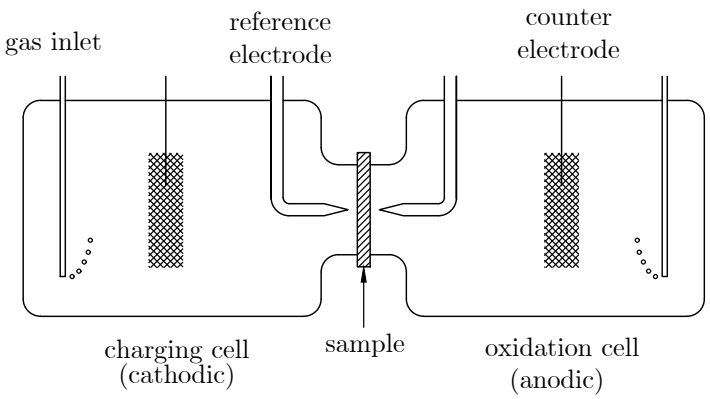

FIGURE 6.7: Schematic representation of a Devanathan–Stachurski (D-S) electrochemical cell.

In hydrogen permeation studies, the barrier effect of the nitrided layer is generally quantified by the diffusion coefficient of hydrogen in the substrate material, mass flow rate of hydrogen (permeation rate) and hydrogen trapping. These concepts are therefore briefly reviewed in the next paragraphs.

In simple terms, diffusion coefficient may be defined as the ability of a solute (in this case hydrogen) to move (random atomic motion) between two points in a solid (in this case the nitrided layer) when a concentration gradient of hydrogen is maintained between these points. In analogy with energy transport during heat transfer, the diffusion coefficient—related to the mass transport in solids—is equivalent to the thermal conductivity. Considering the simple case of diffusion in one direction (e.g. along x axis), Fick's first law of diffusion (Eq. 6.3) states that the diffusion coefficient (or diffusivity) D is the constant of proportionality between the mass flow rate of hydrogen per unit area perpendicular to mass transport direction, i.e. hydrogen flux J ($\mathrm{kg\,m^{-2}\,s^{-1}}$) and the concentration gradient of hydrogen $\partial C/\partial x$ ($\mathrm{kg\,m^{-3}\,m^{-1}}$). The units of D are therefore $\mathrm{m^2\,s^{-1}}$. Assuming that the diffusion coefficient is independent of the concentration, a constant gradient of concentration and thereby a constant flux is obtained when a steady–state condition is achieved. Permeability is often expressed by the anodic current density ($\mathrm{A\,cm^{-2}}$), analogous to the hydrogen flux.

$$J = -D\frac{\partial C}{\partial x} \tag{6.3}$$

At the transient condition, the concentration profile is time–dependent and Eq. 6.3 can be derived to determine the rate of change of concentration with time at any position. The resultant partial differential equation (Eq. 6.4) represents the Fick's second law of

diffusion, assuming that diffusivity is constant and that diffusion is one–dimensional [261].

$$\frac{\partial C}{\partial t} = D\frac{\partial^2 C}{\partial x^2} \tag{6.4}$$

Fick's first and second laws of diffusion assumes that mass transport occurs in a continuous and isotropic medium. This approach is valid for hydrogen diffusing through interstitial sites, but it does not account for hydrogen that gets trapped to inhomogeneities such as surface deffects, grain boundaries, dislocations and vacancies. If hydrogen trapping is considered, Eq. 6.4 become [262]

$$\frac{\partial C_{\mathrm{H,L}}}{\partial t} + \frac{\partial C_{\mathrm{H,tr}}}{\partial t} = D\frac{\partial C_{\mathrm{H,L}}}{\partial x^2} \tag{6.5}$$

where $C_{\mathrm{H,L}}$ is the instant concentration of hydrogen diffusing through interstitial lattice sites and $C_{\mathrm{H,tr}}$ is the concentration of trapped hydrogen. If spatial distribution of traps and trap occupancy are known, they can be substituted in Eq. 6.5 and the effective permeability and diffusivity can be determined. Examples of formulations can be found elsewhere [263]. Traps are generally classified as reversible or irreversible, according to their binding energies. Due to the low energy of reversible traps ($-E_{\mathrm{b}} < 30\,\mathrm{kJ\,mol^{-1}}$), hydrogen can be released and become additional source of diffusible hydrogen in the matrix. Conversely, hydrogen remains trapped if the binding energy is sufficiently large ($-E_{\mathrm{b}} > 50\,\mathrm{kJ\,mol^{-1}}$ [264]). A recent review on hydrogen embrittlement of steels [265] presented a summary of published binding energies and pointed that classifying traps by their energy levels fails to account for variations of the environment (e.g. temperature) and time. Evidence of reversible and irreversible trapping in permeation studies can be

obtained by analysing the build up and decay transients of hydrogen flux, as exemplified later in this section.

Since nitrided materials comprise different structures (compound layer, diffusion zone and unmodified substrate), different diffusion coefficients and trap intensities are expected in each section. A practical challenge that arises due to the small thickness of the compound layer (10 µm or less, in average) is to machine thin membranes containing only the compound layer. One strategy that has been adopted by many authors [21, 23, 26, 27] consists of measuring the hydrogen flux for membranes (from 40 µm up to 1 mm thick) containing different combinations of the nitrided structure and substrate and deducing each diffusion coefficient from effective diffusivities. For example, if a membrane contains the compound layer and the diffusion zone, the effective diffusion coefficient $D_{\mathrm{c+d}}$ can be determined. If the diffusion coefficient of the diffusion zone D_{d} can be obtained by using a membrane containing this phase only, this value can be used in conjunction with $D_{\mathrm{c+d}}$ to obtain the diffusivity of the compound layer D_{c}, assuming that these quantities can be related by $L_{\mathrm{c+d}}/D_{\mathrm{c+d}} = L_{\mathrm{c+d}}/D_{\mathrm{c+d}} + L_{\mathrm{d}}/D_{\mathrm{d}}$ [21]. This relation assumes continuity at the interfaces of the layers; $L_{\mathrm{c+d}}$, L_{c} and L_{d} being their respective thicknesses. The concentration profiles can then be then evaluated at the steady state condition by [21]

$$i_p^{\infty} = \frac{D_{\mathrm{eff}} C_{0,\mathrm{c}} F}{L} = \frac{D_{\mathrm{c}} \left(C_{0,\mathrm{c}} - C_{\mathrm{d}}\right) F}{L_{\mathrm{c}}} = \frac{D_{\mathrm{d}} \left(C_{\mathrm{d}} - C_{\mathrm{s}}\right) F}{L_{\mathrm{d}}} = \frac{D_{\mathrm{s}} C_{\mathrm{s}} F}{L_{\mathrm{s}}} \tag{6.6}$$

where i_p^{∞} is the steady state current density (or permeation rate); F is the Faraday constant; D_{eff} is the effective diffusivity of the membrane comprising the compound layer, the diffusion zone and the substrate; $C_{0,\mathrm{c}}$, C_{d} and C_{s} are the concentrations of hydrogen in the entry side and on each interface, as illustrated in Figure 6.8, a typical concentration profile obtained by this approach.

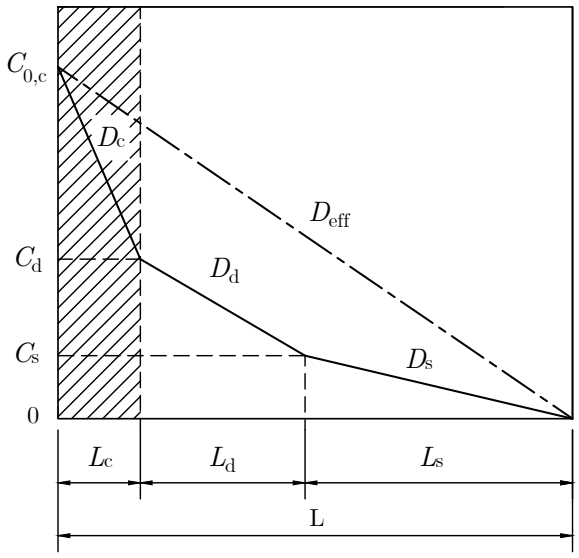

FIGURE 6.8: Schematic representation of typical steady-state concentration profile in nitrided iron. C, D and L refer to concentration, diffusivity and thickness, respectively. Subscripts: c (compound); d (diffusion), s (substrate) and eff (effective). Adapted from [21].

One of the first reports about the reduction of hydrogen absorption in nitrided steels [266] was published in the late 1970s. This study showed that the nitrided layer with approximately 100 µm effectively reduced the absorption of hydrogen—quantified by vacuum extraction and mass spectroscopy techniques—when it was exposed to an aggressive environment containing H_2S and NaCl. A decade later, a report on the hydrogen permeation in nitrided steels—obtained by ion implantation—using the electrochemical method (D-S cell) [267], showed that a thin layer (100 nm) of iron nitride (ε–Fe_2N) effectively acted as a barrier for the entry and transport of hydrogen into the substrate material. The lower permeability was attributed to the lower solubility of hydrogen in the nitrogen–containing layer and partially to hydrogen trapping. The diffusion coefficient decreased from $3.3 \times 10^{-7}\,cm^2\,s^{-1}$ (unmodified material) to $4.5 \times 10^{-8}\,cm^2\,s^{-1}$ (nitrided material).

Subsequent studies conducted with iron [21, 23, 25, 27, 28], low–alloy high–strength pipeline steel [22], high strength alloy steels [24, 29], austenitic stainless steel [26] and structural steels [268–271] provided additional evidence of the barrier effect of the nitrided layer. Some of these results are summarised in Table 6.1.

TABLE 6.1: Typical structures and diffusion coefficients of different parts of nitrided cases obtained for different materials

Material	**Nitriding method**	**Compound layer (thickness)**	**Diffusion coefficient (m^2s^{-1})**		**Ref.**
			Substrate	**Nitrided layer**	
Low carbon steel	Nitrogen ion implantation	ε–Fe_2N (100 nm)	D_s=3.3 × 10^{-11}	D_{eff}=4.5 × 10^{-12}	[267]
Iron	Plasma nitriding	γ'–Fe_4N (10 µm)	D_s=7.3 × 10^{-9}	D_{eff}=1.5 × 10^{-9} D_c=4.1 × 10^{-12} D_d=6.1 × 10^{-10}	[21]
Iron	Plasma nitriding	ε–$Fe_{2-3}N$ + γ'–Fe_4N (10 µm)	D_s=8.0 × 10^{-9}	D_c=1.9 × 10^{-12} D_d=7.2 × 10^{-10}	[27]
LAHSS[(a)] (API-5L-X65)	Nitrogen ion implantation	Not specified	D_s=1.5 × 10^{-10}	D_{eff}=5.6 × 10^{-12} D_{c+d}=5.3 × 10^{-16}	[22]
LAHSS (AISI 4140)	Plasma nitriding	ε–$Fe_{2-3}N$ + γ'–Fe_4N (7-8 µm)	D_s=1.0 × 10^{-10}	D_{eff}=4.9 × 10^{-11}	[24]
LAHSS (AISI 4340)	Plasma nitriding	γ'–Fe_4N (8 µm)	D_s=2.8 × 10^{-10}	D_{eff}=6.5 × 10^{-11}	[29]
ASS[(b)] (AISI 316)	Plasma nitriding	Not specified (8.5 µm)	D_s=1.7 × 10^{-16}	D_{eff}=2.1 × 10^{-16} D_{c+d}=8.7 × 10^{-16}	[26]

[(a)]high–strength low–alloy steel; [(b)]austenitic stainless steel; subscripts: c = compound layer, d = diffusion layer, s = substrate, and eff = effective (compound + diffusion + substrate)

Overall (Table 6.1), the nitrided layer has lower diffusion coefficient than that of the unmodified substrate, with D_{eff} being lower than D_{s} in most of the cases. For the materials investigated, except for austenitic substrate, the reduction of the mobility of hydrogen was more pronounced in the compound layer, with D_{c} being at least one order of magnitude lower than D_{d}. The lower diffusivity after nitriding was attributed to surface and barrier effects.

The surface effect is associated with the reduction of the entry of hydrogen into the compound layer. As noticed in some studies [21, 23], hydrogen uptake—estimated by comparing the initial concentration of hydrogen on the surface of separated membranes containing plasma nitrided and unmodified structures—reduced about 18 times after nitriding. This reduction was reflected in the hydrogen permeation profiles, in which the permeation rate for the nitrided membrane remained nearly constant with increasing charging time—as opposed to the increase observed for the unmodified membrane. This behaviour was explained [21] in terms of the surface characteristics of each membrane: considering that the nitrided material has superior tribological properties, the disintegration (i.e. increase of the actual working surface and decrease of actual cathodic current density) of the compound layer due to prolonged charging would be lower than that of the unmodified material and therefore the entry of hydrogen will rise at a lower rate with increasing the time. No evidence of surface deterioration was provided in this case and the physical cause of the reduced hydrogen absorption still unclear.

The barrier effect corresponds to the reduced mobility of hydrogen in different structures (compound layer, diffusion zone and substrate), evaluated by their diffusion coefficients. In general, $D_{\text{c}} < D_{\text{d}} < D_{\text{s}}$. The lower diffusivity in compound layers was mainly attributed to the accumulation of hydrogen in ε–$Fe_{2\text{-}3}$ and γ'–Fe_4N structures due to their higher hydrogen solubility. In practice, hydrogen trapping to compound layers

have been estimated from permeation studies by analysing hydrogen extraction [25] or successive charging transients [29]. In the latter, it was observed that the greater diffusion coefficient determined from the second charging transient could indicate that irreversible trapping sites were filled during the first charging and lattice diffusion therefore increased when hydrogen started to be generated again in the entry side of the membrane. Traps seemed to be predominantly located in the compound layer, since the diffusion coefficients—determined from the first charging transient—of membranes containing compound and diffusion zones were smaller that those in which the compound layer was removed.

An alternative approach to quantify hydrogen trapping in each part of the nitrided layer [28] involves analysing hydrogen desorption (i.e. hydrogen decay or hydrogen extraction) transients from membranes containing the compound layer and the diffusion zone. Considering that diffusible hydrogen will follow the Fick's law of diffusion, the amount of trapped hydrogen can be deduced by subtracting the theoretical desorption rate of diffusible hydrogen from the total desorption rate determined experimentally in both sides of the membrane. On the exit side of the membrane with thickness $x = L$, the desorption rate of diffusible hydrogen, J_{Hd} ($\mathrm{kg\,m^{-2}\,s^{-1}}$), can be described as [28, 272]

$$J_{\mathrm{Hd}}(\mathrm{x{=}L}) = J_{\infty}\left[1 - \frac{2L}{\left(\pi D_{(\mathrm{c+d})}t\right)^{1/2}}\sum_{n=0}^{\infty}\exp\left(-\frac{(2n+1)^2\,L^2}{4D_{(\mathrm{c+d})}t}\right)\right] \tag{6.7}$$

where J_{∞} is the steady state flux of hydrogen at the beginning of desorption ($t = 0$) and $D_{(\mathrm{c+d})}$ is the effective diffusion coefficient obtained for the whole membrane comprising the compound layer and the diffusion zone. The amount of trapped hydrogen at $x = L$, Q_{Ht} ($\mathrm{mol\,m^{-2}}$), can then be estimated by

$$Q_{\mathrm{Ht}}(x = L) = \int_0^{\infty}(J_{\mathrm{H}} - J_{\mathrm{Hd}})\;\mathrm{d}t \tag{6.8}$$

where J_H is the flux of hydrogen obtained experimentally. By following similar procedure for the entry side of the membrane, the total amount of trapped hydrogen can be determined. A different approach was used to quantify the trapping in the diffusion zone, assuming that the diffusion path was longer than the actual thickness of a membrane containing the diffusion section only [27]. By comparing the results from the single layer and two–layer membranes, the authors [28] concluded that trapping was greater in the compound layer, in agreement with previous observations. Figure 6.9 illustrates the desorption profiles on the exit side of the nitrided membrane.

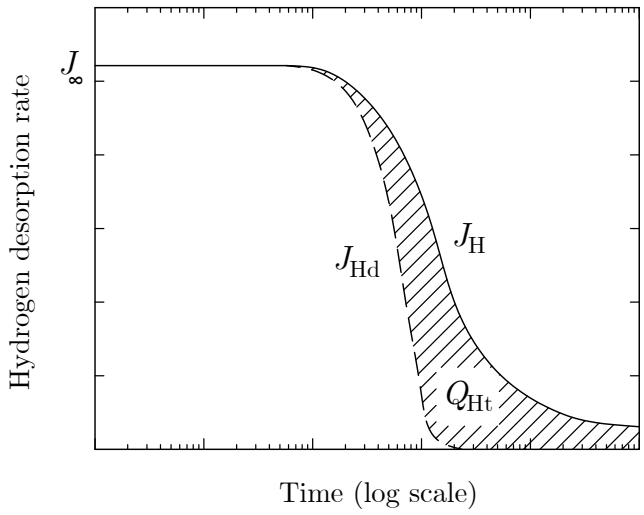

FIGURE 6.9: Schematic representation of the hydrogen desorption profile used to quantify hydrogen trapping.

A similar approach was used to evaluate the transport of hydrogen in austenitic structure [26] and, despite the greater diffusivity on the nitrided membrane compared to the unmodified material, the nitrided layer reduced the hydrogen uptake by the substrate. The steady–state concentration profiles (Figure 6.10) illustrate that the concentration of diffusible hydrogen (C_{Hd}) in the substrate is lower and trapped hydrogen (C_{Ht}) is greater when the material is nitrided.

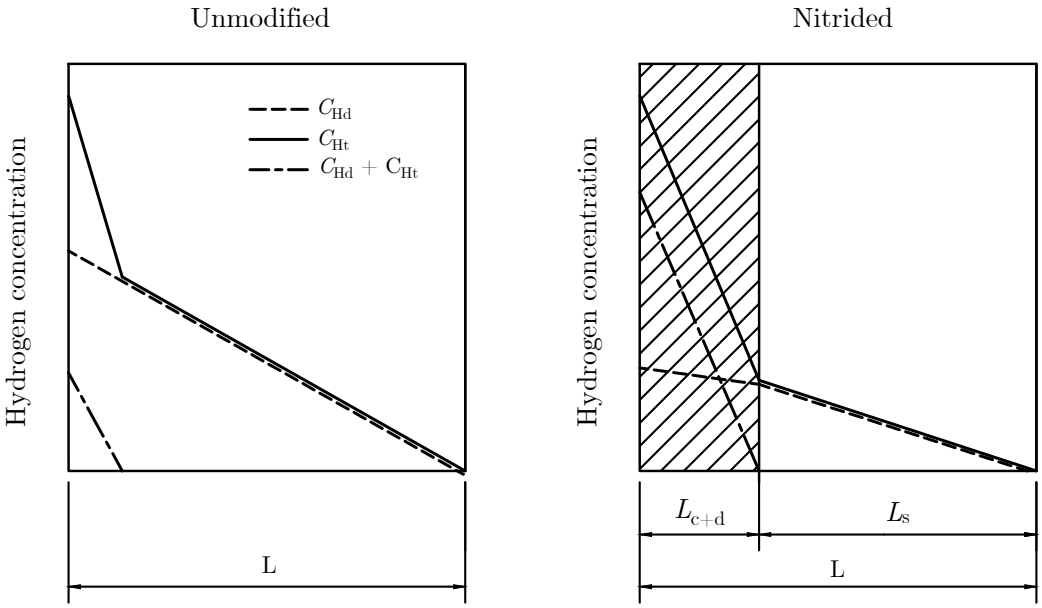

FIGURE 6.10: Schematic representation of hydrogen composition profiles obtained for an austenitic stailess steel: (a) unmodified and (b) nitrided. Adapted from [26].

6.2.2 Experimental

Selection of the test method

Based on the review presented in the previous section, electrochemical methods using Devanathan-Stachurski cells seemed to adequately quantify the barrier effect of plasma nitrided layers. But, unfortunately, this equipment was not available in any research group involved in this project and it was not viable to construct a new set–up.

The hydrogen collection technique [140], a tool developed to monitor the hydrogen flux for corrosion management in the oil and gas industry, was selected for this project. This is a non–destructive technique used to quantify the hydrogen that diffuses through the walls of components (e.g. tubing and vessels) transporting or storing fluids containing sources of hydrogen (e.g. H_2S). As schematically illustrated in Figure 6.11, a probe is magnetically

attached to the external surface and, assuming that diffusible hydrogen that crossed the steel wall will recombine to form H_2 at the exit surface, the hydrogen content can be determined—H_2 present in the air stream conducted by the capillary tubing is detected by an amperometric sensor. The hydrogen collection technique was used successfully in hydrogen permeation studies of carbon steels and structural steels [141, 273].

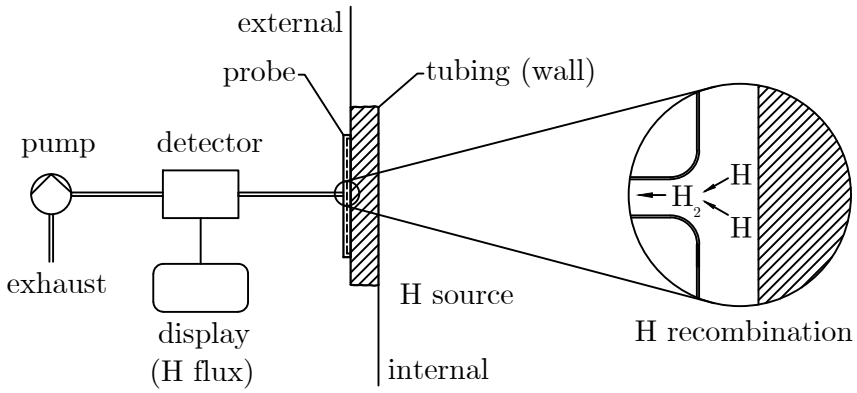

FIGURE 6.11: Schematic representation of the hydrogen collection method.

Apparatus and test procedure

To perform hydrogen permeation measurements, an acrylic vessel with capacity for 1 L of solution (Figure 6.12) was designed. Unmodified and LTPN discs with 90 mm diameter and 0.5-1 mm thick were prepared as described in section 6.1.2. The discs were assembled on the side of the vessel, keeping the nitrided face in contact with the test solution.

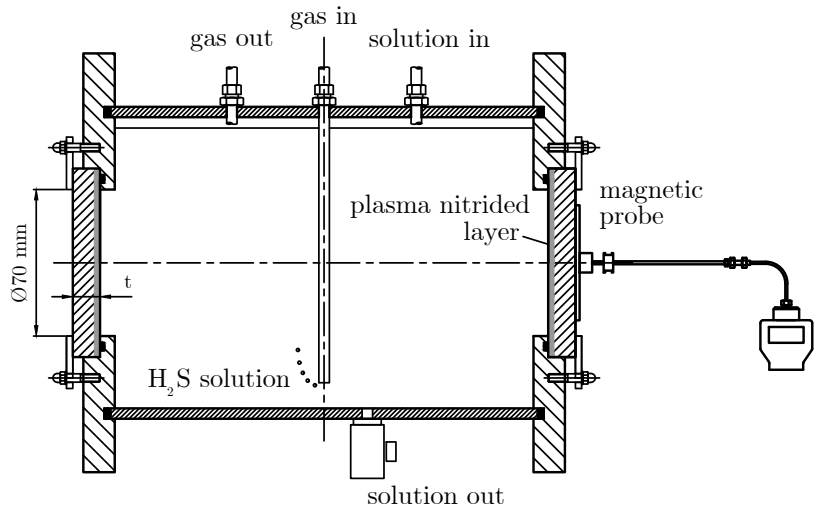

FIGURE 6.12: Schematic illustration of the acrylic vessel used designed for the hydrogen permeation tests.

The vessel was filled with the test solution (i.e. simulated produced water with $165\,\mathrm{g\,L^{-1}}$ NaCl and the pH adjusted to (4.5 ± 0.2)). All the measurements were conducted at $(23 \pm 2)\,^{\circ}\mathrm{C}$ and atmospheric pressure. After sealing the vessel, the solution was de aerated by purging with N_2 for 3 hours and then the test gas (pure H_2S) was flowed in at $2\,\mathrm{L\,min^{-1}}$ and reduced to $50\,\mathrm{mL\,min^{-1}}$ after saturation. Iodometric titration was performed after 1 hour of exposure to determine the concentration of H_2S and confirm that a saturation condition was reached (approximately $2\,\mathrm{g\,L^{-1}}$). The probe was attached to the exit side of each sample and the flux was continuously measured by a commercial kit (Hydrosteel 6000) which quantifies hydrogen by the collection method.

The first experiment was conducted in H_2S–saturated environment with unmodified and low–temperature plasma nitrided (LTPN) specimens and flux readings were recorded for 14 days. After the end of the experiment, the test gas was turned off and the solution was purged with N_2 for 60 minutes before removing the samples. The samples were cleaned with acetone immediately after being removed, dried with air and their surfaces examined using optical and SEM microscopes.

6.2.3 Results and discussion

The concentration of H_2S, measured after 1 hour of exposure, was $1.67\,g\,L^{-1}$. The hydrogen flux readings in both unmodified and LTPN specimens remained stable during all the test period. The absolute value of the flux 1-2 $\times$ $10^{-9}\,mol\,m^{-2}\,s^{-1}$ was equivalent to that of the background reading in the laboratory atmosphere, suggesting that hydrogen did not reach the exit side of the discs (0.5 and 1 mm thick) during 14 days of exposure. The experiment was therefore interrupted and the possible reasons for these unexpected results are discussed later in this section.

Figure 6.13 shows photomacrographs of unmodified and LTPN specimens after hydrogen permeation measurements. Many corrosion pits, revealed by the dark deposits of iron sulphide (FeS_2), can be seen on the surface of the unmodified specimens. The plasma nitrided sample was apparently more resistant to localised corrosion since fewer pits were observed. The darker colour on the centre of the LTPN specimen compared with some regions on the edges suggests that most of the surface was covered with iron sulphide.

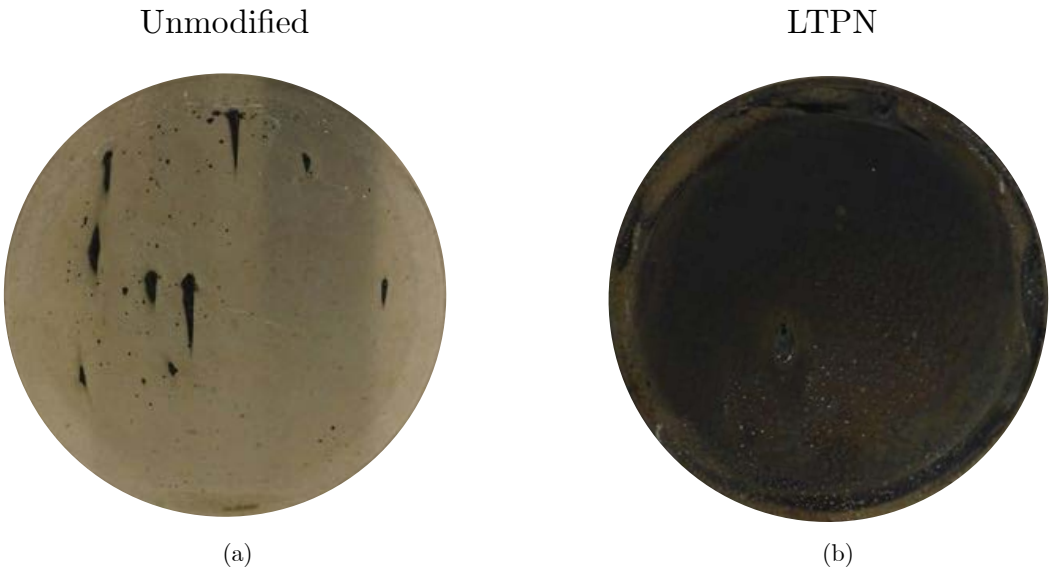

FIGURE 6.13: Photomacrographs of (a) unmodified and (b) LTPN specimens after 14 days of exposure to pure H_2S.

Figure 6.14 shows the morphology of the surface of LTPN specimens. The images revealed that the film of iron sulphide had a crystalline structure with grains approximately 1 mm wide. A dendritic–like pattern was observed and this may be associated with the fast growth of iron sulphide presumably due to the high concentration of H_2S. There are no reports of this type of growth in the literature and its origins and mechanisms still unclear. Besides, this phenomenon was not observed in the SSC experiments in which samples were exposed to pure H_2S for 30 days.

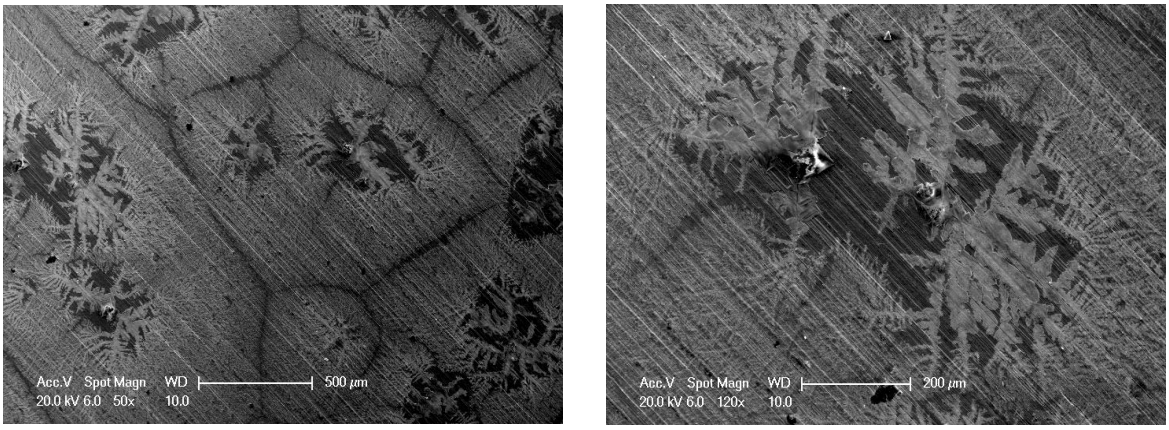

(a) (b)

FIGURE 6.14: SEM micrograph (top view) of the LTPN sample: (a) film of iron sulphide; (b) amplified view.

Cause analysis for invariant flux

A root cause analysis (RCA) process was used to identify potential reasons for the invariant flux through the plates during the hydrogen permeation experiments. As shown in the cause and effect diagram in Figure 6.15, the causes were grouped as being related to the equipment, to the experimental procedure, to the material and to phenomenological aspects.

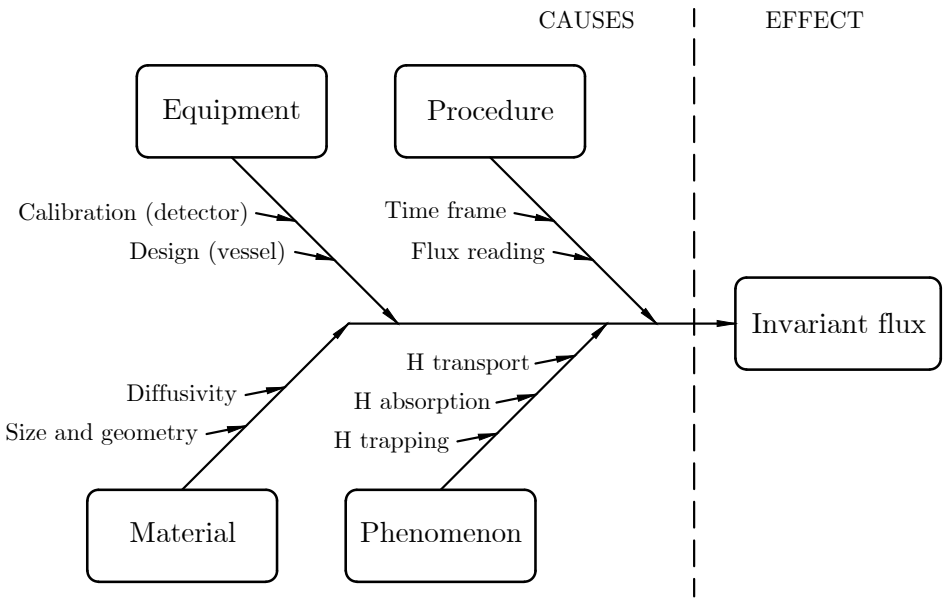

FIGURE 6.15: Root cause analysis to identify the reasons for the invariant flux obtained by the hydrogen collection method.

None of the aspects related to the equipment (i.e. calibration issues and poor design of the permeation vessel) seemed to be the cause, since the permeation kit was sent to the supplier for calibration after preliminary measurements and the vessel was considered adequate—it passed the leak test when the solution was saturated with H_2S.

Incorrect flux readings and insufficient time for flux rise were identified as possible causes related to the experimental procedure. The frequency of reading (continuous during the first 90 minutes and intermittent afterwards) was considered appropriate. Moreover, it seemed that any hydrogen emanating from the exit surface would be collected by the capillary, since the metallic probes were correctly attached to the discs (as in Figure 6.11). To verify the time frame, Fick's law of diffusion was used to estimate the flux transients for both unmodified and plasma nitrided conditions.

By solving Eq. 6.4 numerically for a disc made of the unmodified 17-4 PH and assuming that the concentration of hydrogen is constant on the entry side ($0.1\,\mathrm{mol\,L^{-1}}$) and zero at

the exit side (i.e. all hydrogen leaving the surface immediately combines to form hydrogen gas) and that the diffusion coefficient of the unmodified material is $2.8 \times 10^{-13}\,\mathrm{m^2\,s^{-1}}$[66], it is estimated that steady–flux J_∞ on the exit side of the disc ($L = 0.5\,\mathrm{mm}$) would be achieved after 3-4 days, as shown in Figure 6.16a. The corresponding concentration profiles (transient and steady states) are shown in Figure 6.16b.

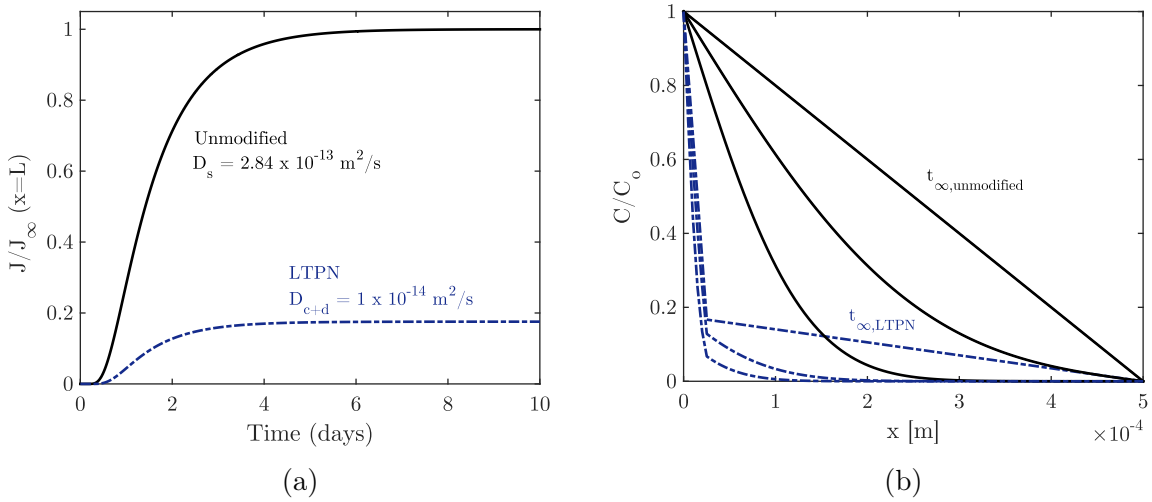

FIGURE 6.16: Results from the numerical solution of Fick's law for unmodified and LTPN conditions: (a) hydrogen flux at the exit side and (b) concentration profile.

For discs comprising the plasma nitrided layer (LTPN) and the substrate material, the time to achieve steady–state flux would be longer (about 5-6 days), as shown in Figure 6.16a. The expected delay is due to the smaller diffusivity of the nitrided layer, as discussed earlier. The numerical solution of Eq. 6.4 for the composite disc (nitride layer and substrate), considered the following assumptions: (i) the thickness of the disc was $L = 0.5\,\mathrm{mm}$ with a $20\,\mu\mathrm{m}$ thick plasma nitrided layer (compound and diffusion zone) facing the test solution; (ii) the concentration on the entry side of the disc was constant and equal to that considered for the unmodified disc (ii) the diffusion coefficient of the plasma nitrided layer ($D_{\mathrm{c+d}}$) was estimated to be approximately one order of magnitude

lower than that of the substrate material; (iv) at the nitride layer/substrate interface, the ratio of the concentrations of hydrogen in the nitrided layer and substrate is constant ($c_{c+d}/c_s = k$), $k > 1$ since the solubility of hydrogen in ε–$Fe_{2\text{-}3}$ and γ'–Fe_4N structures is greater than that in martensite (substrate); (v) continuity of hydrogen flux at the interface, i.e. $\partial c_{c+d}/\partial x = \partial c_s/\partial x$; (vi) to enable direct comparison with unmodified flux, the flux in the nitrided specimen was quantified with respect to the steady–flux J_∞ of the unmodified disc; (vii) absence of hydrogen traps.

In spite of all simplified assumptions, the results shown in Figure 6.16 are sufficient to confirm that hydrogen build–up would occur for both specimens during the first days of exposure and a steady flux would be achieved in less than one week for both conditions. These estimates confirmed that the time frame (14 days) was adequate. Besides, the estimates showed that, for the conditions considered, plasma nitriding reduced the steady–flux of hydrogen, indicating that hydrogen uptake by the substrate can be reduced after the surface modification. Hydrogen trapping, which was not considered in these simulations, would further reduce the flux. Trapping effect is further discussed at the end of this section.

The causes related to the material were attributed to the hydrogen diffusivity and size and shape of the specimens. The diffusivity of $2.8 \times 10^{-13}\,m^2\,s^{-1}$[66] for the unmodified material and 1 to 2 orders of magnitude lower than that for the nitrided layer (Table 6.1) are sufficiently high to allow establishment of steady state flux after a few days of exposure to H_2S and therefore this does not seem to be an issue, as discussed earlier. The size and shape of the specimens also seemed to be adequate: the diameter was defined based on the diameter of the probe and the thickness was sufficiently small compared to the diameter and therefore the flux through the edges was negligible.

Hydrogen absorption, transport and trapping were identified as the main phenomenological aspects that could have caused the unexpected results. Hydrogen absorption seemed not to be the case because there was evidence—particularly for the unmodified material that showed hydrogen embrittlement features—of hydrogen uptake from the SSC experiments. Even though iron sulphide has been deposited on the surface and may have reduced the rate of absorption of hydrogen in both unmodified and nitrided specimens, hydrogen uptake was not avoided.

The transport and trapping of hydrogen may explain the reduction of hydrogen uptake by the substrate when the material was plasma nitrided, but cannot justify the invariant flux for the conditions tested. Even if hydrogen is hypothetically accumulated in the compound layer and its entry into the substrate is avoided, this condition would not occur for the unmodified specimen. The same applies for hydrogen trapping: they can reduce the hydrogen flux but not eliminate it.

In conclusion, there were no clear evidence to explain what could have caused the invariant flux, although it is speculated that issues could have arisen from a combination of phenomenological aspects and the method used to detect hydrogen in the exit side of the discs. Since the sensor of the hydrogen permeation kit detects hydrogen gas, the desorption and recombination mechanisms of atomic hydrogen released from the surface needs to be further investigated. These concepts, along with hydrogen transport and trapping, are therefore revisited in more detail in the next section.

Comments on hydrogen transport, trapping and desorption

As discusser earlier, once hydrogen is absorbed into the bulk of the material, part of it diffuses through interstitial positions (diffusible hydrogen) and part of it migrates to

trapping sites. It is therefore expected that the mobility of hydrogen will be reduced after plasma nitriding since some of the interstitial positions are already occupied by nitrogen.

In γ'–Fe_4N structures (Figure 6.17a), nitrogen occupies only one of the four octahedral interstices of the f.c.c. lattice to minimise strain induced by repulsive forces between nitrogen atoms [274]—the solubility of nitrogen in this structure is therefore limited to 20 at.% at room temperature. However, when the material was plasma nitrided at 420-500 °C, a supersaturated condition was achieved (see section 3.2.2.2) and the nitrogen content near the surface reached more than 50 at%. This suggests, at least for the low–temperature plasma nitriding condition in which CrN was not formed—that nitrogen is occupying all the four octahedral interstitial positions (this alone will result in a concentration of 50 at%) and some tetrahedral interstices. The latter is less likely since they involve higher strain energy, based on the simple argument that the size of tetrahedral interstices in face centred cubic (f.c.c.) structures—estimated by assuming a hard sphere model—are smaller than that of octahedral sites. The same analysis is valid for hydrogen, which also preferentially follows octahedral sites. In this scenario (i.e. γ'–Fe_4N supersaturated with nitrogen), hydrogen will diffuse following less efficient pathways (tetrahedral sites) and the diffusivity is expected to be reduced.

Similarly, nitrogen in the ε–Fe_3N structure (Figure 6.17b) occupies only one third of the octahedral interstices of the hexagonal close packed (h.c.p.) structure [275] and the nitrogen solubility is therefore 25 at.%. If all the octahedral sites were filled during the nitriding process, the concentration would rise to 50 at.%, as in γ'–Fe_4N.

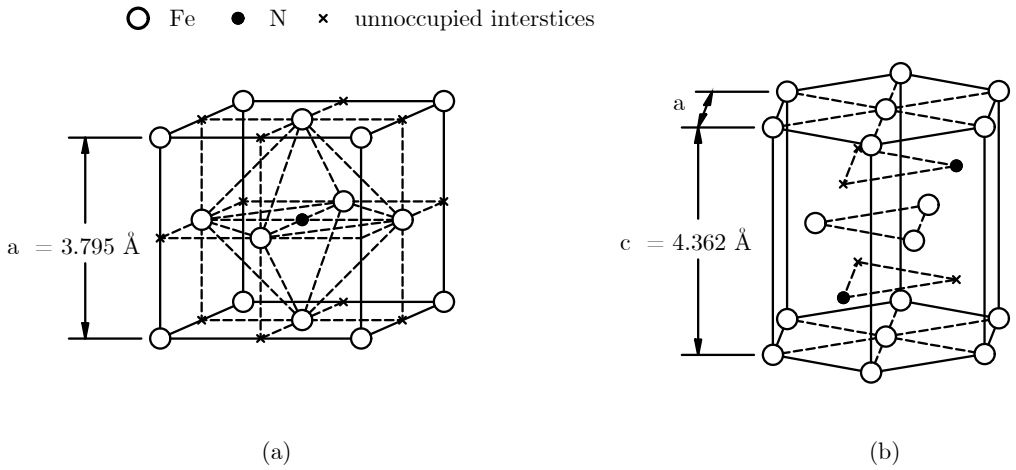

FIGURE 6.17: Crystal structure of (a) γ'–Fe_4N and (b) ε–Fe_3N. Lattice parameters from [274] and [276].

Once hydrogen reaches the diffusion zone, composed of expanded martensite (α'_N) with a body-centred tetragonal (b.c.t.) lattice, hydrogen is expected to diffuse preferentially through tetrahedral sites, as in b.c.c. structures [277]. In this case, nitrogen is occupying octahedral interstices and the increase of hydrogen mobility in α'_N compared to γ'–Fe_4N and ε–$Fe_{2\text{-}3}N$ is mostly due to the lower solubility of hydrogen in this structure, which increases its effective diffusivity. When hydrogen reaches the substrate material, its diffusion further increases due to the absence of nitrogen. It is important to note that the austenite phase (retained and reverted) in the substrate (about 10% in volume) and in the diffusion zone—in this case with nitrogen in solid solution—can interfere with the kinetics of hydrogen transport due to its higher solubility. It is expected that hydrogen will accumulate in the larger octahedral interstices of the f.c.c. structure and the effective diffusivity will be reduced.

As discussed earlier, the main effect of hydrogen trapping is to increase hydrogen solubility and thereby decrease its diffusivity. Experimentally, traps can be quantified by hydrogen permeation experiments using electrochemical techniques, as shown earlier in

this section, or by thermal desorption analysis. In the latter, different theoretical models are used to evaluate the experimental parameters. One example is the classical model [263] that assumes local equilibrium between diffusible and trapped hydrogen.

To perform a comprehensive investigation on trapping in the different structures of the nitrided layer and substrate, it is essential to know the types of traps and their respective binding and de-trapping energies. Trap density and occupancy are also required for the analysis. These quantities are not available in this work since the flux transients were not obtained on the hydrogen permeation studies and therefore the analysis is limited to list the types of traps that are present in the structure and analyse qualitatively how each type have contributed to the barrier effect of the plasma nitrided layer. Table 6.2 shows examples of trap sites present in the material investigated and their binding energies are estimated from data obtained from the literature. Considering the energy criteria for classification (reversible traps if $-E_b < 30\,\mathrm{kJ\,mol^{-1}}$ and irreversible if $-E_b > 50\,\mathrm{kJ\,mol^{-1}}$), major sources of irreversible traps in the substrate and in the diffusion zone appears to be reverted plus retained austenite ($\gamma_{\mathrm{ret/rev}}$)/martensite ($\alpha$') interfaces and non metallic inclusions (e.g. MnS). Another source that seems to be relevant for 17-4 PH are the prior austenite grain boundaries (compound layer, diffusion zone and substrate), classified as intermediate traps. Sub structures of the martensite phase (e.g. lath countours) are believed to have similar effect. Dislocations, classified as irreversible traps, also appear to affect the hydrogen mobility in the nitrided layer: the high stress levels in the structure supersaturated with nitrogen—induced by lattice strain to beyond the elastic limit of the material—can induce plastic deformation [278]. A notable source of traps in the compound layer seems to be nitrogen atoms. Despite being reversible, they may contribute to reduce the hydrogen flux since the lattices are supersaturated with nitrogen and hydrogen is expected to be attracted and accumulate near these sites.

TABLE 6.2: List of traps binding energy

Trap site	**Estimated binding energy -E_b (kJmol^{-1})**	**Reference**
Prior austenite grain boundaries	45-49	Obtained by thermal desorption mass spectroscopy [279] for iron (α)
$\gamma_{ret/rev}/\alpha$' interfaces	52	Obtained by hydrogen permeation (electrochemical technique) [280] for duplex stainless steel
Microvoids	48	Obtained by thermal desorption[281] for 4340 alloy steel (quenched and tempered)
Dislocation	60	Obtained by hydrogen permeation (electrochemical technique) [282] for iron (α)
MnS interfaces	72	Obtained by thermal desorption[281] for 4340 alloy steel (quenched and tempered)
Nitrogen atom	13	Obtained by magnetic relaxation technique [283] for iron (α)

Regarding hydrogen desorption in permeation studies using the electrochemical technique, it is common practice [139] to add a thin film of palladium on the oxidation (exit) side of the cell to optimise hydrogen extraction. Ideally, hydrogen atoms should instantly oxidise ($H \longrightarrow H^+ + e^-$) when they reach the exit side of the sample so that the current can be correctly associated with the hydrogen flux. But, in practice, partial oxidation can occur if hydrogen atoms recombine to form H_2. If palladium films—sufficiently thin to avoid interfering with hydrogen transport near the surface—are applied to the surface, hydrogen oxidation is accelerated and this problem can be minimised [284]. Conversely, when the hydrogen collection technique is used, H atoms leaving the surface to the atmosphere combine to form H_2. Flux issues, therefore, are mainly related to inefficiencies associated with the collection of the air stream containing the hydrogen molecules.

6.3 Summary and conclusions

This chapter showed that plasma nitriding induced compressive residual stress near the surface. This was verified experimentally for the low–temperature plasma nitrided condition. It also presented the unexpected results from the hydrogen permeation experiments by using the hydrogen collection method. The reasons for the invariant flux obtained during 14 days of exposure to H_2S were investigated and are likely to be related to the equipment, procedure, material and phenomenon aspects. Discussions on absorption, transport, trapping and desorption of hydrogen in nitrided structures—based on previously published data—helped clarify the barrier effect of the nitrided layer.

Chapter 7

General discussions and conclusions

A summary of individual topics covered in this work was presented at the end of each chapter. For a more comprehensive analysis, this chapter provides further general discussions on the correlations between corrosion resistance, residual stress, hydrogen permeation and sulphide stress cracking (SSC) susceptibility of the 17-4 PH (H1150D), especially after being plasma nitrided. The main findings are presented at the end of the chapter.

7.1 General discussions

7.2 SSC susceptibility

The results shown in Chapter 4 indicated that LTPN can be successfully used to increase the resistance to SSC of the 17-4 PH (H1150D), without compromising its corrosion resistance. In this section, the possible reasons for the lower susceptibility are further discussed.

7.2.1 Crack initiation and propagation (unmodified material)

For unmodified specimens (smooth surfaces), sulphide stress cracks started even in the absence of surface deffects (e.g pitting or pre–existing flaws). A feasible explanation for this, based on ealier observations [101], is the formation of cleavage planes perpendicular to the loading axis, induced by the Poisson's effect—compressive stresses are then induced, perpendicular to the loading axis. According to this theory, hydrogen ions preferentially accumulate near the expanded structure and induce a repulsive effect on the iron lattice resulting in decohesion and thereby cracking. When prior–austenite grains or martensite laths were favourably oriented, i.e. nearly perpendicular to the loading axis (as in Figures 4.15b, 4.16a and 4.28a), it seems reasonable to assume that decohesion preferentially occurred in these positions. Since hydrogen presumably segregated and diffused following these paths, intergranular or transgranular (interlath) embrittlement occurred when a sufficiently high tensile stress was applied.

When a corrosion pit or a flaw is present on the surface, the stress intensity can make it evolve into a stress corrosion crack due to the synergystic effects of enhanced corrosion activity—the pH is lower inside corrosion pits—and loading. In this case, the crack can start from the bottom of the pit, as apparently occurred in some specimens (e.g. Figure 4.15a) or from the mouth of the pit, in agreement with recent observations [285, 286]. In uniaxial tensile SSC, major cracks propagated (mode I opening) until complete rupture, provided that the loading was sufficiently high (at least 70% of σ_y). In four–point bend, crack propagation was limited to a few millimetres since the the tensile stress gradually reduced towards the neutral line and became compressive after that point. Figure 7.1 illustrates crack initiation and propagation in SSC tensile experiment.

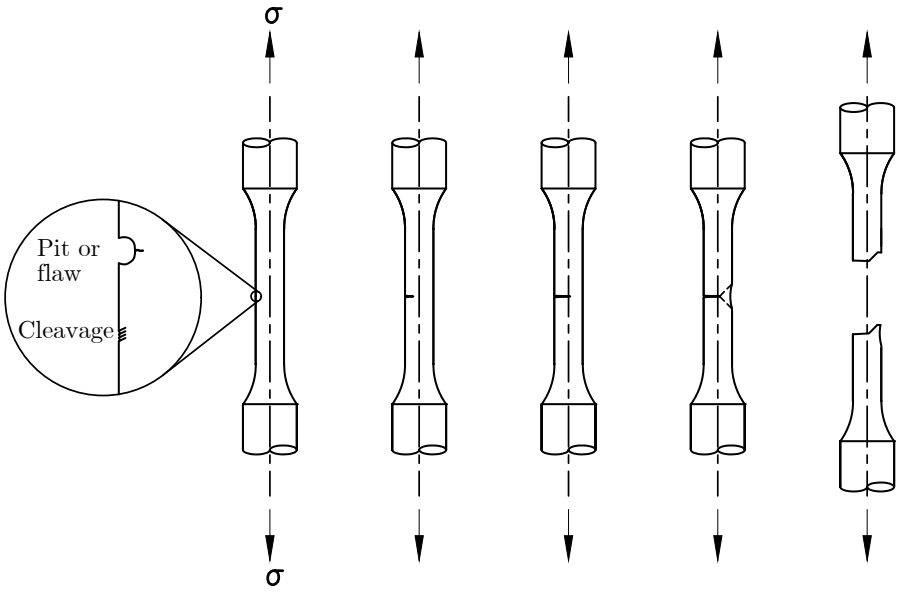

FIGURE 7.1: Schematic representation of SSC crack initiation and propagation in uniaxial tensile method.

7.2.2 The role of the plasma nitrided layer

Three hypothesis are being considered as possible causes for improved SSC resistance of the plasma nitried specimens compared to the unmodified material, observed in Chapter 4: (i) reduction of hydrogen uptake by the substrate material (barrier effect), discussed in Chapter 6; (ii) increased resistance to localised corrosion (Chapter 5) and (iii) the compressive residual stress induced by plasma nitriding (Chapter 6). Each aspect is discussed in the following sections. Even though these effects are being considered separately, they occur simultaneously and a synergistic effect is expected.

7.2.2.1 Hydrogen uptake

Hydrogen absorption into the substrate material is a key factor in the mechanism of SSC. The barrier effect of the nitrided layer, that presumably reduced the hydrogen uptake

according to many observations [268, 271], may have played an important role in preventing cracking. The idea is that hydrogen accumulated at interstitial positions and at irreversible and reversible traps (e.g. prior austenite grain boundaries, dislocations, interfaces between phases and particles) diffuses slowly through the nitride layer. If hydrogen uptake is minimised, the chances of the occurrence of brittle cracking are reduced. Detailed analysis of hydrogen transport in plasma nitrided structures was presented in Chapter 6.

7.2.2.2 Localised corrosion

Even though SSC does not require a surface defect to start, corrosion pits or flaws can be potential sites for crack initiation. Since plasma nitriding had superior corrosion resistance compared to the unmodified material when the treatment was preformed at low temperature (LTPN) (Chapter 5), greater resistance to SSC was anticipated for this condition, justifying the results obtained in Chapter 4. By using the same criteria, it was therefore expected that plasma nitrided specimens treated at high temperature (HTPN) would result in poor resistance to SSC due to their low corrosion resistance—attributed to the presence of CrN. But HTPN specimens did not fail by SSC and this clearly indicates that corrosion resistance must not be used as the only basis to determine SSC susceptibility. Details were presented in Chapter 5.

7.2.2.3 Compressive residual stress

In plasma nitrided specimens, the stress state near the surface was affected by the compressive residual stress induced by the nitriding treatment. The previously described mechanism of crack initiation for the unmodified material (section 7.2.1) may not be applied in this case because the net tensile stress is lowered—the macro compressive residual

stress within the nitrided case was estimated to be $\approx 1\,\mathrm{GPa}$. Even if a pit is formed or a flaw is present on the surface, a crack may not propagate since the stress field may not be sufficient to allow cracks to grow. Compressive residual stress is therefore an important factor in determining the SSC susceptibility. Even when the substrate material was intentionally exposed to the electrolyte (pre-damaged surfaces), plasma nitrided specimens still resisted cracking. Compressive residual stress therefore reduced the net tensile stress and prevented crack initiation and propagation. This topic was covered in detail in Chapter 6.

7.2.2.4 Proposed mechanism of protection against SSC

Since compressive residual stress, localised corrosion and hydrogen uptake occur simultaneously, their individual contributions to SSC resistance were not evaluated. However, it can be rationalised that the compressive stress and barrier effect had major roles in preventing SSC. This assumption was based on the results from the SSC experiments (Chapter 4), in which high–temperature plasma nitrided (HTPN) specimens also resisted SSC in spite of their poor corrosion resistance compared to the low–temperature plasma nitrided (LTPN) condition (Chapter 5). But it was not clear to which proportions the stress state and the reduced hydrogen uptake have contributed to lowering the susceptibility. Considering that hydrogen uptake can be reduced but not avoided when the material is plasma nitrided, as discussed in Chapter 6, it is reasonable to assume that protection against SSC was mostly provided by the compressive stress.

The proposed mechanism for the protection provided by nitride layers against SSC is shown in Figure 7.2. As in the unmodified material, this model assumes that sulphur is adsorbed at the surface ($\mathrm{Fe} + \mathrm{HS}^{-}_{\mathrm{ads}} + \mathrm{H}^{+}_{\mathrm{ads}} \longrightarrow \mathrm{Fe} + \mathrm{S}^{2-}_{\mathrm{ads}} + 2\,\mathrm{H}^{+}_{\mathrm{ads}}$) and preferentially segregates at the grain boundaries. As in the classical recombination poisoning theory for

the SSC mechanism, a fraction of the hydrogen that would otherwise recombine to form H_2 is absorbed into the nitrided structure. Intense trapping is therefore expected near the surface (compound layer) due to the accumulation of hydrogen in the grain boundaries, enhanced by the high concentration of nitrogen. Since the compressive residual stress in the nitrided layer suppresses the magnitude of the applied tensile stress, the driving force for crack propagation is eliminated—for SSC to occur, as discussed in Chapter 2, the three following conditions must be satisfied: (i) the material is susceptible to SSC; (ii) the environment contains H_2S and (iii) the material is submitted to tensile stress (residual or applied). The same applies in the event of pitting corrosion, in which cracks will be impeded rather than preferentially initiated from the locally damaged area.

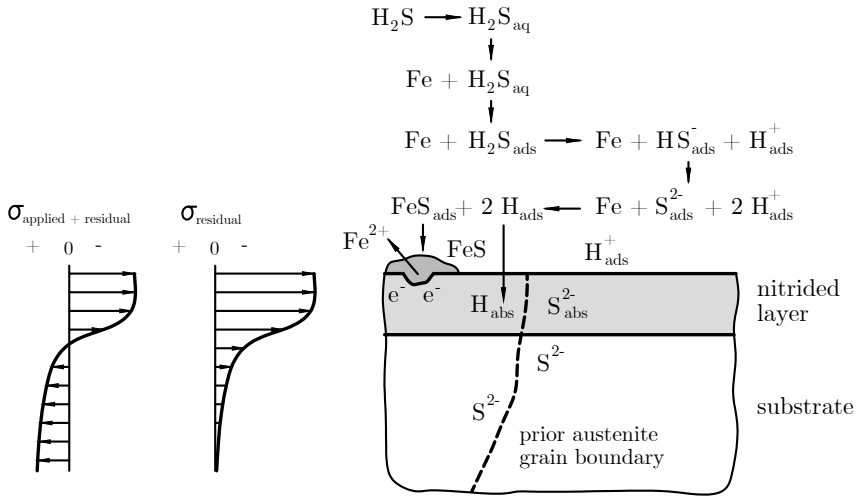

(a)

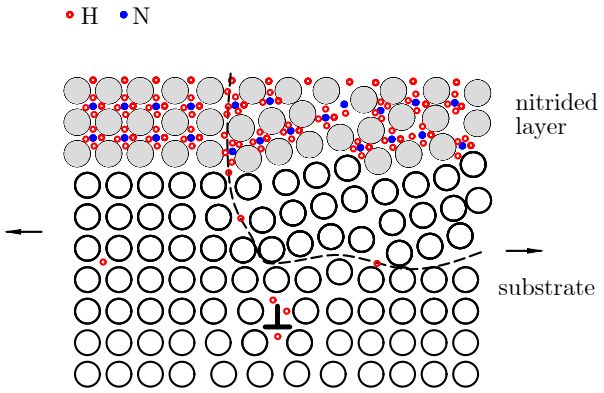

(b)

FIGURE 7.2: Proposed mechanism of protection against SSC after plasma nitriding: (a) SSC prevented by the compressive residual stress; (b) barrier effect due to intense trapping of H to the nitrided layer.

7.3 Conclusions

The following conclusions summarise the main findings from the present work. All the experiments were conducted at $(23 \pm 2)\,°C$ and ambient pressure and specimens were exposed to the same environment, i.e. typical produced water with $165\,g\,L^{-1}$ of NaCl and pH 4.5 ± 0.2, with different gas mixtures:

- The microstructure of the unmodified 17-4 PH, heat treated to the H1150D condition (annealed at 1040 °C followed by two consecutive precipitation hardening at 620 °C and cooled to below 32 °C after each stage), comprised a matrix of low-carbon (lath) martensite (formed after annealing and preserved after precipitation hardening) with (9.6 ± 0.4) % in volume of reverted austenite (mostly formed during the precipitation hardening cycles) and traces of δ-ferrite.

- Unmodified 17-4 PH (H1150D) is highly susceptible to SSC in typical produced water with $pH_2S = (3.4 \pm 0.1)\,kPa$ and CO_2 as balance gas. The threshold stress for SSC to occur lies within 30 and 50% of its actual yield strength, in agreement with earlier observations. Failure by SSC occurred on both intergranular and transgranular modes (interlath and translath), with features of both SSC and SCC mechanisms.

- Plasma nitriding at both low temperature (420 °C) and high (conventional) temperature (500 °C) for 10 h in 25 vol.% N_2 + 75 vol.% H_2 using the active screen method resulted in the formation of uniform compound layers comprising mixed γ'–Fe_4N and ε–$Fe_{2\text{-}3}N$ phases, varying from 10 µm to 15 µm. At high temperature, precipitation of Cr_2N occurred. Underneath the compound layer, both structures comprised a diffusion zone (martensite with interstitial nitrogen, α'_N).

- Low–temperature plasma nitriding (LTPN) reduced the susceptibility of the 17-4 PH (H1150D) to SSC in typical produced water saturated with both mixed pH_2S = (3.4 ± 0.1) kPa and CO_2 (as balance gas) and pure H_2S using constant–load test methods (i.e. four-point bend and uniaxial tensile) with stress levels up to 100% of the yield strength. In mixed H_2S/CO_2, no cracks were identified on the surface after 720 hour of exposure. In a more aggressive condition (pure H_2S), localised corrosion was identified when specimens were loaded to 90 % of the yield strength, although cracking was not observed. The increased resistance to SSC was due to simultaneous occurrence of (i) barrier effect (reduction of hydrogen uptake due to the reduced mobility caused by hydrogen trapping to nitrogen atoms, dislocations and prior–austenite grain boundaries); (ii) compressive macro residual stress of -1.0 to -1.6 GPa induced by the plasma nitrided treatment and (iii) superior resistance to localised corrosion since the nitriding temperature (420 °C) was sufficiently low to avoid precipitation of chromium nitride. The high–temperature plasma nitrided (HTPN) specimens also resisted to SSC but exhibited poor corrosion resistance due to the precipitation of chromium nitride. When the substrate was intentionally exposed to the electrolyte, the susceptibility of the LTPN condition was not affected, whereas general corrosion was observed on HTPN specimens since the nitrided layer became anodic with respect to the unmodified substrate.

- LTPN resulted in superior corrosion resistance (i.e. it exhibited passivation behaviour and had lower corrosion rate, estimated by potentiodynamic polarisation technique) compared to that of HTPN (conventional) condition due to the formation of a nitrogen–rich layer without precipitation of chromium nitride. Compared to the unmodified material, LTPN also resulted in lower corrosion rate and superior resistance to localised attack in mixed H_2S/CO_2. In LTPN specimens, corrosion

resistance was provided by the inner section of the mixed γ'–Fe_4N/ε–$Fe_{2\text{-}3}N$ compound layer—as observed by SEM and EIS results—and deposits of iron sulphide. Complementary experiments with pure H_2S and pure CO_2 revealed that the unmodified condition was more corrosion resistant in pure CO_2 (lower corrosion rate and higher resistance to pitting corrosion) whereas LTPN performed better in pure H_2S (lower corrosion rate and greater pitting and repassivating potentials), owing to the formation of a dense film of iron sulphide). The results also showed that when both gases were mixed, the effect of H_2S predominated and iron sulphide was the major corrosion scale—iron carbonate was not formed, even in pure CO_2, since its formation was not favoured for the conditions tested (temperature and H_2S/CO_2 ratio).

- It was estimated that a macro compressive residual stress of -1.0 to -1.6 GPa was induced near the surface of the 17-4 PH (H1150D) after being plasma nitrided at low temperature (420 °C for 10 h). The residual stress was not determined experimentally for high–temperature plasma nitriding, although it was inferred—based on the nitrogen concentration profile—that its magnitude would be smaller due to the lower nitrogen content.

- Hydrogen flux build–was not observed for the unmodified and low–temperature plasma nitrided 17-4 PH (H1150D) when exposed to H_2S–saturated produced water for 14 days using the hydrogen collection technique. A systematic investigation on the causes for the invariant flux on the detection side of the sample suggested that they were linked to a combination of aspects associated with the equipment, hydrogen transport, trapping and desorption.

- The barrier effect of the plasma nitrided layer—listed as one of the possible causes of

the increased resistance to SSC observed in Chapter 4—was considered to be related to hydrogen trapping in the compound layer (e.g. nitrogen atoms, intensified by the supersaturation condition near the surface, dislocations and prior–austenite grain boundaries) and in the diffusion section (e.g. prior–austenite grain boundaries, martensite lath contours, austenite/martensite interfaces). Hydrogen presumably accumulated in the octahedral interstitial positions of the retained and reverted austenite (diffusion zone and substrate) due to its higher solubility in the f.c.c. structure. These observations were based on analysis of previously published data on hydrogen permeation in plasma nitrided structures using electrochemical techniques and supported by further theoretical discussions. Overall, the hydrogen diffusivity in the nitrided layer is lower in the compound layer (up to 3 orders of magnitude compared with the unmodified material) and the mobility gradually increases toward the substrate.

Chapter 8

Perspectives and future work

The promising results obtaining in this work, demonstrating that the resistance of the 17-4 PH to sulphide stress cracking can be increased by applying low-temperature plasma nitriding, are of technological interest for the oil and gas industry, particularly subsea systems. In environments with that complexity, real components are subject to severe conditions (temperature and pressure) and are exposed to high levels of H_2S, chloride and CO_2. Because of the variety of environments to which components can be exposed during its lifetime, further research is required to understand how the modified surface would respond to a wider range of parameters. In this chapter, I am listing further research that can be performed attempting to further understand the SSC phenomena of plasma nitrided 17-4 PH, starting with an overview of the technological implications.

8.0.1 Technological implications

The susceptibility to SSC in this work was quantified in terms of time–to–failure when the material was submitted to a test solution simulating a specific oilfield environment. For the particular context used as reference in this work, i.e. oilfield components (e.g. tubing hanger and valve stems) applied on subsurface installations, the 17-4 PH (H1150D) is known to be highly susceptible to SSC and this was confirmed in Chapter 4. The

results also suggested that there is potential to increase the limits of application of this material by applying plasma nitriding at low temperature, with positive impact expected on maintenance and capital costs. Current standards, however, do not accept surface modification as a means of prevention against SSC and this may be because there is a concern that general and localised corrosion resistance would be negatively affected after the surface modification, increasing the tendency to SSC. The results from Chapters 4, in fact, showed that specimens plasma nitrided at high temperature (HTPN) passed the SSC test in spite of their poor corrosion resistance (Chapter 5). When the substrate was exposed, intense dissolution occurred due to the galvanic effect between the nitrided layer and the substrate, posing a risk for the integrity of any component exposed to these conditions. For specimens treated at low temperature (LTPN), however, the corrosion resistance was equivalent or superior to the unmodified material.

Although promising results were obtained for LTPN condition, the following aspects must be considered for qualification purposes. This list is not exhaustive, but it is sufficient to exemplify major discrepancies between actual and simulated environments. Recommendations for future work to address some of these limitations are presented in the next section.

- Although standard tensile tests recommend exposure time of 720 h, this may not be representative of the life time of the component.

- Although constant load tests seemed more adequate for comparison purposes (it has been historically used for qualification), real components are subject to intermittent loading rather than constant load used in the laboratory scale.

- Laboratory tests were performed in nearly stagnant conditions, but in practice hydrocarbon fluids in contact with internal components are continuously flowing. This

can result in chemical variations near the surface. The constant flow of the test gas during the experiments were sufficient to maintain saturated condition but may not reflect real environments.

- In offshore systems, the hydrostatic pressure at the seabed level, in which wellhead equipment is installed, can exceed 60 MPa for deep–water operations. Many SSC experiments, including the present work, are conducted at ambient pressure for practical reasons, although this does not represent real environmental conditions.

8.1 Future work

Despite not being approved as a method to prevent SSC, presumably due to the concern with the corrosion resistance, LTPN can be successfully applied to enhance the resistance to SSC and maintain equivalent or superior corrosion resistance compared to the unmodified material. Prospective increase on the limits of application for the 17-4 PH in sour environments after being plasma nitrided, however, require further study to gain additional understanding on the mechanisms involved and to make proper correspondences between laboratory tests and service conditions of real components. The following are recommended for future work:

- **Expose the material to different environments**. In this work, the experiments were conducted in one specific solution, representative of oil production environment. Analysis can be extended to typical environments found in gas production systems (e.g. condensed water with lower levels of sodium chloride).

- **Tests in high-pressure and high-temperature conditions**. Although in this work the susceptibility to SSC was evaluated at the temperature of highest susceptibility of the unmodified material, which is within typical operating temperature

range of wellhead components, further investigations on the behaviour of plasma nitrided layers to different temperature ranges seem adequate.

- **Analyse the effect of geometry**. Successful application of plasma nitriding needs to ensure uniform treatment in the whole area of the component. Active screen plasma nitriding technology is most adequate technique to attend this requirement and specific investigations on uniformity for more complex geometries are recommended, since uneven or not well covered regions could potentially become preferential sites for localised corrosion and crack initiation.

- **Test different loading plans**. During their life time, components may undergo different levels of loading. Further examination under different loading plans would confirm the integrity of the layer during service.

- **Test different materials**. Different corrosion-resistant alloys (e.g. supermartensitic and duplex stainless steels) can be evaluated.

- **Use alternative test methods**: Test methods such as slow strain rate and the newly developed ripple slow strain rate tests can be used to provide further insights on the mechanisms of failure of plasma nitrided layers. Fit-to-purpose tests can anticipate service conditions.

- **Simultaneous plasma nitriding and precipitation-hardening**. Plasma nitriding can be carried out simultaneously with the precipitation hardening cycle. In this case the precipitation hardening temperature and the plasma temperature must be optimised to provide the desired structure and avoid unwanted microstructural changes of the substrate.

- **Detailed quantification of the residual stress**. Residual stress played an important role on the SSC susceptibility and further investigation on the residual stress distribution across the layer (rather than the macro residual stress) would be appropriate. Different techniques can be used, for example X-ray diffraction.

- **Hydrogen permeation**. Key theoretical aspects of the hydrogen transport and trapping on plasma nitrided structures were covered in this work. It is therefore recommended further experimental work using electrochemical method (Devanathan–Stachurski cell) to quantify the barrier effect.

- **Further research on the SSC mechanisms**. Further research can be performed to provide supporting evidence for the mechanisms of SSC, such as in-situ measurements.

- **Evaluate the formation of iron sulphide**. Examine the grow of iron sulphide film for different proportions of H_2S/CO_2.

- **Erosion-corrosion**. Further investigation on the tribo corrosion process (erosion-corrosion and cavitation corroison). Some components, such as drilling tools can be degraded by the synergistic effect of erosion by solid particles and electrochemical degradation. There are some studies [287] showing that the 17-4 PH changed from passive to active corrosion under erosion-corrosion conditions. This can be evaluated for plasma nitrided conditions. Some studies with sliding wear were already carried out in non-sour environments [18] and further research can be performed with H_2S and the analysis can be extended to include impingement of solid particles.

- **Analyse crack growth and propagation**. Use in-situ technology to monitor crack initiation and growth. Use X-ray tomography to analyse the evolution of

cracks from surface defects or pits on the nitrided layer. Use of synchrotron to monitor the propagation of pits in plasma nitrided layer.

Appendix A

Retained austenite

The lattice parameters of crystals from both austenitic (f.c.c.) and martensitic (b.c.t.) phases (b.c.t. was approximated as a b.c.c. structure) were determined by extrapolating the calculated lattices obtained for each reflection line against a particular function of the diffraction angle θ. For cubic systems, this function (right side of Equation A.1 [288]) is proportional to the fraction error of the interplanar spacing $\delta d/d$, which is equivalent to the fraction error of the lattice parameter $\delta a/a$. By extrapolating ($\cos^2\theta/\sin\theta+\cos^2/\theta$) to zero (or $\theta = 90°$), the lattice parameter was therefore determined.

$$\frac{\delta d}{d} = \frac{\delta a}{a} \propto \left(\frac{\cos^2\theta}{\sin\theta} + \frac{\cos^2\theta}{\theta} \right) \tag{A.1}$$

For a cubic crystal, $\sin^2\theta$ was determined by

$$\sin^2\theta = \frac{\lambda^2}{4a_0^2}\left(h^2 + k^2 + l^2\right) \tag{A.2}$$

where k, l, m are the Miller indices.

The atomic scattering factor of iron, f_{Fe}, used to quantify the efficiency of scattering

of an iron atom relative to scattering of an electron in a given direction, was determined by each $(\sin\theta)/\lambda$, assuming a crystal structure of pure iron. Because the wavelength of the incident beam, λ, is near the wavelength scattered from the iron (K absorption), λ_K ($\lambda/\lambda_K = 0.8$), the value must be corrected to $f' = f + \Delta f$, where Δf=-0.5 is the correction factor [288]. The structure factor, F_{hkl}, which represents the resultant wave scattered by a unit cell—considering the individual contribution of each atom—was obtained by

$$F_{hkl} = \sum_{n=1}^{N} f_n e^{2\pi i(hu_n + kv_n + hw_n)} \tag{A.3}$$

where N is the quantity of atoms in the unit cell, u, v and w are their fractional coordinates. The multiplicity factor, which defines the number of planes with the same interplanar distance was determinded from Table A.1.

Table A.1: Multiplicity factor

Form	{h,k,l}	{h,h,l}	{0,k,l}	{0,k,k}	{h,h,h}	{0,0,l}
p	48	24	24	12	8	6

The theoretical intensities, R, were determined by [288]

$$R = \left(\frac{1}{\Omega^2}\right) |F|^2 \, p \left(\frac{1+\cos^2 2\theta}{\sin^2\theta\cos\theta}\right) \left(e^{-2M_T}\right) \tag{A.4}$$

where Ω is the volume of the unit cell and the term $(1+\cos^2 2\theta)/\left(\sin^2\theta\cos\theta\right)$ is the Lorentz-polarization factor, LP, which accounts for the reduction of the intensity of reflected beams due to the instrumentation geometry.

The thermal vibration of diffracted beams are quantified by the temperature factor, e^{-2M_T}, defined by [289]

$$M_T = B_T \left(\frac{\sin \theta}{\lambda} \right)^2 \tag{A.5}$$

in which B_T is defined as [289]

$$B_T = \frac{6Nah^2}{Mk_B} \frac{T}{\Theta} \left[\phi(x) + \frac{x}{4} \right] \tag{A.6}$$

where Na is the Avogadro's number (6.023×10^{22}), M is the atomic weight of iron (55.845 g mol^{-1}), h is the Planck constant (approximately $6.626 \times 10^{-34}\,\mathrm{m^2\,kg\,s^{-1}}$), k_B is the Boltzmann constant (approximately $1.38 \times 10^{-23}\,\mathrm{m^2\,kg\,s^{-2}\,K^{-1}}$) , Θ is the Debye characteristic temperature ($\Theta_F e$=470 K [289]), T is the temperature, x is Θ/T and $\phi(x)$=0.68 [289].

By considering n_γ reflections of austenite and $n_{\alpha'}$ reflections of martensite, the ratio between the volume fraction of each phase, $c_\gamma/c_{\alpha'}$, was obtained by [194]

$$\frac{c_\gamma}{c_{a'}} = \frac{\frac{1}{n_\gamma} \sum_0^{n_\gamma} \left(\frac{I_\gamma}{R_\gamma} \right)}{\frac{1}{n_{\alpha'}} \sum_0^{n_{\alpha'}} \left(\frac{I_{\alpha'}}{R_{\alpha'}} \right)} \tag{A.7}$$

where I_γ and $I_{\alpha'}$ are the integrated intensities of the diffracted peaks of austenite and martensite, respectively. The respecive theoretical intensities, R_γ and $R_{\alpha'}$, determined by Equation A.4.

Assuming that martensite and austenite are the only phases present in the microstructure ($c_{\alpha'} + c_{\gamma} = 1$), the retained austenite can be determined by

$$c_{\gamma} = \frac{\frac{c_{\gamma}}{c_{\alpha'}}}{1 + \frac{c_{\gamma}}{c_{\alpha'}}} \tag{A.8}$$

Tables A.2 and A.3 show the results from Chapter 3 (section 3.1.1.3), obtained following the steps described in this section.

TABLE A.2: Parameters obtained for the f.c.c. phase

n_{γ}	(hkl)	$h^2+k^2+l^2$	2θ	$\sin\theta/\lambda$	f'_{Fe}	$\lvert F\rvert^2$	p	LP	I_{γ}	R_{γ}
1	(111)	3	43.6°	0.241	17.0	4651	8	11.92	0.103	9226
2	(200)	4	50.8°	0.278	15.8	4004	6	8.44	0.043	4172
3	(220)	8	74.6°	0.393	13.0	2684	12	3.66	0.014	2324
4	(311)	11	90.6°	0.461	11.8	2212	24	2.81	0.018	2852

TABLE A.3: Parameters obtained for the b.c.t. phase

$n_{\alpha'}$	(hkl)	$h^2+k^2+l^2$	2θ	$\sin\theta/\lambda$	f'_{Fe}	$\lvert F\rvert^2$	p	LP	$I_{\alpha'}$	$R_{\alpha'}$
1	(110)	2	44.7°	0.247	16.9	4651	12	11.27	0.600	6297
2	(200)	4	65.0°	0.349	14.0	4004	6	4.84	0.063	897
3	(211)	6	82.3°	0.427	12.3	2684	24	3.12	0.110	1745
4	(202)	8	98.9°	0.493	11.2	2212	12	2.73	0.049	610

Appendix B

Four-point bend

The shear and bending momentum, for the specific case of the dimensions shown in Figure 4.8, are represented in Figure B.1, in which the main dimensions are represented in terms of the length of the beam, L. Over the region between the inner supports ($3L/10 \leq x \leq 7L/10$), the specimen is submitted to pure bending. For this interval, the bending momentum $M(x)$ is constant and the shear $V(x)$ is zero.

The bending momentum is given by

$$M(x) = Px - P\langle x - \frac{3L}{10}\rangle - P\langle x - \frac{7L}{10}\rangle \tag{B.1}$$

Assuming a plane state of stress ($t \ll L$ and $\omega \ll L$, ω being the width of the beam), $\sigma_x(y)$ is the only stress in the pure bending section: $\sigma_x(y) > 0$ (tensile) above the neutral plane and $\sigma_x(y) < 0$ (compression) below the neutral plane). In the elastic regime, Eq. B.1 can be written as (ρ being the constant radius of curvature of the neutral axis, E the elasticity modulus and I the moment of inertia):

$$EI\frac{\mathrm{d}y(x)}{\mathrm{d}x} = Px - P\langle x - \frac{3L}{10}\rangle - P\langle x - \frac{7L}{10}\rangle \tag{B.2}$$

Integrating Eq.B.2 twice:

$$EIy(x) = \frac{P}{6}x^3 - \frac{P}{6}\langle x - \frac{3L}{10}\rangle^3 - \frac{P}{6}\langle x - \frac{7L}{10}\rangle^3 + C_1 x + C_2 \tag{B.3}$$

in which the contants of integration can be obtained considering the boundaries conditions: $x = 0; y = 0$ and $x = L; y = 0$. The elastic curve become:

$$y(x) = \frac{P}{2EI}\left[\frac{1}{3}x^3\langle x - \frac{3L}{10}\rangle^3 - \frac{1}{3}\langle x - \frac{7L}{10}\rangle^3 - \frac{21L^2}{100}x\right] \tag{B.4}$$

The maximum deflection in the elastic regime is then given by:

$$y_{\max} = y\left(\frac{L}{2}\right) = \delta = -\frac{33PL^3}{1000EI} \tag{B.5}$$

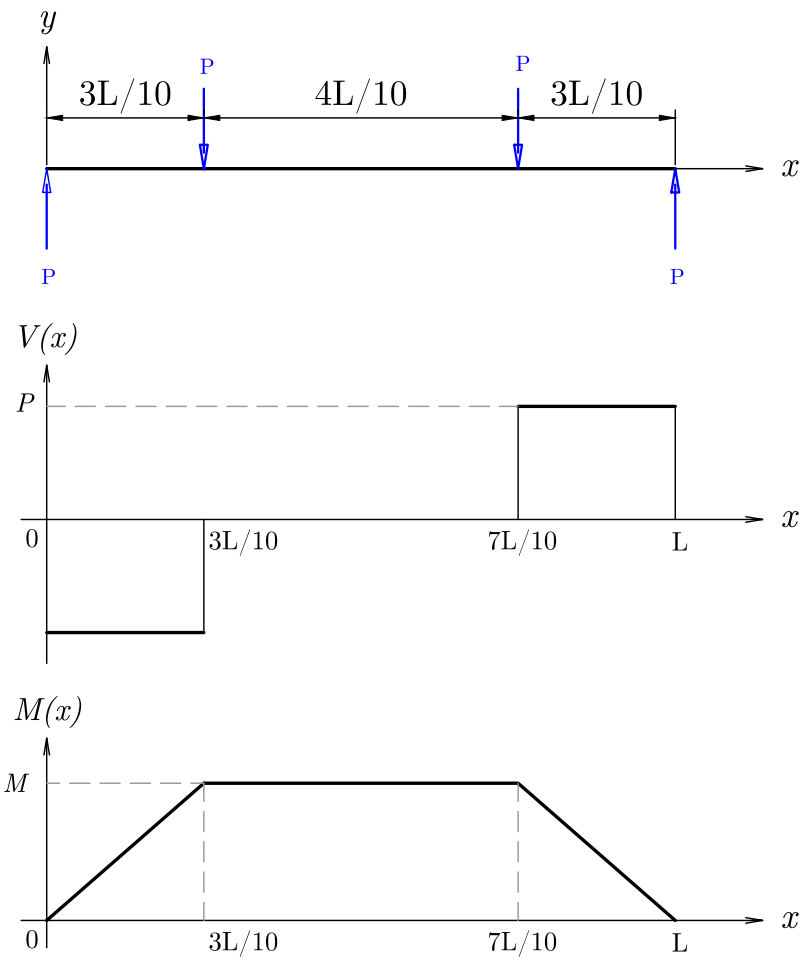

FIGURE B.1: Four-point bend shear and bending diagram.

Bibliography

[1] British Petroleum, "Bp statistical review of world energy 2017", Tech. Rep. 66, 2017, pp. 1–52.

[2] EIA, "International energy outlook 2017 overview", U.S. Energy Information Administration, Tech. Rep. 2017, 2017, p. 143.

[3] E. Lange, S. Petersen, L. Rüpke, E. Söding, and K. Wallmann, "Marine resources - opportunities and risks", Tech. Rep., 2014, p. 165.

[4] United States Environmental Protection Agency, "Report to congress on hydrogen sulfide air emissions associated with the extraction of oil and natural gas", Research Triangle Park, NC, Tech. Rep., 1993, pp. 1–222.

[5] R. Marriott, P. Pirzadeh, J. Marrugo-Hernandez, and S. Raval, "Hydrogen sulfide formation in oil and gas", *Canadian Journal of Chemistry*, vol. 94, no. 4, pp. 406–413, 2016. DOI: 10.1139/cjc-2015-0425.

[6] M Iannuzzi, "Environmentally assisted cracking (EAC) in oil and gas production", in *Stress corrosion cracking: Theory and practice*, 2011. DOI: 10.1533/9780857093769.4.570.

[7] M. Iannuzzi, A. Barnoush, and R. Johnsen, "Materials and corrosion trends in offshore and subsea oil and gas production", *Npj Materials Degradation*, vol. 1, no. 1, p. 2, 2017. DOI: 10.1038/s41529-017-0003-4.

[8] NACE / ASTM G193 - 12d, *Standard terminology and acronyms relating to corrosion*, 2014. DOI: 10.1520/G0193-12D.2.

[9] A. Ikeda and M. Kowaka, "Stress corrosion cracking of low-and high-strength steels in wet hydrogen sulfide environment", *Chemical Economy & Engineering Review*, vol. 10, no. 5-6, pp. 12–22, 1978.

[10] R. P. Badrak, "Investigation of limits for UNS S17400 in H_2S containing environments", in *NACE Corrosion 2017*, San Antonio, TX: NACE International, 2014, Paper 3816.

[11] C. Slunder, A. Hoenie, and A. Hall, "Thermal and mechanical treatment for precipitation-hardening stainless steel", NASA Marshall Space Flight Center, Huntsville, AL, United States, Columbus, Ohio, Tech. Rep., 1967, pp. 1–193.

[12] D. Ludwigson and A. Hall, "The physical metallurgy of precipitation-hardenable stainless steels", Defense Metals Information Center, Columbus, Ohio, Tech. Rep., 1959, pp. 1–70.

[13] R. M. Thompson, G. B. Kohut, D. R. Canfield, and W. R. Bass, "Sulfide stress cracking failures of 12 Cr and 17-4PH stainless steel wellhead equipment", *Corrosion*, vol. 47, no. 3, pp. 216–220, 1991. DOI: 10.5006/1.3585248.

[14] F. Gareau, N. Chambers, and A. Martinson, "Effect of stress and environment on failures of 17-4 PH stainless steel valve", in *NACE Corrosion 1993*, Houston, TX: NACE International, 1993, Paper 146.

[15] S. S. M. Tavares, J. S. Corte, and J. M. Pardal, "Failure of 17-4 PH stainless steel components in offshore platforms", in *Handbook of Materials Failure Analysis with Case Studies from the Oil and Gas Industry*, A. Makhlouf and M Aliofkhazraei,

Eds., Elsevier, 2016, ch. 17, pp. 353–370. DOI: 10.1016/B978-0-08-100117-2.00014-5.

[16] NACE MR0175 / ISO 15156-3, *Petroleum and natural gas industries — materials for use in H_2S-containing environments in oil and gas production — Part 3: Cracking-resistant CRAs (corrosion-resistant alloys) and other alloys*, 2009.

[17] NACE MR0175 / ISO 15156-3, *Petroleum and natural gas industries — materials for use in H_2S-containing environments in oil and gas production — Part 3: Cracking-resistant CRAs (corrosion-resistant alloys) and other alloys - Technical circular 1*, 2009.

[18] M. Esfandiari and H. Dong, "The corrosion and corrosion-wear behaviour of plasma nitrided 17-4PH precipitation hardening stainless steel", *Surface and Coatings Technology*, vol. 202, pp. 466–478, 2007. DOI: 10.1016/j.surfcoat.2007.06.069.

[19] M Esfandiari and H Dong, "Plasma surface engineering of precipitation hardening stainless steels", *Surface Engineering*, vol. 22, no. 2, 2006. DOI: 10.1179/174329406X98368.

[20] E. Granda-Gutiérrez, J. Diaz-Guillén, J. Diaz-Guillén, M. González, F. García-Vázquez, and R. Munóz, "Sulfide stress cracking and electrochemical corrosion of precipitation hardening steel after plasma oxy-nitriding", *Journal of Materials Engineering and Performance*, vol. 23, no. 11, pp. 4148–4153, 2014. DOI: 10.1007/s11665-014-1085-6.

[21] T. Zakroczymski, N. Lukomski, and J. Flis, "Entry and transport of hydrogen in nitrided iron", *Journal of Electrochemical Society*, vol. 140, no. 12, pp. 3578–3583, 1993.

[22] F. Fassini, M. Zampronio, and P. De Miranda, "Design of ion-implanted coatings to impede hydrogen contamination of steel", vol. 35, pp. 549–556, 1993.

[23] T. Zakroczymski, N. Lukomski, and J. Flis, "The effect of plasma nitriding-base treatments on the absorption of hydrogen by iron", *Corrosion Science*, vol. 37, no. 5, pp. 811–822, 1995. DOI: 10.1016/0010-938X(95)80011-5.

[24] P. Bruzzoni, S. P. Bruhl, B. J. A. Gomez, L. Nosei, M. Ortiz, and J. N. Feugeas, "Hydrogen permeation modification of 4140 steel by ion nitriding with pulsed plasmas", *Surface and Coatings Technology*, vol. 110, no. 1-2, pp. 13–18, 1998. DOI: 10.1016/S0257-8972(98)00540-4.

[25] E Lunarska and J Michalski, "Hydrogen behavior in the iron surface layer modified by plasma nitriding and ion boronising", *Materials and Corrosion*, vol. 51, pp. 841–849, 2000.

[26] T. Zakroczymski, J. Flis, N. Lukomski, and J. Mankowski, "Entry, transport and absorption of hydrogen in low-temperature plasma nitrided austenitic stainless steel", *Acta Materialia*, vol. 49, no. 11, pp. 1929–1938, 2001. DOI: 10.1016/S1359-6454(01)00112-4.

[27] Z. Wolarek and T. Zakroczymski, "Hydrogen transport in plasma nitrided iron", *Acta Materialia*, vol. 52, no. 9, pp. 2637–2643, 2004. DOI: 10.1016/j.actamat.2004.02.011.

[28] Z. Wolarek and T. Zakroczymski, "Hydrogen absorption in plasma-nitrided iron", *Acta Materialia*, vol. 54, no. 6, pp. 1525–1532, 2006. DOI: 10.1016/j.actamat.2005.11.018.

[29] J. J. M. Jebaraj, D. J. Morrison, J. B. McLaughlin, and I. I. Suni, "Effect of nitriding on the hydrogen diffusion coefficient through aisi 4340", *Journal of the*

Electrochemical Society, vol. 161, no. 5, pp. C261–C267, 2014. DOI: 10.1149/2.077405jes.

[30] P Buchhagen and T Bell, "Simulation of the residual stress development in the diffusion layer of low alloy plasma nitrided steels", *Computational materials science*, vol. 7, pp. 228–234, 1996. DOI: 10.1016/S0927-0256(96)00085-7.

[31] M. S. D. R. Coseglio, "Sulphide stress cracking of 17-4 ph for applications in oilfield components", *Materials Science and Technology (United Kingdom)*, vol. 33, no. 16, pp. 1863–1878, 2017. DOI: 10.1080/02670836.2017.1330230.

[32] P. Rashmi Bhavsar, S. Silverman, and D. MacWilliam, "Successful use of 17-4PH components in well equipment in sour oilfield environments", in *NACE Corrosion 2004*, New Orleans, LA: NACE International, 2004, Paper 04120.

[33] J. Fraser and R. Treseder, "Cracking of high strength steels in hydrogen sulfide solutions", in *Eight Annual Conference, National Association of Corrosion Engineers*, Galveston, TX, 1952, pp. 29–37.

[34] Prepared by the Working Party on Corrosion in Oil and Gas Production, *Guidelines on materials requirements for carbon and low alloy steels for H_2S-containing environments in oil and gas production (EFC 16 - 3rd edition)*, 2009.

[35] Prepared by the Working Party on Corrosion in Oil and Gas Production, *Corrosion resistant alloys for oil and gas production: guidance on general requirements and test methods for H_2S service (EFC 17 - 2nd edition)*, 2002.

[36] NACE International Work Group T-1F-21g, "Use of corrosion-resistant alloys in oilfield environments", NACE International Work Group T-1F-21g, Tech. Rep. 24010, 2000, pp. 1–68.

[37] NACE MR0175 / ISO 15156-1, *Petroleum and natural gas industries — materials for use in H_2S-containing environments in oil and gas production — Part 1: general principles for selection of cracking-resistant materials*, 2009.

[38] International Energy Agency, "World energy outlook 2008", International Energy Agency, Paris, Tech. Rep. 4, 2008, p. 329. DOI: 10.1049/ep.1977.0180.

[39] International Energy Agency, "Resources to reserves 2013 - oil, gas and coal technologies for the energy markets of the future", Tech. Rep., 2013, p. 272. DOI: 10.1787/9789264090705-en.

[40] H. H. Guyer, *Industrial Processes and Waste Stream Management*. Wiley & Sons, Inc., 1998, vol. 4, p. 616, ISBN: 0-471-29984-7.

[41] L. Smith and B. Craig, "Corrosion mechanisms and material performance in environments containing hydrogen sulfide and elemental sulfur", in *Sulphur-Assisted Corrosion in Nuclear Waste Disposal Systems Workshop*, Brussels, 2008.

[42] Y. S. Choi, D. Young, S. Nešić, and L. G. S. Gray, "Wellbore integrity and corrosion of carbon steel in CO_2 geologic storage environments: a literature review", *International Journal of Greenhouse Gas Control*, vol. 16, pp. 70–77, 2013. DOI: 10.1016/j.ijggc.2012.12.028.

[43] Y. Zhang, X. Pang, S. Qu, X. Li, and K. Gao, "Discussion of the CO_2 corrosion mechanism between low partial pressure and supercritical condition", *Corrosion Science*, vol. 59, pp. 186–197, 2012. DOI: 10.1016/j.corsci.2012.03.006.

[44] ASTM A564/A564M - 13, *Standard specification for hot-rolled and cold-finished age-hardening stainless steel*, 2002. DOI: 10.1520/A0564.

[45] D. Nakhaie and M. H. Moayed, "Pitting corrosion of cold rolled solution treated 17-4 PH stainless steel", *Corrosion Science*, vol. 80, pp. 290–298, 2014. DOI: 10.1016/j.corsci.2013.11.039.

[46] T. J. Mesquita, E. Chauveau, M. Mantel, N. Bouvier, and D. Koschel, "Corrosion and metallurgical investigation of two supermartensitic stainless steels for oil and gas environments", *Corrosion Science*, vol. 81, pp. 152–161, 2014. DOI: 10.1016/j.corsci.2013.12.015.

[47] J. U. N. Wang, Y. Lin, D. Zeng, J. Yan, and H. Fan, "Effects of the process parameters on the microstructure and properties of nitrided 17-4ph stainless steel", *Metallurgical and Materials Transactions B*, 2013. DOI: 10.1007/s11663-012-9781-9.

[48] R. Bhambroo, S. Roychowdhury, V. Kain, and V. S. Raja, "Effect of reverted austenite on mechanical properties of precipitation hardenable 17-4 PH stainless steel", *Materials Science and Engineering A*, vol. 568, pp. 127–133, 2013. DOI: 10.1016/j.msea.2013.01.011.

[49] L. W. Tsay, W. Lee, R. Shiue, and J. Wu, "Notch tensile properties of laser-surface-annealed 17-4 PH stainless steel in hydrogen-related environments", *Corrosion Science*, vol. 44, pp. 2101–2118, 2002. DOI: 10.1016/S0010-938X(02)00023-9.

[50] S Raja and P. Rao, "Environmental cracking behaviour of the precipitation hardened stainless steel , 17-4 PH , under applied potential", *Materials and Corrosion*, vol. 46, pp. 370–375, 1995. DOI: 10.1002/maco.19950460605.

[51] Z. Chen, G. Zhou, and Z. Chen, "Microstructure and hardness investigation of 17-4 PH stainless steel by laser quenching", *Materials Science and Engineering A*, vol. 534, pp. 536–541, 2012. DOI: 10.1016/j.msea.2011.12.004.

[52] F. Christien, R. Le Gall, and G. Saindrenan, "Phosphorus grain boundary segregation in steel 17-4 PH", *Scripta Materialia*, vol. 48, pp. 301–306, 2003. DOI: 10.1016/S1359-6462(02)00310-X.

[53] J. Wang, H. Zou, C. Li, S. Qiu, and B. Shen, "The spinodal decomposition in 17-4 PH stainless steel subjected to long-term aging at 350°C", *Materials Charcterization*, vol. 59, pp. 5–9, 2007. DOI: 10.1016/j.matchar.2007.04.018.

[54] K.-C. Hsu and C.-K. Lin, "Influence of frequency on the high-temperature fatigue crack growth behavior of 17-4 PH stainless steels", *Materials Transactions*, vol. 48, no. 3, pp. 490–499, 2007. DOI: 10.2320/matertrans.48.490.

[55] C. N. Hsiao, C. S. Chiou, and J. R. Yang, "Aging reactions in a 17-4 PH stainless steel", *Materials Chemistry and Physics*, vol. 74, pp. 134–142, 2002. DOI: 10.1016/S0254-0584(01)00460-6.

[56] C. F. Arisoy, G. Başman, and M. K. Şeşen, "Failure of a 17-4 PH stainless steel sailboat propeller shaft", *Engineering Failure Analysis*, vol. 10, pp. 711–717, 2003. DOI: 10.1016/S1350-6307(03)00041-4.

[57] T Bellezze, G Roventi, and R Fratesi, "Localised corrosion and cathodic protection of 17-4 PH propeller shafts", *Corrosion Engineering, Science and Technology*, vol. 48, no. 5, pp. 340–345, 2013. DOI: 10.1179/1743278213Y.0000000082.

[58] R. L. Liu, M. F. Yan, Y. Q. Wu, and C. Z. Zhao, "Microstructure and properties of 17-4 PH steel plasma nitrocarburized with a carrier gas containing rare earth elements", *Materials Characterization*, vol. 61, no. 1, pp. 19–24, 2009. DOI: 10.1016/j.matchar.2009.09.017.

[59] S. S. M. Tavares, F. J. da Silva, C. Scandian, G. F. da Silva, and H. F. G. de Abreu, "Microstructure and intergranular corrosion resistance of UNS S17400 (17-4 PH) stainless steel", *Corrosion Science*, vol. 52, no. 11, pp. 3835–3839, 2010. DOI: 10.1016/j.corsci.2010.07.016.

[60] A. Ziewiec, A. ZieliŃska-Lipiec, and E. Tasak, "Microstructure of welded joints of X5CrNiCuNb16-4 (17-4 PH) martensitic stainlees steel after heat treatment", *Archives of Metallurgy and Materials*, vol. 59, no. 3, pp. 965–970, 2014. DOI: 10.2478/amm-2014-0162.

[61] M. F. Yan, R. L. Liu, and D. L. Wu, "Improving the mechanical properties of 17-4 PH stainless steel by low temperature plasma surface treatment", *Materials and Design*, vol. 31, no. 4, pp. 2270–2273, 2010. DOI: 10.1016/j.matdes.2009.10.005.

[62] M. R. T. Shoushtari, "Effect of ageing heat treatment on corrosion behavior of 17-4 PH stainless steel in 3.5 % NaCl", *International Journal of ISSI*, vol. 7, no. 1, pp. 33–36, 2010.

[63] N. I. Shakshin, G. I. Deordiev, V. E. Scherbinin, V. Moorthy, T. Jayakumar, D. K. Bhattacharya, P. Kalyanasundaram, and B. Raj, "Evaluation of thermal ageing conditions in 17-4 PH stainless steel by Fourier descriptor analysis of magnetic hysteresis loops", *NDT and E International*, vol. 29, no. 6, pp. 379–385, 1996. DOI: 10.1016/S0963-8695(96)00041-2.

[64] H. Mirzadeh and A. Najafizadeh, "The rate of dynamic recrystallization in 17-4 ph stainless steel", *Materials and Design*, vol. 31, pp. 4577–4583, 2010, ISSN: 02641275. DOI: 10.1016/j.matdes.2010.05.052.

[65] P Kochmański and J Nowacki, "Activated gas nitriding of 17-4 PH stainless steel", *Surface & Coatings Technology*, vol. 200, pp. 6558–6562, 2006. DOI: 10.1016/j.surfcoat.2005.11.034.

[66] W. C. Chiang, C. C. Pu, B. L. Yu, and J. K. Wu, "Hydrogen susceptibility of 17-4 PH stainless steel", *Materials Letters*, vol. 57, pp. 2485–2488, 2003. DOI: 10.1016/S0167-577X(02)01298-3.

[67] S. S. M. Tavares, J. M. Pardal, L. Menezes, C. a. B. Menezes, and C. D'Ávila, "Failure analysis of PSV springs of 17-4 PH stainless steel", *Engineering Failure Analysis*, vol. 16, no. 5, pp. 1757–1764, 2009. DOI: 10.1016/j.engfailanal.2008.12.003.

[68] U. Viswanathan, S. Banerjee, and R. Krishnan, "Effects of aging on the microstructure of 17-4 PH stainless steel", *Materials Science and Engineering: A*, vol. 104, pp. 181–189, 1988. DOI: 10.1016/0025-5416(88)90420-X.

[69] R. L. Liu and M. F. Yan, "Improvement of wear and corrosion resistances of 17-4 PH stainless steel by plasma nitrocarburizing", *Materials and Design*, vol. 31, no. 5, pp. 2355–2359, 2010. DOI: 10.1016/j.matdes.2009.11.069.

[70] Y Sun and T Bell, "Low temperature plasma nitriding characteristics of precipitation hardening stainless steel", *Surface Engineering*, vol. 19, no. 5, pp. 331–336, 2003. DOI: 10.1179/026708403225007545.

[71] P. Nice and J. Martin, "Application limits for super martensitic and precipitation hardened stainless steel bar-stock materials", in *NACE Corrosion 2005*, Houston, TX: NACE International, 2005, Paper 05091.

[72] A Leyland, D. B. Lewis, P. R. Stevenson, and A Matthewsa, "Low temperature plasma diffusion treatment of stainless steels for improved wear resistance", *Surface*

and Coatings Technology, vol. 62, pp. 608–617, 1993. DOI: 10.1016/0257-8972(93)90307-A.

[73] R. Gaugh, "Sulfide stress cracking of precipitation hardening stainless steels", *Materials Performance*, pp. 24–29, 1977.

[74] V. M. Salinas-Bravo and J. G. Gonzalez-Rodriguez, "Stress corrosion cracking susceptibility of 17-4 PH turbine steel in aqueous environments", *British Corrosion Journal*, vol. 30, no. 1, pp. 77–79, 1995. DOI: 10.1179/bcj.1995.30.1.77.

[75] S. Kundu, D. Roy, S. Chatterjee, D. Olson, and B. Mishra, "Influence of interface microstructure on the mechanical properties of titanium/17-4 PH stainless steel solid state diffusion bonded joints", *Materials and Design*, vol. 37, pp. 560–568, 2012. DOI: 10.1016/j.matdes.2011.10.041.

[76] F. E. Hilali, M. Habashi, and A Moshine, "Comportement mécanique del'acier inoxydable martensitique 17-4 PH en corrosion sous contrainte et à la fragilisation par l'hydrogène environnemental", *Ann. Chim. Sci. Mat*, no. 24, pp. 169–194, 1999. DOI: 10.1016/S0151-9107(99)80044-0.

[77] J. W. Morris, C. Kinney, K. Pytlewski, and Y. Adachi, "Microstructure and cleavage in lath martensitic steels", *Science and Technology of Advanced Materials*, vol. 14, no. 1, 2013. DOI: 10.1088/1468-6996/14/1/014208.

[78] R. L. Klueh, P. J. Maziasz, and E. H. Lee, "Manganese as an austenite stabilizer in FeCrMnC steels", *Materials Science and Engineering*, vol. 102, no. 1, pp. 115–124, 1988. DOI: 10.1016/0025-5416(88)90539-3.

[79] A. Joshi, "Influence of density and distribution of intergranular sulfides on the sulfide stress cracking properties of high strength steels", *Corrosion*, vol. 34, no. 2, pp. 47–52, 1978. DOI: 10.5006/0010-9312-34.2.47.

[80] H. K. D. H. Bhadeshia, "Physical metallurgy of steels", in *Physical Metallurgy*, Fifth Edit, Elsevier B.V., 2014, pp. 2157–2214. DOI: 10.1016/B978-0-444-53770-6.00021-6.

[81] H. Bhadeshia and R. Honeycombe, *Steels - microstructure and properties*, 3rd ed. Elsevier, 2006, p. 344, ISBN: 9780750680844.

[82] T Cassagne, M Bonis, C Duret, and J. Crolet, "Limitations of 17-4 PH metallurgical, mechanical and corrosion aspects", in *NACE Corrosion 2003*, San Diego, CA: NACE International, 2003, Paper 03102.

[83] F. Christien, M. T. F. Telling, and K. S. Knight, "A comparison of dilatometry and in-situ neutron diffraction in tracking bulk phase transformations in a martensitic stainless steel", *Materials Characterization*, vol. 82, pp. 50–57, 2013. DOI: 10.1016/j.matchar.2013.05.002.

[84] ASTM E975 - 13, *Standard practice for x-ray determination of retained austenite in steel with near random crystallographic orientation*, 2009. DOI: 10.1520/E0975-13.

[85] J. Wang, H. Zou, C. Li, Y. Peng, S. Qiu, and B. Shen, "The microstructure evolution of type 17-4 PH stainless steel during long-term aging at 350°C", *Nuclear Engineering and Design*, vol. 236, pp. 2531–2536, 2006. DOI: 10.1016/j.nucengdes.2006.03.017.

[86] M. Leger, "Aciers moulés inoxydables martensitiques, propriétés d'emploi et de mise en œuvre", *La Revue de Métallurgie - CIT*, pp. 1357–1366, 1993. DOI: 10.1051/metal/199390101357.

[87] D. Porter, K. E. Easterling, and M. Sherif, *Phase Transformations in Metals and Alloys*. Routledge, 2009, p. 536.

[88] NACE TM-0177, *Laboratory testing of metals for resistance to sulfide stress cracking and stress corrosion cracking in H_2S environments*, 2005.

[89] O. Suleimenov and R. Krupp, "Solubility of hydrogen sulfide in pure water and in NaCl solutions, from 20 to 320°C and at saturation pressures", *Geochimica et Cosmochimica Acta*, vol. 58, no. Ii, pp. 2433–2444, 1994. DOI: 10.1016/0016-7037(94)90022-1.

[90] M. Singer, B. Brown, A. Camacho, and S. Nesic, "Combined effect of CO_2, H_2S and acetic acid on bottom of the line corrosion", in *NACE Corrosion 2007*, Nashville TN: NACE International, 2007, Paper 07661.

[91] N. Takeno, "Atlas of Eh-pH diagrams intercomparison of thermodynamic databases", National Institute of Advanced Industrial Science and Technology, Tokyo, Japan, Tech. Rep. No. 419, 2005, p. 287.

[92] R. Biernat and R. Robins, "High temperature potential/pH diagrams for the sulphur-water system", *Electrochimica Acta*, vol. 14, pp. 809–820, 1969. DOI: 10.1016/0013-4686(69)87003-9.

[93] B. J. Berkowitz and H. H. Horowitz, "The role of H_2S in the corrosion and hydrogen embrittlement of steel", *Journal of The Electrochemical Society*, vol. 129, no. 3, pp. 468–474, 1982. DOI: 10.1149/1.2123882.

[94] R. M. Latanision and H. Opperhauser, "The intergranular embrittlement of nickel by hydrogen: the effect of grain boundary segregation", *Metallurgical Transactions*, vol. 5, no. 2, pp. 483–492, 1974. DOI: 10.1007/BF02644118.

[95] J. L. Crolet and M. R. Bonis, "Revisiting hydrogen in steel, part I: theoretical aspects of charging, stress cracking and permeation", in *NACE Corrosion 2001*, Houston, TX: NACE International, 2001, Paper 01067.

[96] J. L. Crolet and M. R. Bonis, "Revisiting hydrogen in steel, part II : experimental verifications", in *NACE Corrosion 2001*, Houston, TX: NACE International, 2001, Paper 01072.

[97] F. W. H. Dean, "A review of hydrogen flux promoters", in *NACE Corrosion 2010*, San Antonio, TX: NACE International, 2010, Paper 10182.

[98] J.-L. Crolet, "Analysis of the various processes downstream cathodic hydrogen charging, I: diffusion, laboratory permeation and measurement of hydrogen content and diffusion coefficient", *Matériaux & Techniques*, vol. 104, no. 2, p. 205, 2016. DOI: 10.1051/mattech/2016007.

[99] J.-L. Crolet, "Analysis of the various processes downstream cathodic hydrogen charging, II: charging transients, precharging and natural permeation", *Matériaux & Techniques*, vol. 104, no. 2, p. 205, 2016. DOI: 10.1051/mattech/2016007.

[100] J.-L. Crolet, "Analysis of the various processes downstream cathodic hydrogen charging III: mechanistic issues on charging, degassing and sulfide stress cracking", *Matériaux & Techniques*, vol. 104, no. 2, p. 205, 2016. DOI: 10.1051/mattech/2016007.

[101] J.-L. Crolet, "Analysis of the various processes downstream cathodic hydrogen charging, IV: detailed mechanism of sulfide stress cracking", *Matériaux & Techniques*, vol. 104, no. 2, p. 205, 2016. DOI: 10.1051/mattech/2016007.

[102] H. Ma, X. Cheng, G. Li, S. Chen, Z. Quan, S. Zhao, and L. Niu, "The influence of hydrogen sulfide on corrosion of iron under different conditions", *Corrosion Science*, vol. 42, no. 10, pp. 1669–1683, 2000. DOI: 10.1016/S0010-938X(00)00003-2.

[103] D. W. Shoesmith, "The formation of ferrous monosulfide polymorphs during the corrosion of iron by aqueous hydrogen sulfide at 21°C", *Journal of The Electrochemical Society*, vol. 127, no. 7, p. 1007, 1980. DOI: 10.1149/1.2129808.

[104] D. W. Shoesmith, M. G. Bailey, and B. Ikeda, "Electrochemical formation of mackinawite in alkaline sulphide solutions", *Electrochimica Acta*, vol. 23, no. 12, pp. 1329–1339, 1978, ISSN: 00134686. DOI: 10.1016/0013-4686(78)80013-9.

[105] M. Watkins, M. Bluem, and J. Greer, "Fractography of sulfide stress cracking", in *NACE Corrosion 1975*, Toronto, Ontatio, Canada, 1976.

[106] R Kane and J Greer, "Sulfide stress cracking of high-strenth steels in laboratory and oilfield environments", *Journal of Petroleum Technology*, pp. 1483–1488, 1977. DOI: doi:10.2118/6144-PA.

[107] H. E. Townsend Jr, "Hydrogen sulfide stress corrosion cracking of high strength steel wire", *Corrosion*, vol. 28, no. 2, pp. 39–46, 1972. DOI: doi:10.5006/0010-9312-28.2.39.

[108] S. P. Lynch, "Hydrogen embrittlement (HE) phenomena and mechanisms", in *Stress corrosion cracking: Theory and practice*, i, 2011, pp. 90–130. DOI: 10.1533/9780857093769.1.90.

[109] L. Pfeil, "The effect of occluded hydrogen on the tensile strength of iron", *Proceedings of the Royal Society A: Mathematical, Physical and Engineering SciencesRoyal Society*, vol. 112, 1926. DOI: 10.1098/rspa.1926.0103.

[110] R. Oriani, "A mechanistic theory of hydrogen embrittlement of steels", *Berichte der Bunsengesellschaft für physikalische Chemie*, vol. 76, pp. 848–857, 1972. DOI: 10.1002.19720760864.

[111] T. C. Lee, I. M. Robertson, and H. K. Birnbaum, "An HVEM in situ deformation study of nickel doped with sulfur", *Acta Metallurgica*, vol. 37, no. 2, pp. 407–415, 1989. DOI: 10.1016/0001-6160(89)90225-3.

[112] C. D. Beachem, "A new model for hydrogen-assisted cracking (hydrogen "embrittlement")", *Metallurgical Transactions*, vol. 3, no. 2, pp. 441–455, 1972. DOI: 10.1007/BF02642048.

[113] I. M. Robertson, P. Sofronis, A. Nagao, M. L. Martin, S. Wang, D. W. Gross, and K. E. Nygren, "Hydrogen embrittlement understood", *Metallurgical and Materials Transactions A: Physical Metallurgy and Materials Science*, vol. 46, no. 6, pp. 2323–2341, 2015.

[114] S. P. Lynch, "Environmentally assisted cracking: overview of evidence for an adsorption-induced localised-slip process", *Acta Metallurgica*, vol. 36, no. 10, pp. 2639–2661, 1988. DOI: 10.1016/0001-6160(88)90113-7.

[115] S. P. Lynch, "Metallographic contributions to understanding mechanisms of environmentally assisted cracking", *Metallography*, vol. 23, no. 2, pp. 147–171, 1989. DOI: 10.1016/0026-0800(89)90016-5.

[116] A. Thompson and I. Bernstein, "The role of metallurgical variables in hydrogen-assisted environmental fracture", in *Advances in Corrosion Science and Technology*, M. G. Fontana and R. Staehle, Eds., vol. 7, Plenum Press, 1980, ch. 2.

[117] S. Lynch, "Mechanistic and fractographic aspects of stress corrosion cracking", in *Stress corrosion cracking: Theory and practice*, 3-4, vol. 30, 2012, pp. 63–104. DOI: 10.1515/corrrev-2012-0501.

[118] B. F. Brown, "Stress-corrosion cracking in high strength steels and in titanium and aluminum alloys", U.S. Department of Defense, Tech. Rep., 1972, p. 376.

[119] V. Kain, "Stress corrosion cracking in stainless steels", in *Stress Corrosion Cracking: Theory and practice*, Woodhead Publishing Limited, 2011, pp. 199–244. DOI: 10.1533/9780857093769.3.199.

[120] ASM International, *Corrosion in the Petrochemical Industry*, G. Linda, Ed. ASM International, 1994, p. 501.

[121] E. Phelps, "Stress corrosion of ferritic-martensitic stainless steels", *Metals Engineering Quarterly*, pp. 44–49, 1973.

[122] NACE TM-0198, *Slow strain rate test method for screening corrosion-resistant alloys (CRAs) for stress corrosion cracking in sour oilfield service*, 2016.

[123] W. Nisbet, R. Hartman, and G Handel, "Rippled strain rate test for cra sour service materials selection", in *NACE Corrosion 1997*, Houston, TX: NACE International, 1997, Paper 58.

[124] ASTM G49 - 85 (Reapproved 2011), "Standard practice for preparation and use of direct tension stress-corrosion test specimens", *ASTM Book of Standards*, vol. 85, no. Reapproved, pp. 6–11, 2000. DOI: 10.1520/G0049-85R11.2.

[125] ASTM G39 - 99 (Reapproved 2011), *Standard practice for preparation and use of bent-beam stress-corrosion test*, 2005.

[126] ASTM G38-01, *Standard practice for making and using c-ring stress-corrosion test specimens*, 2013.

[127] BS EN ISO 7539-2, *Corrosion of metals and alloys — stress corrosion testing — part 2: preparation and use of bent-beam specimens*, 2003.

[128] BS EN ISO 7539-5, *Corrosion of metals and alloys - stress corrosion testing - part 5: preparation and use of c-ring specimens*, 1989.

[129] BS EN ISO 7539-7, *Corrosion of metals and alloys - stress corrosion testing - part 7: method for slow strain rate testing*, 2005.

[130] P. Dent, C. Fowler, S. Bond, and S. Mishael, "New axially loaded full ring test method for assessment of susceptibility of girth welds and parent pipe to sour service cracking", in *NACE Corrosion 2017*, NACE International, 2017, Paper 8965.

[131] OTI 95 635, "A test method to determine the susceptibility to cracking of linepipe steels in sour service", Health and Safety Executive, Norwich, Tech. Rep., 1996.

[132] Turnbull, "Test methods for environment assisted cracking", *British Corrosion Journal*, vol. 27, no. 4, 1992. DOI: 10.1179/000705992798268459.

[133] M Henthorne, "The slow strain rate stress corrosion cracking test - a 50 year retrospective", *Corrosion*, vol. 9312, no. December, pp. 1–33, 2016.

[134] A. Ikeda, M. Ueda, and H. Okamoto, "The role of slow strain rate testing on evaluation of corrosion resistant alloys for hostile hot sour gas production", in *Slow strain rate testing for the evaluation of environmentally induced cracking: Research and engineering applications*, R. Kane, Ed., Pittsburgh, PA: Philadelphia, Pa : American Society for Testing and Materials, 1993, pp. 240–262. DOI: 10.1520/STP1210-EB.

[135] D. N. Wasnik, V. Kain, I. Samajdar, B. Verlinden, and P. K. De, "Resistance to sensitization and intergranular corrosion through extreme randomization of grain boundaries", *Acta Materialia*, vol. 50, no. 18, pp. 4587–4601, 2002. DOI: 10.1016/S1359-6454(02)00306-3.

[136] V Cíhal, S Lasek, M Blahetová, E Kalabisová, and Z Krhutová, "Trends in the electrochemical polarization potentiodynamic reactivation method - EPR", *Chemical and Biochemical Engineering Quarterly*, vol. 21, no. 1, pp. 47–54, 2007.

[137] J. J. Kim and S. J. Cho, "Detection of stress corrosion cracking of a martensitic stainless steel by electrochemical noise analysis", *Journal of Materials Science Letters*, vol. 22, pp. 865–867, 2003.

[138] J. González-Rodriguez, V. Salinas-Bravo, E. García-Ochoa, and A. Díaz-Sanchez, "Use of electrochemical potential noise to detect initiation and propagation of stress corrosion cracks in a 17-4 PH steel", *Corrosion*, vol. 53, no. 9, pp. 693–699, 1997.

[139] ASTM G148, *Standard practice for evaluation of hydrogen uptake , permeation , and transport in metals by an electrochemical technique*, 2011. DOI: 10.1520/G0148-97R11.

[140] F. W. H. Dean and D. J. Fray, "Ultrasensitive technique for detection of hydrogen emanating from steel and other solid surfaces", *Materials Science and Technology*, vol. 16, no. January, pp. 41–46, 2000. DOI: 10.1179/026708300773002645.

[141] F. W. H. Dean, "Measurement of hydrogen permeation through structural steel sections of varying thickness at 19°C", *Materials Science and Technology*, vol. 21, no. 3, pp. 347–351, 2005. DOI: 10.1179/174328405X29212.

[142] N. Mabho, K. Bergers, J. Flock, and U. Telgheder, "Determination of diffusible and total hydrogen concentration in coated and uncoated steel using melt and solid extraction techniques: part I", *Talanta*, vol. 82, no. 4, pp. 1298–1305, 2010. DOI: 10.1016/j.talanta.2010.06.045.

[143] P. G. Kumar and K Yu-ichi, "Diffusible hydrogen in steel weldments", *Transactions of JWRI*, vol. 42, no. 1, pp. 39–62, 2013.

[144] S. Evers, C. Senöz, and M. Rohwerder, "Hydrogen detection in metals: a review and introduction of a Kelvin probe approach", *Sci. Technol. Adv. Mater. Sci. Technol.*

Adv. Mater, vol. 14, no. 14, pp. 14 201–12, 2013. DOI: 10.1088/1468-6996/14/1/014201.

[145] R. Tuttle, "Selection of materials designed for use in a sour gas environment", *Materials Protection*, vol. 9, no. 4, pp. 2–4, 1970.

[146] R. Treseder, "Oil industry experience with hydrogen embrittlement and stress corrosion cracking", in *Stress Corrosion Cracking and Hydrogen Embrittlement of Iron Base Alloys*, 1977, pp. 147–161.

[147] R. D. Kane and P Quiroga, "Evaluation of ssc resistance of "sweet" materials in H_2S environments for development of ballot guidelines in mr0175/iso 15156", in *NACE Corrosion 2008*, New Orleans, LA: NACE International, 2008, Paper 08099.

[148] D. Vitale, "Effect of hydrogen sulfide partial pressure, pH and chloride content on the ssc resistance of martensitic stainless steels and martensitic precipitation hardening stainless steels", in *NACE Corrosion 1999*, Houston, TX, 1999, Paper 584.

[149] K. Denpo and H. Ogawa, "Passivity of corrosion-resistant alloys in environments containing chloride and hydrogen sulfide", *Corrosion*, vol. 53, no. 9, pp. 718–723, 1997. DOI: 10.5006/1.3290305.

[150] T. Hara and H. Asahi, "Effect of δ-ferrite on sulfide stress cracking in a low carbon 13 mass % chromium steel", *The iron and steel institute of Japan*, vol. 40, no. 11, pp. 1134–1141, 2000.

[151] M. Karaminezhaad, S. Sharafi, and K. Dalili, "Effect of molybdenum on SCC of 17-4 PH stainless steel under different aging conditions in chloride solutions", *Journal of Materials Science*, vol. 41, pp. 3329–3333, 2006. DOI: 10.1007/s10853-005-5416-8.

[152] K. G. Solheim, J. K. Solberg, J. Walmsley, F. Rosenqvist, and T. H. Bjørnå, "The role of retained austenite in hydrogen embrittlement of supermartensitic stainless steel", *Engineering Failure Analysis*, vol. 34, no. 4035, pp. 140–149, 2013. DOI: 10.1016/j.engfailanal.2013.07.025.

[153] A. Zeemann, "Failures of 17-4 PH steel parts in non sour environments", in *NACE Corrosion 2014*, San Antonio, TX: NACE International, 2014, Paper 4298.

[154] O. N. Sylyester, O. N. Celestine, I. G. Reuben, and C. E. Okechukwu, "Review of corrosion kinetics and thermodynamics of CO_2 and H_2S corrosion effects and associated prediction / evaluation on oil and gas pipeline system", *International Journal of Scientific & Technology Research*, vol. 1, no. 4, pp. 156–162, 2012.

[155] Y. Cai, P. Guo, D. Liu, S. Chen, and J. Liu, "Comparative study on CO_2 corrosion behavior of N80, P110, X52 and 13Cr pipe lines in simulated stratum water", *Science China Technological Sciences*, vol. 53, no. 9, pp. 2342–2349, 2010. DOI: 10.1007/s11431-010-3093-6.

[156] W. Sun and S. Nesic, "Kinetics of iron sulfide and mixed iron sulfide/carbonate scale precipitation in CO_2/sub>/H_2S corrosion", in *Corrosion 2006*, 2006, Paper 06644.

[157] F. Mancia, "The effect of environmental modification on the sulphide stress corrosion cracking resistance of 13Cr martensitic stainless steel in H_2S-CO_2-Cl^- systems", *Corrosion Science*, vol. 27, no. 10-11, pp. 1225–1237, 1987. DOI: 10.1016/0010-938X(87)90111-9.

[158] Z. Y. Liu, X. Z. Wang, R. K. Liu, C. W. Du, and X. G. Li, "Electrochemical and sulfide stress corrosion cracking behaviors of tubing steels in a H_2S/sub>s/CO_2

annular environment", *Journal of Materials Engineering and Performance*, vol. 23, no. 4, pp. 1279–1287, 2014. DOI: 10.1007/s11665-013-0855-x.

[159] J. Wang, Y. Lin, H. Fan, D. Zeng, Q. Peng, and B. Shen, "Effects of temperature on microstructure and wear of salt bath nitrided 17-4 PH stainless steel", *Journal of Materials Engineering and Performance*, vol. 21, no. August, pp. 1708–1713, 2012. DOI: 10.1007/s11665-011-0077-z.

[160] P Kochmański and J Nowacki, "Influence of initial heat treatment of 17-4 PH stainless steel on gas nitriding kinetics", *Surface & Coatings Technology*, vol. 202, pp. 4834–4838, 2008. DOI: 10.1016/j.surfcoat.2008.04.058.

[161] R. L. Liu and M. F. Yan, "The microstructure and properties of 17-4 PH martensitic precipitation hardening stainless steel modified by plasma nitrocarburizing", *Surface & Coatings Technology*, vol. 204, no. 14, pp. 2251–2256, 2010. DOI: 10.1016/j.surfcoat.2009.12.016.

[162] G.-j. Li, J. Wang, C. Li, Q. Peng, J. Gao, and B.-l. Shen, "Microstructure and dry-sliding wear properties of dc plasma nitrided 17-4 PH stainless steel", *Nuclear Instruments and Methods in Physics Research Section B: Beam Interactions with Materials and Atoms*, vol. 266, pp. 1964–1970, 2008. DOI: 10.1016/j.nimb.2008.02.073.

[163] B. Tesi, T. Bacci, and G. Poli, "Analysis of surface structures and of size and shape variations in ionitrided precipitation hardening stainless steel samples", *Vacuum*, vol. 35, no. 8, pp. 307–314, 1985. DOI: 10.1016/0042-207X(85)90113-7.

[164] T. Aizawa and H. Kuwahara, "Plasma nitriding as an environmentally benign surface structuring process", *Materials Transactions*, vol. 44, no. 7, 2003.

[165] W. Rembges and W. Oppel, "Process control of plasma nitriding and plasma nitrocarburizing in industry", *Surface and Coatings Technology*, vol. 59, no. 1-3, pp. 129–134, 1993. DOI: 10.1016/0257-8972(93)90069-Z.

[166] D. Pye, "An introduction to nitriding", in *Practical Nitriding and Ferritic Nitrocarburizing*, 2003, ch. 1, pp. 71–7812. DOI: 10.1361/pnafn2003p001.

[167] T. Moskalioviene and A. Galdikas, "The effect of hydrogen on plasma nitriding of austenitic stainless steel: kinetic modeling", *Metallurgical and Materials Transactions A*, vol. 46, no. 12, pp. 5588–5595, 2015. DOI: 10.1007/s11661-015-3183-y.

[168] A. Grill, *Cold Plasma Materials Fabrication: From Fundamentals to Applications*. Wiley-IEEE Press, 1994, p. 272.

[169] ASM International Handbook, *ASM Handbook: Heat Treating*, 10th ed. 2001, vol. 4, p. 3470. DOI: 10.1016/S0026-0576(03)90166-8.

[170] D. Pye, "Ion nitriding", in *Practical Nitriding and Ferritic Nitrocarburizing*, 2003, ch. 8, pp. 71–88. DOI: 10.1361/pnafn2003p071.

[171] S. R. Hosseini, F Ashrafizadeh, and A Kermanpur, "Calculation and experimentation of the compound layer thickness in gas and plasma nitriding of iron", *Iranian Journal of Science & Technology,*, vol. 34, pp. 553–566, 2010.

[172] B. Podgornik, J. Vižintin, and V. Leskovšek, "Tribological properties of plasma and pulse plasma nitrided AISI 4140 steel", *Surface and Coatings Technology*, vol. 108-109, no. 1-3, pp. 454–460, 1998. DOI: 10.1016/S0257-8972(98)00571-4.

[173] ASM, *Heat Treating ASM Metals Handbook Volume 4*. 1991, ISBN: 978-0-87170-379-8.

[174] O. Kubaschewski, *Iron—Carbon Fe—C*. 1982, pp. 23–26. DOI: 10.1007/978-3-662-08024-5_12.

[175] S. K. Kim, J. S. Yoo, J. M. Priest, and M. P. Fewell, "Characteristics of martensitic stainless steel nitrided in a low-pressure RF plasma", *Surface and Coatings Technology*, vol. 163, no. 164, pp. 380–385, 2003. DOI: 10.1016/S0257-8972(02)00631-X.

[176] H Dong, "S-phase surface engineering of Fe–Cr, Co-Cr and Ni-Cr alloys", *International Materials Review*, vol. 55, no. 2, pp. 65–98, 2010. DOI: 10.1179/095066009X12572530170589.

[177] M. Lepicka and M. Gradzka-Dahlke, "Direct current and pulsed direct current plasma nitriding of ferrous materials a critical review", *Acta Mechanica et Automatica*, vol. 10, no. 2, pp. 150–158, 2016. DOI: 10.1515/ama-2016-0024.

[178] C. X. Li, "Active screen plasma nitriding – an overview", *Surface Engineering*, vol. 26, no. 1-2, pp. 135–141, 2010. DOI: 10.1179/174329409X439032.

[179] V. V. Budilov, R. D. Agzamov, and K. N. Ramazanov, "Ion nitriding in glow discharge with hollow cathode effect", *Metal Science and Heat Treatment*, vol. 49, no. 7-8, pp. 358–361, 2007. DOI: 10.1007/s11041-007-0065-y.

[180] J. Georges and D. Cleugh, "Active screen plasma nitriding", in *Stainless steel 2000 – thermochemical surface engineering of stainless steel*, T. Bell. and K. Akamatsu, Eds., London: The Institute of Materials, 2001, pp. 377–387. DOI: 10.1179/174329409X439032.

[181] C. X. Li, T Bell, and H Dong, "A study of active screen plasma nitriding", *Surface Engineering*, vol. 18, no. 3, pp. 174–181, 2002. DOI: 10.1179/026708401225005250.

[182] S. Corujeira Gallo and H. Dong, "Study of active screen plasma processing conditions for carburising and nitriding austenitic stainless steel", *Surface and Coatings Technology*, vol. 203, no. 24, pp. 3669–3675, 2009. DOI: 10.1016/j.surfcoat.2009.05.045.

[183] S. C. Gallo and H. Dong, "On the fundamental mechanisms of active screen plasma nitriding", *Vaccum*, vol. 84, no. 2, pp. 321–325, 2010. DOI: 10.1016/j.vacuum.2009.07.002.

[184] P. Hubbard, S. J. Dowey, J. G. Partridge, E. D. Doyle, and D. G. McCulloch, "Investigation of nitrogen mass transfer within an industrial plasma nitriding system II: application of a biased screen", *Surface and Coatings Technology*, vol. 204, no. 8, pp. 1151–1157, 2010. DOI: 10.1016/j.surfcoat.2009.08.030.

[185] P Hubbard, D. G. Mcculloch, E. D. Doyle, S. J. Dowey, and J. N. Georges, "A fundamental contribution to a study of the active screen plasma nitriding process", *Berg Huettenmaenn Monatsh*, vol. 151, no. 2000, pp. 151–441, 2006. DOI: 10.1007/BF03165204.

[186] P. Hubbard, J. G. Partridge, E. D. Doyle, D. G. McCulloch, M. B. Taylor, and S. J. Dowey, "Investigation of nitrogen mass transfer within an industrial plasma nitriding system I: the role of surface deposits", *Surface and Coatings Technology*, vol. 204, no. 8, pp. 1145–1150, 2010. DOI: 10.1016/j.surfcoat.2009.08.029.

[187] H Dong, M Esfandiari, and X. Y. Li, "On the microstructure and phase identification of plasma nitrided 17-4 PH precipitation hardening stainless steel", *Surface & Coatings Technology*, vol. 202, pp. 2969–2975, 2008. DOI: 10.1016/j.surfcoat.2007.10.036.

[188] H. J. Spies, "Corrosion behaviour of nitrided, nitrocarburised and carburised steels", in *Thermochemical Surface Engineering of Steels: Improving Materials Performance*, Woodhead Publishing Limited, 2014, ch. 6, pp. 267–309. DOI: 10.1533/9780857096524.2.267.

[189] D. L. Cocke, M. Jurcik-Rajman, and S. Veprek, "The surface properties and reactivities of plasma-nitrided iron and their relation to corrosion passivation", *Journal of The Electrochemical Society*, vol. 136, no. 12, pp. 3655–3662, 1989. DOI: 10.1149/1.2096526.

[190] H. J. Grabke, "The role of nitrogen in the corrosion of iron and steels.", *ISIJ International*, vol. 36, no. 7, pp. 777–786, 1996. DOI: 10.2355/isijinternational.36.777.

[191] I. Flis-Kabulska, Y. Sun, and J. Flis, "Monitoring the near-surface pH to probe the role of nitrogen incorrosion behaviour of low-temperature plasma nitrided 316L stainless steel", *Electrochimica Acta*, vol. 104, pp. 208–215, 2013. DOI: 10.1016/j.electacta.2013.04.111.

[192] S. D. Chyou and H. C. Shih, "Effect of nitrogen on the corrosion of plasma-nitrided 4140 steel", *Corrosion*, vol. 47, no. 1, pp. 31–34, 1991. DOI: 10.5006/1.3585216.

[193] ASTM E8/E8M, "Standard test methods for tension testing of metallic materials 1", *Annual Book of ASTM Standards 4*, pp. 1–27, 2010. DOI: 10.1520/E0008.

[194] M. Dickson, "The significance of texture parameters in phase analysis by x-ray diffraction", *Journal of Applied Crystallography*, vol. 2, pp. 176–180, 1969. DOI: 10.1107/S0021889869006881.

[195] T. Christiansen and M. A. J. Somers, "Low temperature gaseous nitriding and carburising of stainless steel", *Surface Engineering*, vol. 21, no. 5-6, pp. 445–455, 2005. DOI: 10.1179/174329405X68597.

[196] L. Cook, "Low temperature active-screen plasma surface alloying of precipitation hardening stainless steels", PhD thesis, University of Birmingham, 2012.

[197] S. Mahadevan, R. Manojkumar, T. Jayakumar, C. R. Das, and B. P. C. Rao, "Precipitation-induced changes in microstrain and its relation with hardness and tempering parameter in 17-4 PH stainless steel", *Metallurgical and Materials Transactions A: Physical Metallurgy and Materials Science*, vol. 47, no. 6, pp. 3109–3118, 2016. DOI: 10.1007/s11661-016-3440-8.

[198] C. E. Pinedo, S. I. V. Larrotta, A. S. Nishikawa, H. Dong, X. Y. Li, R. Magnabosco, and A. P. Tschiptschin, "Low temperature active screen plasma nitriding of 17-4 PH stainless steel", *Surface and Coatings Technology*, vol. 308, pp. 189–194, 2016. DOI: 10.1016/j.surfcoat.2016.07.096.

[199] U. K. Viswanathan, P. K. K. Nayar, and R. Krishnan, "Kinetics of precipitation in 17–4 PH stainless steel", *Materials Science and Technology*, vol. 5, no. 4, pp. 346–349, 1989. DOI: 10.1179/mst.1989.5.4.346.

[200] G. Salje and M. Feller-Kniepmeier, "The diffusion and solubility of copper in iron", *Journal of Applied Physics*, vol. 48, no. 5, pp. 1833–1839, 1977. DOI: 10.1063/1.323934.

[201] M Sennour, P. H. Jouneau, and C Esnouf, "TEM and EBSD investigation of continuous and discontinuous precipitation of CrN in nitrided pure Fe-Cr alloys", *Journal of Materials Science*, vol. 39, no. 14, pp. 4521–4531, 2004. DOI: 10.1023/b:jmsc.0000034146.64444.80.

[202] H. Jacobs, D. Rechenbach, and U. Zachwieja, "Structure determination of γ'-Fe_4N and ε-Fe_3N", *Journal of Alloys and Compounds*, vol. 227, no. 1, pp. 10–17, 1995. DOI: 10.1016/0925-8388(95)01610-4.

[203] E. Metin and O. T. Inal, "Formation and growth of iron nitrides during ion-nitriding", *Journal of Materials Science*, vol. 22, no. 8, pp. 2783–2788, 1987. DOI: 10.1007/BF01086471.

[204] S Epstein, H. C. Cross, E. C. Groesbeck, and I. J. Wymore, "Observations on the iron-nitrogen system", *Bureau of Standards Journal of Research*, vol. 3, no. 6, p. 1005, 1929. DOI: 10.6028/jres.003.052.

[205] AK Steel, *17-4 ph stainless steel: product data bulletin*, 2007. [Online]. Available: www.aksteel.com.

[206] J. P. Materkowski and G. Krauss, "Tempered martensite embrittlement in SAE 4340 steel", *Metallurgical Transactions A*, vol. 10, no. 11, pp. 1643–1651, 1979. DOI: 10.1007/BF02811697.

[207] M. Walters, "Sulphide stress cracking test development for weldable 13 % Cr supermartensitic stainless steels in seabed environments", Eng.D. University of Birmingham, 2014.

[208] Y. Zheng, B. Brown, and S. Nesic, "Electrochemical study and modeling of H_2S corrosion of mild steel", in *Nace Corrosion 2013*, Orlando, Florida, 2013, pp. 1–22.

[209] S Rajappa, R Zhang, and M Gopal, "Modeling the diffusion effects through the iron carbonate layer in the carbon dioxide corrosion of carbon steel", in *NACE Corrosion 1998*, Houston, TX, 1998, p. 29.

[210] R. G. Kelly, J. R. Scully, D. W. Shoesmith, and R. G. Buchheit, *Electrochemical Techniques in Corrosion Science and Engineering*, P. A. Schweitzer PE, Ed. Marel Dekker, 2003, p. 426. DOI: 10.1201/9780203909133.

[211] P. C. Pistorius and G. T. Burstein, "Metastable pitting corrosion of stainless steel and the transition to stability", *Philosophical Transactions of the Royal Society A: Mathematical, Physical and Engineering Sciences*, vol. 341, no. 1662, pp. 531–559, 1992. DOI: 10.1098/rsta.1992.0114.

[212] A. Anderko, N. Sridhar, and D. S. Dunn, "A general model for the repassivation potential as a function of multiple aqueous solution species", *Corrosion Science*, vol. 46, no. 7, pp. 1583–1612, 2004. DOI: 10.1016/j.corsci.2003.10.002.

[213] Amirudin, A., D. Thieny, D. T. A. Amirudin, A Amirudin, D Thierry, Amirudin, A., and D. Thieny, "Application of electrochemical impedance spectroscopy to study the degradation of polymer-coated metals", *Progress in Organic Coatings*, vol. 9440, no. 95, pp. 1–28, 1995. DOI: 10.1016/0300-9440(95)00581-1.

[214] E. Barsoukov and J. R. Macdonald, *Impedance Spectroscopy*. 2005, pp. 1–595. DOI: 10.1002/0471716243. eprint: 0709.1163.

[215] M Sluyters-Rehbach, "Impedances of electrochemical systems: terminology, nomenclature and representation - part I: cells with metal electrodes and liquid solutions (iupac recommendations 1994)", *Pure and Applied Chemistry*, vol. 66, no. 9, pp. 1831–1891, 1994. DOI: 10.1351/pac199466091831.

[216] ASTM G61, *Standard test method for conducting cyclic potentiodynamic polarization measurements for localized corrosion susceptibility of*, 2014. DOI: 10.1520/G0061-86R14.2.

[217] M. Stern, "The relation between pitting corrosion and the ferrous-ferric oxidation-reduction kinetics on passive surfaces", *Journal of The Electrochemical Society*, vol. 104, no. 10, pp. 600–606, 1957. DOI: 10.1149/1.2428424.

[218] ASTM G102, *Standard practice for from electrochemical measurements*, 2015. DOI: 10.1520/G0102-89R15E01.2.

[219] 16773-2 ISO/FDIS, "Electrochemical impedance spectroscopy (EIS) on coated and uncoated metallic specimens, part 2: collection of data", 2016.

[220] ISO/TR 16208, *Corrosion of metals and alloys - test method for corrosion of materials by electrochemical impedance measurements*, 2014.

[221] B. S. Covino, M Rosen, and T. J. Driscoll, "The effect if oxygen on the open-circuit passivity of Fe-18 Cr", *Corrosion Science*, vol. 26, no. 2, pp. 95–107, 1986.

[222] Y.-S. Choi, S. Nesic, and S. Ling, "Effect of H_2S on the CO_2 corrosion of carbon steel in acidic solutions", *Electrochimica Acta*, vol. 56, no. 4, pp. 1752–1760, 2011. DOI: 10.1016/j.electacta.2010.08.049.

[223] P. Ernst, N. Laycock, M. Moayed, and R. Newman, "The mechanism of lacy cover formation in pitting", *Corrosion Science*, vol. 39, no. 6, pp. 1133–1136, 1997. DOI: 10.1016/S0010-938X(97)00043-7.

[224] M. Ghahari, D. Krouse, N. Laycock, T. Rayment, C. Padovani, M. Stampanoni, F. Marone, R. Mokso, and A. J. Davenport, "Synchrotron x-ray radiography studies of pitting corrosion of stainless steel: extraction of pit propagation parameters", *Corrosion Science*, vol. 100, pp. 23–35, 2015. DOI: 10.1016/j.corsci.2015.06.023.

[225] G Wranglen, "Pitting and sulfide inclusions in steel", *Corrosion Science*, vol. 14, no. 5, pp. 331–349, 1974. DOI: 10.1016/s0010-938x(74)80047-8.

[226] R. Avci, B. H. Davis, M. L. Wolfenden, I. B. Beech, K. Lucas, and D. Paul, "Mechanism of MnS-mediated pit initiation and propagation in carbon steel in

an anaerobic sulfidogenic media", *Corrosion Science*, vol. 76, pp. 267–274, 2013. DOI: 10.1016/j.corsci.2013.06.049.

[227] C Zhao, C. X. Li, H Dong, and T Bell, "Study on the active screen plasma nitriding and its nitriding mechanism", *Surface & Coatings Technology*, vol. 201, pp. 2320–2325, 2006. DOI: 10.1016/j.surfcoat.2006.03.045.

[228] J. Smith, Z Qin, and D. Shoesmith, "Electrochemical impedance studies of the growth of sulfide films on copper", in *17th International Corrosion Congress*, 2009, pp. 1–9.

[229] J. Ning, Y. Zheng, D. Young, B. Brown, and S. Nešic, "Thermodynamic study of hydrogen sulfide corrosion of mild steel", *Corrosion*, vol. 70, no. 4, pp. 375–389, 2014. DOI: 10.5006/0951.

[230] A. A. Douabul and J. P. Riley, "The solubility of gases in distilled water and sea-water - V. hydrogen sulphide", *Deep Sea Research Part A, Oceanographic Research Papers*, vol. 26, no. 3, pp. 259–268, 1979. DOI: 10.1016/0198-0149(79)90023-2.

[231] R. Kane, "Roles of H_2S in behaviour of engineering alloys", *International Metals Review*, vol. 30, no. 6, pp. 291–301, 1985. DOI: 10.1179/imtr.1985.30.1.291.

[232] S. Nešić, K.-l. J. Lee, and V. Ruzic, "A mechanistic model of iron carbonate film growth and the effect on CO_2 corrosion of mild steel", in *NACE Corrosion 2002*, Houston, TX, 2002, pp. 1–35.

[233] S. N. Smith and J. L. Pacheco, "Prediction of corrosion in slightly sour enviroments", *Corrosion*, no. 02241, Paper no. 02241, 2002, ISSN: 00941492. DOI: 51300-02241.

[234] Y. Hu, "Corrosion behavior of drill pipe steel in CO_2-H_2S environment", *International Journal of Electrochemical Science*, vol. 12, pp. 6705–6713, 2017. DOI: 10.20964/2017.07.81.

[235] E. Abelev, J. Sellberg, T. Ramanarayanan, and S. Bernasek, "Effect of H_2S on Fe corrosion in CO_2-saturated brine", pp. 6167–6181, 2009. DOI: 10.1007/s10853-009-3854-4.

[236] J. R. Scully, D. C. Silverman, and M. W. Kendig, *Electrochemical Impedance: Analysis and Interpretation*, J. R. Scully, D. C. Silverman, and M. W. Kending, Eds. Philadelphia: American Society for Testing and Materials, 1993.

[237] D. D. Macdonald and M. Urquidi-Macdonald, "Application of Kramers-Kronig transforms in the analysis of electrochemical systems, I: polarization resistance", *Journal of The Electrochemical Society*, vol. 132, no. October, pp. 2316–2319, 1985.

[238] D. D. Macdonald, "Application of kramers-kronig transforms in the analysis of electrochemical systems", *Journal of The Electrochemical Society*, vol. 132, no. October, pp. 2316–2319, 1985, ISSN: 00134651. DOI: 10.1149/1.2113570.

[239] Z Kolozváry, "Residual stresses in nitriding", in *Handbook of Residual Stresses and Deformation of Steel*, 2001, pp. 209–219.

[240] C. Mansilla, V. Ocelík, and J. T. M. De Hosson, "Local residual stress measurements on nitride layers", *Materials Science and Engineering A*, vol. 636, pp. 476–483, 2015. DOI: 10.1016/j.msea.2015.04.023.

[241] B. Podgornik, V. Leskovšek, M. Kovačič, and J. Vižintin, "Residual stress field analysis and prediction in nitrided tool steel", *Materials and Manufacturing Processes*, vol. 26, no. 9, pp. 1097–1103, 2011. DOI: 10.1080/10426914.2010.525573.

[242] J. C. Stinville, J. Cormier, C. Templier, and P. Villechaise, "Monotonic mechanical properties of plasma nitrided 316L polycrystalline austenitic stainless steel: mechanical behaviour of the nitrided layer and impact of nitriding residual stresses", *Materials Science and Engineering A*, vol. 605, pp. 51–58, 2014. DOI: 10.1016/j.msea.2014.03.039.

[243] X. Song, Z.-Q. Zhang, S. Narayanaswamy, Y. Z. Huang, and M. Zarinejad, "Numerical and experimental study on the residual stresses in the nitrided steel", *Journal of Materials Engineering and Performance*, vol. 25, no. 9, pp. 4036–4045, 2016. DOI: 10.1007/s11665-016-2236-8.

[244] T. Hirsch, A. Rocha, F. Ramos, and T. Strohaecker, "Residual stress-affected diffusion during plasma nitriding of tool steels", *Metallurgical and Materials Transactions A*, vol. 35, no. 11, pp. 3523–3530, 2004. DOI: 10.1007/s11661-004-0189-2.

[245] V. Leskovšek, B. Podgornik, and D. Nolan, "Modelling of residual stress profiles in plasma nitrided tool steel", *Materials Characterization*, vol. 59, no. 4, pp. 454–461, 2008. DOI: 10.1016/j.matchar.2007.03.009.

[246] N. L. Loh and L. W. Siew, "Residual stress profiles of plasma nitrided steels", *Surface Engineering*, vol. 15, no. 2, pp. 137–142, 1999.

[247] S Thaiwatthana, N Jantaping, and P Limthongkul, "Residual stress measurement of low temperature plasma surface alloyed layer using x-ray diffraction techniques", *Surface Engineering*, vol. 28, no. 4, pp. 273–276, 2012. DOI: 10.1179/1743294411Y.0000000060.

[248] ASTM E2860, *Standard test method for residual stress measurement by x-ray diffraction for bearing steels*, 2012. DOI: 10.1520/E2860.

[249] P. J. Withers and H. K. D. H. Bhadeshia, "Residual stress. Part 1 – measurement techniques", *Materials Science and Technology*, vol. 17, no. 4, pp. 355–365, 2001. DOI: 10.1179/026708301101509980.

[250] W. H. Friske and J. P. Page, "Shot peening to prevent the corrosion cracking of austenitic stainless steels", *Rockwell International Energy Systems Group*, vol. 1, pp. 20–32, 1979.

[251] E. Qin, G. Chen, Z. Tan, and S. Wu, "Shot peening and thermal stress relaxation in 17-4 PH stainless steel", *Journal of Materials Engineering and Performance*, vol. 24, no. 11, pp. 4578–4583, 2015, ISSN: 1059-9495. DOI: 10.1007/s11665-015-1761-1.

[252] D. Karthik, S. Kalainathan, and S. Swaroop, "Surface modification of 17-4 PH stainless steel by laser peening without protective coating process", *Surface and Coatings Technology*, vol. 278, pp. 138–145, 2015. DOI: 10.1016/j.surfcoat.2015.08.012.

[253] Z. Wang, Y. Chen, and C. Jiang, "Thermal relaxation behavior of residual stress in laser hardened 17-4 PH steel after shot peening treatment", *Applied Surface Science*, vol. 257, no. 23, pp. 9830–9835, 2011. DOI: 10.1016/j.apsusc.2011.06.032.

[254] M. A. Terres, R. Bechouel, and S. B. Mohamed, "Low cycle fatigue behaviour of nitrided layer of 42CrMo4 steel", vol. 6, no. 1, pp. 18–27, 2017. DOI: 10.11648/j.ijmsa.20170601.13.

[255] H. Kovaci, A. F. Yetim, Baran, and A. Çelik, "Fatigue crack growth analysis of plasma nitrided AISI 4140 low-alloy steel: Part 1 - constant amplitude loading",

Materials Science and Engineering A, vol. 672, pp. 265–275, 2016. DOI: 10.1016/j.msea.2016.07.002.

[256] H. Kovaci, A. F. Yetim, Baran, and A. Çelik, "Fatigue crack growth analysis of plasma nitrided AISI 4140 low-alloy steel: Part 2 - variable amplitude loading and load interactions", *Materials Science and Engineering A*, vol. 672, pp. 265–275, 2016. DOI: 10.1016/j.msea.2016.07.002.

[257] A. Şengül and A. Çelik, "Effect of plasma nitriding on fatigue crack growth on AISI 4140 steel under variable amplitude loading", *Surface and Coatings Technology*, vol. 205, no. 21-22, pp. 5172–5177, 2011. DOI: 10.1016/j.surfcoat.2011.05.027.

[258] G. G. Stoney, "The tension of metallic films deposited by electrolysis", *Proceedings of the Royal Society of London. Series A*, vol. 82, no. 553, pp. 172–175, 2012.

[259] X. Feng, Y. Huang, and A. J. Rosakis, "On the stoney formula for a thin film/substrate system with nonuniform substrate thickness", *Journal of Applied Mechanics*, vol. 74, no. 6, p. 1276, 2007. DOI: 10.1115/1.2745392.

[260] M. A. V. Devanathan and Z. Stachurski, "The mechanism of hydrogen evolution on iron in acid solutions by determination of permeation rates", *Journal of The Electrochemical Society*, vol. 111, no. 5, pp. 619–623, 1964. DOI: 10.1149/1.2426195.

[261] J. Crank, *The mathematics of diffusion*, 2nd ed., Oxford University Press, Ed. Clarendon Press, 1975, vol. 4, p. 414.

[262] J. O. Bockris and P. K. Subramanyan, "Hydrogen embrittlement and hydrogen traps", *Journal of The Electrochemical Society*, vol. 118, no. 7, p. 1114, 1971. DOI: 10.1149/1.2408257.

[263] R. A. Oriani, "The diffusion and trapping of hydrogen in steel", *Acta Metallurgica*, vol. 18, pp. 147–157, 1970.

[264] H. J. Grabke and E. Riecke, "Absorption and diffusion of hydrogen in steels", *Materiali in Tehnologije*, vol. 34, no. 6, pp. 331–342, 2000.

[265] H. K. D. H. Bhadeshia, "Prevention of hydrogen embrittlement in steels", *ISIJ International*, vol. 56, no. 1, pp. 24–36, 2016. DOI: 10.2355/isijinternational.ISIJINT-2015-430.

[266] U. Arifov, T. Radzhabov, and V. Yakhshiev, "Effect of surface treatment on hydrogen sorption and the mechanical properties of steels", *Fiziko-Khimicheskaya Mekhanika Materialov*, vol. 13, no. 5, pp. 85–88, 1977.

[267] A. M. Brass, J. Chene, and J. C. Pivin, "Influence of nitrogen ion implantation on hydrogen permeation in an extra mild steel", *Journal of Materials Science*, vol. 24, no. 5, pp. 1693–1699, 1989. DOI: 10.1007/BF01105693.

[268] S Sobieszczyk, E Łunarska, J Ćwiek, A Zieliński, and K Nikiforow, "Hydrogen charging of plasma nitrided steel in acid solution", *Manufacturing Engineering*, vol. 17, no. 1, pp. 205–208, 2006.

[269] J Ćwiek, "Plasma nitriding as a prevention method against hydrogen degradation of steel", *Advances in Materials Science*, vol. 9, no. 1, pp. 25–32, 2009. DOI: 10.2478/v10077-009-0001-5.

[270] J. Ćwiek and M. Baczyńska, "Behaviour of nitrided layers subjected to influence of hydrogen", *Archives of Materials Science and Engineering*, vol. 43, no. 1, pp. 30–41, 2010.

[271] J Ćwiek, "Interaction between hydrogen and a nitrided layer", *Journal of achievements in materials and manufacturing engineering*, vol. 47, no. 1, pp. 34–41, 2011.

[272] L Nanis and T. Namboodhiri, "Mathematics of the electrochemical extraction of hydrogen from iron", *Journal of The Electrochemical Society*, vol. 119, p. 691, 1972. DOI: 10.1149/1.2404296.

[273] F. Dean and C. Fowler, "Hydrogen flux and corrosion rate measurements on hydrogen induced cracking susceptible and resistant a516 steels in various sour environments", *Corrosion 2010*, no. 10179, 2010.

[274] D. H. Jack and K. H. Jack, "Invited reviews : carbides and nitrides in steel", *Materials Science and Engineering*, vol. 11, pp. 1–27, 1973.

[275] K. Jack, "The iron-nitrogen system: the crystal structures of ε-phase iron nitrides", *Acta Crystallographica*, vol. 5, no. 4, pp. 404–411, 1952. DOI: 10.1107/S0365110X52001258.

[276] S. B. Hendricks and P. R. Kosting, "The crystal structure of Fe_2P, Fe_2N, Fe_3N and FeB", *Zeitschrift für Kristallographie - Crystalline Materials*, vol. 74, no. 1-6, pp. 511–533, 1930. DOI: 10.1524/zkri.1930.74.1.511.

[277] E. J. Song, H. K. Bhadeshia, and D. W. Suh, "Effect of hydrogen on the surface energy of ferrite and austenite", *Corrosion Science*, vol. 77, no. October, pp. 379–384, 2013. DOI: 10.1016/j.corsci.2013.07.043.

[278] S. Grigull and S. Parascandola, "Ion-nitriding induced plastic deformation in austenitic stainless steel", *Journal of Applied Physics*, vol. 88, no. 11, pp. 6925–6927, 2000. DOI: 10.1063/1.1321019.

[279] K. Ono and M. Meshii, "Hydrogen detrapping from grain boundaries and dislocations in high purity iron", *Acta Metallurgica Et Materialia*, vol. 40, no. 6, pp. 1357–1364, 1992. DOI: 10.1016/0956-7151(92)90436-I.

[280] A. Turnbull and R. B. Hutchings, "Analysis of hydrogen atom transport in a two-phase alloy", *Materials Science and Engineering A*, vol. 177, no. 1-2, pp. 161–171, 1994. DOI: 10.1016/0921-5093(94)90488-X.

[281] J. L. Lee and J. Y. Lee, "Hydrogen trapping in AISI 4340 steel", *Metal Science*, vol. 17, no. 9, pp. 426–432, 1983. DOI: 10.1179/030634583790420619.

[282] A. J. Kumnick and H. H. Johnson, "Deep trapping for hydrogen iron", *Acta Metallurgica*, vol. 28, pp. 33–39, 1980.

[283] J. J. Au and H. K. Birnbaum, "Magnetic relaxation studies of the motion of hydrogen and deuterium in iron", *Acta Metallurgica*, vol. 26, no. 7, pp. 1105–1116, 1978. DOI: 10.1016/0001-6160(78)90138-4.

[284] P. Manolatos, M. Jerome, and J. Galland, "Necessity of a palladium coating to ensure hydrogen oxidation during electrochemical permeation measurements on iron", *Electrochimica Acta*, vol. 40, no. 7, pp. 867–871, 1995. DOI: 10.1016/0013-4686(94)00343-Y.

[285] A. Turnbull, D. A. Horner, and B. J. Connolly, "Challenges in modelling the evolution of stress corrosion cracks from pits", *Engineering Fracture Mechanics*, vol. 76, no. 5, pp. 633–640, 2009. DOI: 10.1016/j.engfracmech.2008.09.004.

[286] A. Turnbull, "Characterising the early stages of crack development in environment-assisted cracking", *Corrosion Engineering Science and Technology*, vol. 52, no. 7, pp. 533–540, 2017. DOI: 10.1080/1478422X.2017.1348761.

[287] M. Reyes and A. Neville, "Mechanisms of erosion-corrosion on a cobalt-base alloy and stainless-steel UNS S17400 in aggressive slurries", *Journal of Materials Engineering and Performance*, vol. 10, no. December, pp. 723–730, 2001, ISSN: 10599495. DOI: 10.1361/105994901770344610.

[288] B. Cullity, *Elements of X-Ray Diffraction*, 1st ed., M. Cohen, Ed. Adisson-Wesley Publishing Company, 1956, p. 525. DOI: 10.1017/CBO9781107415324.004.

[289] Y. Waseda, E. Matsubara, and K. Shinoda, *X-Ray Diffraction Crystallography*. Springer Heidelberg Dordrecht London New York, 2011, p. 322. DOI: 10.1007/978-3-642-16635-8.